Development of a non-invasive beam profile monitor based on hadronic beam-gas interactions for the High Luminosity Large Hadron Collider

Hélène Guérin

Department of Physics
Royal Holloway, University of London

A thesis submitted to the University of London for the degree of Doctor of Philosophy

January 2024

Declaration

I, Hélène Guérin, confirm that the work presented in this thesis is my own. Where information has been derived from other sources, I confirm that this has been indicated in the document.

Signed:

Date: 20/01/2024

To my four grand-parents,

*to Oscar, Ariane, **

Abstract

Emittance measurement at the Large Hadron Collider (LHC) is a challenging task, due to the high energy and intensity of the accelerated proton and ion beams. Current beam size monitors are either limited to low intensity beams or require calibration. There is consequently no continuous beam size, and therefore emittance, measurement available during the energy ramp. With the upcoming High Luminosity LHC (HL-LHC) upgrade, measuring the transverse emittance throughout the cycle becomes crucial to identify sources of emittance growth and maximise the luminosity of the upgraded collider.

The Beam Gas Vertex monitor (BGV) proposes using inelastic hadronic interactions of the LHC beams with a gas target to measure beam size and profile. A forward tracking detector enables the reconstruction of secondary particle trajectories and beam-gas interaction vertices. A beam profile image is then inferred from the distribution of measured vertices.

Based on the lessons learned from a demonstrator instrument operated in the LHC during Run 2, a new design is proposed for the HL-LHC future instrument (HL-BGV). It aims to provide absolute transverse beam size and bunch width measurements throughout the entire acceleration cycle, including the energy ramp. This design was optimised through various Monte Carlo simulation studies, which also served to estimate achievable performance. The revised gas tank and gas target designs benefit from a lower and negligible impact on machine operation concerning wakefield contributions, beam lifetime and emittance growth. The radiation impact of the HL-BGV target was also carefully considered.

The beam profile is unfolded from the distribution of measured vertices by evaluating the response function of the instrument, specific to a set of reconstructed interactions. At

the most demanding beam energy of 7 TeV, the proposed design is expected to reach a beam size accuracy of 5% and a bunch-by-bunch precision of 1% within less than 2.5 min of integration time. The possibility to reconstruct centred double Gaussian beam profiles was also demonstrated.

Acknowledgements

The recent adventures of the BGV involved many personalities. The present work was particularly supported by James, whose advice brought the instrument as close as allowed to life. Thank you Bernadette for sharing this journey with me, bringing your infectious enthusiasm to our work and teaching me all the qualities a researcher requires.

I am extremely grateful to Stephen for encouraging the development of exotic instruments and particularly for supporting my life choices. Thank you for your active support to women in science.

The BGV led me to various exciting fields. Robert introduced me to gaseous detectors, among many things I owe you the reconstruction of my first cosmic rays. Benoit and Manfred kindly guided me to understand the surface of impedance matters. Thank you for sharing your knowledge and reviewing my work. The same goes to Roberto, cheering and training generations of vacuum scientists.

I had the chance to share this experience with many brilliant and caring colleagues in BI and at CERN in general. It was highly enriched by jam sessions, Jura runs, mountaineering escapes, and both grumpy and rejoicing coffees. The good old Alps teams also played a crucial role, ensuring my mind's sanity and keeping me from becoming a serious person.

This work was only made possible thanks to the invaluable support, in all circumstances, of my parents and brother: for everything, thank you.

My most sincere thanks finally go to you, Alban, for your unconditional patience, emotional support, and for making us, me, our family, laugh and dream to infinity and beyond. To our two little sparks: your energy and happiness punctuated each individual sentence of this manuscript. Never lose them!

Contents

List of Figures

List of Tables

Chapter 1

Introduction

1.1 Project context

The Beam Gas Vertex (BGV) instrument [1,2] is a beam profile monitor under development for the High Luminosity upgrade of the Large Hadron Collider (HL-LHC) [3,4]. Its working principle is based on the reconstruction of beam-gas hadronic interaction vertices, through secondary particles tracking.

The idea originated from the LHC beauty (LHCb) experiment during Run 1 [5–7], which provided beam size measurements at collision energy via beam-beam and beam-gas interaction vertices reconstruction. A demonstrator BGV was then built in a short time, commissioned and operated at the Interaction Point 4 (IP4) of the LHC during Run 2, with the aim to exploit this method to measure the LHC beam size throughout the full LHC energy cycle. The tracking detector of this device was built from Scintillating Fibre (SciFi) detectors, provided by LHCb. Yet incapable of vertex reconstruction, the demonstrator BGV successfully provided online average beam size measurement throughout the LHC cycle, in good agreement with standard instruments [8].

Following these promising results, and with the interest raised to build a new beam size and profile monitor to support the commissioning of the HL-LHC, a design was proposed for an BGV instrument capable of measuring the HL-LHC beam size and profile.

1.2 Layout of work

This thesis presents part of the work which lead to the design proposed for the HL-LHC BGV (HL-BGV) instruments, the overall design of which is presented in Reference [2]. It

is structured as follows:

Chapter 2 introduces the CERN accelerator complex, with a focus on the LHC and its High Luminosity upgrade. It also gives an overview of relevant accelerator physics concepts. Chapter 3 discusses the current beam size monitors, and those at the project stage, on the LHC. The performance requirements for the HL-BGV are detailed in Chapter 4, and the Monte-Carlo simulation tool developed to guide the design of this instrument is described in Chapter 5. Chapters 6 and 7 respectively give a comprehensive description of the gas tank and gas target design of the HL-BGV. A method to unfold the response function of the BGV from the measured particle distribution and provide a beam profile measurement is finally proposed and tested on simulated data in Chapter 8. Chapter 9 concludes this thesis.

My main contributions to the design of the HL-BGV regard:

- Identification of possible instrument locations in the LHC;
- Implementation of the BGV simulation tool, in particular the algorithm building the geometry and part of the Geant4 algorithm;
- Identification of relevant detector technologies and assessment of their potential for the instrument's tracker;
- Comparison of gas target technologies and design of the final gas target with optimising its density profile;
- Assessment of the impact of the BGV target on the LHC beams;
- Optimisation of the instrument vacuum chamber shape, and study of its beam-coupling impedance contributions;
- Adaptation and testing of a method to unfold the vertex response of the instrument from the distribution of reconstructed vertices, which is the last step of the beam size and profile reconstruction algorithm.

Chapter 2

The CERN Large Hadron Collider and accelerator physics concepts

The European organisation for nuclear research (CERN) was founded in 1954, after World War II, with the aim to gather European scientists to explore the boundaries of fundamental physics. 70 years later, the organisation has grown and provides researchers with a network of particle accelerators and decelerators, shown in Figure 2.1. The Large Hadron Collider (LHC) [3] is one of these facilities.

Beams entering the LHC are first accelerated through its injectors chain [10], which involves for proton beams: the LINear ACcelerator 4 (LINAC4), the proton BOOSTER, the Proton Synchrotron (PS) and the Super Proton Synchrotron (SPS) [11]. For ion beams, particles are first accelerated in the LINear ACcelerator 3 (LINAC3) and in the Low Energy Ion Ring (LEIR) before entering the PS and SPS. Each of these facilities provides particles with a gain of kinetic energy. When reaching the LHC, proton beams have an energy of 450 GeV and are accelerated to produce 13.6 TeV collisions (6.5 TeV per beam).

2.1 The LHC and its High Luminosity upgrade

The main purpose of the LHC is to collide hadron (proton or ion) beams at high energy, at four independent high luminosity producing experiments. These experiments are installed around Interaction Points (IPs) and aim at detecting and analysing the collision products. This 27 km long machine is so far the largest worldwide accelerator, also reaching the highest colliding energy of 13.6 TeV in the Centre of Mass (CoM).

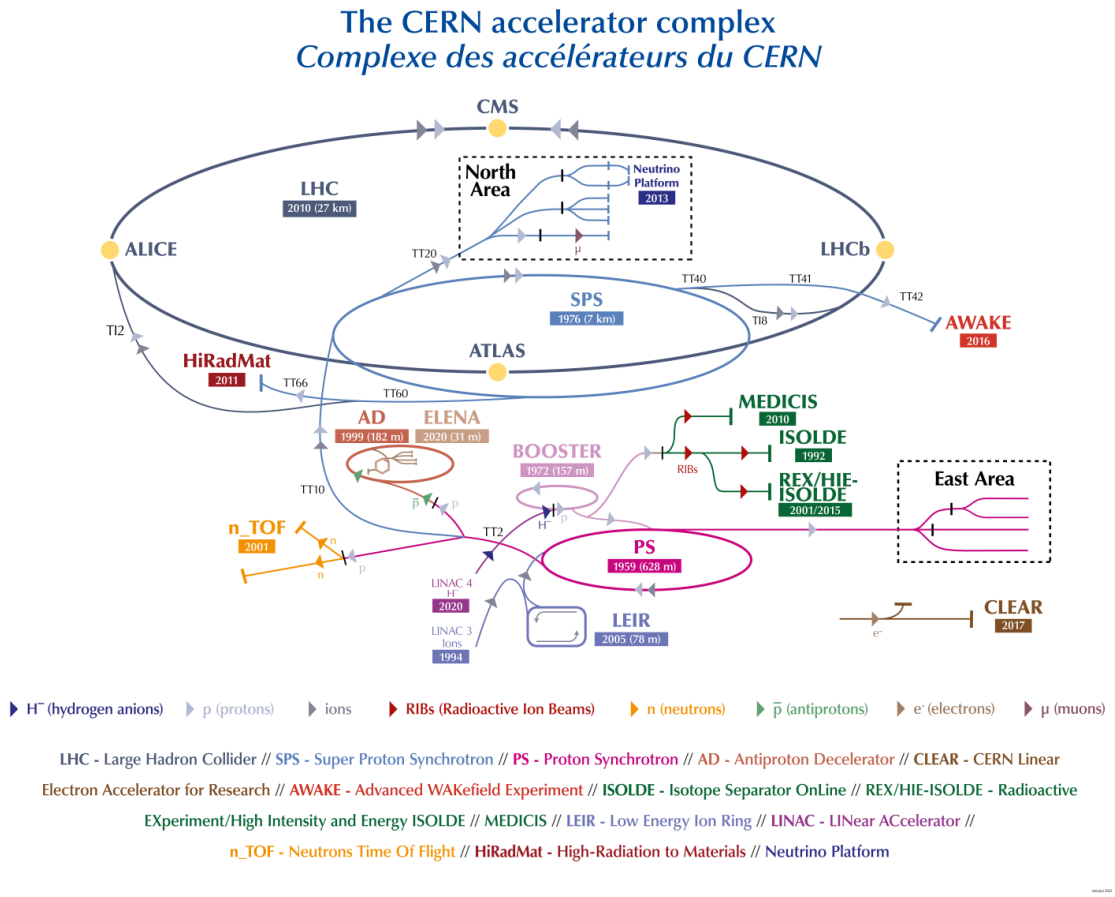

Figure 2.1: The CERN accelerator complex layout in 2022. [9]

The ability of a collider to generate a high amount of interesting and possibly rare events is expressed by its luminosity $\mathcal{L}$ [12]. This quantity corresponds to the factor relating the event production rate $\frac{\mathrm{d}N}{\mathrm{d}t}$ and the cross section σ_p of the event under consideration:

$$\frac{\mathrm{d}N}{\mathrm{d}t} = \mathcal{L}\ \sigma_p\,. \tag{2.1}$$

The instantaneous luminosity is expressed in $\mathrm{cm}^{-2}\,\mathrm{s}^{-1}$, or in fb^{-1} when integrated over time. Considering a circular collider of revolution frequency f_{rev}, it also reads:

$$\mathcal{L} = \frac{N_1 N_2 f_{\mathrm{rev}}}{4\pi\sigma_x\sigma_y} S\,, \tag{2.2}$$

where $\sigma_{x,y}$ represent the horizontal and vertical Gaussian beam widths at the interaction region, identical between the colliding beams, of populations N_1 and N_2. S is a geometrical reduction factor, which is equal to 1 when the two beams are colliding head-on, and smaller

than 1 when a crossing angle is introduced between the beams.

The coordinate system is depicted in Figure 2.2, where the s coordinate denotes the *longitudinal* direction and (x,y) represents the *transverse* plane with respect to the beam direction.

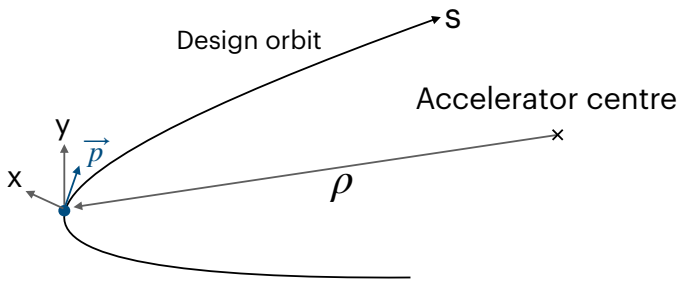

Figure 2.2: Coordinate system of a circulating particle in a circular accelerator. The s coordinate is defined along the design orbit, and refers to the *longitudinal* direction, opposed to the *transverse* plane (x,y).

The LHC machine was first started in 2008 and became fully operational in 2011. Its operation is organised into several phases of about 2 years long each, called Runs, which are separated by Long Shutdown periods (LS), during which significant machine maintenance and elements upgrade are performed. Each operation year also ends with a Year End Technical Stop (YETS). The approximate schedule of the LHC over the years is presented in Figure 2.3, together with the achieved and expected collider performance, indicated by its integrated luminosity and by the centre of mass collision energy.

LHC ⟷ HL-LHC

	Run 1		LS1		Run 2				LS2			Run 3				LS3			Runs 4-5
	2011	2012	2013	2014	2015	2016	2017	2018	2019	2020	2021	2022	2023	2024	2025	2026	2027	2028	2029-2040
Collisions CoM energy	7 TeV	8 TeV			13 TeV							13.6 TeV							13.6 - 14 TeV
Integrated Luminosity	30 fb^{-1}				190 fb^{-1}							450 fb^{-1}							3000 - 4000 fb^{-1}

Figure 2.3: LHC and HL-LHC operation and performance schedule over the years. Runs and LSs duration is rounded to years. Operational energies are given as the energy at the collisions Centre of Mass (CoM). [13]

A major machine upgrade is foreseen after Run 3, currently ongoing, with the aim to increase its instantaneous luminosity by a factor five compared to the original value, reaching $5 \times 10^{34}\,\mathrm{cm}^{-2}\,\mathrm{s}^{-1}$. This upgrade, and by extensions the upgraded machine, is called High Luminosity LHC (HL-LHC) [4]. The beam parameters of the LHC, as of

Run 2 and those foreseen for the HL-LHC are reported in Table 2.1.

Achieving a larger luminosity is envisioned by (1) increasing the beam intensity, with doubling the bunch population, and by (2) reducing the beam size at the IP, through stronger superconducting focusing magnets. *Crab-cavities* are also foreseen to be installed on either side of the interaction regions [4], in order to increase the geometrical factor S. These devices employ transverse electric fields to rotate the bunches so that the interaction region is reached with the bunches oriented longitudinally. In addition to these changes, many equipment systems will be upgraded to cope with the increased beam intensity (eg. beam collimators, injection and extraction systems, dump, etc.).

Table 2.1: Beam parameters for the LHC (as of Run 2) and HL-LHC machines.

Beam parameter	LHC Run 2 Proton runs [4]	HL-LHC Proton runs [4]	HL-LHC Ion runs [14]
Revolution frequency f_{rev}	11 245 Hz		
Number of bunches	2808	2760/2744 (Standard/BCMS)	1240
Particles per bunch	1.15×10^{11}	2.2×10^{11}	18×10^{7}
Total particles in the beam	3.2×10^{14}	6.1×10^{14}	2.2×10^{11}
Beam intensity	0.58 A	1.1 A	0.78 A
Beam energy	6.8 TeV	7 TeV	7 TeV
Normalised emittance (7 TeV)	3.75 µm	2.5 µm	1.65 µm
RMS energy spread (FWHM equiv. Gaussian)	1.13×10^{-4}	1.29×10^{-4}	1.29×10^{-4}

A careful and non-invasive monitoring of the HL-LHC beam size is therefore crucial to support the commissioning of this new machine and optimise its achievable luminosity. The following section introduces beam dynamics theory in circular particle accelerators. More details can be found for instance in [15, 16].

2.2 Motion of charged particles in synchrotrons

The motion of charged particles in accelerators is governed by the Lorentz force $\vec{F}_L$, according to the ElectroMagnetic (EM) fields perceived:

$$\frac{\mathrm{d}\vec{p}}{\mathrm{d}t} = \vec{F}_L = q(\vec{E} + \vec{v} \times \vec{B}). \tag{2.3}$$

A particle of charge q and velocity v can therefore be accelerated (or decelerated) along the direction of the gradient of an electric fields $\vec{E}$. At CERN, this is done with time-varying electric fields, generated in Radio Frequency (RF) cavities, which spawn

bunched beams. Besides, the particles' trajectory can be curved by magnetic fields $\vec{B}$, perpendicular to the particle motion direction. Various magnet types are used in particle accelerators: the beam is for instance bent by dipole magnets and focused by quadrupoles. Sextupole and octupole magnets are also used to compensate some magnet aberrations and beam instabilities. The composition of magnets constituting an accelerator is called the *lattice*. In the following, only transverse linear gradient magnets, i.e. dipoles and quadrupoles, will be considered.

When considering the transverse displacement of particles ($x(s)$,$y(s)$) decoupled between the transverse planes, and for a mono-energetic beam, whose particles share the same momentum, it can be shown that their transverse motion in a synchrotron of radius ρ obey the following homogeneous equations [16]:

$$\begin{cases} x'' + x\Big(\dfrac{1}{\rho^2(s)} + k(s)\Big) = 0 \\ y'' - yk(s) = 0 \end{cases} \Leftrightarrow \begin{cases} x'' + xK_x(s) = 0 \\ y'' + yK_y(s) = 0 \end{cases} . \tag{2.4}$$

These Hill's equations reveal that the particles oscillate in the transverse plane, according to *betatron* oscillations. While the vertical beam focusing is exclusively handled by the quadrupoles, of strength k, the dipoles generate an additional weak focusing effect, which contributes to the horizontal focusing. This effect however becomes small in large accelerators.

The solutions of the Hill's equations along one each transverse plane $u = \{x, y\}$ read:

$$\begin{cases} u_\beta(s) = a\sqrt{\beta_u(s)}\cos(\mu_u(s) + \mu_{u,0}) \\ u'_\beta(s) = -\dfrac{a}{\sqrt{\beta_u(s)}}\Big[\alpha_u(s)\cos(\mu_u(s) + \mu_{u,0}) + \sin(\mu_u(s) + \mu_{u,0})\Big] \end{cases} , \tag{2.5}$$

with $u' = \dfrac{\mathrm{d}u}{\mathrm{d}s}$ a particle's divergence. $\mu_u(s) = \displaystyle\int_0^s \frac{\mathrm{d}s}{\beta_u(s)}$ [rad] is the *phase advance*, and its normalisation to 2π represents the number of oscillations per turn, called *tune*: $Q_u = \dfrac{1}{2\pi}\displaystyle\int_0^s \frac{\mathrm{d}s}{\beta_u(s)}$. The *Twiss parameters* α_u, β_u and γ_u satisfy

$$\alpha(s) = -\frac{1}{2}\frac{\mathrm{d}\beta}{\mathrm{d}s}, \quad \gamma(s) = \frac{1 + \alpha(s)^2}{\beta(s)} . \tag{2.6}$$

$\beta(s)$ [m] is a periodic function, called *beta function*, and is determined by the focusing

properties of the lattice. a^2 is the Courant-Schnyder invariant, so that:

$$a^2 = \gamma_u(s)u(s)^2 + 2\alpha_u(s)u(s)u'(s) + \beta_u(s)u'(s)^2\,. \tag{2.7}$$

An example beam particles distribution in the phase space (u, u') is shown in Figure 2.4. Turn after turn, the position u and divergence u' of a particle evolve in the phase space with describing a ellipse, parameterised by the Twiss parameters at the considered position s.

The geometric *emittance* ε [rad m] is defined proportionally to the area of the ellipse containing a given proportion of the beam particles: $\varepsilon = \pi a^2$. Assuming a Gaussian beam along each transverse plane, the 1-σ emittance will be considered in the following, which includes 68% of the beam particles. Along the machine, the shape of the ellipse varies but its area remains constant in the absence of energy change.

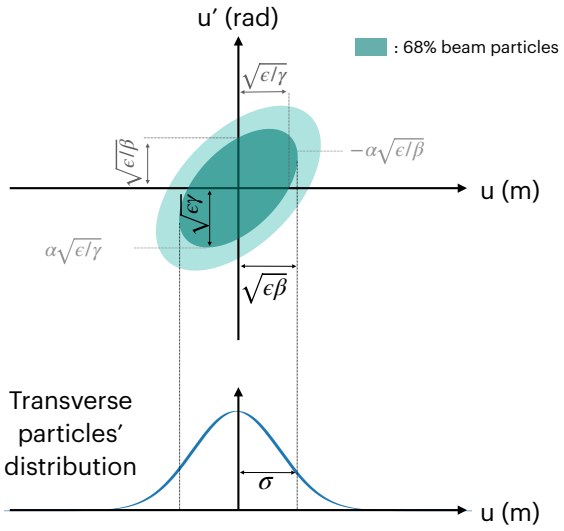

Figure 2.4: Beam particle ellipse distribution in the transverse phase space, and projection along one axis.

For a Gaussian beam profile, the transverse beam size σ_u along one plane is defined as:

$$\sigma_u = \sqrt{\varepsilon_u \beta_u}\,. \tag{2.8}$$

When particles are accelerated, their longitudinal momentum component is increased, and the particles' divergence u' decreases. The phase space ellipse area shrinks, and so do the geometrical emittance and the beam size. This effect is called *adiabatic damping*. Since the geometrical emittance is not constant along the acceleration cycle, the

normalised emittance ε_n is introduced, which takes into account the relativistic beta β_r, with c the speed of light and gamma γ_r factors:

$$\varepsilon_n = \beta_r \gamma_r \varepsilon \,, \quad \begin{cases} \beta_r = \dfrac{v}{c} \\ \gamma_r = \dfrac{1}{\sqrt{1-\beta^2}} \end{cases} . \tag{2.9}$$

A mono-energetic beam was considered so far. In practical cases, most particles circulate with a momentum different from the one of the synchronous particle p_0: $p = p_0 \pm \Delta p$. Each dipole bends the particles' trajectory according to their momentum: particles with a higher momentum circulate on a larger orbit compared to particles with lower momenta. The beam momentum spread therefore leads to a horizontal beam broadening. This effect is characterised along the machine by the *dispersion* function $D(s)$ [m], which relates the momentum deviation Δp to a transverse deviation $x(s)$ as:

$$x_D(s) = D(s)\frac{\Delta p}{p_0} \tag{2.10}$$

The equations of motions can be adapted to account for this effect:

$$\begin{cases} x'' + x\Big(\dfrac{1}{\rho^2(s)} + k(s)\Big) = \dfrac{1}{\rho(s)}\dfrac{\Delta p}{p} \\ y'' - yk(s) = 0 \end{cases} , \tag{2.11}$$

and the new horizontal solution $x(s)$ equals the mono-energetic one $x_\beta(s)$, with a broadening term:

$$x(s) = x_\beta(s) + D(s)\frac{\Delta p}{p_0} \,. \tag{2.12}$$

A complete expression of the beam size is given by

$$\begin{cases} \sigma_x(s) = \sqrt{\varepsilon_x \ \beta_x(s) + \Big(D(s) \ \dfrac{\Delta p}{p_0}\Big)^2} \\ \sigma_y(s) = \sqrt{\varepsilon_y \ \beta_y(s)} \end{cases} . \tag{2.13}$$

A vertical dispersion term may also arise from non-perfect magnets alignment.

The spread of the phase-space ellipse of the LHC beam is limited by a beam collimation system [17]. Its main purpose is to minimise the amount of unavoidable lost particles hitting the superconducting magnets, keeping the deposited energy below quenching thresholds. The collimation system also contributes to limit radiation towards the acceler-

ator equipment and minimises background in the experiment's detectors. The particles at the periphery of the beam, constituting its *halo*, are "trapped" by the numerous collimator jaws, placed close to the beam, and the remaining core beam is called the transverse *envelope*.

The longitudinal particle motion is ruled by RF voltage, and a similar periodic oscillation pattern is observed with a time delay from the ideal synchronous particle. The *synchrotron tune* $Q_s = w_s/\omega_{\text{rev}}$ is defined as the ratio between the angular frequency ω_s of these *synchrotron oscillations*, and the angular beam revolution frequency ω_{rev}.

Another notable consequence of the momentum spread is *chromaticity*. A quadrupole's focusing strength acting on particles is a function of a particle's momentum. Off-momentum particles therefore experience a betatron tune shift ΔQ compared to the betatron tune of the synchronous particle Q. This effect is quantified by the chromaticity ξ:

$$\frac{\Delta Q}{Q} = \xi \frac{\Delta p}{p_0} \,. \tag{2.14}$$

Although introduced by the lattice itself, this effect is unwanted: particles reaching an integer tune would meet a beam resonance and their oscillation amplitude would grow until the particles are lost. Chromaticity can be controlled by introducing sextupole magnets, which provide an energy-dependant focusing effect.

Basic transverse beam dynamic notions were presented in this section. While external EM fields are used to accelerate, guide and focus the beam, particles also perceive the fields generated by their fellow circulating particles. The subsequent *Space Charge* (SC) effects scale with the beam intensity and can be either *direct*, or *indirect*, when involving particles interaction with the beam chamber walls. The first effects are proportional to $\frac{1}{\gamma^2}$ and are negligible for ultra-relativistic beams compared to indirect space charge interactions. With possible consequences on beam particle motion, machine performance limitations and impact on accelerator components, the second phenomenon is introduced in the following section. Detailed descriptions of these concepts can be found in References [18–20].

2.3 Wakefield and impedance concepts

A particle of charge q moving in free space at a velocity v generates electromagnetic fields. In the ultra-relativistic case, the field lines contract into a disk perpendicular to the particle's motion direction, with an opening angle ϕ scaling with $1/\gamma_r$. This case is represented in Figure 2.5 left. The same conclusion applies to a particle travelling in a constant cross section (smooth) pipe with perfectly conducting walls, depicted in Figure 2.5 right.

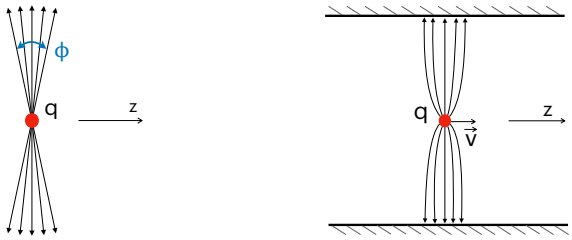

Figure 2.5: Electric field of a relativistic point charge moving along z in free space (left) and in a constant cross-section geometry with perfectly conducting walls (right).

In the more general case where a relativistic charged particle travels through a beam pipe of finite conductivity or faces changes in the pipe cross section, as illustrated in Figure 2.6, the generated electromagnetic fields are distorted compared to the free space case to satisfy the boundary conditions imposed by the walls. The passing particle generates so-called *wakefields* that cause forces on the trailing particles altering their motion. For some simple geometry cases, analytical expressions can be derived by solving Maxwell's equations. In most practical cases, wakefields are computed using numerical methods with dedicated software like *CST Studio* [21].

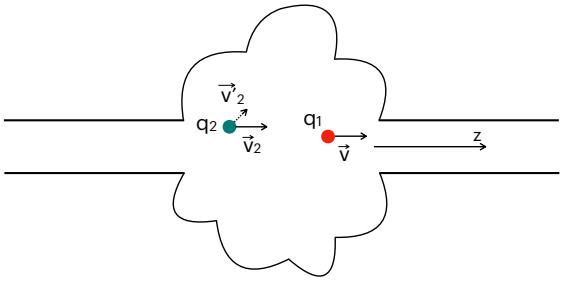

Figure 2.6: Point particle of charge q_1 traversing a cavity with finite conductivity walls, followed by a trailing particle of charge q_2.

A general case is considered in the following, where a trailing test particle of charge q_2, with the transverse position vector $\vec{r_2}$, travelling behind a source particle of charge

q_1, with the transverse position vector $\vec{r_1}$. In the Cartesian coordinate system ($\vec{x}$, $\vec{y}$, $\vec{z}$) considered here, both the source and the test particles are travelling along $\vec{z}$, with respective offsets $\vec{r_1} = (x_1, y_1)$ and $\vec{r_2} = (x_2, y_2)$. The test particle travels at a distance $s = z_1 - z_2 = v\,\tau$, or arrives with a delay τ behind the source particle. The Lorentz force it perceives from the EM fields generated by the leading particle is:

$$\vec{F}(\vec{r_1}, \vec{r_2}, t) = q_2[\vec{E}(\vec{r_1}, \vec{r_2}, t) + \vec{v} \times \vec{B}(\vec{r_1}, \vec{r_2}, t)]\,, \tag{2.15}$$

where $\vec{E}$ and $\vec{B}$ are the electric and magnetic fields generated by the source particle respectively.

The time-space dependent wakefields generated by the source particle q_1, travelling with constant velocity v, will only affect the trajectory of the test particle q_2, which follows at some constant distance s, through a change of its momentum $\Delta\vec{p}$:

$$\Delta\vec{p}(\vec{r_1}, \vec{r_2}) = \int_{-\infty}^{\infty} \vec{F}(\vec{r_1}, \vec{r_2}, t)\ \mathrm{d}t\,. \tag{2.16}$$

2.3.1 Definitions

The *wake function* $\vec{w}(s)$ is defined for a point source as:

$$\vec{w}(\vec{r_1}, \vec{r_2}; s) = -\frac{1}{q_1}\int_{-\infty}^{\infty} \vec{F}(\vec{r_1}, \vec{r_2}, t)\ \mathrm{d}z, \quad t = \frac{z_1}{v} + \tau\,, \tag{2.17}$$

so that $\Delta\vec{p} = \dfrac{1}{v}\ q_1 q_2\ \vec{w}(s)$. The wake function of a beam chamber piece or accelerator component corresponds to the response of the system to a pulse excitation, equivalent to a Dirac delta function, and is independent on the beam properties.

The *wake potential* $\vec{W}(s)$ is defined in the case where, instead of a point charge, the considered excitation source is a bunch of particles of longitudinal charge distribution $\lambda(z)$, and total charge $q_1 = \displaystyle\int_{-\infty}^{\infty} \lambda(z)\ \mathrm{d}z$. The wake potential is equal to the convolution of the wake function with the source charge distribution:

$$\vec{W}(\vec{r_1}, \vec{r_2}; s) = \int_{-\infty}^{\infty} \vec{w}(\vec{r_1}, \vec{r_2}; s + z')\ \frac{\lambda(z')}{q_1}\ \mathrm{d}z'\,. \tag{2.18}$$

The force $\vec{F}(\vec{r_1}, \vec{r_2}, t)$ perceived by the test particle can be decoupled into longitudinal

($F_\parallel$) and a transverse ($\vec{F}_\perp$) components, which can be treated separately:

$$F_\parallel(\vec{r_1}, \vec{r_2}, t) = q_2 E_\parallel \,, \tag{2.19}$$

$$\vec{F}_\perp(\vec{r_1}, \vec{r_2}, t) = q_2[\vec{E}_\perp + (\vec{v} \times \vec{B})_\perp] \,. \tag{2.20}$$

The same applies to the wake function and wake potential, respectively noted $w_\parallel$ and $W_\parallel$ in the longitudinal direction, and $\vec{w}_\perp$ and $\vec{W}_\perp$ in the transverse plane.

The Panofsky-Wenzel theorem demonstrates, that for constant particle velocities, the rotation of the momentum change vector is null: $\vec{\nabla} \times \vec{\Delta p} = 0$. Therefore follows the longitudinal wake function is the derivative of the transverse wake function with respect to s:

$$w_\parallel(s) = \frac{\partial}{\partial s} \vec{w}_\perp(s) \,. \tag{2.21}$$

$w_\parallel$ has the dimensions [V/C] and $\vec{w}_\perp$ [V/C m].

2.3.2 Longitudinal properties

When considering ultra-relativistic particles with trajectories parallel to $\vec{z}$, since $F_\parallel$ has only electrical field components, $\vec{B}$ is purely transverse. At a given distance s of the test particle from the source particle, the longitudinal wake potential therefore corresponds to the voltage gained by the unit test charge due to the longitudinal wakefields. The wake function at $s = 0$ corresponds to the energy lost by the source particle due to the generation of the wake. This energy stored in the wake fields will either (1) be trapped in the structure, in which the resonant modes will oscillate until the energy dissipates in the non-perfectly conducting walls or in specifically designed absorbers, or be transferred to the following particles, possibly driving beam instabilities, or (2) travel as guided EM-waves in the accelerator beam pipes, if satisfying the boundary conditions given by the beam pipe cross-section, or otherwise unguided.

In circular accelerators it often is more convenient to address beam dynamic problems in the frequency domain. The *longitudinal beam-coupling impedance* $Z_\parallel$ is introduced for this purpose, and is the analogue quantity of the wake function, expressed in the frequency domain and is obtained from its Fourier transform:

$$Z_\parallel(\vec{r_1}, \vec{r_2}; \omega) = \int_{-\infty}^{\infty} w_\parallel(\vec{r_1}, \vec{r_2}; s)\; e^{-\frac{j\omega s}{v}}\; \frac{\mathrm{d}s}{v} \quad [\Omega] \,, \tag{2.22}$$

where j is the imaginary unit and $\omega = 2\pi f$ the angular frequency. It is a property of a given vacuum chamber or accelerator component, and a complex quantity of the frequency, with a resistive $\mathrm{Re}(Z)$ and a reactive $\mathrm{Im}(Z)$ part. Because the wake function is real, $\mathrm{Re}(Z)$ is an even and $\mathrm{Im}(Z)$ an odd function of the frequency. A strong coupling between the beam and a vacuum chamber component occurs if both the vacuum device impedance and beam spectrum have high values at a given frequency.

In the case of axi-symmetric structures, the source (or beam) charge can be considered as a superposition of charged rings, exciting azimuthal modes. The subsequent EM fields can be expanded into a multipole series $\sum_{m=0}^{\infty} \cos(m\theta)$ in a cylindrical frame (r,θ,z), and so can be the resulting wakefield and impedance, which are integrals over these fields. In the ultra-relativistic limit, it can be shown that:

$$Z_{\parallel}(r_1, r_2, \theta; \omega) = \sum_{m=0}^{\infty} r_1^m r_2^m \bar{Z}_{\parallel,m}(\omega) \cos(m\theta)\,, \quad m \geq 0\,, \tag{2.23}$$

where $\bar{Z}_{\parallel,m}$ has the dimension $[\Omega/\mathrm{m}^{2\mathrm{m}}]$. For such structures, close to the beam axis, $Z_{\parallel}$ is dominated by the monopole term $m = 0$, which is independent on the transverse position of the beam particles.

2.3.3 Transverse properties

In the transverse plane, the wake potential represents the transverse momentum perturbation ("kick") perceived by the test particle.

The *transverse beam-coupling impedance* $Z_{\perp}$ is defined as:

$$\vec{Z}_{\perp}(\vec{r_1}, \vec{r_2}; \omega) = j \int_{-\infty}^{\infty} \vec{w}_{\perp}(\vec{r_1}, \vec{r_2}; s)\; e^{-\frac{j\omega s}{v}}\; \frac{\mathrm{d}s}{v} \quad [\Omega\,\mathrm{m}^{-1}]\,. \tag{2.24}$$

Similarly to the longitudinal impedance, $\vec{Z}_{\perp}$ can be expanded in a multipole series of the source and test particles with transverse offsets. The Panofsky-Wenzel theorem relates the longitudinal and transverse impedance components by:

$$\vec{Z}_{\perp}(\omega, \vec{r_2}) = \frac{v}{\omega} \vec{\nabla}_{\perp} Z_{\parallel}(\omega, \vec{r_2})\,, \tag{2.25}$$

where $\vec{\nabla}_{\perp}$ only acts on the $\vec{r_2}$ coordinates. It follows that, in the case of axi-symmetric structures and for small displacements, the transverse impedance is dominated by the

dipole mode $m = 1$. Neglecting second order and coupling terms, in the frame represented in Figure 2.2, its components can be approximated to:

$$Z_{x,y}(\omega) \simeq r_1 \, Z_{x,y}^{\mathrm{dip}}(\omega) + r_2 \, Z_{x,y}^{\mathrm{quad}}(\omega) \,, \tag{2.26}$$

where $Z_{x,y}^{\mathrm{dip}}$ is called dipolar (or driving) term and $Z_{x,y}^{\mathrm{quad}}$ quadrupolar (or detuning) term. For resistive wall contributions in axi-symmetric structures, this last term becomes negligible if the considered beam is ultra-relativistic.

2.3.4 Wakefield sources

The beam-coupling impedance of a given vacuum device in an accelerator can be dominated by geometrical or resistive wall effects.

Cavity-like structures traversed by a charged particle beam behave like a passive resonant cavity. Their impedance is equal to the sum of the contribution of each resonant mode i, each characterised by a shunt impedance $R_{s,i}$ [Ω] (longitudinal modes), a transverse resistance $R_{\perp,i}$ [$\Omega\,\mathrm{m}^{-1}$], and a quality factor Q_i for a specific resonant frequency $\omega_{r,i}$. The resulting resonator model for i separate modes reads:

$$Z_{\parallel}(\omega) = \sum_i \frac{R_{s,i}}{1 + jQ_i\Big(\dfrac{\omega}{\omega_{\mathrm{r},i}} - \dfrac{\omega_{\mathrm{r},i}}{\omega}\Big)} \tag{2.27}$$

$$Z_{\perp}(\omega) = \sum_i \frac{\omega_{r,i}}{j\omega} \frac{R_{\perp,i}}{1 + jQ_i\Big(\dfrac{\omega}{\omega_{\mathrm{r},i}} - \dfrac{\omega_{\mathrm{r},i}}{\omega}\Big)} \,. \tag{2.28}$$

The beam excited modes trapped in the vacuum structure are often characterised by a series of narrow-band resonant peaks in the frequency domain, and can oscillate for a long time in the structure after the bunch passage.

Beam chamber walls with poor electrical conductivity lead to pulling or decelerating forces, which are proportional to the beam current. Several regimes can be identified, depending on how the frequency-dependent skin depth compares to the wall thickness of the vacuum chamber. The resulting wakefields may generate broad-band impedance contributions, which increase with the resistivity of the wall material and with the proximity of the beam to the resistive wall, particularly in the transverse plane.

Each vacuum chamber component of an accelerator can be represented in the fre-

quency domain by its beam-coupling impedance, and assuming no or only negligible EM coupling is present between those components, the impedance model of the entire machine is obtained by summing the impedance contributions of all individual vacuum components. Such a model is valuable to study beam instabilities potentially caused by wakefields.

2.3.5 Impacts of wakefields

In some cases, wakefields can generate heating of vacuum components and affect the beam stability.

2.3.5.1 Beam-induced RF heating

The energy dissipated into the walls of the vacuum component due to wakefields induces a heating of the wall material of finite electrical conductivity and therefore may damage the equipment. In case high temperatures are reached locally, outgassing from the beam chamber may also occur.

For devices traversed by a single beam, this effect is driven by the real part of the longitudinal coupling impedance $\mathrm{Re}[Z_{\parallel}]$. In a circular machine, the power lost by a circulating beam of current I_{b} and normalised power density spectrum $\Lambda(\omega)$, interacting with a component of impedance Z is given by:

$$P_{\mathrm{loss}} = 2I_{\mathrm{beam}}^2 \sum_{p=0}^{p} |\Lambda(p\,\omega_{\mathrm{rev}})|^2 \,\mathrm{Re}[Z_{\parallel}(p\,\omega_{\mathrm{rev}})]\,, \tag{2.29}$$

where $\omega_{\mathrm{rev}} = 2\pi f_{\mathrm{rev}}$ is the angular revolution frequency, and the sum is made over the beam harmonics $p\,\omega_{\mathrm{rev}}$. The beam spectrum, which is related to the bunch length, also plays an important role in the dissipated power. To limit RF heating related issues, the bunch length of the LHC was already increased during Run 1. Careful attention also was taken to minimise the impedance of each accelerator component being part of the vacuum system by optimising its design. A numerical analysis of the eigen-mode patterns was performed for resonant structures, enabling to guide the design and estimate which area of the vacuum structure may suffer from beam-induced RF heating.

2.3.5.2 Beam stability and effective impedance

Acting as external EM forces, wakefields can also affect the beam dynamics, potentially leading to emittance growth or triggering beam instabilities. A beam instability limit is

defined through the maximum beam intensity ensuring a safe operation of the accelerator. Therefore, impedance thresholds or *budgets* can be imposed to limit impedance-driven instabilities and enhance the machine performance.

Different types of instabilities can be induced by the wakefields, e.g., depending on their decay time: *short-range wakes* generated by the head of a bunch can impact the motion of the particles at the bunch tail (head-tail coupling), while multi-bunch or even multi turn instabilities may arise from narrow-band impedance sources, and are caused by *long-range wakes*.

A quantity called the *effective coupling impedance* was introduced for both, the longitudinal $(Z_\parallel/n)_{\text{eff}}$ and the transverse $(Z_\perp)_{\text{eff}}$ planes, specifically to study single bunch instabilities. Here, n designates the revolution harmonic number $n = \dfrac{\omega}{\omega_{\text{rev}}}$. The effective impedance is defined as the convolution, i.e. a multiplication in the frequency domain, of the coupling impedance and the normalised beam spectral density $h_l(\omega)$ for a specific type of oscillation mode l of the bunch:

$$\left(\frac{Z_\parallel}{n}\right)_{\text{eff}} = \frac{\sum_{p=-\infty}^{\infty} Z_\parallel(\omega')\frac{\omega_{\text{rev}}}{\omega'}\, h_l(\omega')}{\sum_{p=-\infty}^{\infty} h_l(\omega')} \tag{2.30}$$

$$(Z_\perp)_{\text{eff}} = \frac{\sum_{p=-\infty}^{\infty} Z_\perp(\omega'+\omega_\beta)\, h_l(\omega'+\omega_\beta-\omega_\xi)}{\sum_{p=-\infty}^{\infty} h_l(\omega'+\omega_\beta-\omega_\xi)}\,. \tag{2.31}$$

with $\omega' = p\,\omega_{\text{rev}} + l\,\omega_s$, ω_s being the angular synchrotron oscillation frequency, ω_β the betatron angular oscillation frequency, and ω_ξ the frequency shift due to the chromaticity. $l = 0$ represents no bunch oscillation, therefore the unperturbed bunch distribution, and higher order modes ($l > 0$) correspond to oscillations of the bunch, e.g. dipole mode for $l = 1$, quadrupole mode for $l = 2$, etc.

For long bunches compared to the beam chamber aperture, as it is the case in the LHC, $(Z_\parallel/n)_{\text{eff}}$ is constant and purely imaginary.

2.3.6 Conclusion

Wakefields can lead to challenges in the beam operation, impacting the beam quality and even damaging accelerator equipment. Wakefield effects are proportional to the beam intensity. With the upcoming increase of the LHC beam intensity towards the HL-LHC upgrade, a careful limitation and accurate estimation the beam-coupling impedance of the overall machine are critical to optimise its performance.

The impedance footprint of a given accelerator component can be characterised for both the longitudinal and the transverse plane by two contributions:

- a broadband contribution, called the effective impedance, which is constant and purely imaginary at low frequency,
- and resonant modes, each represented by a shunt impedance, quality factor and resonant frequency.

The quantities introduced in this section will be used in Chapter 6.

Chapter 3

Transverse beam size and profile monitoring in the LHC

The transverse emittance is a particularly crucial beam parameter impacting the LHC luminosity. Its preservation, and thus the optimisation of the LHC performance, rely on a precise monitoring at all stages of the machine energy cycle. With high intensity and high energy, the LHC hadron beams present a particular challenge in terms of instrumentation and diagnostics, given the high power carried by the beam and the need to provide a non-invasive measurements, preserving the beam quality for the physics experiments.

The transverse emittance can be derived from a beam size measurement at any location along the ring:

$$\varepsilon = \frac{1}{\beta(s)}\left[\sigma^2 - \left(D(s)\frac{\Delta p}{p}\right)^2\right]. \tag{3.1}$$

Locations with negligible dispersion are preferred to perform the beam size measurement, in which case the emittance can be derived with knowing the beam optics functions. When this is not the case, deriving the transverse emittance requires knowing dispersion and momentum spread.

Several types of monitors have been used or considered to measure the LHC transverse beam profile. All of them are installed around the Interaction Point 4 (IP4), as illustrated in Figure 3.1, which corresponds to the straight section of the LHC hosting the accelerating RF cavities, where the beam optics remain by design almost identical along the acceleration cycle, and where the dispersion is low.

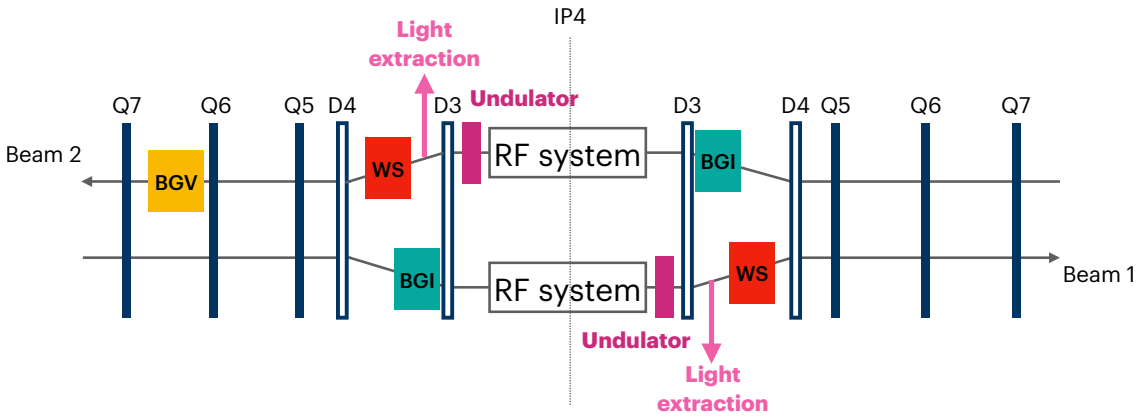

Figure 3.1: Location of the beam size instruments around the LHC IP4. The position of dipole (D) and quadrupole (Q) magnets are indicated.

3.1 Beam intercepting wire monitor

Each LHC beam is equipped with two Wires Scanners (WS) [22] for beam size measurement along each transverse plane. These instruments, schematised in Figure 3.2, consist of a thin carbon wire, which is passed through the beam at a speed of $1\,\mathrm{m\,s^{-1}}$. The beam-wire interactions generate radiation showers, detected downstream by scintillating detectors, coupled to Photo Multiplier Tubes (PMTs). As the wire traverses the beam, the emitted radiation, and therefore the current issued from the PMTs, is proportional to the beam density at the wire position, which allows to reconstruct the beam profile along each transverse plane.

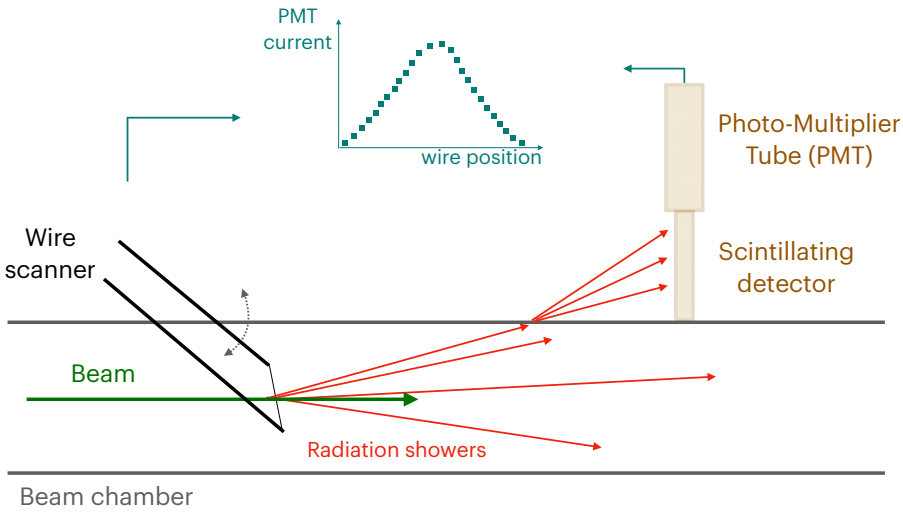

Figure 3.2: Functioning principle of a wire scanner. The beam profile is reconstructed with considering the intensity recorded by the detector as the wire traverses the beam.

The WS are considered to provide very accurate measurements thanks to the high

resolution in the wire position, in the order of 1 µm, and to the low wire thickness (36 µm at the LHC). The wire scanning speed however limits the usage of the WS to low intensity beams, in order to avoid wire breakage or quenching of the downstream superconducting magnets at collision energy, caused by the WS radiation. Although unable to monitor the bunch-by-bunch beam size during physics fills, the LHC wire scanners provide the reference beam size measurement and serve to calibrate other beam size monitors.

3.2 Synchrotron radiation based monitor

The parasitic Synchrotron Radiation (SR) emitted by highly relativistic charged particle beams when deviated is commonly used for non-invasive beam diagnostics in high energy synchrotrons. At the LHC, the Beam Synchrotron Radiation Telescope monitors (BSRTs) [23] measure the size of the beam by imaging the SR generated by a separation dipole D3, intended to deviate the beams to make room for the RF accelerating cavities. The synchrotron light is extracted from the beam chamber thanks to a mirror placed about 20 m downstream via a view port. It is then transferred to an optical bench and collected by an intensified camera.

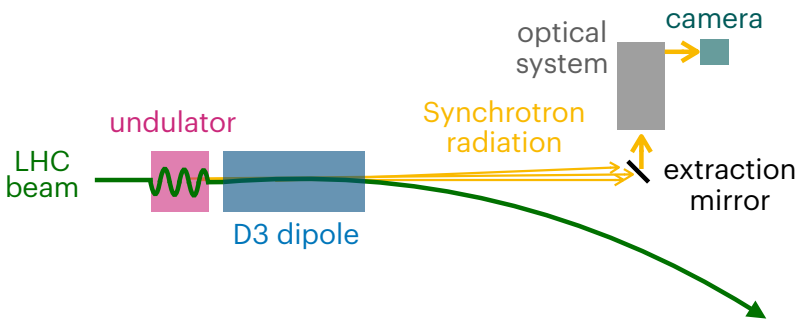

Figure 3.3: Functioning principle of the LHC BSRT.

At low energy, an undulator installed upstream of the dipole enhances the visible component of the generated SR. As the beam gains energy during the ramp, the wavelength spectrum of the generated SR shifts and the dipole becomes the main source of SR of the BSRT.

Due to the complexity of the radiation source, and to the diffraction introduced by the long optical path, a large correction has to be applied to the measured profile in order to reconstruct the beam size. The BSRT is therefore calibrated with the WS at injection and collision energies. It provides a continuous and non-invasive average and bunch-by-bunch

beam size measurement during these two steps. During the energy ramp however, the source change prevents a meaningful measurement. Interferometry techniques are under study, for a SR based monitor to provide an independent beam size measurement [24].

3.3 Beam-gas ionisation based monitor

Beam Gas Ionisation monitors (BGIs), also known as Ionisation Profile Monitors (IPMs), were installed on the IP4 of the LHC, in addition to the previously described monitors. Their principle is based on the ionisation of residual or injected gas by the beam. The resulting electrons are accelerated towards one side of the vacuum chamber, thanks to a strong transverse electric field. On the LHC devices, depicted in Figure 3.4, the ionisation electrons are multiplied by a Multi-Channel Plate (MCP), before reaching a phosphor screen, which illuminates the electrons distribution. The resulting image is then transferred to an intensified camera located outside the beam chamber, by a dedicated optical system.

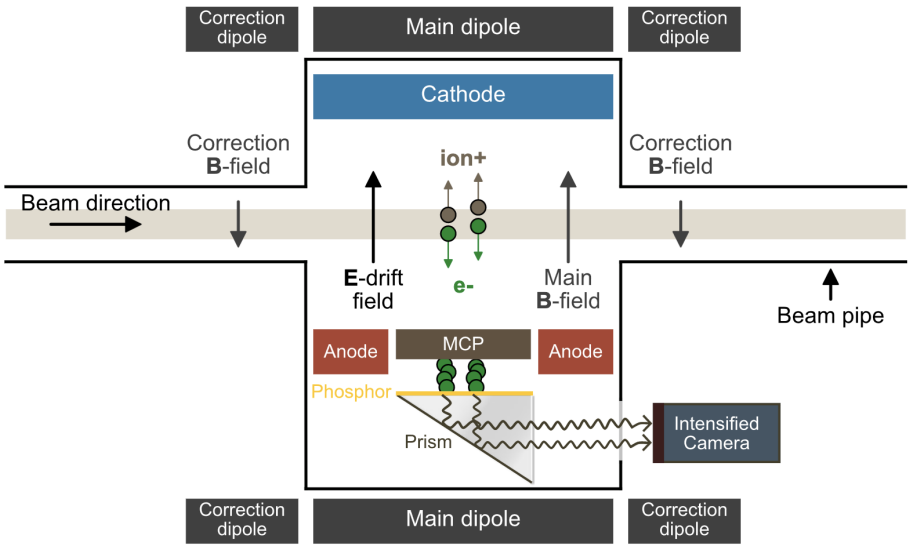

Figure 3.4: Functioning principle of the LHC BGIs. *(Courtesy J. Storey)*

These instruments however suffered from beam-induced RF heating and radiation damages from the ionisation electrons, which caused an in-homogeneous ageing of the MCP and phosphor screen. Measurements comparison with other profile monitors also revealed profile distortions, due to both material ageing and space charge effects, at beam energies above 4 TeV [25]. The BGIs could therefore not be used to provide a reliable LHC beam size measurement and were removed from the machine.

A new BGI design is being deployed at the PS [26] and SPS, where the electron profile is directly detected by a Hybrid silicon Pixel Detector (HPD) placed inside the vacuum chamber. This design will be adapted for the LHC, tackling the issues encountered by the previous version, and new BGIs should be installed in the LHC during LS3.

3.4 Beam-gas hadronic interaction based monitor

The idea to use inelastic hadronic interactions to measure the beam size emerged from promising results obtained by the LHCb experiment [27]. The VErtex LOcator (VELO) detector of LHCb demonstrated the feasibility to image the LHC beam profile at collision energy, with reconstructing beam-beam or beam-gas interaction vertices, via means of secondary particles tracking [28]. A beam profile image is obtained from the accumulation of vertices over time.

To perform this measurement, the VELO detector layers are brought close to the beam, which is only allowed at collision energy, when the beam size is small. These results therefore only concern 7 TeV beams.

A demonstrator instrument exploiting this principle [1, 29, 30] was conceived, installed and commissioned during Run 2 to study the possibility to monitor the beam size and profile throughout the full LHC energy cycle. Such a device is called Beam Gas Vertex monitor (BGV). Figure 3.5 presents the working principle of the BGV:

- The beam traverses a gas target, the pressure of which is adjusted to generate the desired interaction rate;
- Inelastic hadronic interactions between the beam particles and gas nuclei generate secondary particles, which traverse the beam chamber and are detected by tracking detectors, placed outside of the LHC vacuum;
- Reconstruction algorithms process the tracker information to reconstruct the interaction vertices: the secondary particles transverse positions recorded by the detectors, *hits*, are associated to reconstruct their trajectories, *tracks*, and a vertex position is computed from a collection of synchronous tracks.
- The beam profile image is unfolded from the density distribution of the reconstructed vertices.

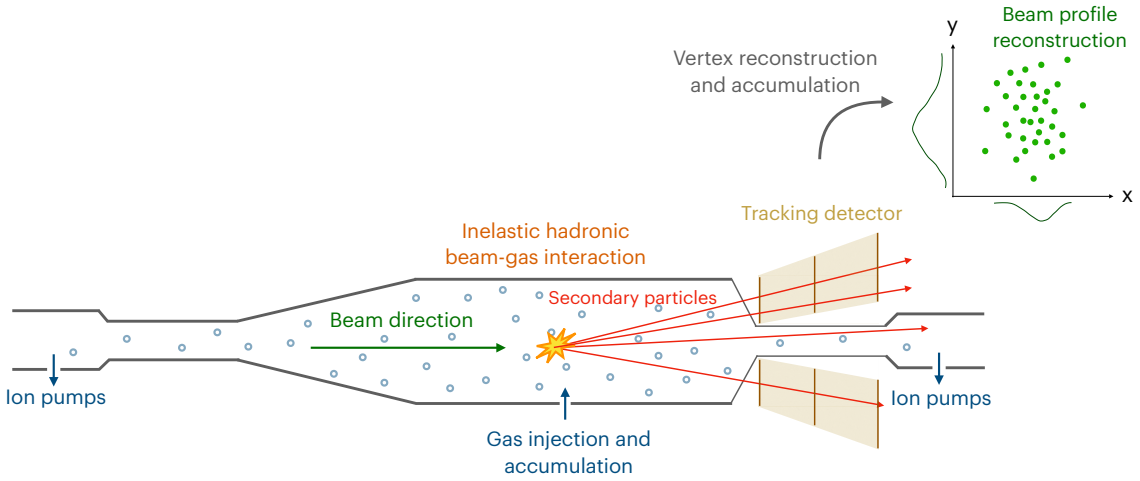

Figure 3.5: Functioning principle of the BGV.

The demonstrator BGV, shown in Figure 3.6, was built in collaboration with the LHCb experiment and installed on the LHC Beam 2. Its gas target consists of a 1.8 m long tank containing Neon at a 10×10^{-7} mbar pressure. The instrument's tracker was built using scintillating fibre modules, read out with silicon photo-multipliers, originally developed for the LHCb SciFi detector upgrade [31]. The measurements and the performance of this instrument are presented in [8]. The demonstrator instrument did not achieve vertex reconstruction. However, a correlation method was used, which allowed to provide horizontal and vertical average beam size measurements, in good agreement with the WS and BSRT, all along the acceleration cycle. Beam size measurement during the ramp in particular had not been achieved yet by any other instrument at the LHC. An average beam size precision in the order of 3% was reached for an integration time of about 1 min. This device thus successfully demonstrated the feasibility to use beam-gas hadronic interactions to measure the beam size along the LHC cycle, without needing cross-calibration with another monitor.

Despite its promising results, this system is not maintainable by the beam instrumentation team in the long term, partly due to dependencies of the event reconstruction tool on a no longer maintained LHCb computing framework. At the end of Run 2, its operation was deemed potentially beneficial for the upcoming LHC runs, but a greater interest was found in the development of an operational BGV, capable of vertex and therefore beam profile reconstruction for the HL-LHC.

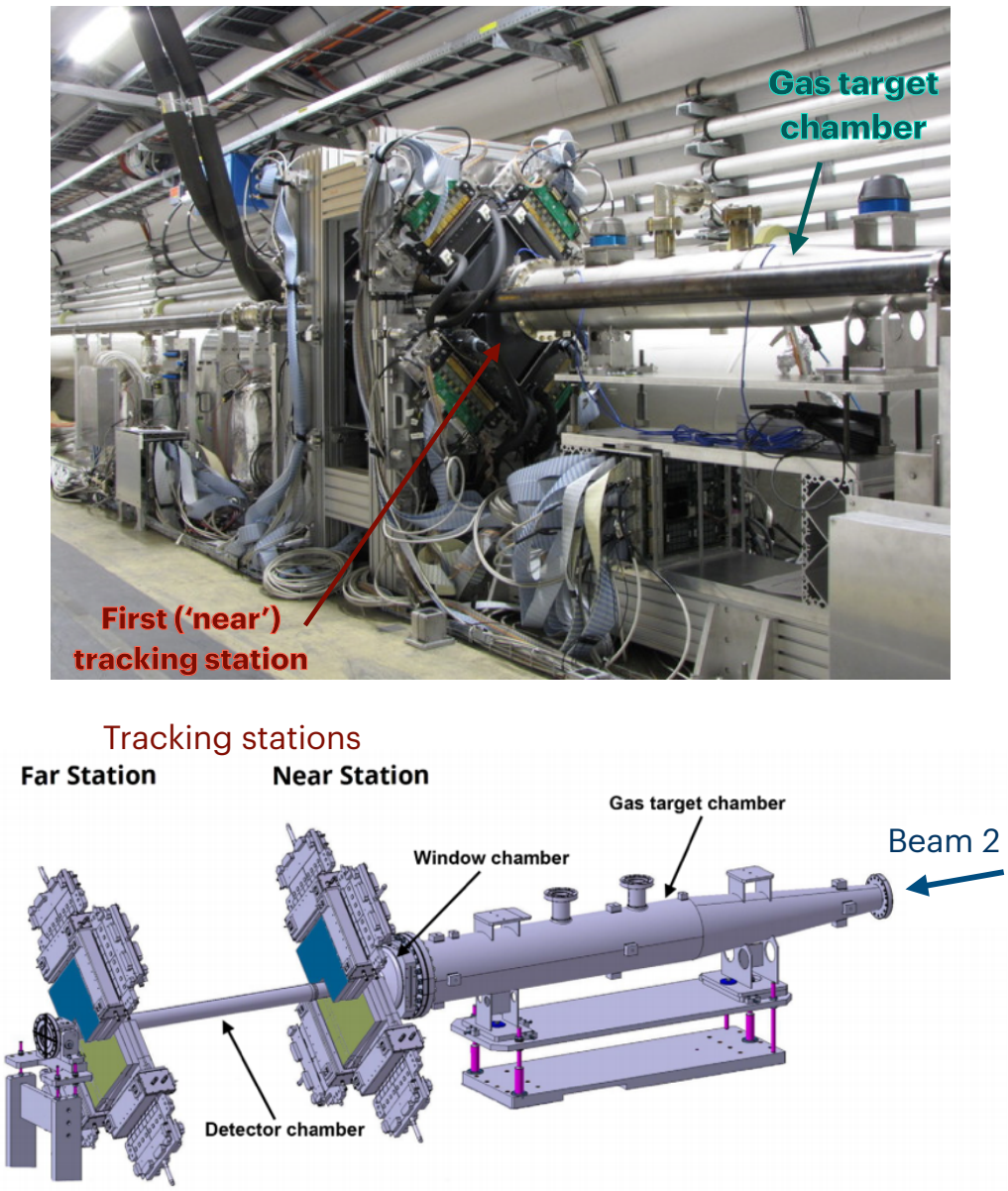

Figure 3.6: Picture (top) and scheme (bottom, courtesy R. Kieffer) of the demonstrator BGV installed in the LHC.

3.5 Summary

The beam size monitors currently operated at the LHC present limitations related either to the beam intensity or to its energy. There is currently no emittance measurement available during the energy ramp, which notably is a break for studying emittance growth mechanisms [32]. Besides, a discrepancy in the order of 10% was observed between the LHC emittance measurements obtained from the beam instruments and from the high luminosity producing experiments luminosity measurements during Run 2 [33].

At the end of this Run, a beam size measurement review was held, and the need was emphasised for a non-invasive instrument capable to provide an absolute bunch-by-bunch transverse beam size and profile measurement throughout the LHC energy cycle, for all beam intensities [34]. With the encouraging results obtained with the demonstrator BGV, this conceptual instrument, together with an adapted HPD BGI, were selected as a potential candidates to meet the specifications towards the commissioning and operation of the HL-LHC. This thesis presents part of the work leading to a BGV design proposal for the HL-LHC (HL-BGV) [2].

Chapter 4

Requirement for a HL-LHC BGV

Performance specifications for a new beam size monitor for the HL-LHC, complementary to the existing devices, were addressed at the 2019 LHC beam size review [34], and are discussed in this chapter. The design of the BGV is driven by the beam size at the foreseen instrument installation locations, and by these specifications.

4.1 Possible instrument locations

The demonstrator BGV was installed to the left of IP4, at a distance of about 220 m from its centre, between the quadrupoles Q6 and Q7, as shown in Figure 3.1 in the previous chapter. Its position is also noted −220 m, the minus sign referring to the left-hand side of the IP. A large space was reserved for the BGV in 2013, before the installation of the demonstrator, which spread from −200 m to −244 m. Another space was symmetrically allocated to the future Beam 1 HL-BGV (*B1-BGV*), on the right side of the IP. The main arguments considered for finding suitable locations for the two devices were the following:

- A longitudinal free available space of at least 7 m;
- Beam optics stability along the energy cycle, and low beam dispersion, as is the case by-design around IP4, which is partly dedicated to beam instrumentation;
- β-functions values:
  - Sufficiently high β-functions, leading to large beam sizes, to relax the vertex resolution required to achieve the targeted accuracy, as will be detailed in Section 4.3.2;

  - Moderate β-functions, to allow for a small aperture chamber downstream of the gas target. It will be shown in the following chapter that the instrument performance is enhanced with placing the tracking detectors close to the beam axis, where the secondary track density is high, in particular with high momentum particle tracks;
  - β values as close as possible between the two locations, in order to avoid major design differences between the two instruments;

- Secondary showers directed towards the arcs, to prevent radiation damages to sensitive equipment downstream of the gas target;
- A round beam is preferred (but not required), leading to similar vertex and thus beam size resolutions in both transverse planes.

Years after these space reservations were made for the BGVs, the HL-LHC beam optics have changed: the optics version 1.5 is plotted in Figure 4.1 for each beam. The initially reserved spaces are indicated with the purple rectangles, and the precise location of the demonstrator BGV with the magenta one. On Beam 2, the HL-BGV (*B2-BGV*) is foreseen to be installed in place of the demonstrator. The situation is more involved for the BB1-BGV, since the β-function along y is lower than 100 m at the initially reserved space (right purple zone in Figure 4.1a), leading to very small beam sizes and demanding vertex resolutions along y for this instrument.

A new suitable location was hence chosen for the B1-BGV, closer to the IP centre, which is indicated in orange in Figure 4.1a. Despite the presence of some beam instruments downstream of this place, it is one of the rare regions of this long straight section offering a sufficiently long free space and meeting the above-listed constraints.

4.2 Expected beam size

The beam sizes $\sigma_{x,y}$ expected along each transverse plane x and y of these two location are summarised in Table 4.1. Their expression as a function of the beam optics is reminded from Chapter 2:

$$\sigma_{x,y}(s) = \sqrt{\epsilon_{x,y}\ \beta_{x,y}(s) + \left(D_{x,y}(s)\ \frac{\Delta p}{p}\right)^2}. \tag{4.1}$$

These values are computed from the HL-LHC beam parameters given in Table 2.1 of Chapter 2 (from Ref. [4]), and from the beam optics functions shown in the previous

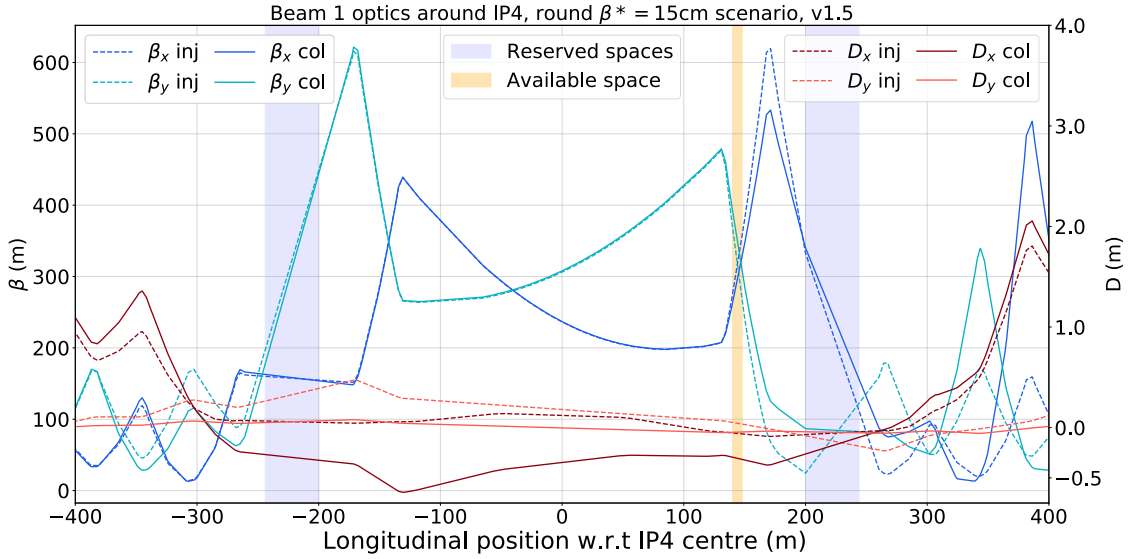

(a)

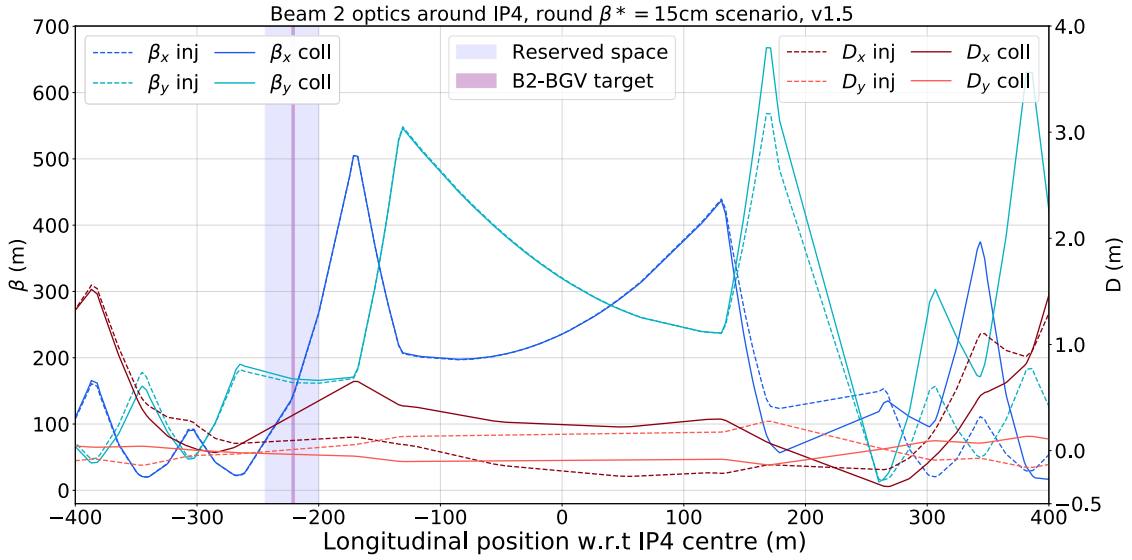

(b)

Figure 4.1: Beam optics around IP4 for Beam 1 (4.1a) and Beam 2 (4.1b), at both injection (dashed lines) and collision (full lines) energy. β-functions are shown in blue for the x plane and green for the y plane, and dispersion functions D in purple (x plane) and orange (y plane). The initially reserved spaces for the BGVs are shown in purple, and the new location targeted for the B1-BGV is indicated in orange.

section. At these two locations, the dispersion term contributes at most for 0.4% of the beam size (where the dispersion has the highest value, which corresponds to the B2-BGV location and at collision energy). Therefore, in the following, the measured beam size will be approximated to its β term:

$$\sigma_{x,y}(s) = \sqrt{\epsilon_{x,y}\ \beta_{x,y}(s)}\,. \tag{4.2}$$

Two beam filling scheme are currently distinguished at the LHC, called Standard and Bunch Compression Merging and Splitting (BCMS) [35]. BCMS beams have smaller transverse emittance at injection from the SPS (obtained via complex RF manipulations at the injectors), and consequently narrower beam sizes. The same normalised emittance is assumed between these two schemes at collision energy, which is estimated with accounting for the currently known blow-up effects along the acceleration cycle [4].

Table 4.1: Expected beam sizes at B1-BGV and B2-BGV locations.

Instrument	Energy	Beam size σ_x/σ_y (µm)	
		Standard filling scheme	BCMS filling scheme
B1-BGV	450 GeV	1180/1180	1120/1060
	7 TeV	468/355	
B2-BGV	450 GeV	803/843	764/758
	7 TeV	**232**/246	

A beam size evolution of one order of magnitude is observed during the cycle going from about 1 mm down to about 200 µm. With lower β-functions, B2-BGV will measure beam sizes smaller by few hundreds of µm compared to the other instrument. The smallest size among all cases is highlighted in bold and will be used to calculate the required instrument vertex resolution, driving design choices, as will be discussed in Section 4.3.2.

4.3 Instrument performance requirements

The *accuracy* of a set of measurements represents how close the measured values are from the true one. For independent Gaussian-distributed measurements, their *precision* corresponds to the width of their distribution, as illustrated in Figure 4.2 for an arbitrary quantity x [36].

The specifications for the future instrument are presented below, together with their meaning for the HL-BGV.

4.3.1 Specifications and motivations

The specifications for the future instrument concerning operation with proton beams are the following [34]:

1. 10% accuracy on the emittance measurement, without need for cross-calibration with another device;

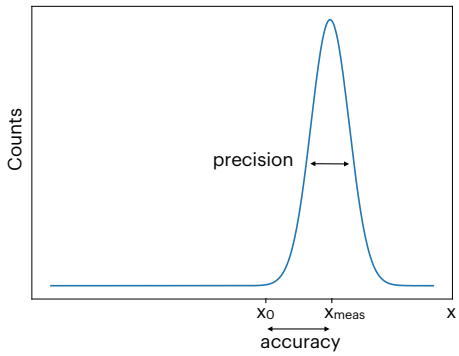

Figure 4.2: Distribution of independent and repeated measurements of a quantity x. The true physical value is x_0 and the measurements mean x_{meas}.

2. 1% bunch width precision within 1 min of integration time[1];

3. Continuous measurement throughout the LHC energy cycle, in particular during the energy ramp;

4. For all beam intensities, i.e. number of bunches and bunch populations.

These specifications are driven by HL-LHC performance and machine optimisation needs: for an accurate determination of the collider luminosity and towards identifying potential sources of emittance growth and bunch-by-bunch luminosity variation. The integration time of 1 min corresponds to typical time scales of the machine operation processes, like optics changes and energy ramp.

In addition, measuring the *beam profile*, i.e. the projection of the particle distribution along the transverse axes, was also deemed beneficial for accurate luminosity predictions and to study tail population mechanisms and effects that are sensitive to it, like electron clouds and beam-beam effects.

The requirements are the same for ion beams operation. Since ion runs are usually short (in the order of a month), an additional request is made to avoid lengthy calibration procedures.

Considering a negligible contribution of the dispersion at the BGV locations, and assuming that the beta function at these places is known with an error smaller than 5% [37], requirement 1. , which is expressed in terms of emittance, leads to 5% relative accuracy on the measured beam size. This is demonstrated in Appendix A.

[1]In order to sort data bunch by bunch, the data acquisition system is connected to the LHC control system.

For the BGV, these specifications drive the required vertex resolution and interaction rate.

4.3.2 Measurement accuracy and vertex resolution

The BGV principle is based on the reconstruction of beam-gas inelastic interaction vertices. The beam profile is obtained from the transverse distribution of reconstructed vertices, after deconvolution of the vertex response of the instrument. The *response function* (identified in blue in Figure 4.3) is characteristic of the instrument and is defined as the distribution of residuals between reconstructed and true vertex positions, for multiple independent measurements of a beam-gas interaction. In the following, the gas density is assumed to be homogeneous, so that the distribution of beam-gas interactions is representative of the beam profile. This aspect will be discussed in Chapter 7.

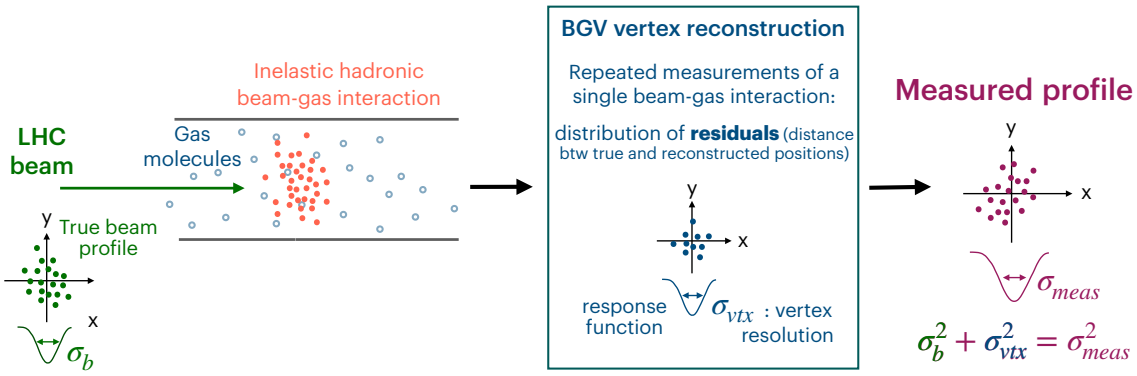

Figure 4.3: Convolution of the BGV measured profile with its response function, assuming Gaussian distributions.

Considering a Gaussian beam and Gaussian response function, the deconvolution of the beam width σ_{b} from width of the raw measured profile σ_{meas} is given by:

$$\sigma_{\mathrm{b}}^2 = \sigma_{\mathrm{meas}}^2 - \sigma_{\mathrm{vtx}}^2 \,. \tag{4.3}$$

where σ_{vtx} is the Gaussian width of the BGV response function. In this case, it can be shown that, with neglecting the uncertainty on the measured profile ($\delta\sigma_{\mathrm{meas}} \to 0$), the variance formula for error propagation [38] relates the relative accuracy of the beam size

measurement $\frac{\delta\sigma_\mathrm{b}}{\sigma_\mathrm{b}}$ to the vertex resolution as [39]:

$$\frac{\delta\sigma_\mathrm{b}}{\sigma_\mathrm{b}} = \frac{\sigma_\mathrm{vtx}^2}{\sigma_\mathrm{b}^2}\frac{\delta\sigma_\mathrm{vtx}}{\sigma_\mathrm{vtx}}\,, \tag{4.4}$$

where $\frac{\delta\sigma_\mathrm{vtx}}{\sigma_\mathrm{vtx}}$ is the relative uncertainty on the vertex resolution. This relationship highlights the importance of minimising σ_vtx (in particular ensuring it is small compared to the beam size σ_b), and/or to know it precisely, i.e. minimise $\frac{\delta\sigma_\mathrm{vtx}}{\sigma_\mathrm{vtx}}$, for an accurate beam profile unfolding.

Based on Equation (4.4), and assuming that the vertex resolution is known with a precision of 10%, which will be shown in Chapter 8 to be a fair and conservative approximation, the vertex resolution required to reach the accuracy of $\delta\sigma_\mathrm{b}/\sigma_\mathrm{b} = 5\%$ is given for the smallest beam size configurations and for both instruments in Table 4.2.

Table 4.2: Minimum expected beam sizes at the HL-BGV instrument locations, and corresponding required vertex resolution to achieve a beam size measurement accuracy of 5%. The case of B2-BGV at collision energy is given with more precision, as leading to the most demanding vertex resolution.

Instrument	Beam Energy	Beam size $\sigma_\mathrm{b} \leq$	Vertex resolution $\sigma_\mathrm{vtx} \leq$
B1-BGV	450 GeV	1060	750
	7 TeV	360	250
B2-BGV	450 GeV	760	540
	7 TeV	**232**	**164**

The smallest beam size ($\sigma_\mathrm{b} = 232\,\mu\mathrm{m}$) leads to $\sigma_\mathrm{vtx} = 164\,\mu\mathrm{m}$, which is the target vertex resolution for the future instrument. This requirement is relaxed to 540 µm at injection, given the larger beam sizes. The beam sizes, and therefore the required vertex resolutions are identical for both proton and ion beams.

The vertex resolution depends on several factors:

- The number of reconstructed tracks issued from the considered vertex N_tr;
- The quality of these tracks, which relies on the secondary particle energy, traversed material and intrinsic spatial resolution of the detectors;
- The distance between the vertex and the first detector layer;

- The distance between the tracking detector planes.

Some of these factors relate to the BGV design, which shall be optimised to limit the associated contributions. For a given instrument configuration, the vertex resolution still depends on N_{tr}, on the longitudinal position of the vertex z and on the multiple scattering experienced by secondary particles, impacting the tracks quality. As a result, a selection may be applied to filter events with an insufficient vertex resolution. This aspect will be discussed in more details in Chapter 8.

The dependence of σ_{vtx} on the minimum N_{tr} considered is shown in Figure 4.4 for the final HL-BGV design. This result was obtained with the simulation and event reconstruction tool described in Chapter 5. It can be seen that, for this configuration, a vertex resolution of 164 µm, required for the B2-BGV measurement to reach a 5% accuracy at collision energy, can be achieved with considering events reconstructed with 5 or more tracks. Such a selection provides a very small margin but offers a better measurement precision, as will be detailed in the following section. For this specific most demanding case, a trade-off will have to be made between the measurement accuracy and precision. In all the other cases presented in Table 4.2 (B2-BGV at injection energy and B1-BGV at any beam energy), a beam width measurement accuracy of 5% can be reached with considering all events with 3 or more tracks in the tracker acceptance.

Such selected events, i.e reconstructed beam-gas interactions with $N_{\mathrm{tr}} \geq 3$ at injection energy, and those with $N_{\mathrm{tr}} \geq 5$ at collision energy, will hereafter be called *useful* or *reconstructable* events. This event selection filter was considered along the instrument design optimisation process, before a more refined vertex resolution parametrisation and beam profile unfolding method was implemented, which will be presented in Chapter 8.

It can be noted that for the B1-BGV, the required vertex resolution to measure the beam size with a 5% accuracy at any time of the cycle and in both planes is of about 250 µm at collision energy and 750 µm at injection energy. Following Figure 4.4, these values can be achieved with considering all events with $N_{\mathrm{tr}} \geq 3$.

4.3.3 Measurement precision and beam-gas interaction rate

Assuming that the transverse beam profile is Gaussian, the minimum achievable bunch width precision $\Delta\sigma_{\mathrm{b}}$ for a measurement made with N_{vtx} accumulated vertices, is given by [36]:

$$\frac{\Delta\sigma_{\mathrm{b}}}{\sigma_{\mathrm{b}}} = \frac{1}{\sqrt{2N_{\mathrm{vtx}} - 2}}\,. \tag{4.5}$$

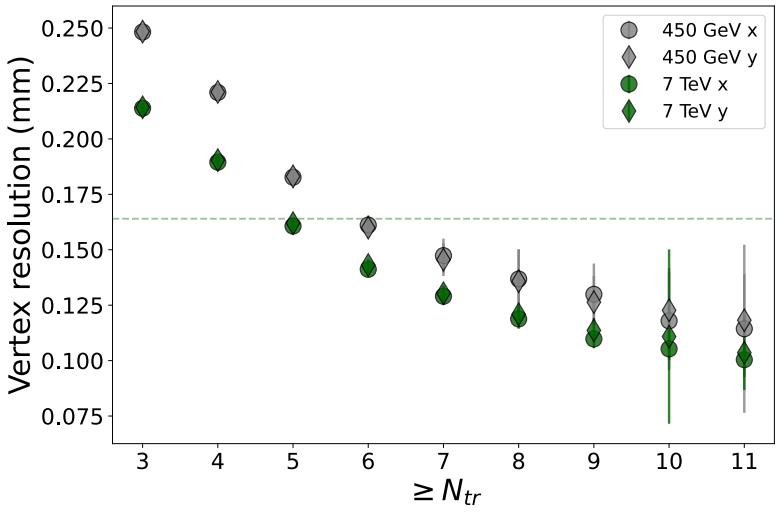

Figure 4.4: Vertex resolution of the final HL-BGV setup, as a function of the minimum events N_{tr} used for the reconstruction, for 450 GeV events (grey) and 7 TeV events (green). The horizontal dashed line indicates the target vertex resolution of 164 µm at collision energy. Increasing error bars are due to the lack of statistics for events with large track multiplicities.

To achieve a relative bunch width precision of 1%, the beam profile image therefore needs to be made upon a minimum of 5000 reconstructed vertices. This number drops to 1250 if the relative precision is relaxed to 2%.

Considering an integration time of 1 min, the 1% relative precision requirement leads to a rate of useful beam-gas interactions of 83 Hz, and 2% relative precision gives 21 Hz. The rate of measurable interactions is determined by the gas density in the measurement region. More details will be given in Section 5.2.2 of Chapter 5 and in Chapter 7.

4.3.4 Operation time

A minimum instrument operation time of about 2 h per fill was estimated to be an asset in order to measure beam size and emittance at the key phases of the energy cycle. This estimate includes 1 h at injection energy and during the energy ramp, and 1 h at flat top energy. This scheme would allow, if desired, to calibrate the BSRT at collision energy for longer measurements. Depending on the number of fills per year, this scheme used for each fill would lead to a total of about 400 h of BGV operation time per year, considering only proton runs.

This minimum operation duration will be considered in Chapter 7 to evaluate the impact of the gas target on the LHC radiation environment.

4.4 Lessons learnt from the demonstrator operation

The incapacity of the demonstrator to reconstruct vertices highlighted the importance of carefully designing the future instrument. Several improvements are suggested.

The available equipment for the demonstrator tracker only allowed to mount two detector stations. The addition of a third layer would greatly improve the track reconstruction accuracy, along with providing a reference frame for a software alignment of the detectors.

Furthermore, the scintillating fibre panels providing a uni-dimensional information on the particle hits, two layers of these panels are needed to reconstruct a two-dimensional hit position. In the event where two tracks traverse a detector at the same time, multiple position possibilities are found, as illustrated in Figure 4.5. To overcome this issue and identify the true cluster positions, two detectors are superimposed to build a tracking plane, the second detector being positioned with a rotation angle w.r.t the first one. Each tracking plane therefore consists in a stack of four scintillating fibre panels, which represents a large amount of material to be traversed by secondary particles.

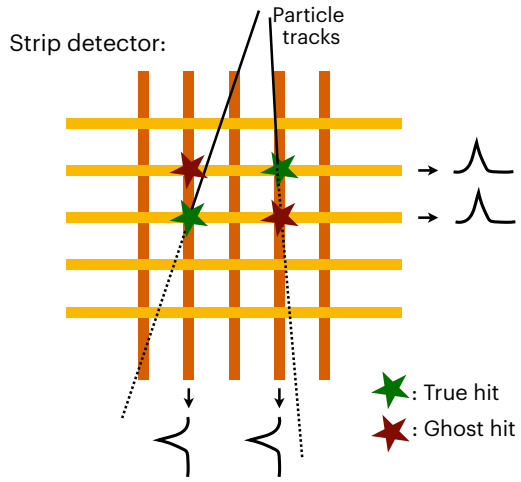

Figure 4.5: Illustration of cluster finding difficulties with strip readout detectors. When two tracks hit the detector at the same time, two channels per plane are fired, leading to four possible hit positions.

The upstream distance from which vertices can contribute to the beam size measurement is in fact limited by the extrapolation error from the deviations of particle trajectories, due to the multiple Coulomb scattering[2] experienced when traversing the large

[2]Deviation of a charged particle trajectory when passing through a medium, due to repeated interactions with the Coulomb potential of the material atom nuclei and electrons.

amount of material introduced by these multiple detector layers. Lower material budget detectors would therefore limit the extrapolation error and enhance the tracking precision. The exit window also significantly contributes to this effect, although the design of the demonstrator one was already optimised to this respect, as will be detailed in Section 6.4 of Chapter 6.

The insufficient average number of reconstructed tracks per event also limited vertex reconstruction possibilities. With the forward nature of the beam-gas interaction showers, the tracker acceptance can be optimised to improve the amount of tracks traversing the tracker, with placing the detectors closer to the beam axis.

The lack of flexibility in the tracker design was generally considered as the main obstacle against achieving vertex reconstruction.

Regarding the gas target, the possibility to reduce the longitudinal spread of the recorded events was evoked as a mean to reduce the uncertainty on the vertex position.

4.5 Approach for the HL-LHC BGV design

With a tracking detector aiming at reconstructing vertices, the BGV is a complex instrument compared to the existing equipment in the LHC. In addition to the previously detailed requirements, the design of the future instrument should be kept as simple as possible, for the instruments to be maintained and operated by a small number of people, and should operate reliably, given the rare opportunities to access the LHC tunnels during Runs.

A Monte-Carlo simulation tool was implemented to ease the navigation through the instrument design parameter phase space, and guide design choices. This tool and the main conclusions of the corresponding studies are presented in the following chapter.

This thesis describes part of the work that was done to propose a design for the HL-LHC BGV. The design of the gas tank and of the gas target are detailed in Chapter 6 and Chapter 7 respectively, while Chapter 8 presents a method to determine the response function of the instrument and unfold the beam profile.

The detailed HL-BGV design (hereafter called *final design* or *revised design*) and its expected performance are presented in the instrument design report [2].

Chapter 5

Simulation tool for the BGV design and performance study

In order to guide the design of the future instrument, a detailed Monte Carlo simulation tool and event reconstruction algorithms were implemented to model the BGV and study the impact of the main design parameters on the vertex resolution. This chapter gives a description of these tools and discusses some of the results which led to the main technological choices.

5.1 Simulation tool description

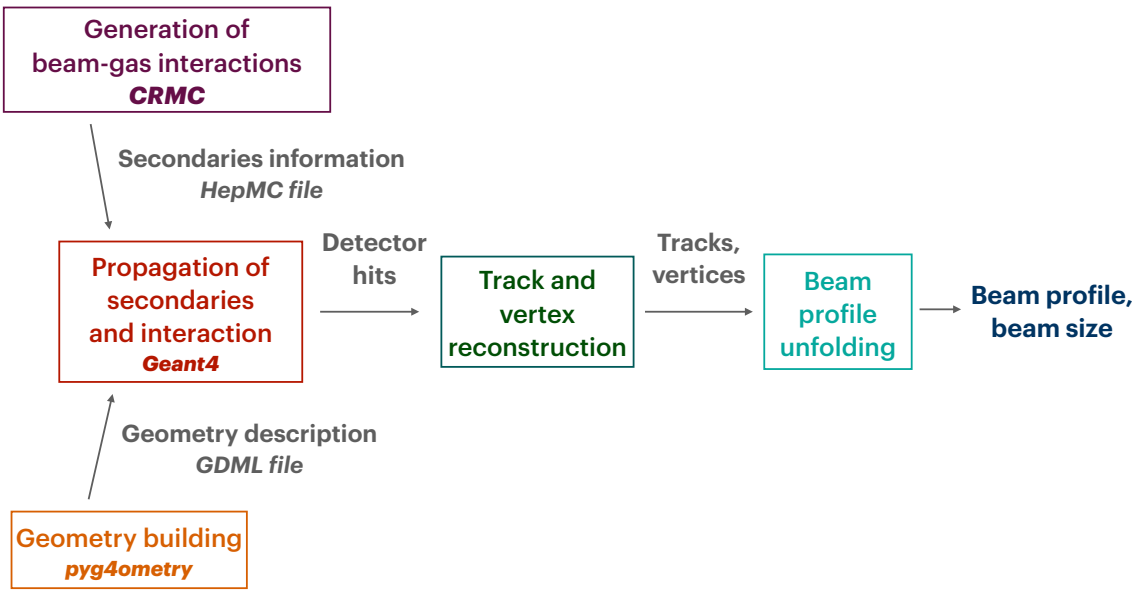

Figure 5.1: BGV simulation tool chain.

The simulation chain of the BGV model[1] is schematised in Figure 5.1, and an example of the main steps of a track and vertex reconstruction algorithm is shown in Figure 5.2. The BGV simulation tool is organised as follows.

Beam-gas interactions are generated using the Cosmic Ray Monte Carlo (CRMC) [40] interface, which allows to access a variety of hadronic event generators. The secondary particle information, together with the instrument geometry description, built using the pyg4ometry package [41], are read-in by the Geant4 [42] model, which propagates the secondary particles through the geometry and simulates their interaction with matter. The beam-gas interaction vertices are spatially distributed to model a given beam profile shape and gas target density map. At the detectors' location, the hit positions are extracted event-wise, and Gaussian smeared, to model the detector resolution (digitisation). An event reconstruction algorithm then processes the recorded hits to reconstruct the secondary particle tracks and interaction vertices. The final step to extract the beam profile is to unfold the vertex resolution (response) from the distribution of reconstructed vertices. This last step will be presented in Chapter 8.

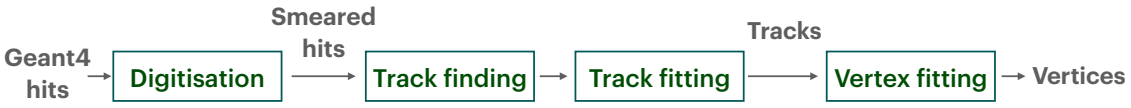

Figure 5.2: Example steps of a track and vertex reconstruction algorithm.

Details regarding the track and vertex reconstruction algorithm, which was implemented by Bernadette Kölbinger, can be found in Ref. [2]. It mainly includes track fitting and vertex fitting, for which several methods were tested. The track finding step, which consists of associating hits to tracks, was omitted at this stage, and all hits are assumed to be associated with the correct track without mistakes. Preliminary tests with the final instrument geometry give confidence that a very high efficiency of this step can be reached [2].

In the case of strip detectors, a cluster finding step is required after the digitisation step, consisting of associating horizontal and vertical hit information to locate the transverse hit position.

For each event, the truth information on the vertex position and track characteristics (momentum components, particle species) are extracted from Geant4 along with the detector hit information. This feature allows for instance to compute the vertex resolution

[1] https://gitlab.cern.ch/hl-bgv/g4-bgv/-/tree/master/

using the true vertex position, and allows to assess the performance of each step of the reconstruction algorithm.

At various stages of the algorithm, selection filters can be applied on the hits, tracks or vertices considered for the beam profile reconstruction (eg. small angle tracks, events with a given track multiplicity or in a given region of the gas target, etc.).

As a first step in the design process, the secondary particle distributions are compared in the following section. A simplified instrument geometry was then built and used to study the effect of various gas target and tracker technologies on the instrument performance. This is presented in Section 5.4. As the design progressed, the instrument geometry was refined and the simulation tool helped to estimate achievable instrument performance. The final instrument performance is presented in Chapter 8.

5.2 Beam-gas interactions and secondary particles propagation

The characteristics, i.e. particle species, multiplicity, angular and momentum distributions, of the generated secondary particles depend on both the impinging beam particles and gas species. An accurate estimate of these characteristics is of high importance to assess achievable instrument performance.

5.2.1 Gas species choice

Several constraints are imposed to the choice of the BGV gas target species, for the instruments to be installed in the LHC. Firstly, the injected gas is required not to interact with the chambers' Non-Evaporable Getter (NEG) coating, which acts as a passive pumping system. This implies the selection a noble gas. Moreover, the leak detection system of the LHC relies on the detection of helium and argon, which discourages the usage of these two species. For this reason, neon was chosen for the demonstrator target. At the time of writing, no higher mass gases have yet been injected in the LHC vacuum and further studies would be needed in order to assess the impact of such species on the saturation of the ion pumps, required to pump out noble gases from the beam pipe. Neon therefore remains the baseline choice for the BGV target. The impact of using gases of higher mass, like argon and xenon, on the instrument's performance will be discussed in Section 7.5 of

Chapter 7.

5.2.2 Interaction rate

For a given gas volume of longitudinal density profile $\rho(z)$, the beam-gas interaction rate R can be expressed as:

$$R = f_{\text{rev}} N \sigma \int \rho(z) \mathrm{d}z \,, \tag{5.1}$$

for a beam containing N particles and circulating with a revolution frequency $f_{\text{rev}} = 11\,245\,\text{Hz}$ in the LHC. The interaction cross section σ can be scaled from the proton-proton interaction cross section σ_{pp}, as in Equation (5.2) [43,44] for proton-gas interactions (σ_{pX}) and estimated from Equation (5.3) for lead ion-gas interactions ($\sigma_{\text{Pb-X}}$), as is suggested in Ref. [45]. Here, the gas species is noted X, of atomic number A_{X}.

$$\sigma_{\text{pX}} = \sigma_{\text{pp}} \times A_{\text{X}}^{0.77} \tag{5.2}$$

$$\sigma_{\text{Pb-X}} = \sigma_{\text{pp}} \times (A_{\text{Pb}}^{1/3} + A_{\text{X}}^{1/3})^2 \tag{5.3}$$

As a matter of example, Table 5.1 lists the beam-gas elastic, inelastic and total interaction cross-section and rates for proton and ion beams, for a 1 m long neon gas target at 1×10^{-7} mbar. The HL-LHC beam parameters considered are taken from Table 2.1 from Chapter 2.

Table 5.1: Cross-sections and interaction rates for a 1 m long neon gas target at 1×10^{-7} mbar.

		p runs		Pb runs	
		450 GeV	7 TeV	450 GeV	7 TeV
Cross-section	total σ^{tot}	400 mb	480 mb	3.0×10^3 mb	3.6×10^3 mb
	inelastic σ^{inel}	280 mb	330 mb	2.5×10^3 mb	2.9×10^3 mb
	elastic σ^{el}	130 mb	160 mb	0.13×10^3 mb	0.16×10^3 mb
Interaction rate (entire beam)	total R^{tot}	**750 kHz**	**900 kHz**	2.0 kHz	2.3 kHz
	inelastic R^{inel}	510 kHz	600 kHz	1.6 kHz	1.9 kHz
	elastic R^{el}	230 kHz	290 kHz	0.081 kHz	0.10 kHz
Interaction rate per bunch	total R^{tot}	270 Hz	320 Hz	1.6 Hz	1.9 Hz
	inelastic R^{inel}	**190 Hz**	**220 Hz**	1.30 Hz	1.5 Hz
	elastic R^{el}	84 Hz	100 Hz	0.066 Hz	0.081 Hz

For proton beams and considering such a gas volume, total interaction rates in the order of 0.75 MHz at injection and of almost 1 MHz at collision energy are expected for the entire beam. In this energy range, beam-gas interactions are dominated by inelastic

collisions, representing about 2/3 of the total interactions for proton beams. Regarding beam size measurement purposes, inelastic interactions are in the order of 200 Hz per bunch, and only a small fraction of these collisions will generate a sufficient amount of tracks entering the BGV tracker acceptance and contribute to the measurement. One requirement of the gas target is to ensure that a sufficient rate of useful events is reached, to meet the bunch width precision specification presented in the previous chapter. This particular question will be treated in Chapter 7.

It can be noted that despite higher cross-sections, interaction rates for lead ion beams are two orders of magnitude smaller, due to a significantly lower beam intensity compared to proton run beams.

5.2.3 Secondary particle characteristics

This section investigates some characteristics of the secondary particles generated by p-Ne inelastic interactions. The DPMJET 3.06 generator [46] was chosen among other hadronic generators, which were compared in Ref. [47]. The considered generators showed a satisfying agreement for the purpose of the BGV design optimisation. In this section, error bar in figures presenting distributions are derived using Poisson error.

The distribution of the most represented particle species is shown in Figure 5.3. Among these interaction products, those capable to traverse the vacuum chamber and reach the BGV tracker are mostly charged pions [2]. Photons from neutral pions decay are not considered to be easily detectable with the considered detector technologies. Therefore, only charged pions will be considered in the following.

The number of tracks (charged pions) $N_{\mathrm{tr,tot}}$ distribution per simulated event is shown in Figure 5.5. A total of 12 tracks in 4π are generated in average per p-Ne collision at injection energy, increasing to around 22 tracks at collision. Their emission direction can be seen in Figure 5.6, where it is represented by their pseudorapidity η, often used in high energy physics to describe the angular acceptance of a detector, and which relates to the angle θ defined between the three-momentum of the particle and the beam axis direction as:

$$\eta = -\ln\left[\tan\left(\frac{\theta}{2}\right)\right]. \tag{5.4}$$

This relationship is illustrated in Figure 5.4: compared to the propagation direction of the incident particle, secondary particles with a pseudorapidity < 0 travel backwards, and the

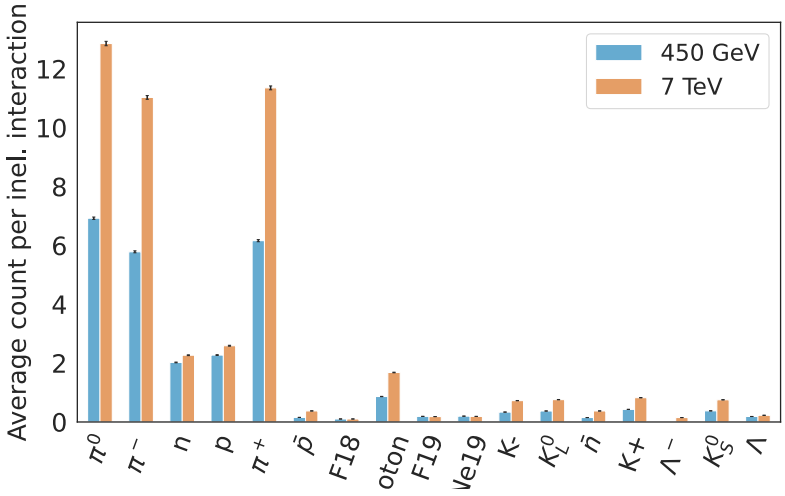

Figure 5.3: Secondary particles generated in a p-Ne inelastic collision at the LHC injection and collision energies. Only particles present in $> 10\%$ of collisions are shown.

higher the pseudorapidity, the closest the particle trajectory to the beam axis.

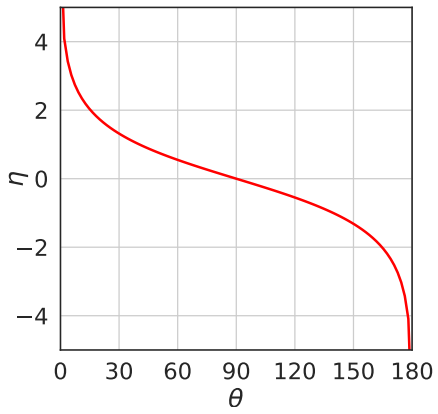

Figure 5.4: Pseudorapidity as a function of the associated angle.

Figure 5.6 highlights how the particle direction is related to their absolute momentum. Most particles, and in particular those with high momenta, are emitted in the forward direction, close to the beam axis. On the two plots, the vertical dashed line corresponds to a pseudorapidity limit above which secondary tracks generated 550 mm upstream of the first tracker detector, which will be shown in Section 5.4 to be a optimised distance, would travel inside the beam pipe and "miss" the tracking detector.

Figure 5.7 shows the absolute momentum distribution, which is dominantly of few GeV, and increases in average with the beam energy.

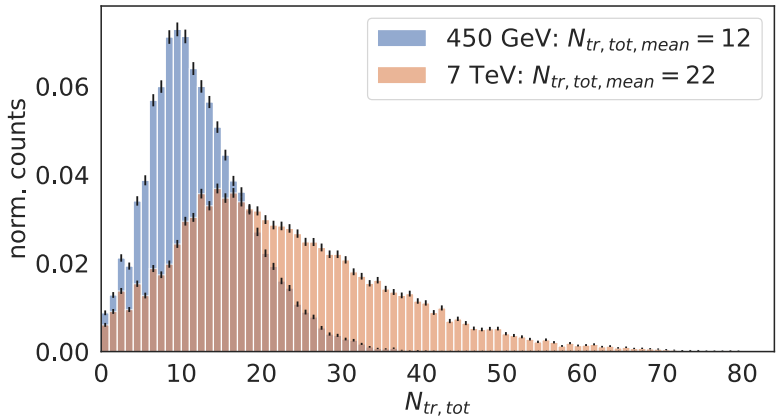

Figure 5.5: Track multiplicity $N_{\mathrm{tr,tot}}$ distribution for p-Ne interactions at injection and collision energy.

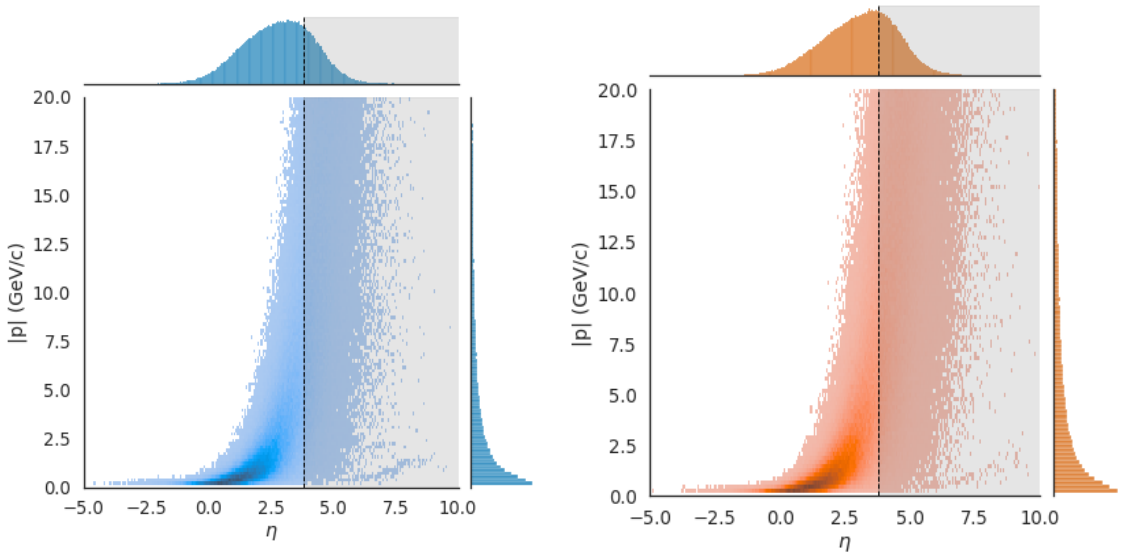

(a) 450 GeV (b) 7 TeV

Figure 5.6: Bidimensional absolute momentum vs. pseudorapidity distributions of charged pions generated in p-Ne interactions, at injection (5.6a) and collision (5.6b) energy. The vertical dashed line gives an estimate of the pseudorapidity limit above which secondary particles will travel inside the beam pipe further away than the BGV tracker located 550 mm downstream of the interaction point.

In summary, among the particles issued from beam-gas interactions, the BGV tracker will mostly record charged pions. Most of these particle have an absolute momentum of few GeV, but positioning the tracking detector as close as possible to the beam axis will allow to record tracks with larger momenta, which are less prone to multiple scattering. With the increase of the beam energy, beam-gas interactions generate more secondaries, with higher energy and more forward trajectories. These characteristics should help to

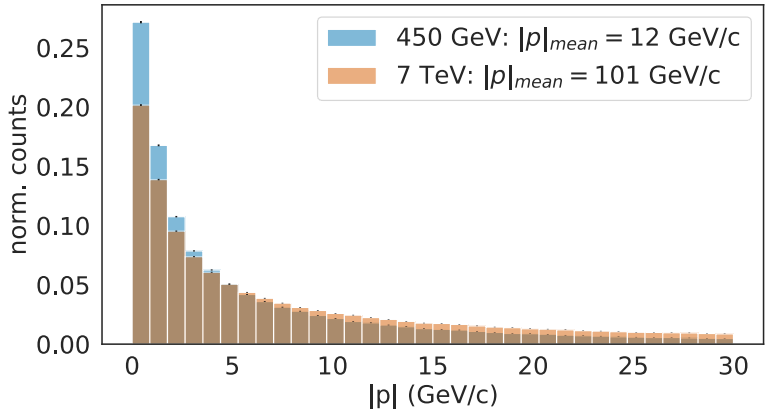

Figure 5.7: Absolute momentum distribution of charged pions issued from p-Ne inelastic interactions.

improve the vertex resolution of the instrument, which is required to be smaller at high energy due to the smaller beam sizes.

5.3 Ion beam size measurement

This section discusses the feasibility to measure the ion beam size with the BGV. Given that the beam optics are identical between proton and ion runs, the beam size at the instrument location will be the same for both types of beams, and the accuracy and precision requirements on the beam size measurement are therefore unchanged.

The lower interaction rates are partly compensated by the fact that Pb-Ne showers provide much higher tracks multiplicities: 75% of inelastic collisions have $N_{\mathrm{tr}} \geq 5$ when considering the final HL-BGV setup, dropping the required inelastic interaction rate down to 110 Hz to achieve the bunch width precision specification. Such a rate is 6 times smaller than in the proton case, but about 100 times higher than the expected Pb-Ne inelastic interaction rate in the region of interest at 1×10^{-7} mbar. Apart from the track multiplicity, no significant change is observed with respect to track momenta nor spatial distribution.

Considering a BGV design reaching the proton beams specifications, the same device would need a longer accumulation time to achieve the same performance with lead ion beams, or a significant increase of the gas target pressure. Owing to a high track multiplicity, the accuracy on ion beam width measurement is not expected to be degraded compared to proton beam performance.

5.4 Performance optimisation study

A design optimisation study detailed in Ref. [48] was conducted with the BGV simulation tool and helped to make key design choices. Some of the most important results are presented below.

5.4.1 Generic instrument geometry and design parameters

A generic instrument geometry, shown in Figure 5.8, was defined in order to study the impact of the main design parameters of the BGV on its performance.

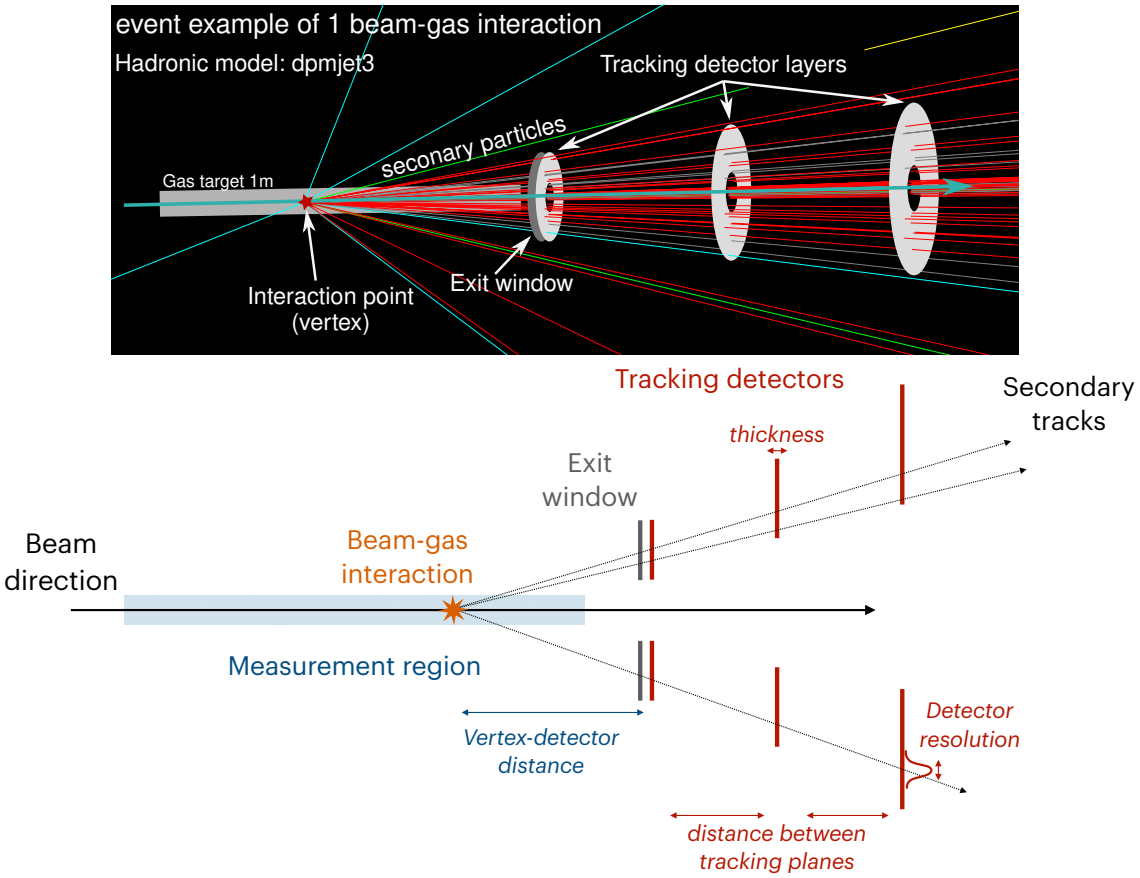

Figure 5.8: Test geometry for the performance optimisation study. The top image shows the geometry, viewed in Geant4 [2], and the bottom sketch indicates the main considered design parameters.

In this setup, beam-gas interactions are uniformly distributed in a volume spread over 1 m, and following a 200 µm wide Gaussian distribution along the transverse planes, to model a Gaussian beam.

The first detector layer is placed downstream of this volume. It consists of a sensitive disk layer of 130 mm diameter and pierced with a central hole of 46.8 mm diameter,

representing the beam pipe passage. Its dimensions are defined according to the minimum possible beam pipe aperture and to the maximum gas tank diameter allowed regarding beam-coupling impedance, as will be detailed in the following chapter. This disk is positioned perpendicularly to the beam axis and centred on it.

A 0.9 mm thick aluminium sheet is placed at the front of the first detector plane, of the same shape than the detector described in the previous section. Also called Exit Window (EW), its purpose is to model the beam chamber wall to be traversed by the secondary particles before reaching the tracking detectors. It is acknowledged that the exit window has to be placed as close as possible to the first detector layer, in order to limit extrapolation error in track reconstruction, due to multiple scattering occurring within it. Details regarding the thickness and shape of this piece will be given in the following Chapter.

The tracker consists of three detector layers, each with the shape of a pierced disk, similar to the first layer described in the previous section. Each layer is made of silicon, the thickness of which can be varied. A 100 µm thick part of the detector layers is set sensitive. The recorded hit position corresponds to the mean position between the entry and exit points of the particle in the sensitive layer. Each detector is placed 250 mm downstream of the preceding layer, and with dimensions adjusted to preserve the solid angle defined by the first detector, with respect to the centre of the gas target.

This setup allows to study design parameters related to the instrument's gas target and tracker, with the vertex resolution as the main figure of merit of the instrument's performance.

5.4.2 Distance between the beam-gas interaction and the first detector plane

The distance d_t between beam-gas interactions and the first tracking detector plane was first optimised with respect to the number of tracks reaching this detector layer [2]. For this purpose, the beam-gas interactions are constrained to a point source target, of which the position with respect to the first detector plane is varied.

It was observed that, in general, the amount of tracks recorded by the detector increases with d_t, as the tracks gain more distance to open up. At injection energy, where tracks propagate with large angles with respect to the beam axis, the amount of tracks hitting the first detector reaches a plateau at $d_t \simeq 550$ mm and then slightly decreases.

This value will be considered as the optimised distance in the following.

5.4.3 Impact of the longitudinal vertex position

Considering then reconstructed events, the simulation setup was used to compare the characteristics of reconstructed vertices as a function of their distance from the tracker.

In Figure 5.9, the vertices from 7 TeV interactions are grouped together in 100 mm wide bins, according to their distance from the first detector layer. For each bin, the vertex resolution, average track momentum and proportion of events showing with a sufficient N_{tr} are shown. It is revealed that interactions occurring close the tracker lead to better vertex resolutions. These events are however less numerous to show a signal in the detector than those generated very close to the tracker. The expected degradation of the vertex resolution with the distance from the tracker due to extrapolation error is however limited by the increase of the average track momentum.

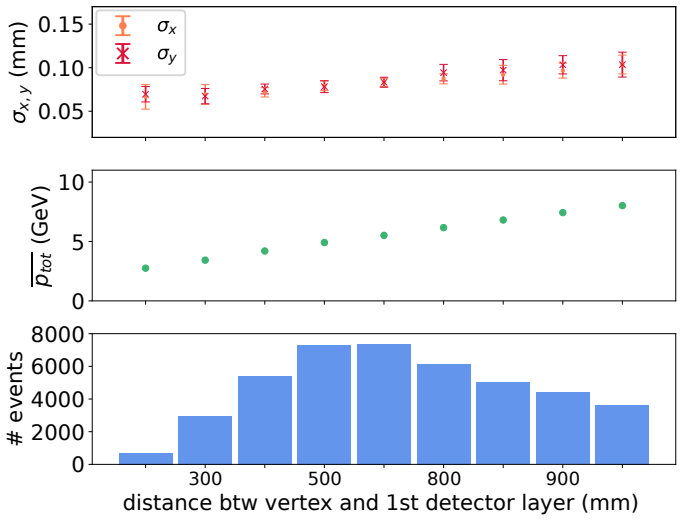

Figure 5.9: Characteristics of the reconstructed events, as a function of their position distance from the first detector plane. Vertices are grouped together as a function of their originating position, in bins with a width of 100 mm, represented along the horizontal scale. For each bin, the vertex resolution in x and y is given in the top plot (with a cut on events with $N_{\text{tr}} \geq 5$), the average track momentum in the middle plot, and the number of events showing a signal is shown in the bottom one. [2]

Based on these results, a longitudinal volume extending from 1050 mm upstream of the first detector layer, up to 50 mm from it, was defined as the *measurement region*, the beam-gas interaction originated from which will be considered for the beam size measurement. This volume includes events close to the tracker, with a good vertex resolution, and

is sufficiently long (1 m) to include a decent amount of events, while staying in a range where the vertex resolution is reasonable. The tracker design was then optimised with respect to this region.

5.4.4 Detectors comparison

Three main detector technologies were considered for the BGV tracker: GEM (Gaseous Electron Multiplier) [49] based gaseous detectors, hybrid and monolithic pixel detectors. This selection focused on radiation tolerant [50–52] high energy physics detectors with low material budget[2], or detectors already used within the CERN beam instrumentation group and suiting for the detection of minimum ionising particles.

1. The possibility to use gaseous detectors, in particular triple GEM detectors, was investigated early in the instrument design process [53]. With very small achievable material budgets, and thanks to a relatively low surface cost, this technology allows to cover large transverse areas in a hermetic way, while limiting the amount of material traversed by secondary particles. Among gaseous detectors, triple GEMs offer a high signal gain, suiting for detecting the BGV pions. R&D possibilities were explored to conceive an extremely low material budget triple GEM detector. A conceptual design was proposed [2], achieving a material budget (X/X_0) of 0.18% per detector in the sensitive area (compared to 0.25-0.30% for standard triple GEMs [54]) and is depicted in Figure 5.10. A spatial resolution in the order of 50 µm, as for standard triple GEMs [55], is expected, which is relatively large compared for instance to silicon detectors.

   Triple GEM detectors are read out with strips, implying the need for an additional cluster finding step in the event reconstruction algorithm. To identify the true cluster position, as illustrated in Figure 4.5, each tracking plane should consist of two detector layers positioned with a rotation angle, as explained in the previous chapter. Four cluster coordinates are extracted per tracking plane, increasing the event processing load compared to pixel readout detectors. Regarding the tracker design, another constraint of gaseous detectors comes from the fact that a side structure is required to stretch the GEM foils and to contain the gas in the sensitive

[2]The material budget of a detector corresponds to the ratio between the length of material traversed by a particle, over the radiation length of this material; the radiation length corresponding to the mean length traversed by an electron before its energy is reduced by 1/e.

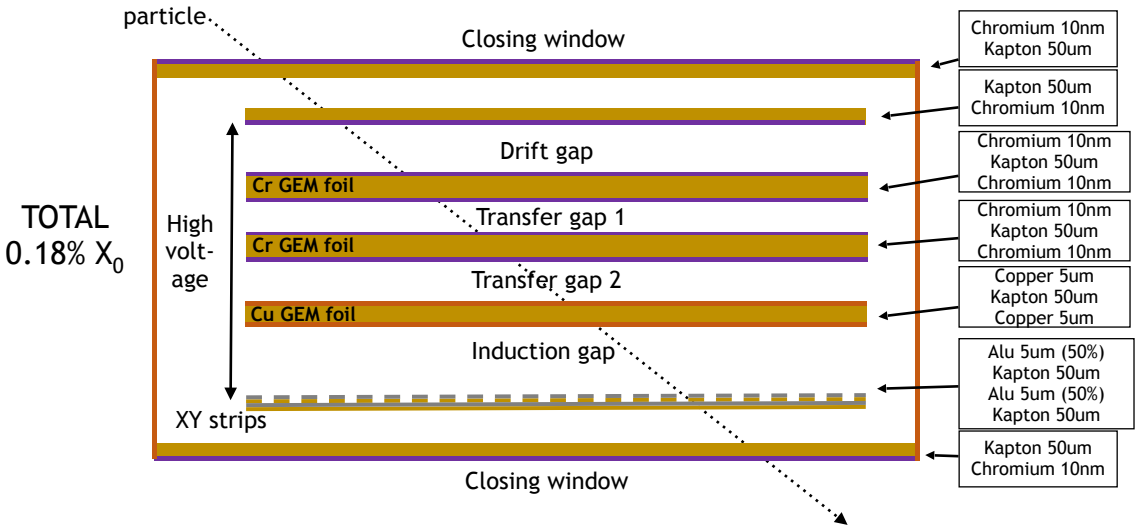

Figure 5.10: Cross section of the conceptual design of a low material budget triple GEM for the BGV. [2]

volume. A few millimetres of non-sensitive material would therefore occupy the inner diameter of the detector modules, restricting the sensitive area and causing small angle particles to scatter or possibly shower onto this structure. Finally, for the BGV application, depending on the detector operation gain, the effect of highly ionising particles on performance and ageing of the GEMs would need further studies.

2. Silicon pixel detectors were also considered, of which two families can be distinguished: monolithic and Hybrid Pixel Detectors (HPD) [56]. Both technologies, schematised in Figure 5.11, benefit from the simplicity of a pixel readout, with a spatial resolution in the order of 10 µm. Silicon detectors are significantly more expensive than gaseous detectors, particularly HPD, and less adapted for covering large areas. On the other hand, their high spatial resolution and the possibility to place them very close to the beam chamber leads to the possibility to design a more compact tracker, with an acceptance focused on small angle but more energetic secondary particles.

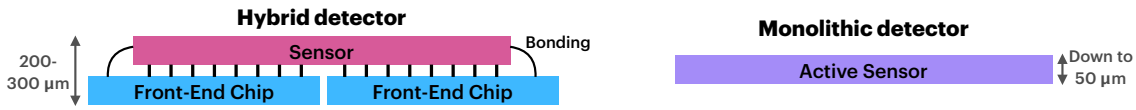

Figure 5.11: Scheme of a the silicon pieces constituting a hybrid and a monolithic pixel detectors.

- Hybrid Pixel Detectors consist of a silicon sensor layer, bonded to front-end

chips. The particular TimePix detectors family [57–59] is used in several beam instruments at CERN [26,60]. Despite a rather high material budget due to the presence of these separate layers, a standard readout data acquisition chain was already developed within the section, which can be easily adapted for the BGV application. Standard TimePix3 HPD assemblies are made with a 300 µm thick sensor and a 700 µm thick Application Specific Integrated Circuit (ASIC), leading to a total thickness of in the order of 1 mm. However, sensors are available with a thickness down to 50 µm, and the ASIC can be thinned down to 220 µm. The total detector thickness can then reach 270 µm, with a corresponding material budget in the order of 0.27%. The pixel pitch of TimePix detectors is of 55 µm, leading to a spatial resolution of at least $\frac{55\,\mu\text{m}}{\sqrt{12}} = 16\,\mu\text{m}$ under the assumption of equal charge distribution within a pixel.

- Monolithic silicon pixel detectors [61] are made of a single piece of silicon with the same CMOS process, incorporating both the sensing material and the amplifying and logic circuitry. Avoiding flip-chip bonding [62], such detectors are four to five times less expensive than HPD, for a similar coverage. With thicknesses down to 100-50 µm, their material budget is between 0.10-0.05%, and spatial resolutions in the order of 5 µm are expected with pixel dimensions of 20 µm × 20 µm. Despite very attractive features, this option was discarded due to its early development stage.

For each technology, contact was established with the corresponding detector development and user communities to assess possible developments for the BGV tracker. The simulation tool described in the previous section was then used to understand how the material budget and spatial resolution of the detectors impact the resolution of reconstructed vertices, and therefore the tracker performance, in the specific case of the BGV. Detector resolutions of 50 µm and 16 µm were considered, and silicon thicknesses of 1 mm and 270 µm were considered. The tracker dimensions were also considered with varying the distance between the tracking planes, adapting the second and third planes' dimensions accordingly, to keep the solid angle constant.

Figure 5.12 summarises the results of this study, with a selection made on events with $N_{\text{tr}} \geq 5$. The cluster reconstruction step was omitted.

Following these results, it can be noted that:

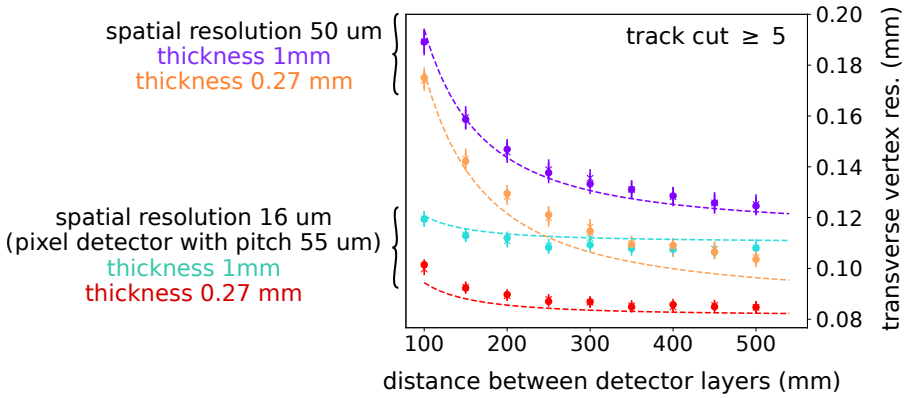

Figure 5.12: Vertex resolution in dependence of the distance between the detector layers, for different generic BGV configurations, as labelled on the left. [2]

- When considering detectors with poor intrinsic resolution (purple and orange curves), large tracking plane dimensions (right-hand side of the graph) greatly improve the vertex resolution. This effect is much less pronounced for high resolution detectors (green and red curves).
- In the case where a compact tracker is desired (left-hand side of the graph), a good detector resolution (green and red curves) is required to achieve vertex resolutions below 160 µm.
- For any given configuration, the vertex resolution is improved with low material budget sensors. The gain is slightly reduced when considering low resolution and compact tracker.

Based on these conclusions, and considering the tight space restrictions at the foreseen location for the B1-BGV, it was deemed optimal to focus on a compact tracker design. TimePix3 HPDs were the selected detector technology due to their high spatial resolution, and to the possibility to thin down the ASIC and sensor to achieve a low material budget. Placing tracking detector layers 250 mm apart allows for a compact tracker design, minimising the number of (expensive) TimePix3 required.

The tracker design will not be discussed in more details in this thesis. The final design can be found in [2].

5.5 Summary

A detailed Monte Carlo simulation tool of the instrument was implemented, together with an event reconstruction algorithm. After a careful analysis of the characteristics of the secondary particles generated in beam-gas interactions, a performance study was conducted, focusing on the vertex resolution of the BGV. The drawn results helped to define the measurement region, specify the global dimensions of the tracker and choose a detector technology.

Chapter 6

Gas tank design

Several requirements are imposed to the gas tank of the HL-BGV, which required specific studies. An overview of these requirements is presented here, followed by discussions on the constraints related to the beam stability, in particular the beam aperture protection and limitations due to the expected impedance contributions. The final design is then presented, together with its impedance contributions. Studies related to the gas target are presented in the following chapter.

6.1 Guidance for the gas tank shape

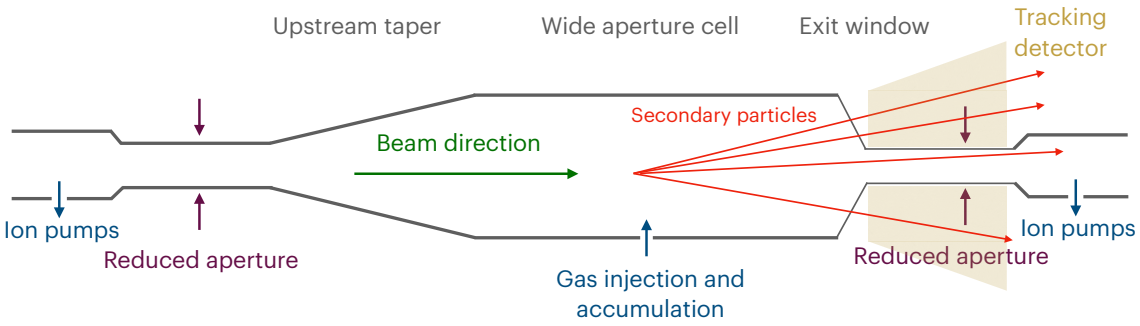

Figure 6.1: Sketch of the BGV gas tank.

The overall shape of the BGV gas tank is schematised in Figure 6.1.

In order to minimise the material crossed by secondary particles, and limit multiple scattering, a transition is introduced between a large and a reduced aperture beam chambers, where the amount of material is lowered compared to a standard straight chamber. The transition piece connecting the aperture change is called *Exit Window* (EW) and needs to be designed with special care, with a minimised material budget. The material

and thickness gradient of the exit window are important parameters to consider, which can substantially ease the event reconstruction.

Other parameters influence the shape of the gas tank.

- The choice for a distributed gas target requires a wide aperture cell, surrounded by small aperture chambers, to hold the gas into the volume of interest for the beam size measurement. The **density map of the gas target**, as shown in the following chapter, is also impacted by the length of the various BGV beam chambers.

- For a maximum acceptance of the tracker, the minimum possible **aperture** for the downstream small radius chamber is desired. Utilising a small inner radius, the tracker will profit from the high density of secondary particles travelling under a small angle with respect to the beam axis, which are generally more energetic. The minimum possible aperture is dictated by the transverse beam envelope and thus by the beam optic functions at the instruments' location.

- The diameter of the wide aperture cell should be large enough to maximise the amount of tracks traversing the exit window, and therefore being detectable, but not too big in order to limit unwanted **wakefield contributions** of the gas tank to the beam, as will be discussed in Section 6.3. The presence of an upstream taper also serves to limit the BGV wakefield contributions.

- The instrument is finally imposed to fit in the **regions of the LHC tunnel** foreseen for the two instruments installation, which restricts the length of the gas tank and the longitudinal spread of the BGV equipment, including the four ion pumps installed upstream and downstream of the tank.

6.2 Gas tank aperture

As explained in the previous chapter, the angular distribution of the secondary tracks shows a high density of secondary particles emitted under a small angle with respect to the beam axis, in the forward direction. Most of these tracks also benefit from a high momentum, making them less prone to large trajectory deviations due to multiple scattering. Placing the first detector layer as close as possible to the beam axis is therefore very beneficial, in order to achieve the maximum performance of the BGV.

All along the circumference of the LHC, the minimum transverse physical chamber aperture allowed is defined as the transverse beam size at injection, multiplied by 14.6 [63]. This *protected aperture* sets the minimum beam chamber aperture in radius, at a given location along the accelerator ring, which is guaranteed to be in the "shadow" of the beam collimation systems, i.e. with limited exposure to particle losses.

Figure 6.2 shows the protected aperture at the foreseen BGV instrument locations. The mechanical aperture profile of the HL-LHC BGV final design is also shown, in green color and including a 1.5 mm radial tolerance for manufacturing and alignment of the chambers. Due to higher β-functions, the protected aperture is larger at the foreseen B1-BGV location.

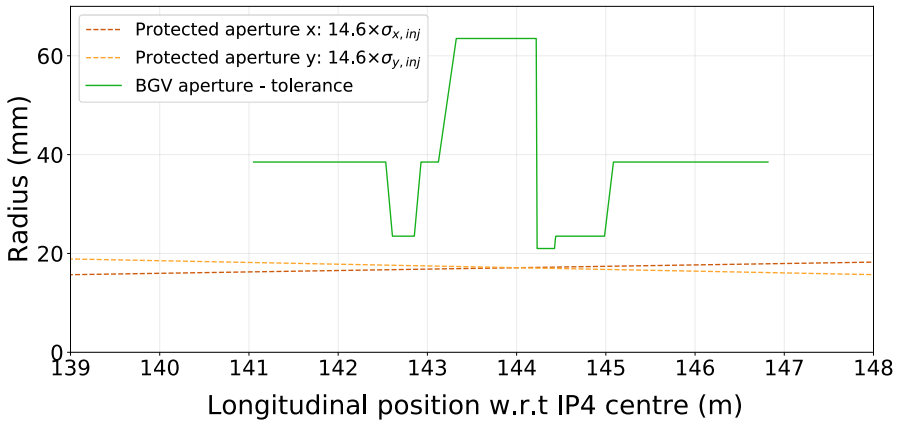

(a) B1-BGV location, on the right of IP4.

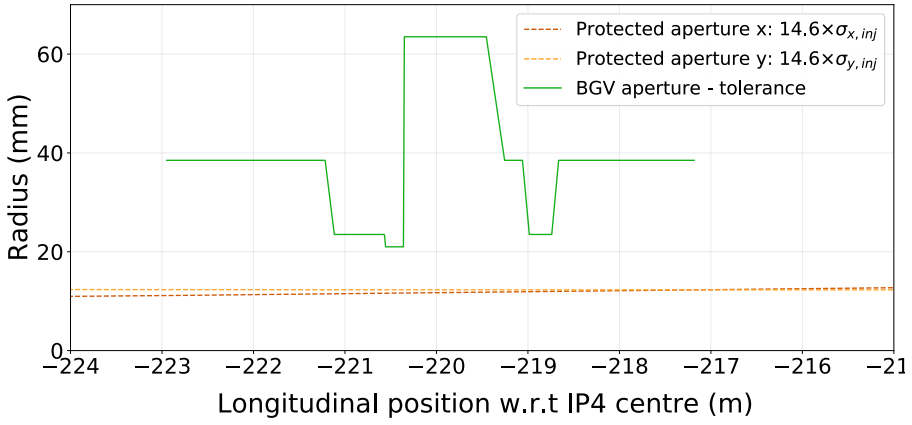

(b) B2-BGV location, on the left of IP4.

Figure 6.2: Protected aperture in x (orange line) and y (yellow line) planes, considering the LHC beam optics version 1.5, and BGV aperture profile (green line), at the foreseen instrument locations. The BGV aperture includes a 1.5 mm tolerance.

A radius of 22.5 mm was chosen for the 20 cm-long beam pipe holding the first detector plane [64]. Figure 6.2a shows that, taking 1.5 mm tolerance into account, such

a BGV aperture is only few millimetres larger than the aperture required by the beam, for the B1-BGV location. In case of a beam optics change, this value may need to be increased.

In terms of instrument performance, an increase of 0.5 mm in radius of the BGV aperture in this area would approximately reduce the accepted number of interactions used for a measurement by 7% with respect to the 22.5 mm radius aperture. An increase of 1 mm would lead to a 12% reduction. It should be noted that such a change of the BGV aperture would also impact the tracker design.

Upstream of the restricted aperture region of the BGV, the beam pipe aperture is less critical for the performance of the instrument, and therefore a slightly larger value of 25 mm radius was chosen.

6.3 Impedance optimisation study

The BGV gas tank is a cavity-like structure and represents a wakefield source in the LHC machine, increasing the beam-coupling impedance. Early in the instrument design process, its contribution was carefully considered.

6.3.1 Simulation tool

The commercial software *CST Particle Studio* [21] is commonly used to compute the wakefields and beam-coupling impedance contributions of accelerator components. It features two numerical solvers of interest for this purpose.

The time domain *Wakefield solver* allows to analyse the wakefield effects of a bunch of particles rigidly travelling through a defined structure by utilising an equivalent line-charge density distribution and computing the electromagnetic (EM) fields in the geometric volume of the component. The simulated volume is divided into hexahedral mesh cells, in which Maxwell's equations are solved with a finite difference method, for each time sample. The wake potential is obtained with integrating EM fields along the predefined integration path. The corresponding beam-coupling impedance is calculated by applying a Fourier transform to the wake function.

In a complementary way, the *Eigenmode solver* allows to calculate the frequency and field patterns of the eigenmodes resonating within a structure, using finite element method, which involves approximations [65]. All geometry boundaries are considered closed (with

vanishing transverse electric field), and no excitation signal.

In the following, the longitudinal eigenmodes and effective impedance of the BGV tank are studied.

The shunt impedance $R_{s,n}$, quality factor Q_n and resonant frequency $f_{\mathrm{res},n}$ of each eigenmode n are determined using *CST Eigenmode solver* simulations. The broadband spectrum is then reconstructed using the resonator model [19], which was presented in Chapter 2 and consists in summing the contribution of each resonant mode identified by the *Eigenmode solver*:

$$Z_{\parallel}(\omega) = \sum_{n=0}^{\infty} \frac{R_{s,n}}{1 + jQ_n\Big(\frac{\omega}{\omega_{\mathrm{res},n}} - \frac{\omega_{\mathrm{res},n}}{\omega}\Big)} \tag{6.1}$$

$$= \mathrm{Re}[Z_{\parallel}(\omega)] + j\ \mathrm{Im}[Z_{\parallel}(\omega)]. \tag{6.2}$$

An example impedance spectrum is given in Figure 6.3, obtained for the structure shown in 6.12, made with 2 mm thick walls of stainless steel with a conductivity of $\sigma_{\mathrm{el,SS}} = 1.35 \times 10^6\,\mathrm{S/m}$. In this chapter the shunt impedance values are given using the circuit convention [66]: $R_s = \dfrac{V^2}{2P}$ where V is the induced voltage and P is the dissipated power.

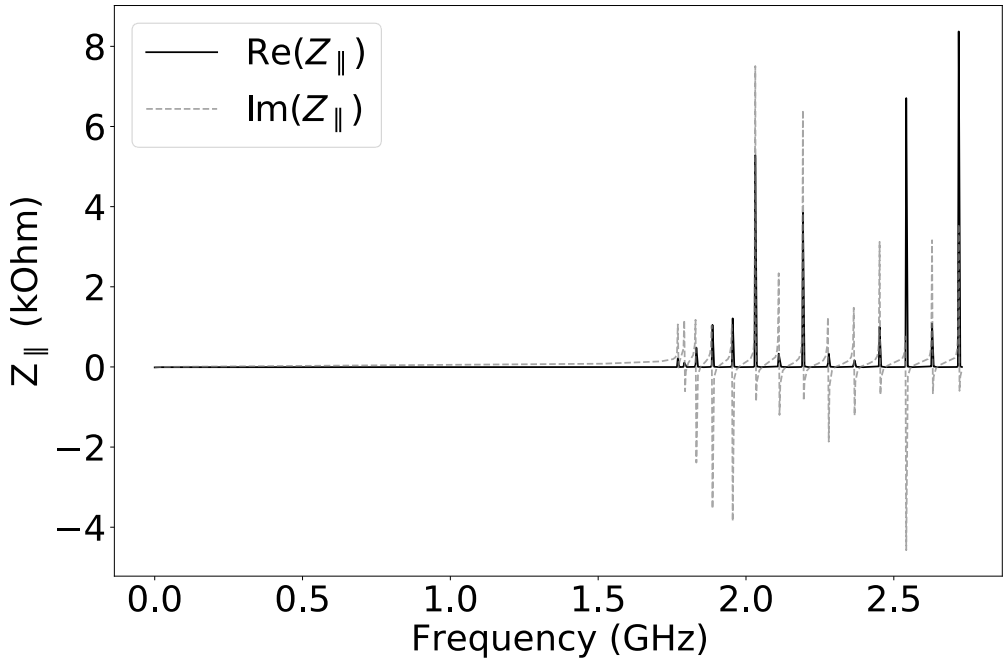

Figure 6.3: Example longitudinal impedance.

The other figure of merit considered here is the longitudinal effective impedance

$(Z_{\parallel}/n)_{\text{eff}}$, introduced in Chapter 2. Also noted $\text{Im}(Z_{\parallel}/n)$, it is derived by multiplying the slope of the imaginary impedance $\text{Im}[Z_{\parallel}]$, obtained with *Wakefield solver* simulations, with the LHC revolution frequency $f_{\text{rev}} = 11\,245\,\text{Hz}$.

6.3.2 Impedance of the demonstrator BGV

The beam-coupling impedance of the demonstrator tank was simulated in 2014 [67] and is dominated by a series of resonant modes. The real part of the longitudinal impedance of the demonstrator BGV is shown in Figure 6.4a, indicating the contribution of a series of resonant higher order modes (HOMs) deemed significant. With the LHC Run 3 beam parameters, the estimated power loss in the BGV gas tank is in the order of tens to hundreds of Watts, depending on the exact longitudinal particle distribution of the bunch.

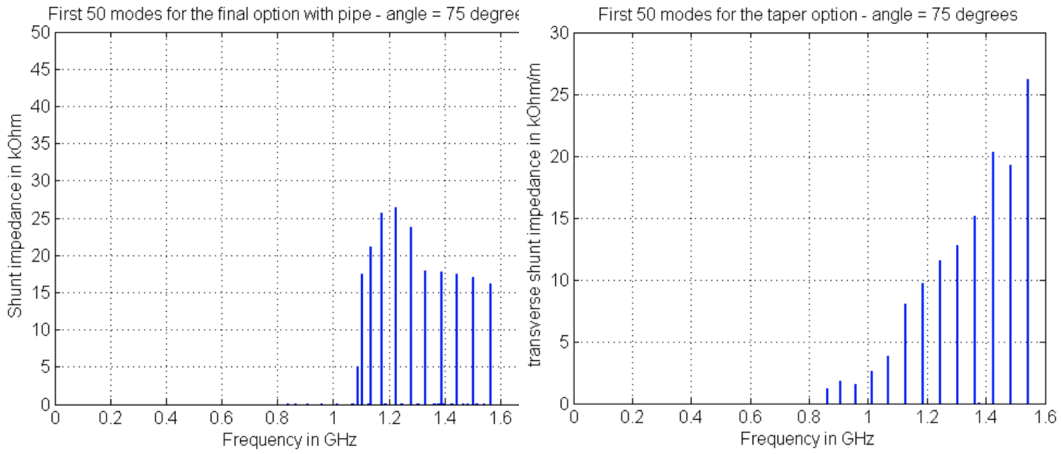

(a) Longitudinal modes. (b) Transverse modes.

Figure 6.4: Real part of the beam-coupling impedance of the major longitudinal (6.4a) and transverse (6.4b) resonant modes, as simulated with CST Particle Studio for the demonstrator BGV [67]. The transverse impedance is shown weighted by the beam displacement.

The longitudinal effective impedance of the demonstrator was evaluated to $0.74\,\text{m}\Omega$, which, although representing $< 1\%$ of the overall machine effective impedance, is large relative to the device's length.

Recommendations encouraged for the future instrument to minimise these contributions when possible. In particular, in case the tank shape of the HL-BGV would be similar, the diameter of the wide part of the tank should be minimised and the existing tapers on each side of this wide part should be kept, with a trade-off to be found with instrument performance.

The transverse contributions raised less concerns:

- The transverse effective impedance was evaluated to 10 kΩ/m, which is small compared to the overall transverse beam-coupling impedance of the machine;
- The transverse resonant modes show shunt impedance peaks - weighted by beta function - below 100 kΩ/m, as witnessed by Figure 6.4b. Such values were stated to be at least two orders of magnitude lower than the LHC overall impedance model in this frequency range. Therefore the demonstrator transverse eigenmodes were considered to be in the background of the rest of the machine, as well.

Given the beam intensity increase foreseen with the HL-LHC upgrade, it was deemed important to investigate a BGV instrument with a reduced impedance, in particular lowering the contribution of the HOMs with respect to the demonstrator BGV.

With the above mentioned conclusions in mind, and aiming for a similar tank shape for the future instrument, a design optimisation study was performed, focusing on reducing the longitudinal impact of the tank's eigenmodes. The impact of the tank shape on the longitudinal effective impedance is also considered.

6.3.3 Parametric study

In the following, the impact of several dimension parameters of the BGV gas tank geometry on its longitudinal eigenmodes and longitudinal effective impedance are studied.

6.3.3.1 Cylindrical cavities

The diameter D and length L of the gas tank structure are considered first, focusing on a cylindrical shape of the cavity structure, sometimes referred as "pill-box" cavity, as shown in Figure 6.5. This approach also serves to benchmark the simulation and validate simulation parameters, since results can be compared with analytical solutions.

To be consistent with the BGV constraints, the simulated cavities are connected upstream to a 50 mm diameter beam pipe, and downstream to a beam pipe of 45 mm diameter. The structures are modelled with a vacuum volume, surrounded by a *perfect electric conductor (PEC)* material background. This choice prevents the field's energy to dissipate in the walls, and focuses on the impact of the geometrical dimensions of the structure.

Figure 6.6 shows the impact of varying the cavity diameter on the resonant modes. Reducing D, the shunt impedance of the modes decreases and their frequency increases.

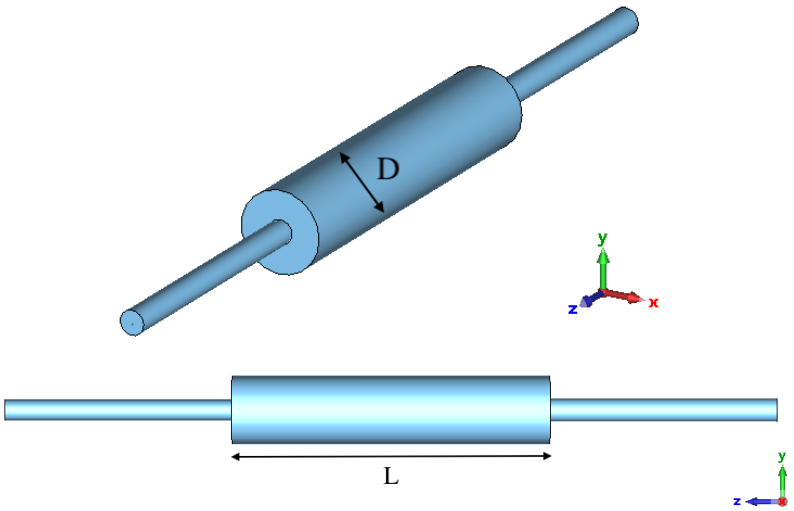

Figure 6.5: Geometry of a pillbox-shaped cavity, visualised in *CST Particle Studio*.

In particular, the eigenmode with the shunt impedance of the highest peak value for a given configuration increases linearly with D, as shown in Figure 6.7. The dependency of the frequency of the fundamental TM010 mode f_0 to the diameter $D = 2r$ is shown in Figure 6.8, and follows the expected behaviour: $f_0 = \frac{c}{2.61 \times r} \simeq \frac{229 \times 10^6}{D}$, where c is the speed of light [68]. In Figures 6.7, 6.8 and 6.9a, the configurations that were already shown in Figure 6.6 are denoted in the same colour to ease their identification, while grey crosses indicate configurations which are new.

For instruments to be installed in the LHC, shifting the frequency of the HOMs to high values above $\sim 1\,\text{GHz}$, is extremely valuable, since the harmonics of the LHC beam power spectrum have significantly lower intensities in this frequency range, in particular above 1.4 GHz [69]. An example LHC beam power density spectrum is shown in Figure 6.21 (light green).

The longitudinal effective impedance is also decreased for small diameters, as can be seen in Figure 6.9a.

Thus, the diameter D is a key parameter to be minimised to avoid strong beam-coupling interactions.

Figure 6.10 shows the impact of varying the length L of a $D = 130\,\text{mm}$ diameter cavity on its HOMs. It can be noted that the eigen-frequencies of the tested configurations are always above 1.7 GHz, which is a significant improvement compared to the previous (demonstrator) design. In addition, in the range of interest, longer cavities develop more eigenmodes, but with lower R_s values. The maximum shunt impedance among these modes

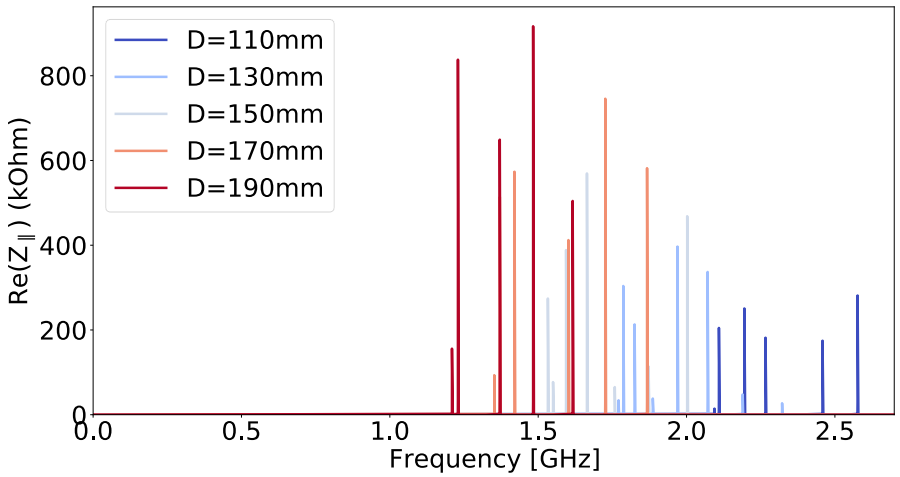

Figure 6.6: Real part of the longitudinal impedance of 700 mm long pillbox cavities, varying their diameter. Only the first 10 modes are shown.

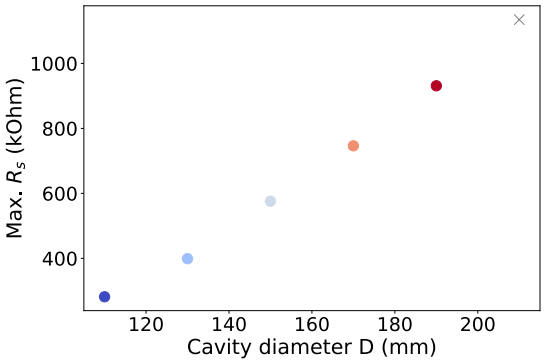

Figure 6.7: Simulated peak shunt impedance of resonant modes vs. diameter of the cylindrical cavity.

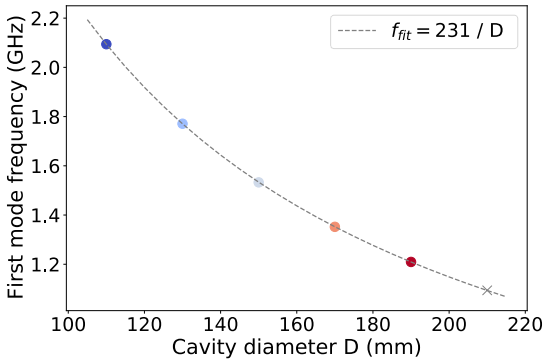

Figure 6.8: Simulated frequency of the first resonant mode as a function of the cavity diameter.

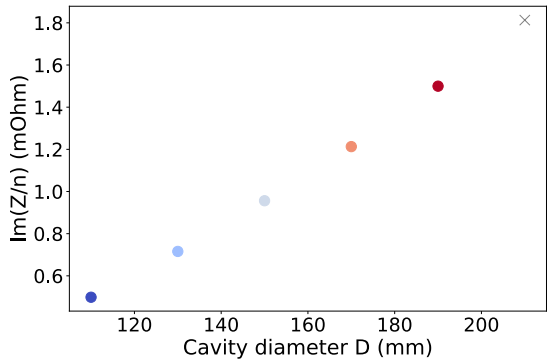

(a) D scan.

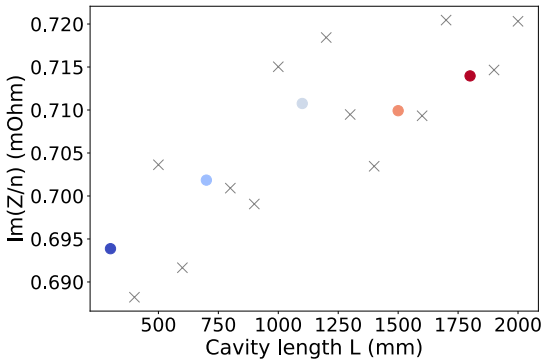

(b) L scan.

Figure 6.9: Longitudinal effective impedance, varying D (6.9a) and L (6.9b).

for each configuration is shown in Figure 6.11. Below $L \simeq 1$ m, increasing the length of the cavity has a strong impact on the maximum shunt impedance, which decreases quickly.

This effect is less pronounced for longer cavities.

$\mathrm{Im}(Z_{\parallel}/n)$ of a cylindrical cavity structure also shows a global increase with its length, as is shown in Figure 6.9b. The colour scale used in Figures 6.9b and 6.11 corresponds to the configurations shown in Figure 6.10. Grey crosses are additional geometry cases.

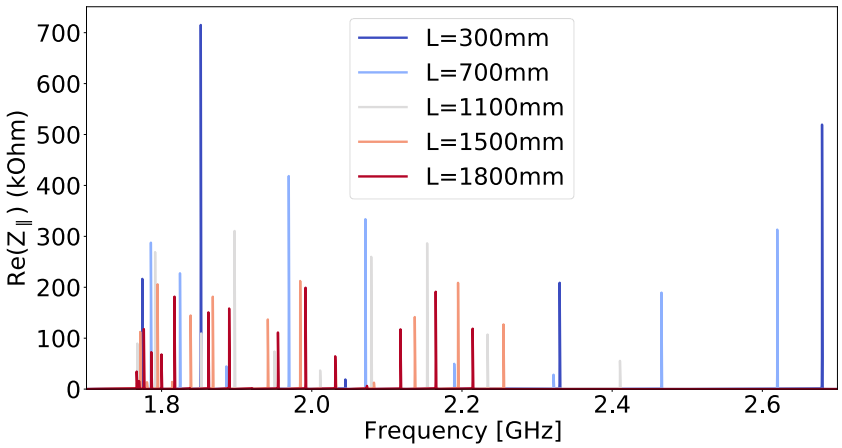

Figure 6.10: Real part of the longitudinal impedance of a cylindrical cavity of diameter $D = 130\,\mathrm{mm}$, for different lengths. Only the first 20 modes of each configuration are shown, with resonant frequency $< 2.7\,\mathrm{GHz}$.

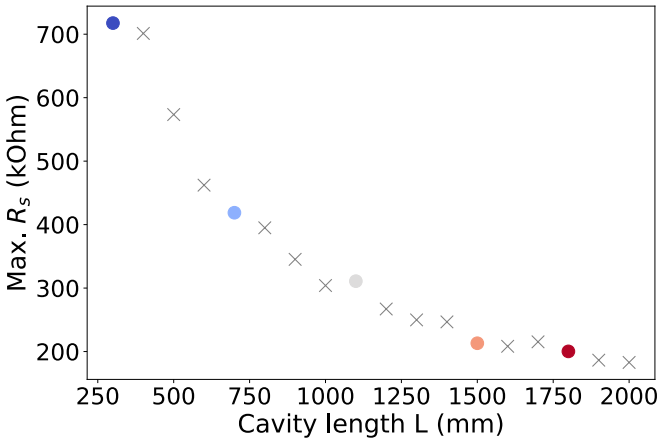

Figure 6.11: Highest peak value of the shunt impedance of resonant modes vs. length of the cylindrical cavity.

The choice of the tank length thus results in a compromise between the number of eigenmodes and their shunt impedance. Other parameters including the gas density profile and spatial constraints were taken into account to decide the final tank length.

6.3.3.2 Tapers

Tapering abrupt discontinuities of a change of the diameter of the vacuum chamber is a common mitigation measure to reduce cavity-like impedance sources [19]. In the BGV case the exit window is a critical element of the BGV instrument in terms of performance with little margin for geometric arbitration, as will be detailed in Section 6.4, the presence of the upstream taper exclusively aims at lowering the contribution of the BGV HOMs.

The impact of the length of the upstream taper and exit window, L_{in} and L_{out}, respectively, positioned as shown in Figure 6.12, on the longitudinal gas tank impedance was investigated in detail. The case of the exit window is presented in the following. Similar conclusions were observed with the upstream taper, which can be found in Appendix C, for $L_{\text{in}} \in [100, 500]$ mm.

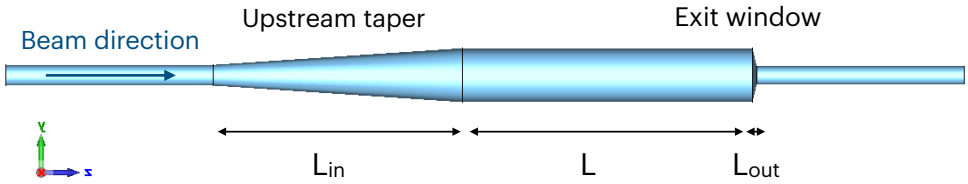

Figure 6.12: Geometry of the tapered BGV tank, visualised in *CST Particle Studio*.

Starting from a 130 mm diameter and 700 mm long cylindrical cavity, the impact of L_{out} was studied in two different ways.

- Variation of the exit window taper by subtracting $L_{\text{out}} \in [10, 50]$ mm from the cylindrical part of the BGV, $L + L_{\text{out}} = 700$ mm
- Variation of the exit window taper by adding $L_{\text{out}} \in [10, 50]$ mm to the cylindrical part of the BGV of constant $L = 700$ mm.

When considering the upstream taper, a wider range was considered for the taper length, while taking into account integration space constraints.

Figure 6.13 shows the results corresponding to the first approach. Configurations with longer tapered sections (red) show higher eigenmode frequencies. The shunt impedance of the different modes have disparate behaviours with the increase of L_{out}. It should be noted that with this approach, structures with longer tapers also have shorter L.

The conclusions are less apparent when a taper of length variation L_{out} in the same range is added to the cavity, instead of tapering the corresponding extremity. The results are shown in Figure 6.14, where in general, the configurations with a longer taper result in

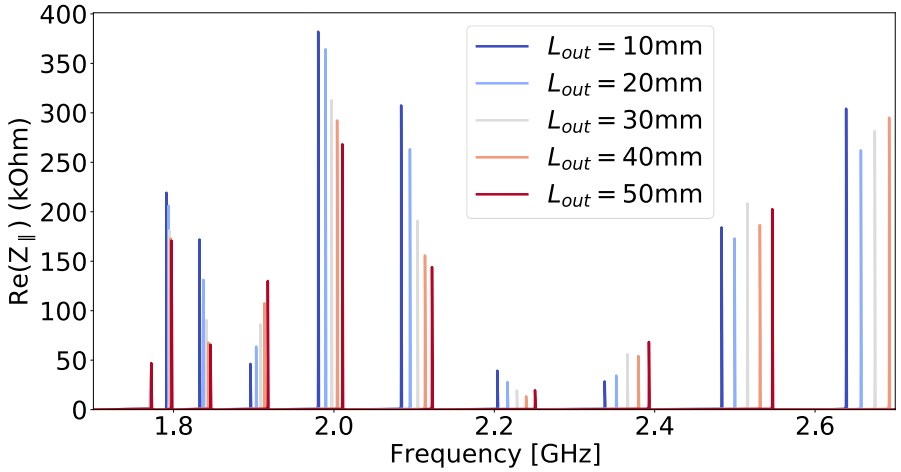

Figure 6.13: Real part of the longitudinal impedance of 700 mm long cylindrical cavities of 130 mm diameter, tapering the downstream extremity.

modes producing a lower R_s. Small frequency shifts are also observed, but sometimes are towards higher frequencies, sometimes towards lower ones, depending on the considered eigenmode.

The cylindrical length L turns out to be the main impact parameter regarding the eigen-frequencies of the modes, while the length of the taper foremost controls R_s.

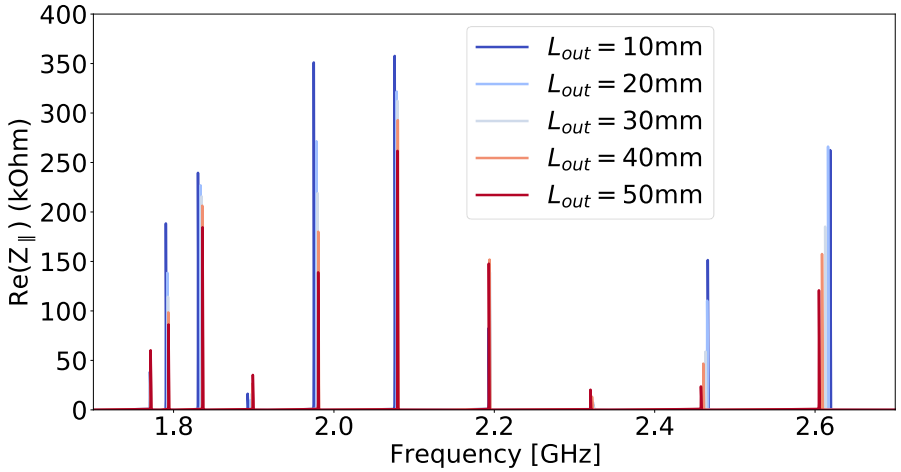

Figure 6.14: Real part of the longitudinal impedance of 700 mm long cylindrical cavities of 130 mm diameter, adding a downstream taper corresponding to the exit window.

Regarding the effective impedance however, both approaches lead to a lower $\mathrm{Im}(Z_\parallel/n)$ when L_{out} is increased, as shown in Figure 6.15. The main interest in tapered cavities is therefore to reduce their effective impedance contribution.

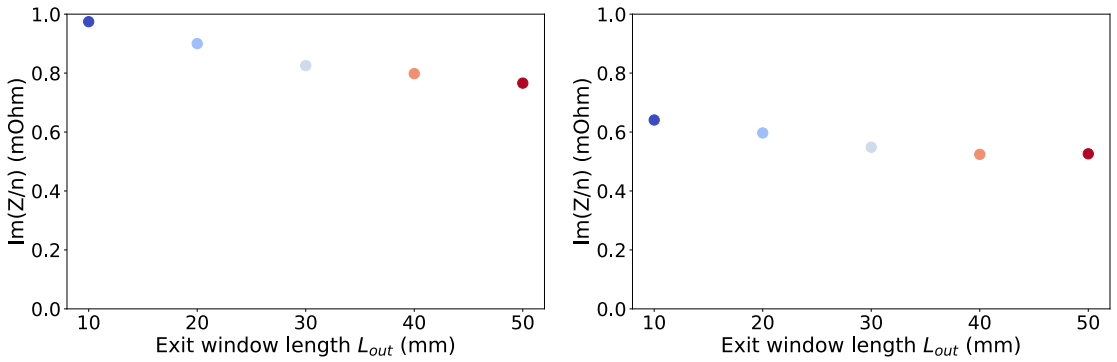

(a) Adding an exit window taper of length L_{out}. (b) Tapering the cavity extremity by L_{out}.

Figure 6.15: Longitudinal effective impedance as function of L_{out}, by adding (6.15a) or subtracting (6.15b) a downstream taper to the cylindrical part of the cavity .

6.3.3.3 Summary

In summary, the diameter D is a critical parameter which should be minimised to reduce the contribution of the resonant modes, which was the main source of concern for the demonstrator BGV tank. A longer cylindrical cell also helps reducing the shunt impedance of these modes, with the downside making them more numerous. Once L and D are fixed, tapers at the extremities of the cylindrical cavity help to reduce the longitudinal effective impedance of the structure and, to a certain extent, limits the contribution of its HOMs.

Based on these results, D was set to 130 mm, hence limiting the risks of strong beam coupling due to the structure's eigenmodes. Restricting the outer diameter of the first detector layer to the same value, and therefore constraining the tracker acceptance, this choice results in a trade-off between the gas tank impedance and the amount of tracks entering the first detector layer.

The impedance impact of the length of the tapers (L_{in} and L_{out}) and cylindrical part of the tank (L) was considered for the final design. L_{out} was chosen by taking material budget constraints into account, and will be discussed in the following section. The following chapter details how L and L_{in} were optimised to obtain a satisfying longitudinal density profile of the gas target and to meet the various integration constraints.

The resistive wall impedance of the BGV, which was not considered in this discussion, is mainly defined by the diameter of the tank. The associated quantities, which are the transverse effective impedance, deemed negligible for the demonstrator, and the beam-induced power loss, will be carefully considered for the final geometry, given the increased beam-walls proximity compared to the demonstrator structure.

6.4 Shape of the exit window

Performance-wise, the secondary particles should traverse the smallest possible amount of material before reaching the tracking detectors, to minimise trajectory deviations due to multiple scattering. This is achieved on one hand by adapting the vacuum chamber shape such that it is perpendicularly traversed by the measured secondaries, and on the other hand by the selection of materials with long radiation length for the chamber piece traversed by the secondaries. This specific part of the BGV tank is called the *Exit Window* (EW).

The optimised EW inclination θ_{out} with respect to the beam axis is determined with considering the tracker acceptance, as shown in the top sketch of Figure 6.16.

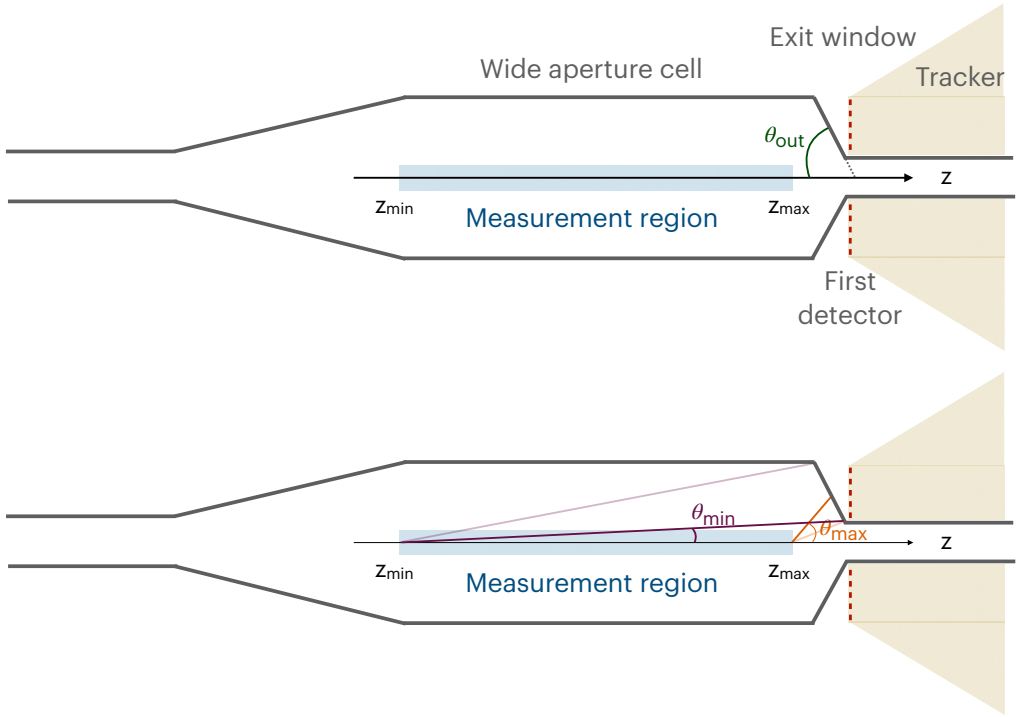

Figure 6.16: Sketches of the BGV gas tank, highlighting the formalism for the exit window angle θ_{out} (top sketch) determination. θ_{min} (purple) and θ_{max} (orange) are shown in the bottom sketch. These angles are determined wrt. the acceptance of the first detector layer (red).

On this figure, the measurement region, defined in the previous chapter, is depicted in blue. As we aim to measure beam-gas interactions inferring from this volume, the tracks with the smallest angle θ_{min} with respect to the beam axis in the tracker acceptance originate from the upstream end of the measurement region. Tracks with the largest angle θ_{max} originate from beam-gas interactions located close to the exit window. Both angles

are indicated in the bottom sketch.

With an inner radius of about 24.5 mm and an outer radius of 65 mm, the first detector layer will detect tracks with angles ranging from $\theta_{\text{min}} = 38°$ to $\theta_{\text{max}} = 89°$ ($\eta \in [0.7, 4.5]$). Depending on the transverse position of the subsequent detector layers, such tracks may not cross the entire tracker, but these values give a hint of the range of track angles in the tracker acceptance. In order to ensure that most of these tracks cross the exit window perpendicularly, θ_{out} should be in the range [38°, 89°] ($L_{\text{out}} \in [0.7\,\text{mm}, 54\,\text{mm}]$). $\theta_{\text{out}} = 75°$ was chosen as final value, which is the same angle that was used for the demonstrator EW, and corresponds to $L_{\text{out}} = 10\,\text{mm}$.

Given the change of diameter along the EW part, some gradient of the material thickness had to be included in the mechanical design to stand the difference between the LHC vacuum and the atmospheric pressure.

This gradient contributes in lowering the material budget of the EW. The thickness of the demonstrator EW wall was already minimised at its inner diameter end, as shown in Figure 6.17. With the smaller chamber diameters foreseen for the HL-LHC BGV, compared to the demonstrator BGV, the thickness along the EW can be further reduced, as suggested by preliminary studies [70]. For an EW part made out of the same aluminium alloy as for the demonstrator EW, a thickness gradient ranging from about 2.1 mm on the outer diameter to 0.9 mm on the inner diameter would be achievable, and is being considered at the time of writing. The choice of the EW material will be discussed in Section 6.5.2.

6.5 Final layout

Based on the previously presented mechanical aperture, beam-coupling impedance and EW investigations, and after a careful consideration of the gas target density profile, presented in the following chapter, the chamber dimensions were chosen and the final layout is presented below.

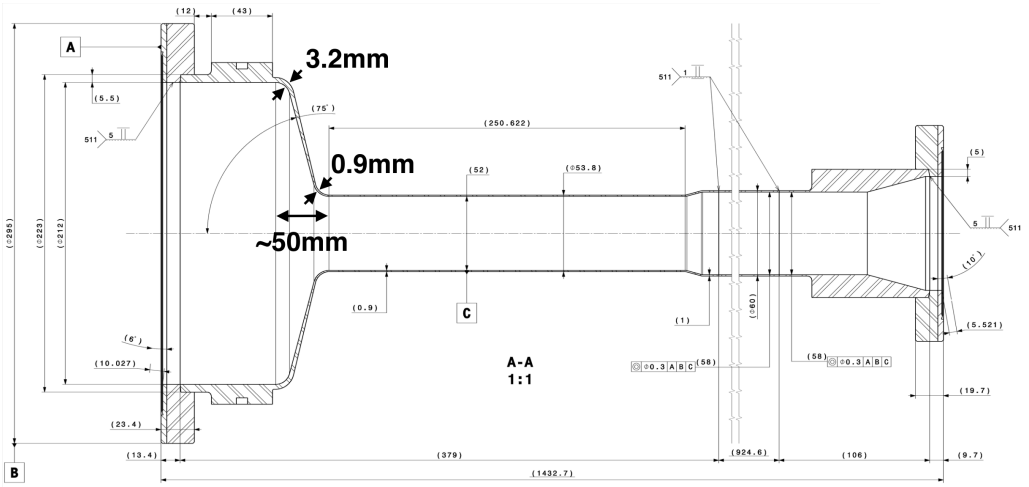

Figure 6.17: Mechanical drawing of the demonstrator BGV exit window.

6.5.1 Chamber dimensions

The dimensions of the final version of the BGV tank is depicted in Figure 6.18, showing an overall 3D drawing (top picture) and a longitudinal section view (bottom picture) of the final tank design. The beam first encounters a 250 mm long restricted aperture section of 50 mm diameter, followed by the upstream taper, which transitions to the 130 mm wide aperture cell and is about 477 mm long. The gas cell is 700 mm long and is connected to the exit window, which reduces the diameters down to 45 mm over a length in the order of 10 mm. The exit window part also includes a 200 mm long beam pipe which holds the detectors constituting the first tracking layer. The subsequent tracking planes are placed on a slightly wider beam pipe of 50 mm diameter and of length 550 mm.

This entire vacuum tank assembly is rigid, and shall be mounted on a girder and connected to the LHC beam pipes with bellows, allowing for small displacements and for a careful alignment with respect to the rest of the machine.

The overall design is more compact compared to the demonstrator BGV, which was 11 m long in total, including the gas pumps. The new design is about 6 m long and fits in the tight available space at the foreseen B1-BGV location. The main modifications are related to the dimensions of the beam chamber elements, most of them could be made shorter and narrower. Notably, the wide aperture cell and the downstream reduced aperture sections have smaller diameters compared to the demonstrator: the first one was reduced from 212 mm down to 130 mm diameter, and the downstream low aperture beam pipe which was 52 mm wide now has a diameter of 45 mm.

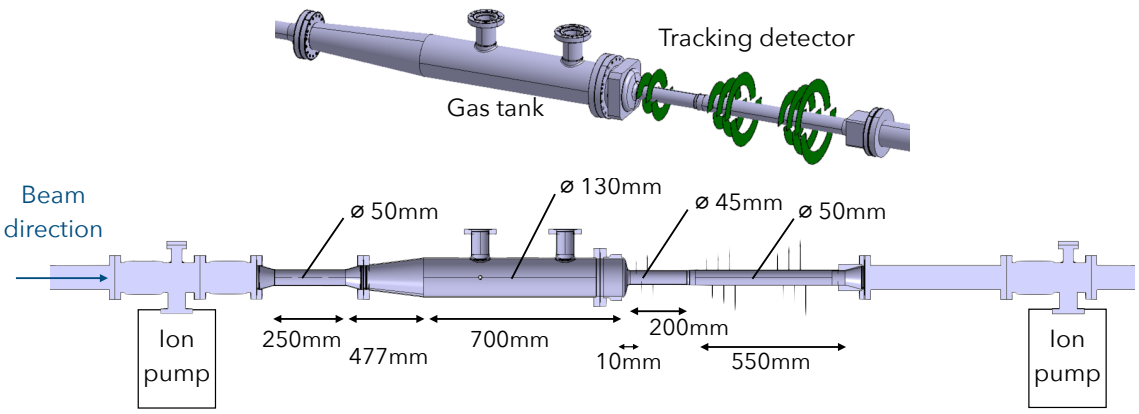

Figure 6.18: *Catia* [71] drawings of the final design of the BGV gas tank. Both drawings are oriented with the beam entering from the left side.

6.5.2 Materials and coating

Alike most vacuum chambers in the LHC warm sectors, the entire BGV assembly will be coated with a TiZrV NEG layer [72, 73], which acts as a passive pumping treatment for most residual gases. This coating also serves to limit the growth of electrons clouds, thanks to its low secondary-electron emission yield.

In order to activate and regenerate the absorbing capacity of the NEG coating, an activation step is required, consisting of baking the chamber with a heating jacket operated at high temperatures, circa 200°C [74]. Therefore, the tracker has to be easy to dismount, and all chamber materials must be able to handle these temperatures without damage.

Most parts of the BGV tank assembly will be made of stainless steel, except the exit window. Here, an aluminium alloy was chosen, benefiting from a radiation length about five times higher than steel. Because of its specific shape, the EW would be forged from an aluminium alloy block, with the same composition than was used for the demonstrator piece [1]: AA2219, containing 6% of copper. This specific alloy is resistant to high NEG activation temperatures while being weldable. Taking into account the EW thickness gradient from 2.1 mm to 0.9 mm, a particle traversing 1.5 mm of aluminium would experience a material budget (x/X_0) of 1.7%.

With an even higher radiation length, beryllium was also considered for the manufacturing of the exit window. The aluminium alloy was preferred, due to the high manufacturing costs of beryllium, caused by its toxicity.

6.6 Beam-coupling impedance of the new BGV tank design

The beam-coupling impedance contributions of this new BGV tank design were estimated and are presented in this section.

6.6.0.1 Simulation settings

The geometry of the BGV tank shown in Figure 6.19 was simplified compared to the mechanical design. The differences are however minor and have negligible effects on the impedance results.

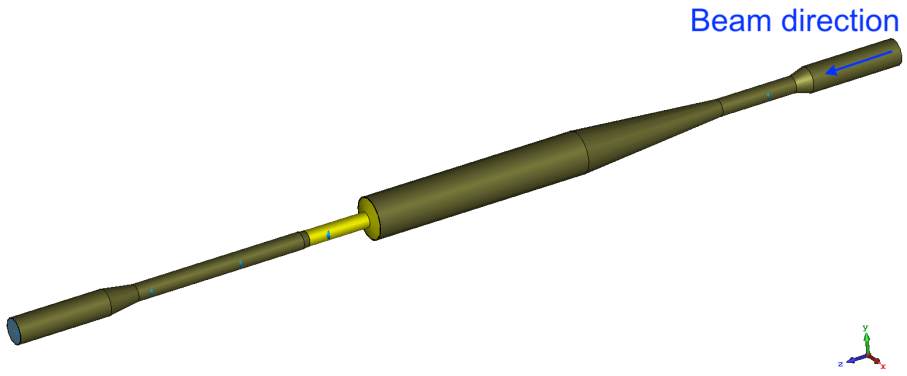

Figure 6.19: Final gas tank geometry, visualised in *CST Particle Studio*, with the beam entering the geometry from the left side. Brownish parts are made of stainless steel, of electrical conductivity $\sigma_{SS} = 1.35 \times 10^6\,\mathrm{S/m}$, and yellow ones of aluminium, of conductivity $\sigma_{Al} = 3.6 \times 10^7\,\mathrm{S/m}$. The walls are all 2 mm thick, and the volume is filled with vacuum.

The CST *Wakefield solver* was used to obtain the beam-coupling impedance spectra, discussed as follows. The results were first compared and showed good agreement with the resonant mode parameters obtained from the CST *Eigenmode solver* analysis. The wakefield time domain simulations were run with a wake length of 100 m, that ensured the remaining energy stored in the cavity-like structure was decreased by 40 dB.

As shown in Chapter 2, the longitudinal impedance is dominated by the monopole mode ($m = 0$) for axi-symmetric geometries. Both, the source beam and the wake integration path are therefore set on the symmetry, i.e. the beam axis to compute the longitudinal BGV impedance contributions. An ultra-relativistic Gaussian bunch ($\beta_r = 1$) with a length of 0.5 ns (4-σ) is used as excitation signal, and the mesh is defined with 20 cells per wavelength. The wake is integrated via the indirect interfaces method [75], which is typically used for structures with unequal beam ports, or with concave shapes, as is the

case for this setup.

6.6.1 Longitudinal impedance and its impact on the beam stability

The real and imaginary parts of the longitudinal impedance of the new gas tank design are shown in Figure 6.20.

The resonance pattern of the HOMs is very similar to the one of the demonstrator structure, given the similar tank shape and wall materials. The resonant modes however, are pushed to higher frequencies: starting from 1.7 GHz, versus 1.1 GHz for the demonstrator. Furthermore, Figure 6.21 depicts the frequency region of the beam power density spectrum, which is reasonably well below the eigenmode resonances of the new BGV tank. Finally, thanks to a lower diameter and sufficient length of the tank, and to the presence of tapers, the shunt impedance R_s of those modes are also decreased and do not exceed 16 kΩ, compared to the maximum of 27 kΩ reached by the demonstrator BGV. A table summarising the parameters of the main resonant modes of the final BGV structure can be found in Appendix D.

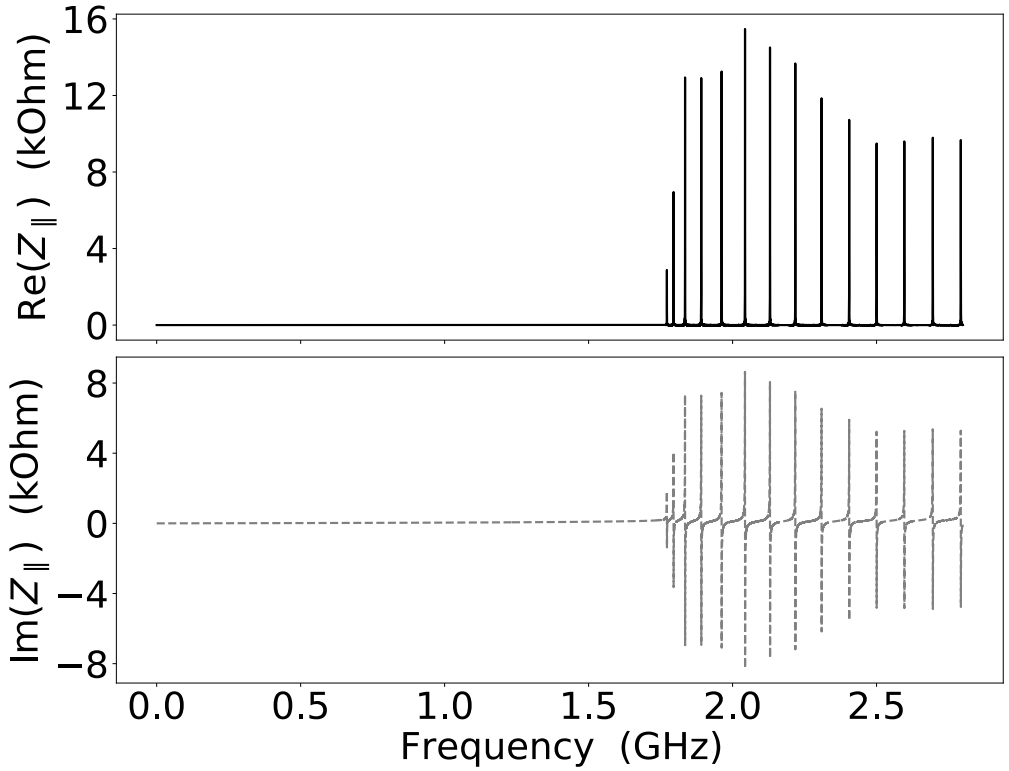

Figure 6.20: Longitudinal impedance of the final BGV tank, analysed with *CST Particle Studio*.

Regarding the beam stability, in this high frequency range the estimated growth

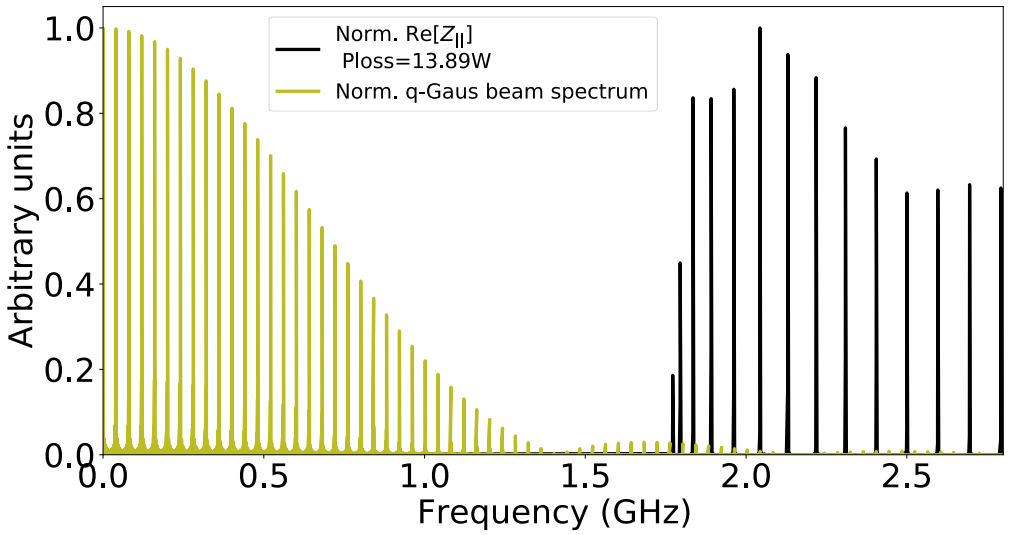

Figure 6.21: Real part of the normalised impedance spectrum of the final BGV and LHC beam power density spectrum. The beam power spectrum is obtained considering a q-Gaussian distribution function, populated with 2.3×10^{11} particles, with a 4-σ length of 1.2 ns and spaced by 25 ns.

rates of the longitudinal instabilities due to the presence of the BGV tank are lower than the growth rates driven by the resonant modes which are already present without BGV tank in the LHC model [64, 76].

The longitudinal effective impedance is obtained from the slope of $\mathrm{Im}(Z_{\parallel})$ at low frequencies, and is 0.38 mΩ. This value is almost two-times smaller than that of the demonstrator tank (0.74 mΩ). This contribution is small compared to the total foreseen HL-LHC effective impedance, which is in the order of 75 mΩ [64, 76].

The impact of this HL-BGV design is therefore optimised with respect to longitudinal beam stability.

6.6.2 Beam-induced heating

An expression of beam-related RF power losses P_{loss} due to interaction with the BGV structure was discussed in Chapter 2, and is related to the intensity I_{beam} and normalised power density spectrum $\Lambda(\omega)$ of the LHC beam.

$$P_{\mathrm{loss}} = 2I_{\mathrm{beam}}^2 \sum_{i=0}^{p} |\Lambda(p\omega_i)|^2 \mathrm{Re}[Z_{\parallel}(p\omega_i)] \,. \tag{6.3}$$

$\Lambda(\omega)$ is defined by the longitudinal particle distribution of the beam. Here, four different distributions were considered and the related normalised power density spectra

are shown in Figure 6.22.

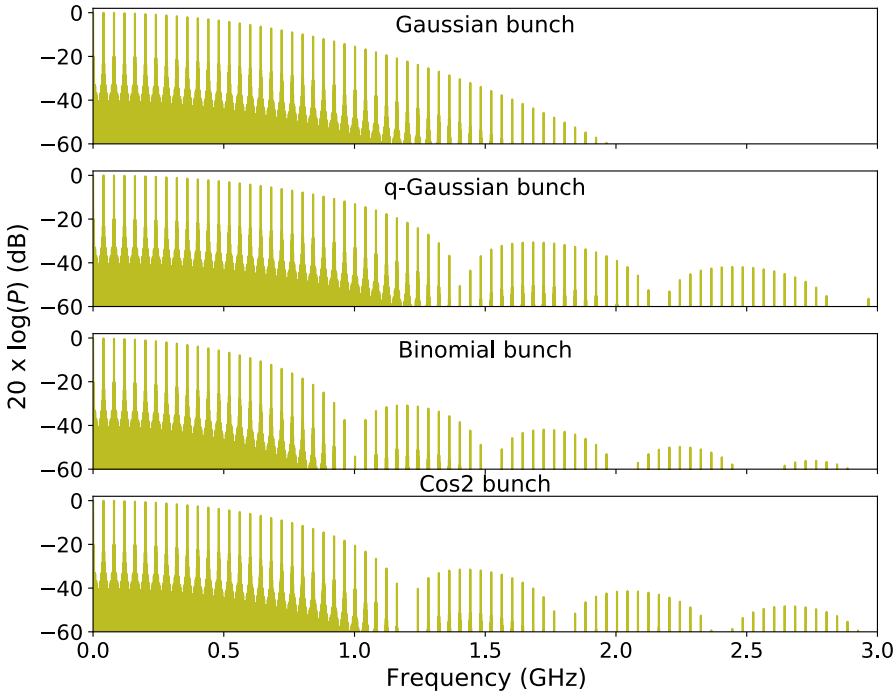

Figure 6.22: Normalised HL-LHC beam power density spectrum for different bunch shapes, considering a bunching frequency of 40 MHz and a bunch length of 1.2 ns.

To account for errors in the impedance model of the BGV, for instance due to mechanical tolerances of the manufactured device, or since the spectrum of the circulating beam is highly sensitive to the operational longitudinal bunch distribution and filling pattern, a perturbation analysis was performed.

For each case of the four bunch shapes the impedance spectrum was randomly shifted by an offset frequency varying between −20 MHz and 20 MHz, in order to consider all possible cases of overlap between the coupling impedance resonances and the beam harmonics. For each bunch shape, the average power loss of all the shifted impedance configurations was calculated, and the case with the maximum value was considered as worst possible configuration. Table 6.1 summarises the obtained results, listing for each bunch shape the average and the maximum power loss among the tested configurations. While the average beam induced power loss is estimated in the order of 10 W, the worst case scenario leads up to 42 W of extracted power, and is presented in Figure 6.23. It corresponds to a beam with a q-Gaussian bunch shape and a shift of 8.6 MHz of the BGV impedance spectrum.

As shown in Figure 6.23, most of the extracted power is due to the coupling of the

Table 6.1: Beam Induced Power Loss

Bunch shape	**average P_{loss}**	**maximum P_{loss}**
Gaussian	11 W	12 W
q-Gaussian	14 W	**42 W**
$\cos^2$	10 W	12 W
Binomial	8 W	9 W

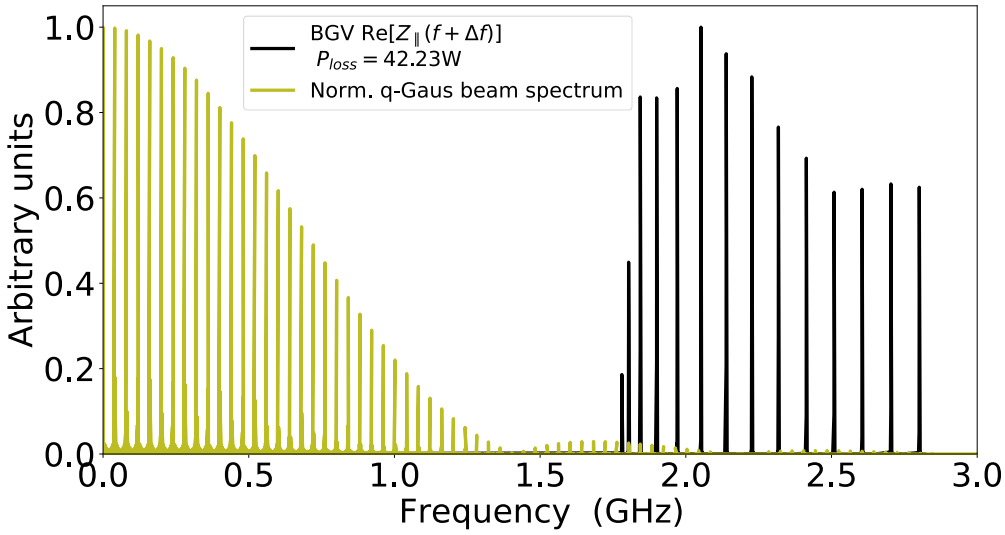

(a)

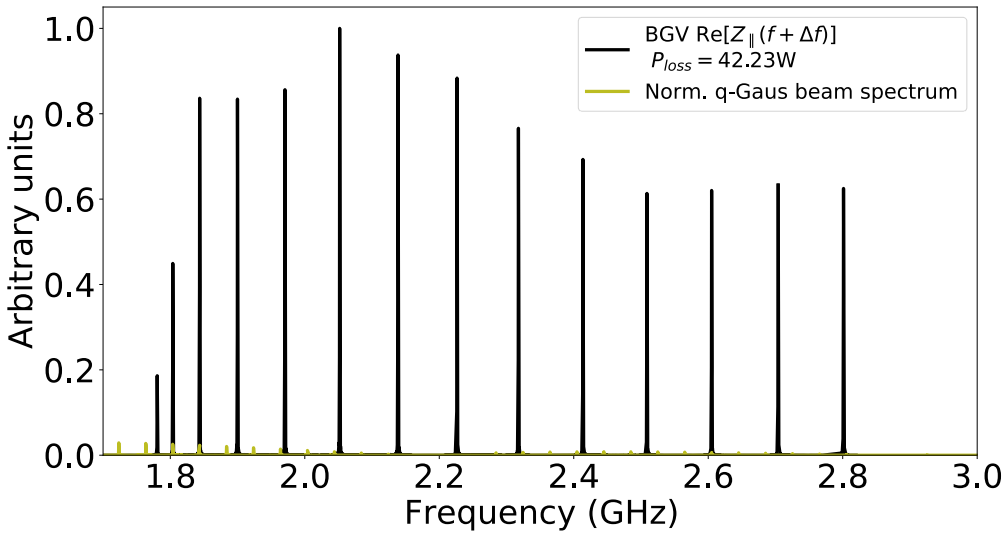

(b)

Figure 6.23: Normalised impedance spectrum of the BGV, shifted by $\Delta f = 8.6\,\text{MHz}$ and LHC beam power spectrum for a q-Gaussian bunch shape. Figure 6.23a shows the entire spectrum up to 3 GHz, and Figure 6.23b zooms on the high frequencies. This configuration leads 42 W of extracted RF beam power.

beam harmonics to the second and third resonant eigenmodes of the BGV tank, around 1.8 GHz. The magnetic field pattern of these modes, presented in Figure 6.24, indicates the regions of the walls where the extracted energy is likely to be dissipated through heating.

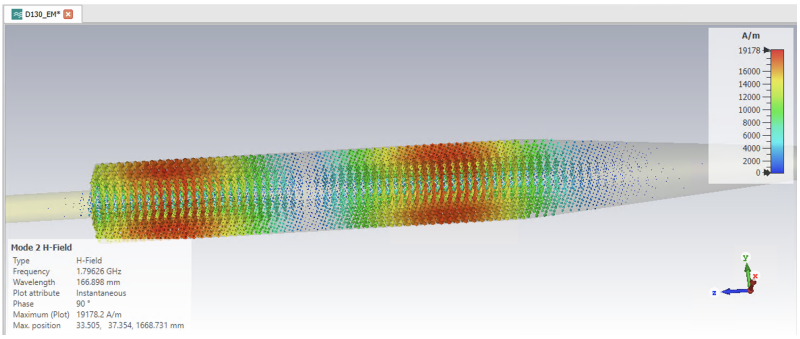

(a) Second resonant mode.

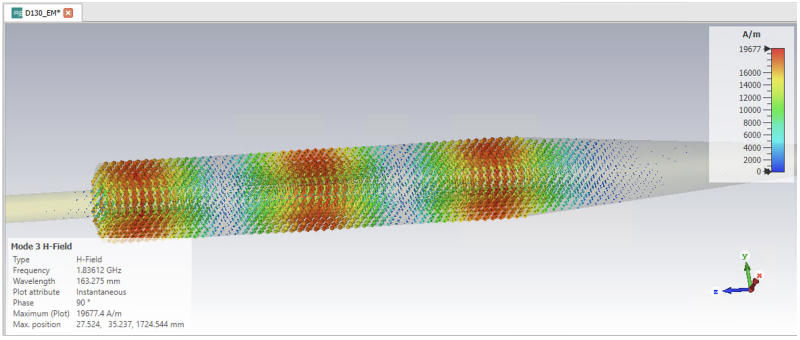

(b) Third resonant mode.

Figure 6.24: Magnetic field pattern of the two resonant modes extracting most of the beam induced power for the worst case scenario, as computed with the *Eigenmode solver* of *CST*. In the geometry shown here the beam enters from the right.

A dissipation of heat, equivalent to 42 W, on the vacuum tank walls of the BGV does not raise concerns regarding it's mechanical stability. Concerning the generation of vacuum outgassing, local hot spots of approximately 50 $\mathrm{W\,m^{-2}}$ are expected at the inner wall surface for the average scenarios and based on the shown magnetic density maps. This RF beam power induced heat will be directly evacuated via lateral conduction, from the warm regions of the structure to neighbouring regions where the dissipated power is small, also utilising the circulation of the external ambient air. Therefore, the structure wall heating is not expected to reach critical levels, resulting in vacuum outgassing, but staying always below a concerning threshold which would be in the order of 100 $\mathrm{W\,m^{-2}}$ [77].

6.6.3 Transverse impedance and impact on beam stability

The transverse beam-coupling impedance of the HL-LHC BGV was simulated with transverse offsets of the beam and the integration path. Since the BGV geometry modelled in CST is rotationally symmetrical with respect to the beam axis, the horizontal and vertical components are equivalent. Assuming the absence of transverse coupling between the two planes and neglecting terms of second and higher orders, the expression of the transverse (here the horizontal, Z_x) impedance $Z_\perp(\omega)$ was discussed in Chapter 2:

$$Z_x(\omega) \simeq x_1 Z_x^{\mathrm{dip}}(\omega) + x_2 Z_x^{\mathrm{quad}}(\omega)\,, \tag{6.4}$$

for small transverse offsets x_1 of the source and x_2 test charge. A displacement of the source bunch of x_1 =12.5 mm was simulated first, to assess the dipolar (driving) term Z_x^{dip}, and the witness integration path was then transversely moved by the same amount $x_2 = 12.5$ mm with the source bunch on the symmetry axis, to compute the quadrupolar (detuning) term Z_x^{quad}. This value is the smallest which could be implemented as offset, comprising three mesh cells within the offset distance, as illustrated in Figure 6.25, while staying in the region where the linear approximation of Equation (6.4) is still valid. The results are shown in Figure 6.26 and 6.27, respectively. Similarly to the longitudinal impedance, for the revised BGV tank the dipolar eigenmodes appear at higher frequencies compared to the demonstrator structure, and with lower amplitudes. The quadrupolar contribution, simulated for the sake of completeness, is negligible, which was expected given the axial symmetry of the BGV structure.

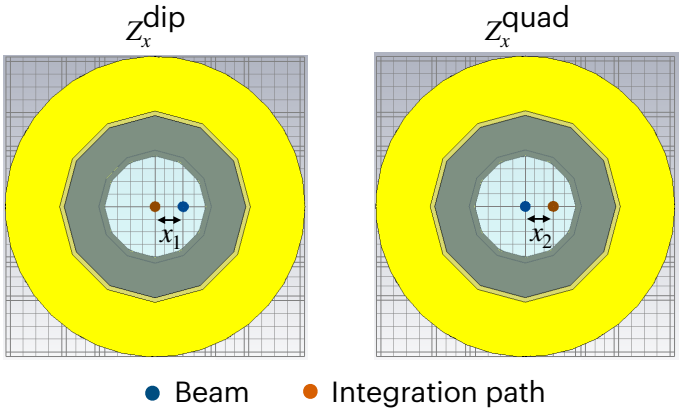

Figure 6.25: Cross-section view of the BGV geometry, with the transverse position of the beam and integration path set for the computation of the horizontal dipolar (left) and quadrupolar (right) impedance.

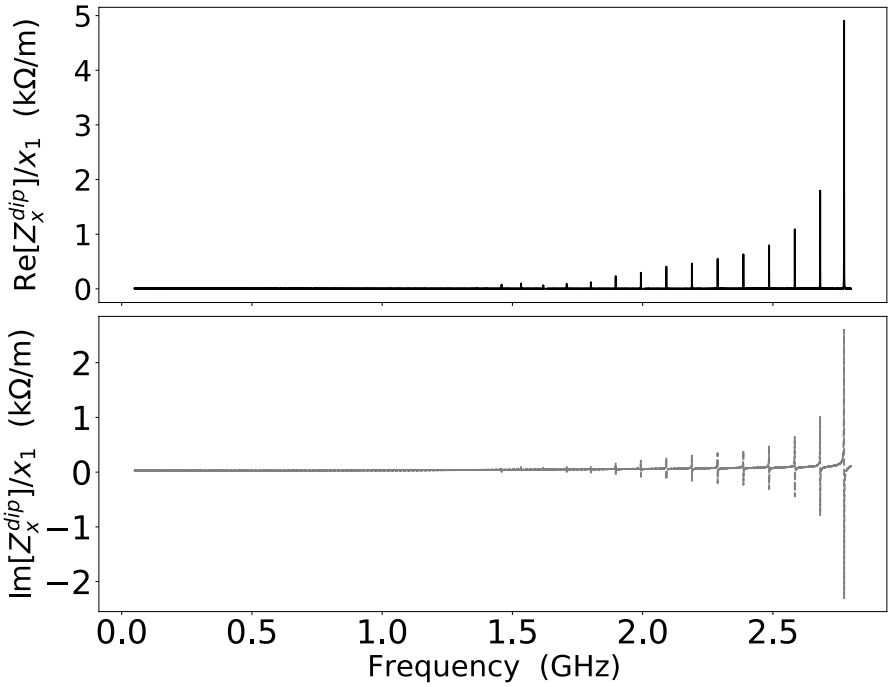

Figure 6.26: Transverse dipolar impedance of the HL-BGV, weighted by the horizontal source beam displacement of 12.5 mm. The real part of the impedance is shown in the upper graph and the imaginary part in the lower graph.

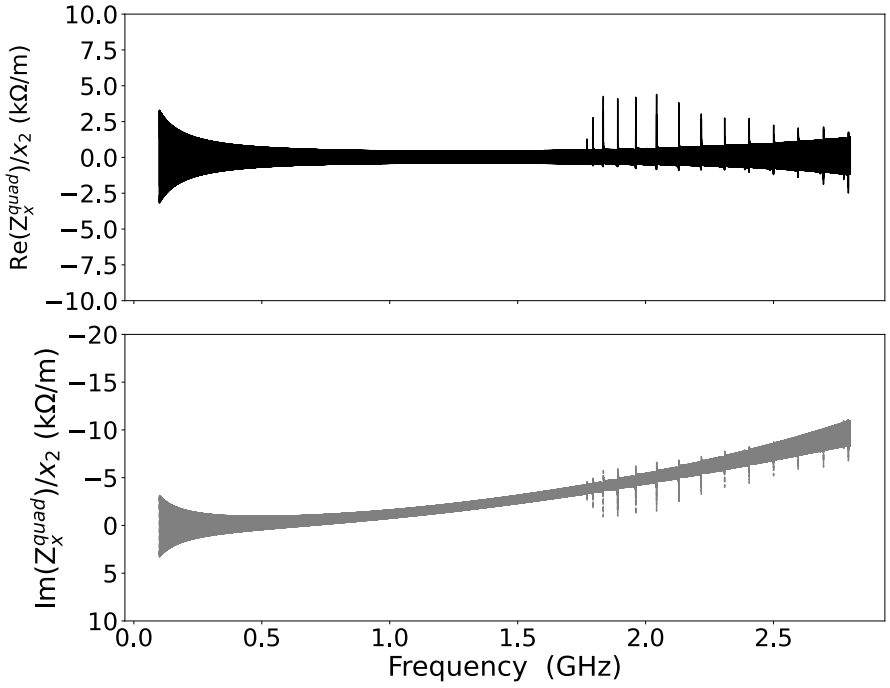

Figure 6.27: Transverse quadrupolar impedance of the HL-BGV, for a horizontal integration path displacement of 12.5 mm. The real part of the impedance is shown in the upper graph and the imaginary part in the lower graph. The vertical scale was adjusted to visualise the modes' peaks.

The transverse effective impedance of the BGV was also computed [67], and the total BGV transverse impedance was added to the HL-LHC impedance model, weighted by the β-functions at the foreseen installation locations. As for the demonstrator device, the main contribution of the revised BGV tank to the LHC impedance model is through its HOMs. Preliminary beam dynamics simulations revealed that the BGV impedance does not have a significant impact on the transverse beam stability [64].

6.6.4 Conclusions

The beam-coupling impedance contributions of the final HL-BGV tank were analysed in detail, and its impact on beam stability was deemed negligible regarding both, longitudinal and transverse beam dynamics. Despite the increased beam intensity foreseen for the HL-LHC upgrade, the efforts put into the impedance optimisation of the future BGV design allow to avoid mechanical damage and outgassing risks associated to RF heating.

6.7 Summary

A revised BGV gas tank design was proposed and presented in this section, optimised with respect to its wakefields contributions, and satisfying instrument performance needs while being compliant with the constraints related to beam aperture, beam stability, vacuum compatibility and manufacturing feasibility.

The following chapter details how this design was also shaped to host a gas target fulfilling the instrument's specifications.

Chapter 7

Gas target

This chapter describes the distributed gas target system proposed for the HL-LHC instrument, and the different steps which led to this design. The first section details the requirements addressed to the gas density profile and the gas target technologies envisioned. The final choice is also motivated here. The second section presents the optimisation study of the longitudinal gas density profile, based on simulations. The impact of the gas target on the LHC beam and radiation environment in the tunnel is addressed in the following section. The consequence of measuring vertices spread in a wide volume on the measurement uncertainty, together with the potential gain of choosing a higher mass gas species than neon, are finally broached at the end of this chapter.

Some insights to ultra-high vacuum and molecular flow physics are given in this chapter. The book from Ref. [78] helped to write the corresponding parts.

Where BGV performance simulation results are presented, involving beam-gas interaction reconstruction, these were obtained using the simulation tool presented in Chapter 5.

7.1 Gas target technologies

Three main requirements are addressed to the gas target, which were mentioned in Chapter 4 and 5:

1. The integrated pressure along the tracker acceptance should allow to reach a sufficient interaction rate, to achieve the bunch width precision specification;

2. The gas density should be homogeneous over the transverse region traversed by the

beam, in the time scale of the measurement, to avoid distortion of the measured beam profile;

3. Outside of the measurement region, the density of residual gas originating from the BGV target should be minimised as much as possible, to limit undesired beam-gas interactions.

Different gas target technologies were considered, each showing different advantages with respect to these requirements.

7.1.1 Envisioned technologies

7.1.1.1 Distributed target

A simple distributed gas target can be made with injecting gas in the beam chamber via a capillary. This solution was used for the demonstrator BGV, and is illustrated in Figure 7.1. The gas is injected into a wide aperture cell, surrounded by restricted aperture chambers, followed by dedicated ion pumps eliminating the gas molecules from the beam chambers. The tracking detector sits on the small aperture section located downstream of the wide cell, with respect to the beam direction. Two ion pumps are installed up- and downstream of the main chamber (four pumps in total per instrument). The restricted aperture sections guarantee a high pressure differential between the wide cell and the outer regions where the pumps are placed.

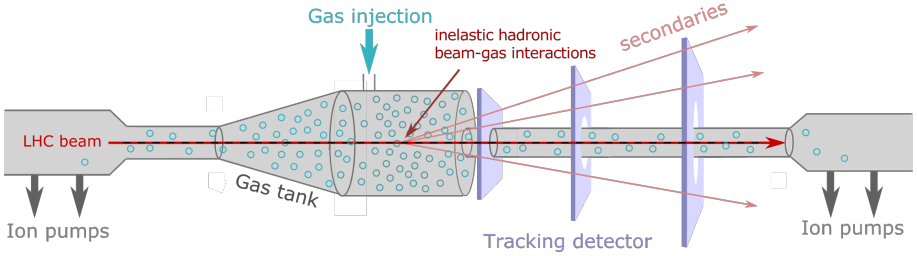

Figure 7.1: Sketch of the BGV distributed target.

This system was proven to be reliable with the operation of the demonstrator target during Run 2, where it helped to prove that beam-gas hadronic interactions can be used to measure the transverse beam size along the LHC energy cycle [8]. In the measurement region, since the gas is distributed over a wide volume, no concern is raised related to the transverse gas density homogeneity, as was confirmed with simulations [2]. However, the total amount of gas introduced in the LHC vacuum is beyond what is required for

the measurement. Radiation stemming from the instrument therefore need to be carefully considered, together with the gas target impact on beam population and beam dynamics.

7.1.1.2 Gas jet target

Other gas target solutions exist with a smaller impact on the machine vacuum, that are supersonic gas jets [79–81]. This technology was introduced to enhance the performance of Ionisation Profile Monitors (IPMs) and Beam Induced Fluorescence (BIF) monitors, otherwise measuring ionisation or fluorescence of residual or distributed gas. The system consists of injecting, on one side of the beam chamber, a highly directional gas jet, which can be efficiently pumped out on the opposite side, after traversing and interacting with the beam. Thanks to the directional flow of the gas, the beam chamber vacuum can be preserved more easily with this technique than in the case of a distributed target, where gas molecules, randomly bouncing on chamber walls, are harder to evacuate. This phenomenon will be further discussed in Section 7.2.3.3.

There is already an application using the gas jet system in the LHC: the beam gas curtain monitor (BGC) [82, 83]. This specific gas jet interacts with the beam with an incident angle of 45 degrees, and has a thickness in the order of 1 mm traversed by the beam. The supersonic gas jet is obtained by applying 5 bars into a vacuum chamber through a 30 µm wide nozzle. The gas jet is then collimated via a series of two circular skimmers of 400 µm and 2 mm wide opening. A last 0.3×9 mm large rectangular skimmer provides the target with its sheet-like shape. The gas is finally collected in a dedicated dump. This setup is of particular interest since it was designed to be operated in the LHC ultra-high vacuum environment.

The possibility of adapting this system for the BGV instrument was considered, as conceptually shown in Figure 7.2, with some questions left opened.

To meet the BGV specifications, a 1 mm thick condensed interaction region would require an average gas density in the order of 2.5×10^{18} Ne/m^3 (consistently with the density envisioned for a distributed target, as will be calculated in Section 7.1.2). This level represent three times the BGC gas jet core density obtained in its 1 mm thick target [83]. Therefore, the gas jet production system and the gas dump should be adapted, and feasibility studies would be needed to ensure that the desired throughput can be generated while maintaining an adequate background pressure in the vicinity of the instrument.

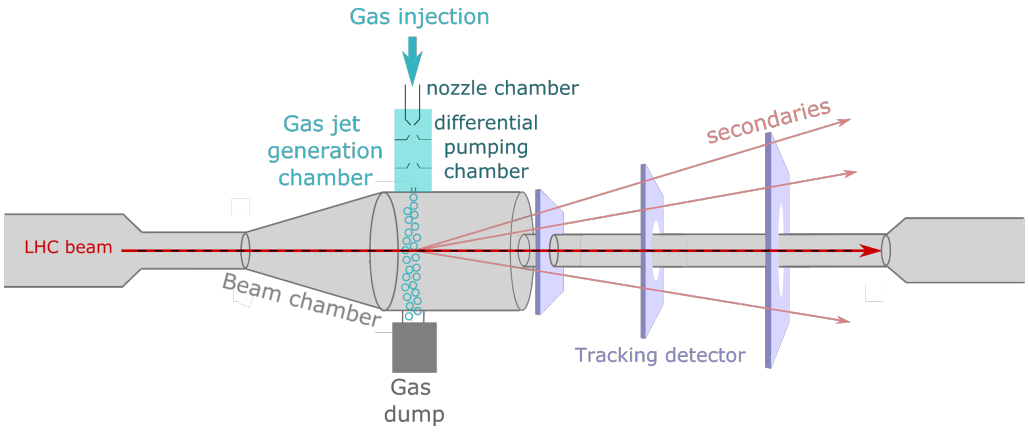

Figure 7.2: Sketch of a possible adaptation of a gas jet target on the BGV.

Furthermore, a careful assessment of the transverse density homogeneity is of high importance to avoid beam profile distortion. With such a system, a higher pressure is expected at the core of the jet, and the distribution of beam-gas interaction vertices will be a convolution of the beam profile with the gas jet density profile. Where the gas density encountered by the tail of the beam profile would be 1% lower than at its centre, 1% less events would be accumulated on the impacted side of the measured distribution. To prevent the need to introduce compensation means, one should ensure that the density differential encountered by the widest beam to measure has a negligible impact on the beam size measurement, compared to the 5% accuracy required. That is, for a beam width of 1.00 ± 0.05 mm for instance, the width of the Gaussian distribution of reconstructed vertices should not differ by more than few microns compared to the width of a distribution with a transversely uniform target. The required level of density homogeneity can be estimated with the widest beam to measure, and with determining what difference in tail population, for a distribution of 5000 vertices, leads to a noticeable Gaussian width variation.

A roadmap to adapt the BGC gas jet target to the BGV could consist in (1) assessing the required density homogeneity, (2) perform a feasibility study with optimisation of the gas jet production setup and gas dump, based on simulations, and (3) perform a precise measurement of the transverse density profile of the experimental gas jet.

It is also important to acknowledge that achieving a high level of precision in measuring the jet density is not a trivial task. The BGV target density was measured using a movable vacuum gauge with a 1 mm aperture [84]. In order to provide a transverse profile measurement of beams in the order of 1 mm and below, without distortion of the tails' population, a higher resolution in the mapping of the gas target density profile will likely

be required. Other techniques could be investigated such as interferometry, as used in Ref. [85].

The final difficulty of using a gas jet target is due to the system's complexity. Compared to the distributed gas target, the gas jet technology is a complex system. The high precision manufacturing and tight alignment of the nozzle and thin wall skimmers are delicate steps, and multiple turbo-molecular pumps and pressure gauges are needed for the different stages of the differential pumping chamber and for the gas dump. An additional set of pump and pressure gauge should also be added to the beam chamber to guarantee a sufficiently low background pressure. A dedicated control system for all these elements to be installed in the demanding LHC tunnel environment should also be designed, taking advantage from the system developed for the BGC target. The costs related to the installation of a large set of cables in the LHC tunnels should finally be accounted too.

7.1.1.3 Impact of the target spread on instrument's performance

The impact of accumulating events generated in a transversely uniform target spread over 1 m or 1 cm was simulated [2] using the simulation tool described in Chapter 5. Figure 7.3 shows how the vertex resolution is impacted, for different track multiplicities.

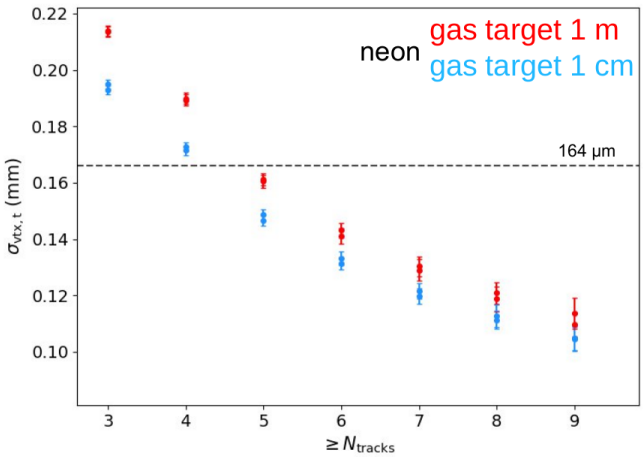

Figure 7.3: Comparison of the simulated transverse vertex resolution obtained for 7 TeV p-Ne interactions, generated in a distributed (red) or gas jet (blue) target. [2]

It is revealed that the vertex resolution, and thus the beam size accuracy, is improved when the interactions are generated in a smaller volume, such as the gas jet case. Nevertheless, both technologies permit to achieve the required vertex resolution of 164 µm, by restricting the event selection to those with 5 or more tracks. According to the simu-

lations performed, employing a distributed gas target is hence not a showstopper to fulfil the instrument's specifications.

In summary, the gas jet option is a more complex technology, and assessing the transverse homogeneity level of such a gas target is a complicated task. Given that the use of a distributed target does not impede the fulfilment of the instrument's specifications, and in line with the aim for a simple instrument with low R&D and maintenance needs, this second option was preferred.

7.1.2 Chosen target description

Following the decision for a distributed target, the measurement region, that is the volume in which useful beam-gas interactions are generated, was defined longitudinally as a 1 m long volume centred at the optimised distance of 550 mm between the interaction vertex and the first detector plane. The tracker design was optimised to reconstruct interactions occurring in this volume.

The average gas density required along this region can be determined from simulations. In terms of gas species, neon will be considered in the following, as justified in Section 5.2.1 of Chapter 5. Alternative possibilities with higher mass gases will be discussed at the end of the present chapter.

It was seen in Chapter 4 that, in the most stringent case of measuring the Beam 2 size at the foreseen instrument location and at collision energy, only events with 5 or more tracks entering the tracker acceptance ($N_{\mathrm{tr}} \geq 5$) can be used in the beam size measurement, called useful events. Such a constraint guarantees that a sufficient vertex resolution is reached, to achieve a beam size accuracy of 5%. At injection energy and for the same instrument, events with $N_{\mathrm{tr}} \geq 3$ can be used.

Figure 7.4 shows the longitudinal distribution of such events, in the measurement region, from simulation of 500 000 inelastic proton-neon interactions, and with the final tracker geometry, described in Ref. [2]. The simulated vertices were initially uniformly distributed along the z axis, and the bars height is given in percentage of the 500 000 simulated interactions.

In total, only 13% of inelastic beam-gas interactions occurring in the measurement region can contribute to the beam size measurement at 7 TeV, and 37% at 450 GeV.

It was mentioned in Section 4.3.3 that a minimum rate of $R^{\mathrm{inel}}_{\mathrm{useful}} = 83\,\mathrm{Hz}$ useful

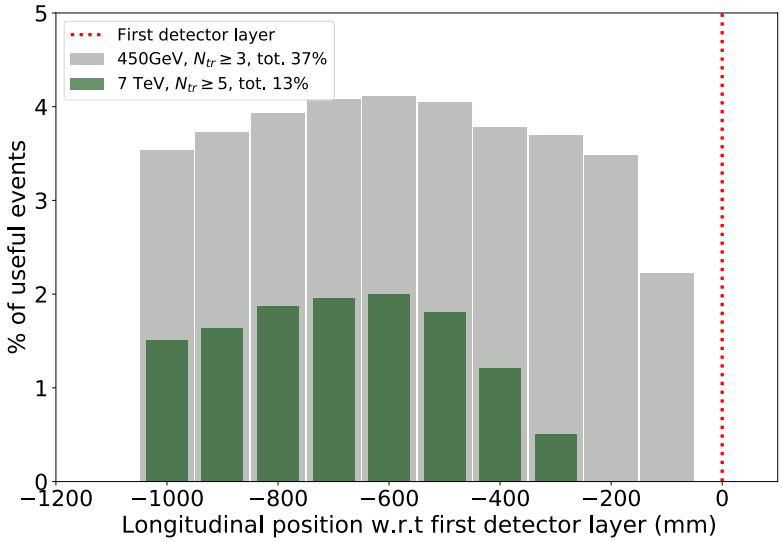

Figure 7.4: Longitudinal distribution of useful events: with 3 or more tracks in the tracker acceptance at injection energy and 5 or more at collision energy. The vertical scale is given in percentage of the total simulated p-Ne inelastic interactions.

events is required to reach 1% bunch width precision in a 1 min integration time. At collision energy, this leads to a total inelastic interactions rate in the measurement region of $R_{\text{tot}}^{\text{inel}} = \frac{83\,\text{Hz}}{0.13} = 640\,\text{Hz}$. Considering Equation (5.1) introduced in Chapter 5, the corresponding integrated gas density is of $\int \rho(z)\text{d}z = \frac{R_{\text{tot}}^{\text{inel}}}{f_{\text{rev}} N \sigma} \simeq 3 \times 10^{-7}\,\text{mbar}$. Relaxing the precision requirement to 2% in 1 min, which is still in the order of magnitude of the specifications, the required pressure drops down to $0.8 \times 10^{-7}\,\text{mbar}$. At injection energy, the required pressure reads $1 \times 10^{-7}\,\text{mbar}$ for a 1% bunch width precision. Hence, the gas target will be designed to achieve a nominal operation pressure of $1 \times 10^{-7}\,\text{mbar}$ in the measurement region. It should be noted that a longer accumulation time will be needed for one of the instruments, at collision energy, to reach the bunch width precision specification. In the following, the ideal distributed target profile will be represented with a grey step function covering the measurement region, and with a plateau pressure of $1 \times 10^{-7}\,\text{mbar}$.

The amount of residual gas target molecules spreading outside of the measurement region should be minimised to prevent undesired beam-gas interactions, increasing the LHC tunnel radiation levels, and unnecessarily impacting the beam lifetime or causing emittance growth. These interactions would also generate background noise for the BGV tracker, although such events should be easily filtered.

7.1.3 Demonstrator system description

As discussed in Chapter 5, a noble gas was chosen to avoid interactions with the chambers NEG coating. Among available pumping systems, ion pumps or cryogenic systems are the main candidates capable to pump out the neon molecules of the BGV target. For integration and cost reasons, the addition of cryogenic equipment to that currently existing in the LHC is not possible, specifically for the BGV. Only ion pumps are therefore considered for a proximity pumping system to the instrument gas target.

On the demonstrator system sitting in the LHC tunnel, two $410\,\mathrm{L\,s^{-1}}$ ion pumps are installed on either side of the main chamber. The gas injection system is equipped with a controlled valve tuning the gas flow, and the pressure in the wide accumulation chamber is monitored by a pressure gauge. A commercial NEG filter reduces the level of impurities of the injected gas down to ppb level [86]. Data recorded during Run 2 by the pressure gauge shows a pressure rise from $1 \times 10^{-9}\,\mathrm{mbar}$ to $1.5 \times 10^{-7}\,\mathrm{mbar}$ when the gas injection was turned ON, and a quick decrease back to $1.4 \times 10^{-8}\,\mathrm{mbar}$ within less than 30 s when the system was turned OFF. The initial pressure level was reached back in about 1 min.

With a similar setup foreseen for the future instruments, part of the demonstrator equipment already in place in the LHC tunnel can be refurbished for B2-BGV. A new system shall be installed for B1-BGV.

7.2 Longitudinal gas density profile optimisation

Various parameters impacting the longitudinal gas density profile of the BGV target were considered in order to achieve the required pressure within the measurement region, while limiting induced radiation and impact on the beam.

7.2.1 Molecular flow regime

In the pressure range of the LHC vacuum environment, the gas molecules behave in the free molecular flow regime, which means that their mean free path is long compared to the geometry dimensions. In this case, collisions between gas molecules can be neglected. In other words, the Knudsen number $K_n = \lambda/D$ is greater than 1, where λ is the molecules' mean free path and D the typical vacuum chamber dimension. The mean free path can be expressed as a function of the pressure p and temperature T for a given molecule m of diameter d_m as in Eq. (7.1), with $k = 1.38 \times 10^{-23}\,\mathrm{J\,K^{-1}}$ being the Boltzmann constant.

$$\lambda = \frac{k \cdot T}{\sqrt{2}\pi \cdot p \cdot d_m^2} \tag{7.1}$$

Considering a background pressure of 10^{-9} mbar H_2 equivalent in the LHC [87] and $d_m^{H_2} = 289\,\text{pm}$ [88], the mean free path of residual gas molecules at ambient temperature is λ_{LHC} =109 km. For the BGV target with neon gas at 10^{-7} mbar and $d_m^{\text{Ne}} = 275\,\text{pm}$ [89], the mean free path becomes λ_{BGV} =1.2 km. Both values fall into the ultra-high vacuum range, and with vacuum chambers in the order of few centimetres diameter, the molecular flow conditions applies to these two cases.

7.2.2 Molflow+ simulation tool

Molflow+ [90] is the standard Monte-Carlo simulation tool for ultra-high-vacuum simulations in the molecular flow regime, when gas molecules are to be treated individually.

In *Molflow+*, the setup geometry is defined with physical surfaces and test particles are generated from given surfaces to which an outgassing rate is assigned, together with an angular emission distribution. Gas molecules travel in straight trajectories, until a geometry wall is reached, on which they bounce back in a randomly distributed direction. Particles exit the system when they hit a sticking surface, to which a sticking coefficient is assigned, modelling the probability of the particle to be caught by the pump. Physical or virtual meshed surfaces can be defined to record the molecule hits density, and calculate local pressure or gas molecules density. In this chapter, the word *hit* refers to the event of a gas molecule traversing a transparent surface or bouncing against a physical geometry surface.

7.2.3 Parametric study

Starting from the demonstrator geometry, a parametric study was performed to understand how the vacuum chamber layout design would impact the longitudinal gas density profile of the gas target and ensure a judicious gas target and gas tank design.

7.2.3.1 Simulated setup

Figure 7.5 shows different views of the simulated geometry.

The parameters of interest in this study are indicated in the top picture. Each parameter was scanned within a meaningful range for the BGV instrument, restricting to

values which could be used for the final setup:

- The length of the central cylindrical part L and the one of the upstream taper l,
- The distance d_1 between the two inner pumps, as compared to a minimum reference position as is explained in Section 7.2.3.4,
- The symmetrical distance d_2 between the inner and outer pumps,
- The vertical distance h between the ion pump and the vacuum pipe,
- The longitudinal position z_{inj} of the gas injection capillary along the gas tank,
- The gas injection rate R_{inj}.

The gas injection is modelled by a 1 cm circular surface placed inside the tank, shown in red in the middle left picture. The angular emission distribution of generated molecules takes into account the "beaming effect", i.e. the presence of an injection tube which modifies the angular emission profile at its exit in the chamber, as compared to the commonly used $\cos(\theta)$ distribution. A $\cos^5(\theta)$ is assumed here, based on geometric assumptions. A higher value for the exponent would change the result very marginally [91]. The gas injection rate, typically called *outgassing rate* in Molflow+, can be adjusted in order to reach a plateau level in the order of 1×10^{-7} mbar, equivalent to $2.6 \times 10^{15}\,\mathrm{m}^{-3}$ neon molecules density. This condition is achieved with an outgassing rate of $3.8 \times 10^{-6}\,\mathrm{mbar\,L\,s^{-1}}$.

Only neon is considered in the simulations described in this section, which is why no desorption is assigned to the the vacuum chamber walls.

The ion pumps are modelled based on a detailed geometry provided by the CERN vacuum group [91]. The molecules' absorption is done on a horizontal surface, highlighted in the picture 7.5e, to which was assigned a 0.2 sticking factor, modelling a pumping speed of about $80\,\mathrm{L\,s^{-1}}$ for neon. This surface corresponds to the actual location of the pump, which is connected to the LHC beam pipe with a dedicated chamber assembly, including an 80 mm pierced layer, acting as a RF beam screen.

A sticking coefficient of 0.05 is also set to the two circular surfaces representing the extremities of the setup, shown in picture 7.5c, to model the probability for the molecules going further in the LHC than the modelled BGV region, to be caught by nearby cryogenic equipment. For optimisation purposes, the BGV layout was first simulated this way, independent of the surrounding vacuum environment in the LHC, which actually depends

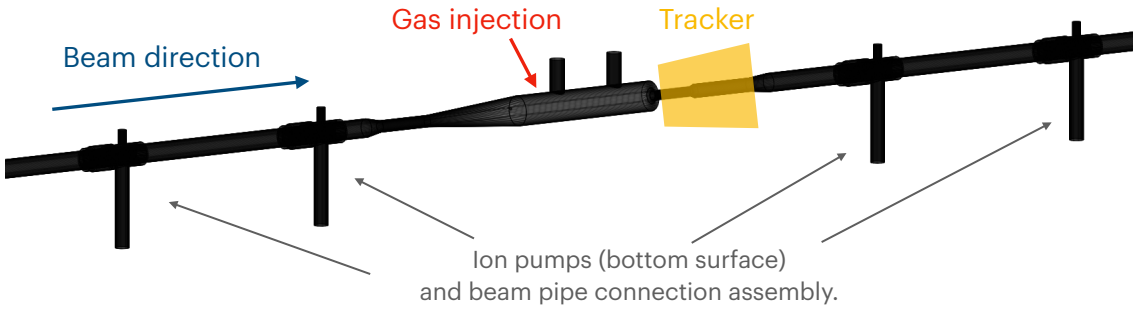

(a) General setup.

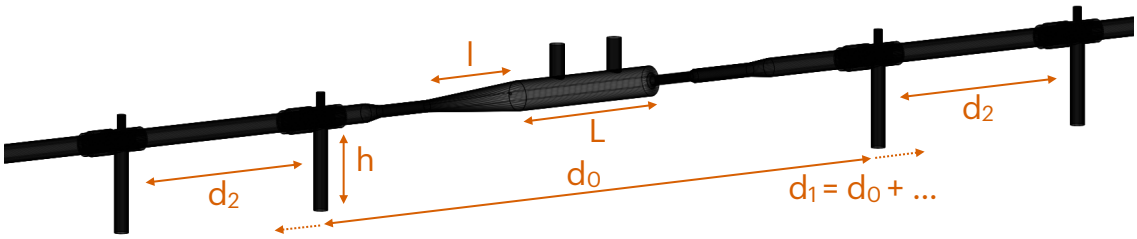

(b) Studied parameters.

(c) Beam pipe extremity surface.

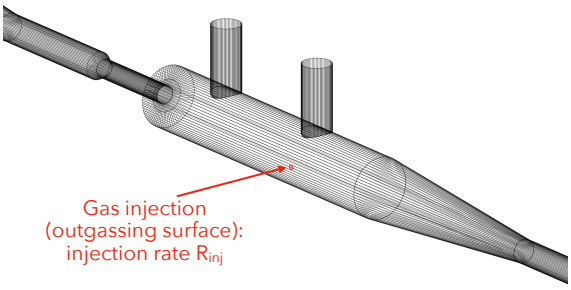

(d) Gas injection surface.

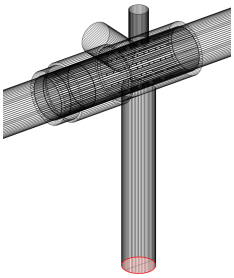

(e) Ion pump assembly.

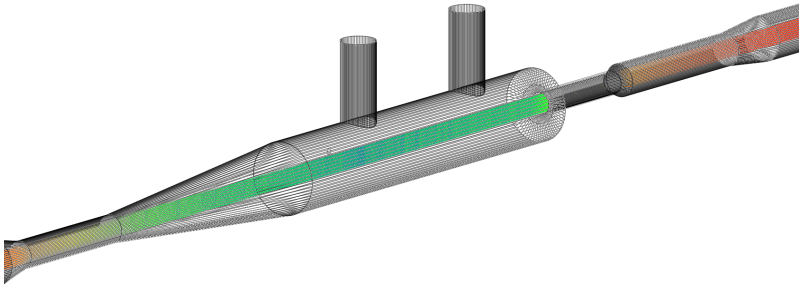

(f) Surface recording gas molecules hits density.

Figure 7.5: Geometry screenshots from *Molflow+* showing the main elements (7.5a), the studied parameters (7.5b), sticking (7.5c and 7.5e) and outgassing (7.5d) surfaces, and the one used to extract the gas density profiles (7.5f).

on each instrument's location. The longitudinal gas density profile is in fact quite sensitive on the absorption capacity of the surrounding environment. This impact is discussed in Section 7.2.5.

A virtual surface highlighted in picture 7.5f was defined inside the geometry beam pipe, along the YZ vertical plane, between the two extremities of the structure, and with a height corresponding to the minimum diameter of the structure. A mesh of 1400 vertical cells of about 1 mm long each was defined on this surface. The longitudinal gas molecule density profiles presented in the figures of this section were extracted from this surface, each value corresponding to the average density in the cell. Unless otherwise stated, the simulations were run for a sufficiently long time so that the statistical error in each cell is below 1% for the tail mesh cells, and in the order of 0.1% in the measurement region.

7.2.3.2 Tank and upstream taper lengths (L and l)

Changing the length L of the central cylindrical part of the tank, or the length l of the upstream taper mainly affects the span of the density plateau, as revealed in Figure 7.6a and Figure 7.6b respectively. The longitudinal gas density profiles are compared on these figures for different lengths of L and l, with shifting upstream elements to the left. Variations of the gas density are observed at each change of the beam chamber cross section, highlighting the importance of the reduced aperture sections to generate a pressure bump around the measurement region. These two parameters L and l were thus used to adjust the length of the pressure bump, selecting the most compact configuration for which the plateau extends up to the upstream (left) end of the measurement region: $L = 700\,\text{mm}$ and $L = 500\,\text{mm}$. This selection aligns with the aim for a small beam-coupling impedance contribution of the tank, with reasonably low shunt impedances of the resonant modes, as was presented in the previous chapter.

7.2.3.3 Ion pump assemblies (h)

In the molecular flow regime, the particles are not "sucked in" by the pumps but can only fall on the pump entrance as the result of a random motion. The layout around the BGV ion pumps is thus critical to maximise their pumping efficiency, and minimise the profile tails to reduce the rate of undesired beam-gas interactions.

In fluid dynamics, the gas flow Q ($\text{mbar}\,\text{L}\,\text{s}^{-1}$) and pressure differential $\Delta P = P_2 - P_1$ (mbar) between two extremities of a structure are proportional to a quantity called flow conductance C and expressed in units of $\text{L}\,\text{s}^{-1}$: $Q = C \cdot \Delta P$.

The analogy can be made with electrical circuits, with the gas flow behaving as the electrical current and the pressure representing the electrical potential. Similarly to

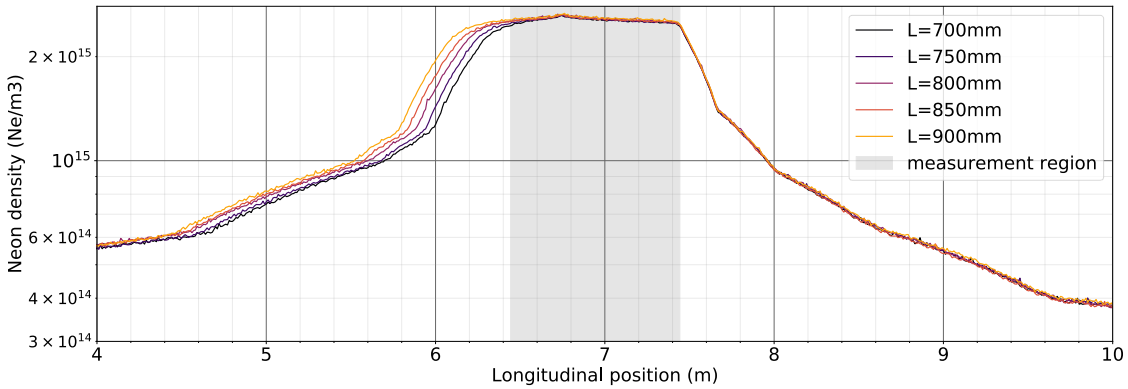

(a) Scan of the wide aperture cell length L.

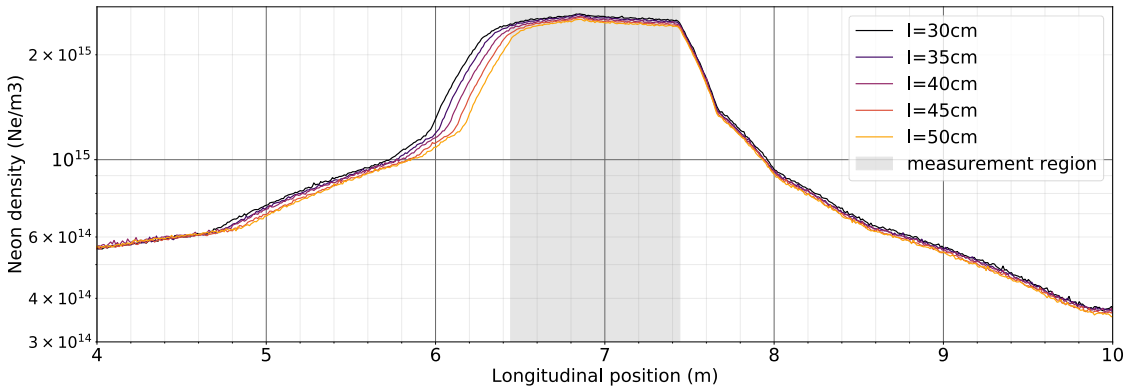

(b) Scan of the upstream taper length l.

Figure 7.6: Longitudinal gas density profile along the BGV target, changing the central cylinder length L (7.6a), and the upstream taper length l (7.6b), with a focus on the density plateau.

electrical conductors, the conductance C_i of individual pipes or structures add up if they are connected in series: $\frac{1}{C} = \sum_i \frac{1}{C_i}$. In particular, the effective pumping speed S_{eff} available at the beam chamber level is determined by the series connection of the pump, of pumping speed $S \simeq 80\,\text{L}\,\text{s}^{-1}$ for neon in the BGV case, and of a tube of conductance C_{pipe}, as shown in Eq. (7.2).

$$\frac{1}{S_{\text{eff}}} = \frac{1}{S} + \frac{1}{C_{\text{pipe}}} \Leftrightarrow S_{\text{eff}} = \frac{S \cdot C_{\text{pipe}}}{S + C_{\text{pipe}}} \tag{7.2}$$

In molecular flow, the conductance of a beam pipe or of a set of pipes does not relate to the pressure, and exclusively depends on the geometrical dimensions. For thin apertures, the conductance values can be expressed as $C_A = \frac{\bar{c}}{4}A$, where A is the aperture area and $\bar{c}$ the particle velocity, scaling with $\sqrt{\frac{T}{m}}$, where m is the gas mass. In the case of long tubes, the conductance C_{pipe} corresponds to the product of the conductance of

the opening surface times a transmission probability P: $C_{\text{pipe}} = C_A \times P$. Intuitively, the longer the pipe, the lower the probability for a particle entering it to exit through the pipe's exit. While the transmission probability of a tube has a complex analytical form, the conductance of a straight cylindrical pipe of diameter d and length L, for air gas at room temperature, can be approximated with the Dushman formula [92]:

$$C_{\text{pipe}} = \frac{12.4\dfrac{d^3}{L}}{1 + \dfrac{4d}{3L}}. \tag{7.3}$$

In our specific case, the gas flow from the beam pipe to the pump will be favoured by a large opening diameter and a short length.

Finally, in the LHC, the openings in the beam pipe corresponding to a pump connection have to be shielded from the beam electromagnetic fields, to limit beam-coupling interactions with the walls. An RF shielding is therefore installed at the connection between each pump and the beam pipe. Visible in Figure 7.5e, it consists of a copper tube pierced with race-track shaped holes, and is installed as a continuity of the beam pipe. Although necessary from a beam-coupling impedance perspective, this shielding also affects the pumping efficiency, as it obstructs the connection hole with an opacity of 75%.

In sum, the effective pumping speed of the BGV ion pumps is significantly impacted by the presence of the RF shielding and connection pipe. These components already have a specific and optimised design used in the LHC. The support module of the pumps, each weighting in the order of 200 kg, includes a 150 mm connection flange between the beam chamber and the connection pipe, which is 40 cm long.

This length, modelled by the vertical distance h between the sticking surface of all four BGV pumps and the beam chamber, was scanned with *Molflow+* simulations, and the impact on the BGV gas profile is visible in Figure 7.7. The position of the four ion pumps is revealed by the change in the slope of the tails, at about 4.6 m, 5.7 m, 8.6 m and 9.7 m. While the plateau pressure is not significantly affected by this parameter and stays in the desired range, the pressure in the profile's tails is smaller for shorter h. For the actual BGV setup, when installed in the LHC, the neon pressure introduced by their target will only drop to small levels ($< 10^{13}\,\text{Ne/m}^3$) when reaching a cryogenic equipment, and the tails shown in the figures of this profile optimisation study will expand until this point, as will be shown in Section 7.2.5. Here, the tails reduction observed for small h values will

likely propagate in the entire vacuum sector, and the impact on the total amount of gas molecules present in the LHC beam pipes can become significant. The ion pumps already installed in the LHC are mounted on a support placing them at a distance h =40 cm from the beam pipe. This parameter cannot be easily improved, but was still shown to have a strong impact on the profile's tails. If needed and allowed in the future, reducing h would be an effective way of reducing the profile's tails.

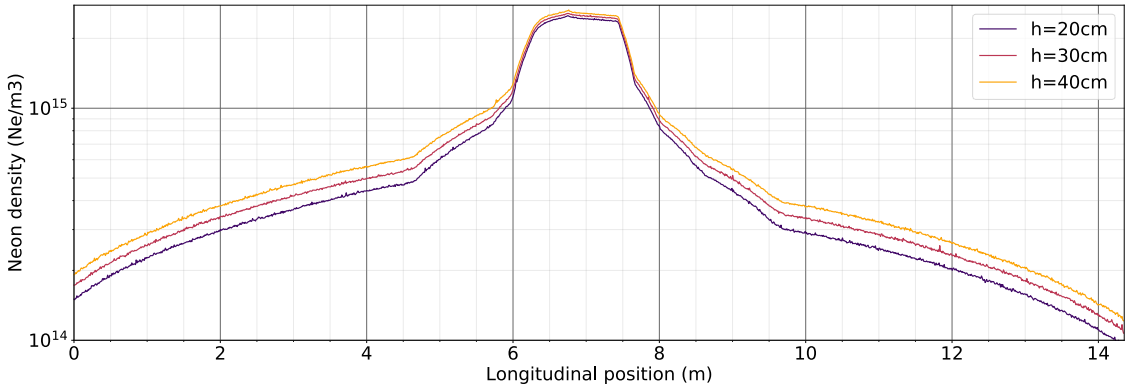

Figure 7.7: Longitudinal gas density profile along the BGV target, varying the vertical distance h between the beam pipe and the sticking surface of the pump.

The importance of the pipes' layout at the insertion of the vacuum pumps was discussed in this section with limited improvement possibilities. In the following section, the horizontal placing of the BGV ion pumps with respect to the gas accumulation chamber is investigated.

7.2.3.4 Horizontal position of the vacuum pumps (d_1 and d_2)

As mentioned above, the gas tank includes restricted aperture chambers preceding the first, so-called *inner*, ion pumps. The presence of these sections is required to confine the gas in the wide aperture part, where the density distribution should be fairly uniform.

The smallest possible diameters granting a sufficient margin for beam aperture were chosen for the restricted aperture sections on each side, as discussed in Section 6.2 of the previous chapter. In terms of length, the downstream chambers are holding the tracker detector, and should therefore be long enough to support the detector modules. On the upstream side, a minimum length of 25 cm was set to the restricted aperture section, to ensure gas containment within the tank. Based on these dimensions defining the shortest possible configuration, a reference position for the two inner vacuum pumps was defined, and the corresponding distance between the inner pumps called d_0, as in Figure 7.5. The

distance d_1 between the inner pumps was increased by steps of 40 cm, symmetrically distributed between the two sides. The obtained profiles are shown in Figure 7.8, where the densities are given with a statistical precision better than 0.6% in the tails and 0.06% at the density plateau.

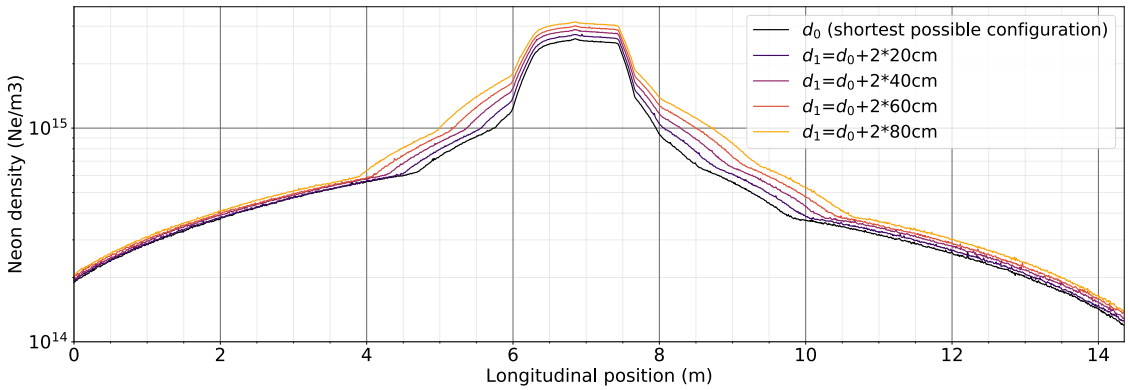

Figure 7.8: Longitudinal gas density profile along the BGV target, symmetrically varying the distance d_1 between the two inner pumps.

Based on this plot, the closest positions of the inner pumps to the gas injection show smaller tails, but also a lower plateau density. To achieve a similar beam-gas interaction rate in the measurement region, the injected gas flow should thus be increased, rising in turn the proportion of gas molecules populating the profile's tails, as will be shown in the following section. The tails population hereafter designates, at equilibrium, the ratio of the gas target density integrated over the distance and excluding the measurement region (which represents the density of the profile tails), over the total integrated target density.

Table 7.1 compares these configurations by showing for each the proportion of gas molecules outside of the measurement region in the simulated zone, at equilibrium. Uncertainties on the tails population are obtained by propagation of the statistical errors.

Table 7.1: Tails population varying d_1.

d_1	d_0	d_0+2×20 cm	d_0+2×40 cm	d_0+2×60 cm	d_0+2×80 cm
Tails population	$73.3 \pm 0.1\%$	$73.5 \pm 0.1\%$	$73.8 \pm 0.1\%$	$74.2 \pm 0.1\%$	$74.8 \pm 0.1\%$

For the five simulated cases, the tails population is close to 75%, highlighting the drawback of a distributed gas target for which only about a quarter in this case of injected gas molecules spread in the measurement region. The impact of d_1 on the tails population is very small in the range considered: the difference in tails population between the two

extreme cases, increasing d_1 by 1.60 m, is smaller than 2%. A small trend is still observed, where the bigger distances between the inner pumps show slightly larger tail populations. For the final setup, a short d_1 is preferred, but the position of the inner pumps can be adjusted to match other constraints, for instance to select standard beam pipe lengths, or fit into the tight space constraints at the foreseen location of the Beam 1 instrument.

The same approach was used to study the impact of the distance d_2 between the inner and outer pumps, which is equal on either side of the instrument. Results are shown in Figure 7.9. As expected, due to their larger distance from the measurement region compared to the inner pumps, the gas density in the measurement region is less affected by the position of the outer pumps. Its density level is still slightly lower for smaller d_2 configurations. A change in the tails shape is again noticed.

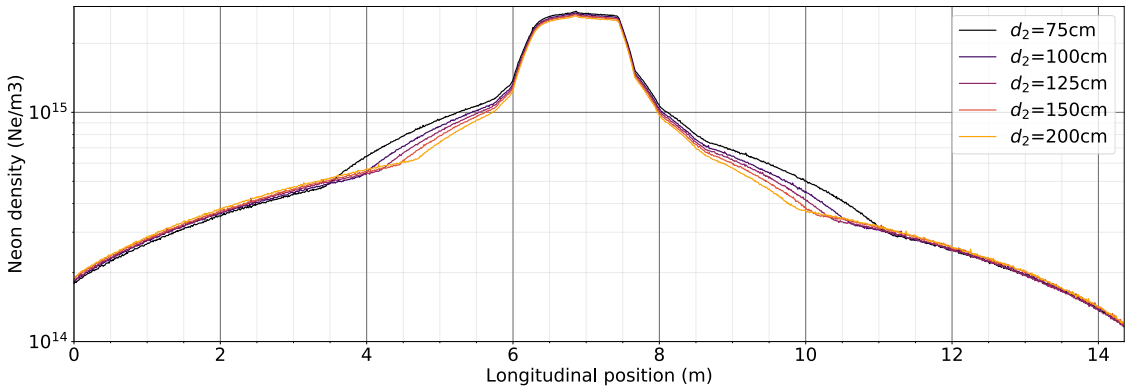

Figure 7.9: Longitudinal gas density profile along the BGV target, symmetrically varying the distance d_2 between the inner and outer pumps.

Table 7.2 lists the tails population for each of these new configurations, quantifying the changes observed in Figure 7.9.

Table 7.2: Tails population varying d_2.

d_2	75 cm	100 cm	125 cm	150 cm	200 cm
Tails population	$74.2 \pm 0.1\%$	$73.7 \pm 0.1\%$	$73.5 \pm 0.1\%$	$73.4 \pm 0.1\%$	$73.4 \pm 0.1\%$

In the considered range, the impact of d_2 on the tails population is again limited and even smaller than the one observed for d_1. Larger d_2 encourage smaller tails populations, with a negligible impact above about 1.25 m distance between the inner and outer pumps.

Following these results, these two distances were preliminary set to $d_1 = d_0$ and $d_2 = 1.3\,\mathrm{m}$, in order to make the instrument compact but with reasonable free spaces kept to install and maintain the BGV equipment, and bake-out the beam chambers. Both of these values can be adjusted in the future without significantly affecting the tails population, that is the radiation and beam impacts of the BGV gas target.

7.2.3.5 Gas injection system (z_{inj} and R_{inj})

Regarding the injection of the gas in the gas tank, the position z_{inj} of the capillary along the cylindrical part of the tank was varied between the different profiles shown in Figure 7.10. The vertical scale is this time linear, to highlight the slight differences in the shape of the plateau. Provided that the gas is injected along the cylindrical part of the tank, the tails population is not affected by z_{inj}. The longitudinal plateau density is more homogeneous with placing the capillary at the centre of the wide cylindrical part.

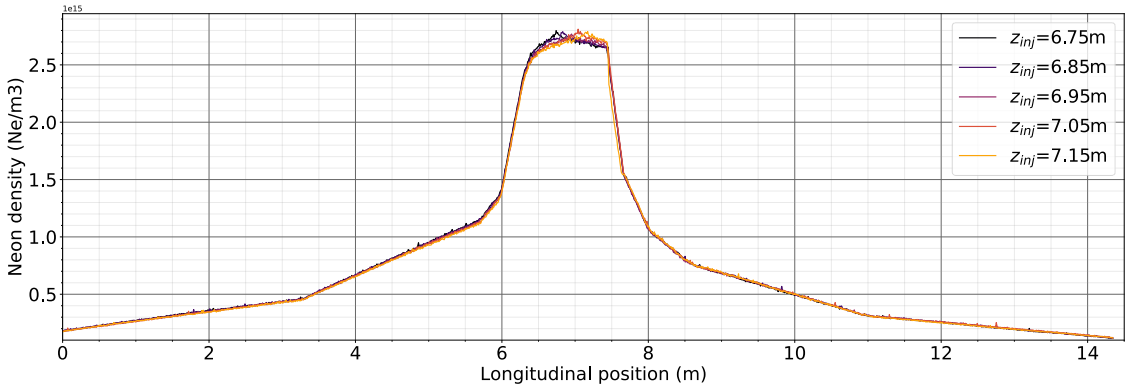

Figure 7.10: Longitudinal gas density profile along the BGV target, varying the horizontal position of the emitting surface z_{inj} along the cylindrical part of the tank.

The gas injection rate R_{inj} was also considered. As verified in Figure 7.11, the entire gas density profile linearly scales with the outgassing rate set to the surface modelling the injection capillary. The purple curve shows the simulated profile for an outgassing rate of $3.0 \times 10^{-6}\,\mathrm{mbar\,L\,s^{-1}}$ and the orange one for $4.0 \times 10^{-6}\,\mathrm{mbar\,L\,s^{-1}}$. The linear evolution is verified with the yellow profile, corresponding to the purple one, scaled by a factor 1.33, which agrees well with the orange one. This behaviour matches the expectation that for a similar pumping probability (same sticking capacity of the sticking surfaces, without changing their surface nor the geometry), a higher injection rate simply increases the amount of molecules evolving in the system at a given time.

From instrument operation point of view, this means that tuning the gas flowing

through the capillary with the injection valve should proportionally increase or decrease the gas density seen by the beam all along its trajectory.

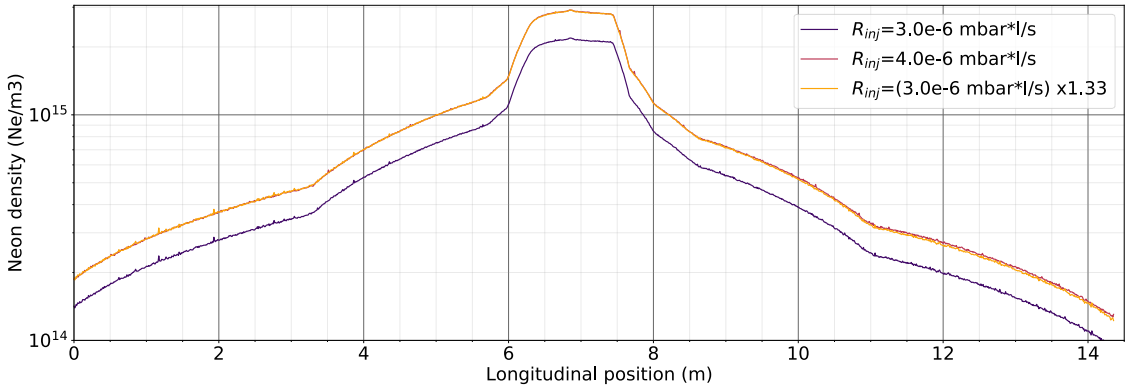

Figure 7.11: Longitudinal gas density profile along the BGV target, varying the gas injection rate R_{inj}.

7.2.3.6 Summary

Test Particle Carlo simulations helped to understand how the longitudinal gas target profile is influenced by the gas tank layout and by the main elements of the gas target injection and pumping system.

Regarding the gas injection, the horizontal position of the injection capillary does not affect the gas density distribution, while increasing the gas throughput proportionally raises the gas density levels at any point of the profile.

The pressure bump around the measurement region is guaranteed by the reduced aperture sections surrounding the wide tank in which the gas is injected. The final lengths of the upstream taper and of the wide cylindrical part of the gas tank are chosen in order to ensure that the gas density plateau includes the entire measurement region.

Several parameters were investigated with aiming at reducing the tails population, without great success: in the simulated region, the horizontal position of the ion pumps was slightly optimised but has a very limited impact on the tails population. Reducing the horizontal distance between the pumps and the beam pipe could significantly affect the tails level, but would require modifying the module supporting the heavy pumps, which is not a trivial task. Adding a third pair of ion pumps would help to further decrease the tails population, but also increase the instrument's length, cost and complexity, and is therefore not an option. Alternatively, the BGV residual gas molecules will be captured by the cryogenic pumping systems of the nearby magnets, as will be discussed in Section 7.2.5.

7.2.4 Optimised gas density profile

The gas profile was simulated for the final version of the tank layout, presented in the previous chapter, where each design parameter was optimised taking into account instrument performance needs, beam-coupling impedance minimisation, mechanical stability and integration constraints. The ion pump positions correspond to those discussed in the previous section.

The final profile of the BGV, simulated with the boundary condition of a 0.05 sticking coefficient at the beam pipe extremities, as for the above presented simulations, is shown in Figure 7.12 with the orange curve. The position of the ion pumps is indicated with vertical arrows, and the one of the first tracking detector layer by the vertical dotted line, in orange too.

The tank dimensions and gas injection rate guarantee a homogeneous density plateau with the desired gas density level in the measurement region, indicated by the grey rectangle. The inner pumps are placed as close as possible to the gas tank to ensure a quick pressure drop, and separated from the outer pumps by a distance of 1.3 m. As previously discussed, this length can be adjusted depending on the vacuum chamber layout at each instrument location.

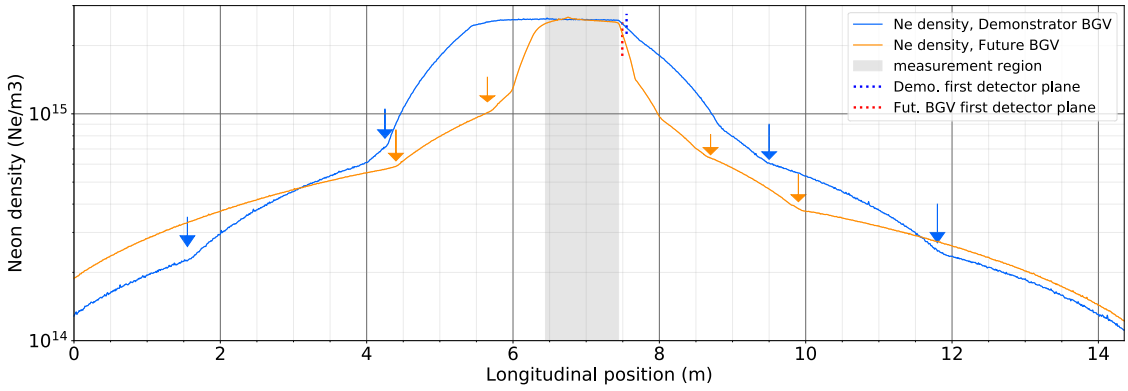

Figure 7.12: Longitudinal gas density profile of the optimised BGV setup (orange) and of the demonstrator (blue). Pump positions are shown with the vertical arrows, and the first detector location is indicated with the vertical dotted line. The measurement region is also represented by the grey block. The density values are given with a precision of at least 0.1%.

For comparison, the simulated profile of the demonstrator geometry is also shown in blue in this figure, with the position of the pumps and first detector layer indicated in blue. The main differences between these two layouts, shown side-by-side in Figure 7.13, are the dimensions of the tank and the distances of the four ion pumps to the target

centre. The injection rate of the demonstrator was scaled to reach $2.5 \times 10^{15}\,\mathrm{Ne/m^3}$ in the measurement region. Here the integrated gas density of the new configuration appears 25% smaller than the one of the demonstrator. This value is to be considered very carefully as these simulations do not take into account the cryogenic equipment in the surrounding of each instrument. Once integrated in their respective foreseen locations, the tails may expand and the total integrated pressure of each instrument may significantly differ from the values obtained from these simulations. In particular, the higher gas density levels of the new setup at the beam pipe extremities (longitudinal positions 0 m and 14 m) give a hint that the demonstrator gas density may decrease quicker in distance on either side of this region than the density of the new setup.

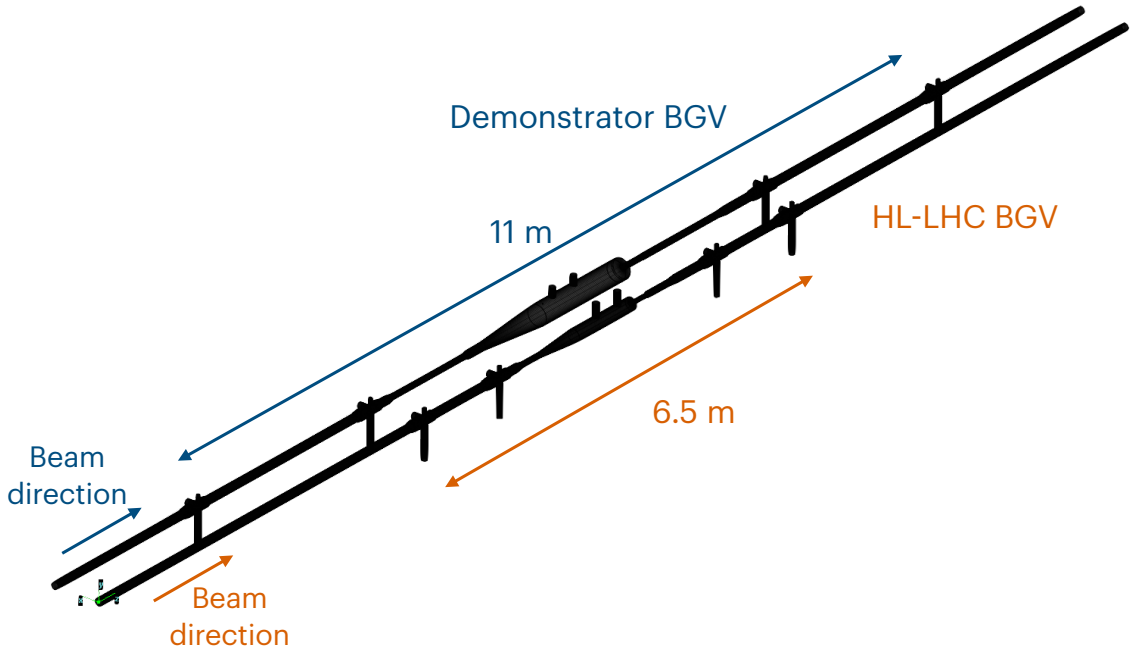

Figure 7.13: Layout of the optimised HL-LHC BGV and of the demonstrator instrument, shown side-by-side in *Molflow+*.

7.2.5 Effect of cryogenic pumping

In order to assess the impact of the BGV gas target on the LHC beam and radiation environment, and accurately compare the density profiles of the two setups, further simulations placing the BGV final geometry in the vacuum environment corresponding to the foreseen locations are required.

7.2.5.1 B2-BGV

Such simulations were performed by the CERN vacuum group, for the Beam 2 instrument and with the HL-LHC version of the setup, placed at −220 m with respect to IP4 centre [93]. The resulting profile is shown with the purple curves in Figures 7.14a and 7.14b. In comparison, the orange curves show the profile obtained with the simulations detailed in the previous section, that was shown with the same colour in Figure 7.12. The top plot 7.14a reveals that the gas profile tails only decrease to a negligible level when reaching a cryogenic equipment, represented here by the grey blocks. At the foreseen location of the B2-BGV, the closest cryogenic systems are quadrupoles, as will be shown in Figure 7.15b. For this specific device, the gas density levels in the tails were underestimated by the simulations discussed in the previous sections. In particular the sticking coefficient of 0.05 at the beam pipe extremities was, in this case, an optimistic estimate of the absorption capacity of the surrounding environment.

7.2.5.2 B1-BGV

At the time of writing, the B1-BGV instrument location has not been reserved, and a similar simulation was not yet performed with integrating the updated BGV geometry in the B1-BGV vacuum sector. However, at the foreseen location, the closest cryogenic quadrupoles shown in Figure 7.15a are located closer to the BGV instrument compared to the case of the Beam 2 device. The integrated pressure of the B1-BGV target is therefore expected to be significantly lower.

7.2.5.3 Conclusion

The longitudinal gas density profile of the BGV instruments was optimised with a hypothetical representation of the absorption capacity of the surrounding vacuum chambers. The distance or proximity of the closest cryogenic systems significantly affects the tails of the simulated profile in the case of the B2-BGV. Smaller tails are expected for the B1-BGV profile. In the following and to be conservative, the radiation impact of the BGV target and its impact on the HL-LHC beam emittance growth and lifetime will be estimated considering the B2-BGV updated gas profile, shown in purple in Figure 7.14a.

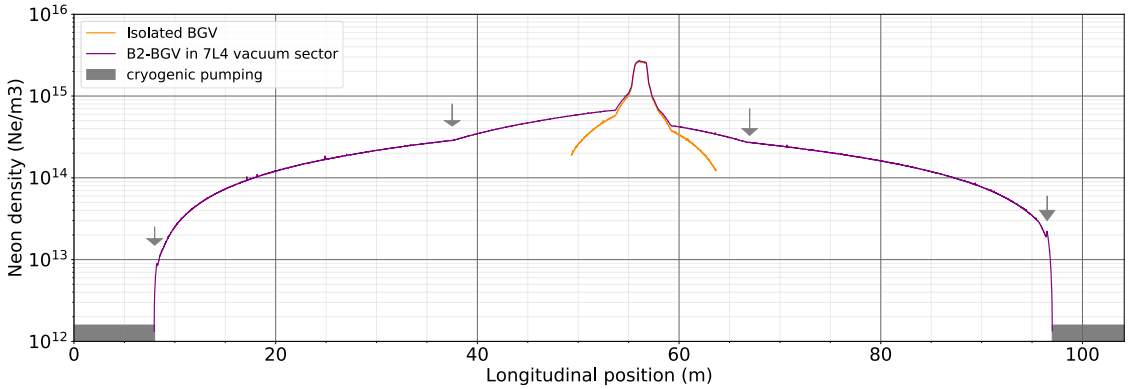

(a) Entire vacuum sector region. The position of the sector valve ion pumps are shown with the grey arrays, and cryogenic equipment with the grey blocks.

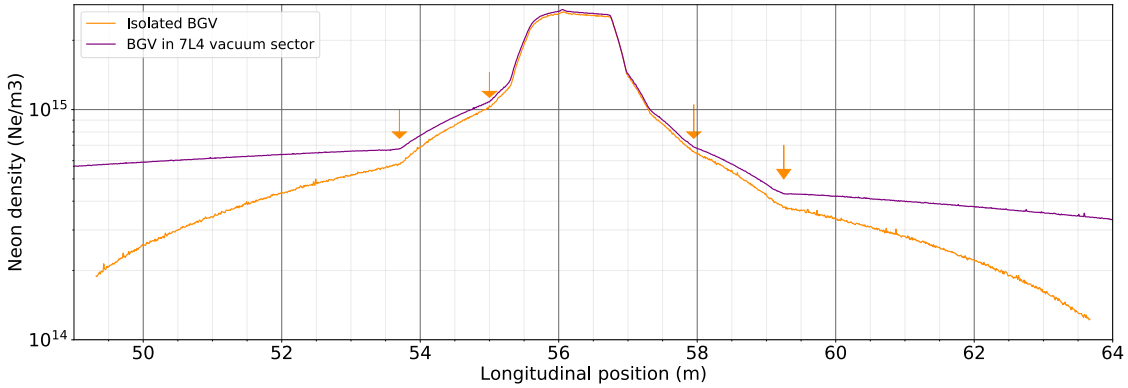

(b) Zoom on the BGV target. The position of the BGV ion pumps are shown with the orange arrays.

Figure 7.14: Longitudinal gas density profile of the final B2-BGV setup, integrated in the vacuum sector at the foreseen installation location (purple curves). The profile from the simulation independent of the BGV location in the LHC, obtained from the profile optimisation study and already shown in Figure 7.12, is displayed in orange for comparison.

7.3 Impact on the radiation environment and LHC beam

The BGV instrument aims to provide a beam size and profile measurements in a non-invasive way. This necessitates ensuring that beam-gas interactions have a negligible impact on the beam lifetime and emittance. This section addresses the impact of the BGV gas target on the LHC beams. The contribution of the secondary showers introduced by the BGV gas target to the radiation levels in the LHC tunnel is also discussed here.

7.3.1 Radiation

Analyses of the Total Ionising Dose (TID) rates and High Energy Hadron equivalent (HEHeq) fluence in the vicinity of the demonstrator BGV revealed that, when turned ON, the demonstrator BGV became the main source of radiation in its vacuum sector

and up to 150 m downstream [94, 95]. During data taking runs, the demonstrator target was operated with a gas density profile with a similar shape to the blue one shown in Figure 7.12, although as already discussed, this simulation underestimates the tails which likely extend up to the closest cryogenic chambers few tens of meters away from the instrument. According to the data recorded during Run 2 by the gas tank pressure gauge, the average plateau pressure was of 1.45×10^{-7} mbar, and this level was the same for both proton and ion runs.

Simulations were performed [95], from the CERN team in charge of studying Radiation to Electronics (R2E) [96–98], to estimate the radiation stemming from the BGV instrument. The main conclusions are summarised in this section, and the detailed study can be found in [2]. The simulations were first successfully benchmarked, based on the data recorded during Run 2 by Beam Loss Monitors (BLM) [99] and Radiation Monitors (RadMons) [100] in the vicinity of the demonstrator BGV. Estimates were then made for the future instruments, considering the HL-LHC beam parameters presented in Chapter 2, and the expected gas density profile of the HL-LHC BGV (purple profile from Fig 7.14). The same extended gas profile obtained from B2-BGV simulations was used for B1-BGV estimates. This consideration corresponds to a worst case scenario, as the B1-BGV integrated profile is expected to be smaller thanks to the closer proximity of cryogenic equipment to the foreseen B1-BGV location. TID rates and HEHeq fluences for the HL-LHC instruments were first computed for 1 h of instrument operation, and then scaled to obtain the expected quantities per year, with considering a minimum of 400 h of instrument operation in a year. To be conservative, the per hour quantities are considered for 7 TeV beams and scaled as if the beam was at collision energy during the yearly 400 h operation time.

The impact of secondary showers on the closest cryogenic magnets is considered first. Figure 7.15 shows the location of the neighbour cryogenic magnets at the two instrument locations and the expected TID rates at beam height, induced by 1 h of BGV target operation at collision energy, in the vicinity of each instrument. B2-BGV would become the main source of radiation for the Q7 quadrupole downstream, and for the two first dipoles of the downstream arc: BA8 and BB8. B1-BGV showers would affect the Q5 quadrupole upstream of the instrument, and Q6 and Q7 quadrupoles downstream, in addition to BA8 and BB8. Beyond these magnets, the TIDs induced by the BGV target drop below the levels measured during Run 2.

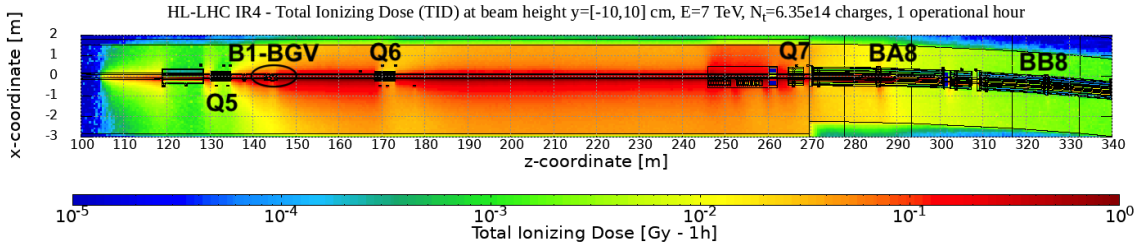

(a) B1-BGV.

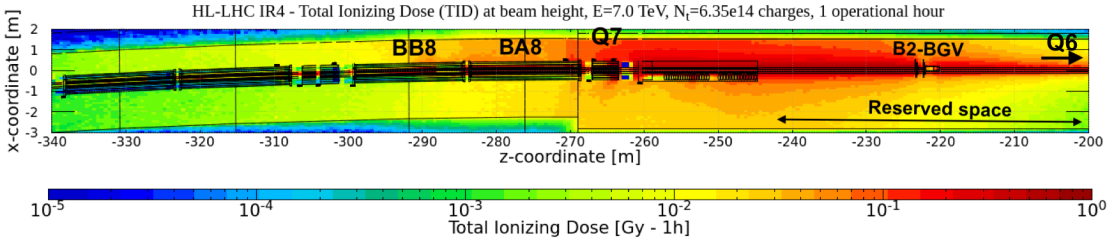

(b) B2-BGV. The Q6 quadrupole is located further to the right.

Figure 7.15: Simulated TID rates induced by 1 h of operation of the B1-BGV (7.15a) and B2-BGV (7.15b) instruments at 7 TeV. The position of the closest quadrupoles are indicated. [2]

Maximum heat load and TID rates in the magnets of each kind (dipole or quadrupole) and for each location are listed in Table 7.3. The total power dissipated in the entire magnet is given in the first column, and the maximum power density in the second column. At both location, the Q7 quadrupoles are the one absorbing the most radiation energy. The first dipole, BA8, receives most of the radiations at the right of IP4 (B1-BGV), whereas downstream of the B2-BGV, a higher peak is observed in the second dipole, BB8.

Table 7.3: Heat load and TID rates induced by the operation of the BGV target in the neighbour cryogenic magnets. Each value corresponds to the maximum among the magnet of the same kind (quadrupole or dipole).

	Most affected magnet of its kind	Total deposited power	Maximum power density	Quench limit [101]	Maximum TID rates
Beam 1	Q7	760 mW	1 mW cm^{-3}	40 mW cm^{-3}	0.2 kGy h^{-1}
	BA8	1600 mW	0.3 mW cm^{-3}	13 mW cm^{-3}	0.1 kGy h^{-1}
Beam 2	Q7	290 mW	0.2 mW cm^{-3}	40 mW cm^{-3}	0.2 kGy h^{-1}
	BA8	1200 mW	0.7 mW cm^{-3}	13 mW cm^{-3}	0.3 kGy h^{-1}

Even for the magnets receiving the highest doses, neither the maximum power density nor the total dissipated power on the whole magnet are worrying in terms of total heat load, which is way below the design limit of tens of Watts [101]. The maximum

expected power density does not exceed 5% of the assumed quench limit, excluding the risk of quenching. Cumulative damages are no cause for concern either, with TID rates of at most about 100 kGy per year, which is two orders of magnitude below the long term radiation dose limit being of few tens of MGy [101]. The BGV showers therefore do not represent a threat for the nearby and downstream superconducting magnets.

Regarding the risks to electronic systems, the HEHeq fluence levels were evaluated in air at the floor level. A plateau at $1 \times 10^{10}\,\mathrm{cm}^{-2}$/year, starting downstream of each gas target and spreading up to BB8 downstream, on each side of the IP. Stochastic failure due to single event effect are expected from about $3 \times 10^{10}\,\mathrm{cm}^{-2}$/year. Moreover, TID levels of about 10 Gy/year are expected at the floor level, leading to reduced lifetimes of the nearby electronic systems. While being far below the levels measured and expected close to the high luminosity producing experiments [102], these levels are significantly higher than the arcs baseline [103] and may represent a threat for the lifetime and well functioning of the nearby devices after few years of operation of the BGV targets.

Thanks to the long space reservation made for the B2-BGV, and to the proximity of the arc, there is no sensitive equipment downstream of the B2-BGV target. However, various electronic devices, mainly beam instruments, are installed downstream of the foreseen B1-BGV location. At the time of writing, this location was not yet finally approved. Once it will be, a systematic investigation involving equipment owners should be performed, with the aim to estimate whether the expected levels are acceptable for each system. Shielding mitigation solutions will be envisioned where needed. Although unlikely, a limitation on the operation time of the BGV may arise from these discussions.

For operation times of about 400 h with 7 TeV proton beams, the radiation showers introduced by the BGV are far below worrying levels for the nearby cryogenic magnets. They still represent a threat for the electronic devices already installed in the tunnel, from about 150 m on the right side of IP4 and up to the beginning of the arc. In case limitation of the ON time of the target is set for radioprotection reasons, the BGV could be used in priority during fills dedicated to emittance growth study, in machine development runs. One could for instance define a radiation budget corresponding to an operation time budget per year, to spread over the fills according to the operation and machine optimisation needs. Operators of the instruments should also keep in mind that the radiation impact

of the BGV target scales linearly with the beam energy, i.e. radiation levels are 10 times lower at injection energy, as is shown in [2].

The BGV tracking detectors are expected to be exposed to radiation doses in the order of 0.1 Gy/h [2]. TimePix detectors are known to show degraded functionalities from about 1 kGy [51], which confirms that this technology is suitable for the BGV application. Regarding the Data AcQuisition (DAQ) system, front-end boards will be placed on the floor, few meters away from the instrument, and back-end boards in the tunnel gallery, which is shielded from the beam tunnel, to avoid unnecessary radiation exposure. More details regarding the BGV DAQ system can be found in Ref. [2].

7.3.2 Beam lifetime

The amount of beam particles interacting with the gas target is discussed and assessed below.

The time evolution of the beam population $N(t)$ due to the presence of the gas target follows Equations (7.4) and (7.5), where λ represents the interaction probability of a beam particle with a gas molecule [45].

$$\frac{\mathrm{d}N}{\mathrm{d}t} = -\lambda N(t) \tag{7.4}$$

$$N(t) = N_0 \mathrm{e}^{-\lambda t} \tag{7.5}$$

At $t = 0$, the interaction probability λ is equal to the ratio of the interaction rate R by the initial beam population N_0: $\lambda = N_0/R$. The beam lifetime ξ is defined as the time after which the beam population has decayed by $\frac{1}{\mathrm{e}}$, and is equal to the inverse of the interaction rate R: $\xi = \frac{1}{\lambda} = \frac{R}{N_0}$.

The expression of R is reminded from Chapter 5, and depends on the integrated gas density profile $\int \rho(z)\mathrm{d}z$ and on the interaction cross-section σ:

$$R = f_{\mathrm{rev}} N_0 \sigma \int \rho(z)\mathrm{d}z\,. \tag{7.6}$$

While it is clear that the interacting beam particles are lost in inelastic collisions, elastic interactions, representing 1/3 of the total interactions [43], only cause the lost of the beam particle if the deviated trajectory leads it outside of the dynamic aperture (beam stability

region in phase space). Since the proportion of elastic collisions causing a beam particle loss cannot be exactly determined, the actual ξ is assumed to lie between the lifetime due to inelastic interactions and the one due to all types of interactions.

The interaction rates corresponding to the wide B2-BGV gas profile shown in Figure 7.14 are listed in Table 7.4, together with expected lifetimes at injection and collision energy, and for both proton and ion beams. The rate of particles lost in one hour of BGV operation, R_{lost}, is also given for each case, considering that all types of interactions lead to a particle loss.

Table 7.4: Impact of the gas target on LHC beam population, considering the B2-BGV longitudinal profile shown in Figure 7.14

Beam		R^{tot}	R^{inel}	R_{lost} (h^{-1})	Beam lifetime
p runs	450 GeV	7.5 MHz	5.2 MHz	1.0×10^{10}	$3.0 < \xi < 3.9$ years
	7 TeV	9.1 MHz	6.2 MHz	1.2×10^{10}	$2.2 < \xi < 3.3$ years
Pb runs	450 GeV	7.2 kHz	6.0 kHz	2.6×10^{7}	$130 < \xi < 160$ days
	7 TeV	8.7 kHz	7.1 kHz	3.1×10^{7}	$110 < \xi < 130$ days

In comparison, the nominal beam population is reminded to be 6.1×10^{14} for proton runs and 2.3×10^{11} for ion runs. At collision energy, the beam lifetimes are in the order of 100 h [14].

Expected lifetimes due to the presence of the BGV target are in the order of years, meaning that its impact is very limited and should not be noticeable at the time scale of a fill. The amount of beam particles lost per hour of BGV operation, in the order of 1×10^{10} for proton beams, also represent a very small fraction of the total 6×10^{14} protons per beam.

7.3.3 Emittance growth

Elastic scattering of the beam particles on the gas molecules from the BGV target can deviate the incident particles from their initial trajectory, and cause emittance growth. For a 1σ beam size, the emittance growth per turn $\Delta\epsilon$ due to the presence of the BGV target can be calculated with Eq. (7.7), as detailed in Ref. [104], where the gas target is considered as a distributed thin scatterer. In this formula, q_p is the charge number of the projectile, ie. of a beam particle, of momentum p and relativistic velocity β_r. $\bar{\beta_x}$ represents the average transverse β-function along the gas target of length Δz.

$$\Delta\epsilon = \frac{1}{2} q_p^2 \Big(\frac{13.6\,\mathrm{MeV}}{p\beta_r} \Big)^2 \bar{\beta}_x \frac{\Delta z}{L_{\mathrm{rad}}} \quad . \tag{7.7}$$

In the case of the BGV, the radiation length of the neon target is $L_{\mathrm{rad,\,Ne}} \simeq L_{\mathrm{rad,\,Ne,\,1atm}}/(\bar{P}/1\ \mathrm{atm}) = 1.2 \times 10^{13}\,\mathrm{m}$, where $\bar{P} = 1.0 \times 10^{-8}\,\mathrm{m}^{-3}$ is the average gas pressure along the target obtained with the B2-BGV projection (as seen in Section 7.2.5) and $L_{\mathrm{rad,\,Ne,\,1atm}} = 344\,\mathrm{m}$ the radiation length of neon at atmospheric pressure [43]. The same gas profile is assumed for the two instruments' targets. Since the two BGV devices will be installed in regions with different beta functions, the impact of their targets on the transverse emittance of each beam will be different.

The normalised emittance growth rate $\Delta\epsilon_n$ can be expressed in $\mu\mathrm{m\,h}^{-1}$ by scaling $\Delta\epsilon$ with the beam relativistic velocity β_r, Lorentz factor γ_L of the corresponding energy and with the LHC revolution frequency. The resulting values are summarised in Table 7.5 for each beam at injection and collision energy, and plotted as a function of the beam momentum in Figure 7.16.

Table 7.5: Emittance growth rates due to elastic scattering.

	Energy	$\Delta\epsilon$ (π **rad m/turn**)	$\Delta\epsilon_n$ (μ**m h**$^{-1}$)	$\Delta\epsilon_n/\epsilon_n$ (**%/h**)
Beam 1	450 GeV	4.7×10^{-19}	9.2×10^{-3}	0.5
	7 TeV	2.0×10^{-21}	5.9×10^{-4}	0.03
Beam 2	450 GeV	2.4×10^{-19}	4.6×10^{-3}	0.2
	7 TeV	9.8×10^{-22}	2.9×10^{-4}	0.01

Consistently with the instrument operation time per fill mentioned in section 7.3.1, an estimate of the emittance growth per fill can be calculated. Considering a normalised emittance of 1.7 µm at 450 GeV and 2.5 µm at 7 TeV, the emittance growth rates corresponding to 1 h of BGV operation at injection and 1 h at collision energy are of about 0.5 % for Beam 1 and 0.2 % for Beam 2.

These results are small compared to the emittance measurement accuracy requested of 10%, and also small compared to the currently identified sources of emittance growth [105, 106]. This impact was deemed acceptable [64], but should nevertheless be kept in mind for machine performance, when operating the BGV instruments. It will scale with the instrument's operation time, but is highly dominated by the impact at injection energy, as revealed in Figure 7.16. Longer instrument operation at flat top will cause very little change to these values.

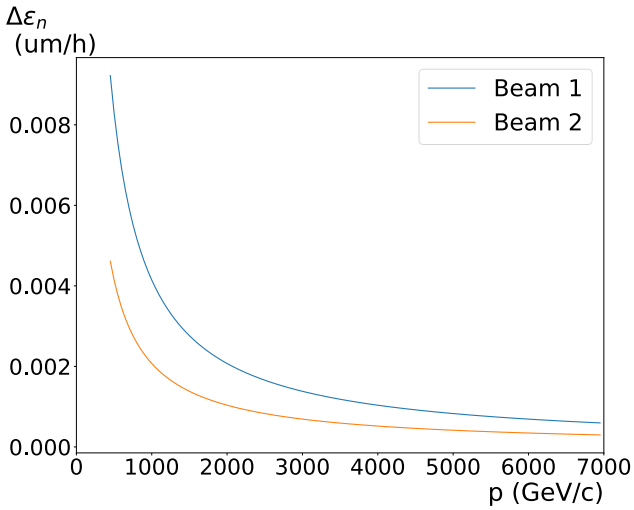

Figure 7.16: Expected emittance growth rate $\Delta\epsilon$ in $\mu m\,h^{-1}$ due to the BGV target for Beam 1 (blue curve) and Beam 2 (orange curve), along the LHC energy cycle, assuming the same longitudinal gas density profile for the two instruments.

It can be noted that during Run 2, the demonstrator target that was turned ON during multiple hours in a row for beam size measurement, and sometimes also during most of the LHC energy cycle. No problem was raised regarding the LHC operation with this use of the gas target, operated with the same pressure for both proton and ion runs. The HL-LHC BGV targets would be operated at a similar pressure level, which gives confidence that their operation will be safe regarding machine operation.

7.3.4 Electron clouds from beam-gas ionisation

In the LHC, electron clouds are generated through several mechanisms [107]. Primary electrons can originate from ionisation of residual gas, or be extracted of from the beam chamber walls by the synchrotron radiation issued from the beam (photoelectrons). At collision energy, this second mechanism dominates. When hitting then chamber walls, these primary electrons can either be elastically reflected, or extract secondary electrons. These electrons can also be accelerated by the beam fields, leading to higher secondary emission yields.

The build-up of electron clouds can lead to pressure rise, heating of accelerator components, in particular cryogenic chambers in the arcs, and beam instabilities at injection.

At collision energy, the presence of NEG coating on the BGV walls will limit the photo-electron production yield, like for most vacuum chambers in warm sectors. The electron production rate due to beam-gas ionisation of the BGV gas target was however

not yet investigated at the time of writing. The experience gained with the demonstrator BGV target gives confidence that this effect will not be a showstopper, but it should be considered in details before the instruments' implementation [108].

7.3.5 Conclusion

Given the small expected impact of the HL-BGV targets on the HL-LHC beams, and thanks to negligible impedance contributions of the final gas tank design, this measurement technique can be considered as a non-invasive. The HL-BGV targets would introduce a significant radiation source on either side of IP4, but their impact on nearby equipment only concerns the electronic systems installed on the second half of the right side of the IP4 long straight section. Further work is needed to implement mitigation solutions in this regard, and a limitation of the BGV target operation time for radiation protection reasons cannot excluded so far. The contribution of the target to electron clouds build-up through beam-gas ionisation should also be assessed before implementation.

While the radiation impact of the BGV targets linearly increases with the beam energy, the introduced emittance growth mainly concerns Beam 2 at injection energy, and become negligible when the beam energy increases.

7.4 Beam size measurement with a distributed target

It was seen in Chapter 4 that the beam optics, in particular β-functions, are not constant along the measurement regions at the foreseen installation locations. This results in a beam size gradient in the order of up to 1-2%, along the 1 m long regions in which the beam-gas interactions are generated. The gradient values are summarised in Table 7.6.

Table 7.6: Expected beam size gradients at B1-BGV and B2-BGV locations.

Instrument	Energy	Beam size gradient		Percent of beam size	
		$\Delta\sigma_x/\Delta s$ µm m^{-1}	$\Delta\sigma_y/\Delta s$ µm m^{-1}		
B1-BGV	450 GeV	17	24	1.5%	2.3%
	7 TeV	4.5	5.0	1.0%	1.4%
B2-BGV	450 GeV	14	~ 0	1.8%	negligible
	7 TeV	4.0	~ 0	1.7%	negligible

The resulting linear beam size variations are significant compared to the beam size accuracy specification of 5%. This effect can be compensated by located the measured

beam size at the centre of mass longitudinal position of the vertices contributing to this measurement. This is made possible by the longitudinal vertex resolution of the instrument in the order of few millimetres [2]. The β-function values at the obtained position shall be consider accordingly, to derive the emittance.

7.5 Higher mass gases

The choice for a neon gas target was already discussed in section 5.2.1. For the sake of completeness, this section questions the potential interest of using higher mass gas species.

For higher mass gases, the beam-gas interaction rates are increased, due to the higher atomic mass A impacting the interaction cross-sections: $\sigma^{\text{tot}} \propto A^{0.77}$, $\sigma^{\text{inel}} \propto A^{0.71}$, as was presented in Section 5.2.2 of Chapter 5. The beam-gas interaction rates, average number of tracks entering the tracker acceptance and average tracks momentum are listed for neon, argon and xenon in Table 7.7 for 7 TeV protons beams. The values are given for a 1 m-long target at a pressure of 1×10^{-7} mbar and the number of tracks in the tracker acceptance is estimated with the final tracker geometry.

Table 7.7: Comparison of beam-gas inelastic cross-sections and interaction rates for 7 TeV proton bunches on a 1 m-long target of neon, argon and xenon, at an average pressure of 1×10^{-7} mbar.

	Inelastic interaction rate per bunch (Hz)	Average N_{tr} in tracker acceptance	Average track momentum (GeV/c)
Neon ($A_{\text{Ne}} = 20$)	220	3.2	6.3
Argon ($A_{\text{Ar}} = 40$)	360	3.5	6.2
Xenon ($A_{\text{Xe}} = 132$)	840	4.2	5.9

Considering the BGV target volume described above, the same interaction rate compared to neon can thus be achieved with argon (or xenon) with decreasing the pressure by 28% (respectively 61%).

Regarding the impact on instrument performance, the average number of tracks per event in the tracker acceptance is increased by a factor 1.24 for argon and 1.79 for xenon compared to neon. With one of these two gases and with a similar interaction rate, more events could thus be reconstructed (higher bunch width precision or shorter integration time) and the vertex resolution would be improved (better beam size accuracy). Nevertheless, more tracks per interaction also lead to higher radiation levels stemming from

the instrument.

On the other hand, the average track momentum is slightly reduced with the increase of gas mass, meaning lower quality tracks. The vertex resolution for events with the same tracks multiplicity was compared for neon, argon and xenon, with the result shown in Figure 7.17, to estimate how the vertex resolution is impacted by the reduced tracks momenta. A slight vertex degradation is indeed observed with the higher mass species.

The same analysis performed for lead ion beams lead to the same conclusions (see Appendix E).

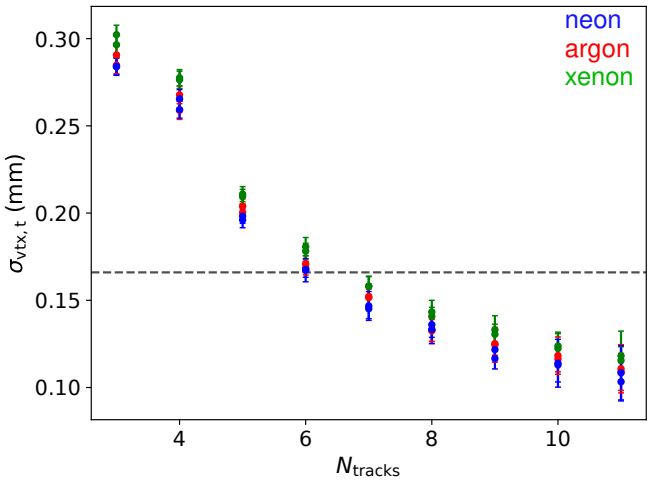

Figure 7.17: Impact of the gas species on the transverse vertex resolution, for events with similar number of tracks in the tracker acceptance. [2]

There is therefore no strong interest in using a higher mass gas in terms of instrument performance, considering the vertex resolution and beam size measurement accuracy. A higher mass gas would however allow to operate the instrument with a lower pressure to achieve a similar precision to neon, thus reducing the impact of the gas target on the beam lifetime. The impact on radiation environment should also be reduced with a lower pressure, but the increase in average tracks multiplicity per inelastic collision will also impact the resulting radiation levels.

7.6 Summary

The HL-LHC BGV gas target design is based on the distributed system that proved to work reliably with the demonstrator target operated in the LHC during Run 2. The longitudinal gas density profile was optimised in order to meet instrument requirements

while ensuring a sharp drop of the profile tails to minimise undesired beam-gas interactions. The impact of this new target on the LHC beams was quantified and is expected to be very small. Radiation studies were done to estimate induced levels in the LHC tunnel due to beam-gas interaction with the BGV gas target. A limitation to the up time of the gas target may be defined, to limit its impact on the surrounding electronic systems.

Chapter 8

Unfolding the beam profile from the vertices distribution

As was shown in Chapter 4, the distribution of reconstructed vertices provided by the BGV is a convolution of the beam profile with the instrument response function. A good understanding of this response function is therefore critical for an accurate beam profile unfolding (deconvolution). A method is proposed in this chapter to determine the response function, specific to a set of measured vertices, that was inspired by the method used by the LHCb experiment [6, 7]. It is tested on simulated data, and unfolded beam size and profile results are presented.

8.1 Vertex resolution

The transverse vertex resolution $\sigma_{\mathrm{vtx},u}$ along one of the transverse planes $u = \{x, y\}$ is defined as the width of the distribution of residual distances $r_{u,i}$ between the true vertex position $u_{\mathrm{true},i}$ and the measured position $u_{\mathrm{meas},i}$ for each vertex i:

$$r_{u,i} = u_{\mathrm{true},i} - u_{\mathrm{meas},i}\,. \tag{8.1}$$

An example residual distribution is shown in Figure 8.1. This distribution is fitted with a sum of a core and a tail Gaussian functions, of respective amplitude and width (p_c, σ_c) and (p_t, σ_t), and sharing the same mean. The width σ_{r_u} of the distribution is obtained

by weighting the width of each Gaussian function, as:

$$\sigma_{r_u} = \sqrt{f_c \sigma_c^2 + f_t \sigma_t^2}\,, \tag{8.2}$$

where the core f_c and tail f_t weighting factors are given by $f_i = \dfrac{p_i \sigma_i}{p_c \sigma_c + p_t \sigma_t}$ for each Gaussian function ($i \in \{c, t\}$). The error on σ_{r_u} is obtained via error propagation of the errors on p_c, p_t, σ_c and σ_t.

A double Gaussian function is used here instead of a single Gaussian function, since it was shown to model best the obtained distributions in most cases. This is likely due to to the accumulation of vertices with dissimilar characteristics.

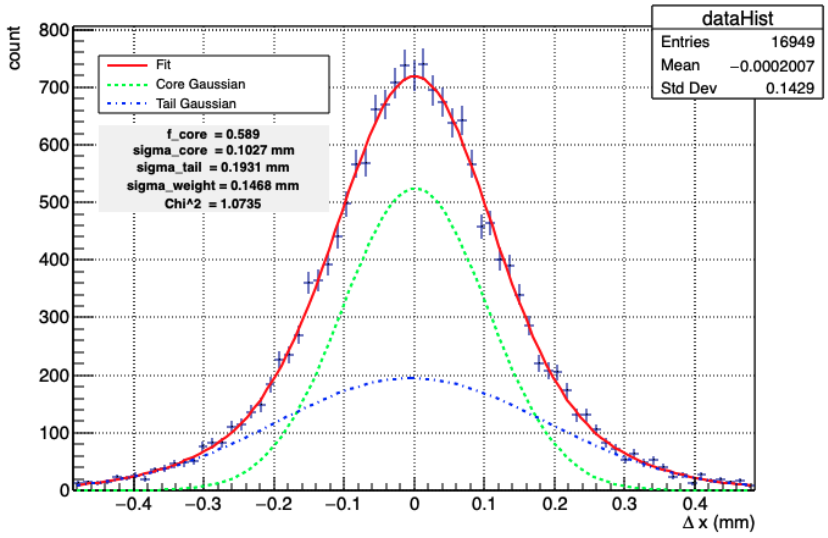

Figure 8.1: Distribution of horizontal residuals between the reconstructed and true vertex positions, for vertices reconstructed with $N_{\text{tr}} = 7$ tracks. The double Gaussian fit is shown in red, and the core and tail Gaussian functions are respectively plotted in green and blue.

Assessing the vertex resolution of the BGV requires to know the true position of each measured vertex. This is the case when working with simulations. This method will be called *true residuals method* (*TRM*), and the residuals from Eq. (8.1) noted $r_{u,i}^{\text{TRM}}$.

Experimentally, the vertex resolution can be determined via the *split vertex method* (*SVM*), used by some of the main experiments at high luminosity collider facilities [5,109]. This data driven method consists in dividing the set of tracks issued from a primary vertex into two subsets, as illustrated in Figure 8.2. A so-called *split vertex* is reconstructed from each set, independently. The width of the distribution of residuals between the two split

vertex positions gives a measurement of the vertex resolution. In this case, the vertex resolution impacts the position of both split vertices, and the distribution width is a convolution of the resolution of each split vertex $\sigma_{\text{vtx},1}$ and $\sigma_{\text{vtx},2}$:

$$\sigma_{r^{\text{SVM}}} = \sqrt{\sigma^2_{\text{vtx},1} + \sigma^2_{\text{vtx},2}}\,. \tag{8.3}$$

If both split vertices share the same resolution $\sigma_{\text{vtx,split}}$, then $\sigma_{r^{\text{SVM}}} = \sigma_{\text{vtx,split}} \times \sqrt{2}$. Therefore, the resolution of these split vertices is measured by the distribution width divided by $\sqrt{2}$.

Alternatively, the residuals can be directly divided by $\sqrt{2}$ in the accumulation process:

$$r^{\text{SVM}}_{u,i} = (u_{1,i} - u_{2,i})/\sqrt{2}\,, \tag{8.4}$$

in which case the split vertex resolution is directly measured by the distribution width.

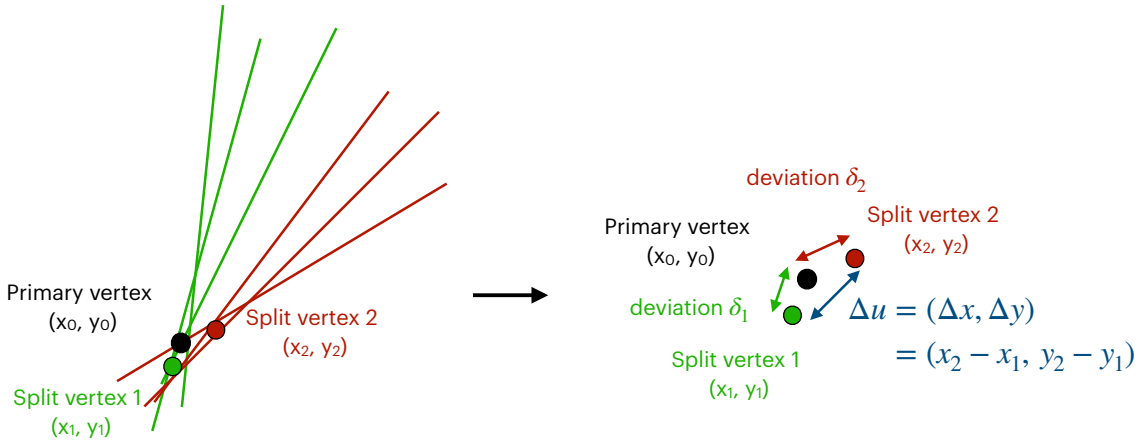

Figure 8.2: Illustration of the split vertex method. All tracks represented on the left are issued from the true primary vertex (black dot). They are randomly split into two sets (red and green). A vertex position is reconstructed independently from each of these sets, leading to two split vertices (red and green dots), distant by Δu. The deviation of the position (x_i, y_i) of each split vertex i from the primary vertex position (x_0, y_0) is noted $\delta_i = (x_i - x_0, y_i - y_0)$.

Two algorithms were implemented to assess the vertex resolution of the HL-BGV with each of these two methods. For the SVM, the tracks of the primary vertices are split into two sets, denoted by indices $i = 1, 2$, with equal number of tracks: $N_{\text{tr},1} = N_{\text{tr},2}$. In case the primary vertex has an odd number of tracks, the track with the highest χ^2 is removed from the primary set.

In the following, one objective is to determine the ability of the SVM to measure

the true beam width.

8.2 Response function determination method

For a given geometry of the HL-BGV instrument, the vertex resolution of a reconstructed vertex is impacted by:

- The number of tracks N_{tr} combined to reconstruct the vertex;
- The quality of these tracks, that is how close they are to the true particle trajectory, which depends on the trajectory deviation experienced by the particle due to multiple Coulomb scattering;
- And the longitudinal position z of the vertex, through the extrapolation error.

Since the vertex resolution depends on the characteristics of the beam-gas interactions, the BGV response function is unique for a each set of reconstructed vertices. A method is proposed here to determine the instrument's response function to any individual beam size measurement.

Since all vertices involved in a measurement have different properties, it is important to disentangle these dependencies. Using either the TRM or the SVM, the vertex resolution can be parametrised as a function of N_{tr} (Section 8.2.1) and z (Section 8.2.3), which are measurable vertex characteristics. The vertex resolution also depends on the track momentum, itself impacting the track quality through multiple scattering. This quantity is however not directly measurable with the BGV. Nevertheless, the track quality can be estimated via the quality of the track fit (with the fit χ^2, goodness of fit indicator, for instance). The influence of this parameter will not be considered here, but could be used to improve the accuracy of the vertex resolution.

Once the vertex resolution has been parametrised for all possible characteristics, individual vertex resolutions can be assessed based on the characteristics of each vertex contributing to a beam size measurement. The response function for a given beam size measurement is obtained from the accumulation of individual vertex resolutions. This step will be detailed Section 8.2.5).

With the future instrument, the parametrisation of the vertex resolution would be done in a *calibration* step of the instrument, where a large set of beam-gas interactions will be collected and reconstructed at various beam energies, to account for the change of secondary particle momentum with the beam energy, which impacts the parametrisation.

In the following, the vertex response is determined on simulated data. For demonstration, several sets of independent beam-gas inelastic interactions were generated and propagated through the final HL-BGV geometry, using the simulation tool described in Chapter 5. The three data sets (1a, 1b and 2) correspond to unbiased events, dedicated to assess the instrument performance, while the last one (3) serves to parametrise the vertex resolution:

1. Two sets of reconstructed vertices, from beam-gas interactions with **7 TeV** protons:
   (a) One with the vertices **Gaussian**-distributed in the transverse planes, simulating a 200 µm wide Gaussian beam profile,
   (b) The other one with a **double Gaussian**[1] vertex distribution, which allows to model a distribution where the tails are broader than they would be with a single Gaussian distribution,
2. One set from **Gaussian**-distributed beam-gas interactions, generated with **450 GeV** protons, with a width of 800 µm;
3. One set generated with a **Gaussian**-distributed 7 TeV proton beam, similar to set 1a, where a filter was applied at the generator level to select only **high track multiplicity** events. This last set is dedicated and solely used for parametrisation of the vertex resolution with the SVM method. The need for this biased set will be motivated in the following section.

Data sets 1a, 1b and 2 contain about 300 000 events each, and the high N_{tr} set 3 about 500 000. The distribution of number of reconstructed tracks per event for data sets 1a and 3 are shown in Figure 8.3. Data set 3 was obtained by selecting beam-gas interactions with $N_{\mathrm{tr,tot}} \geq 11$ tracks generated in all directions, which is why some events still show a low N_{tr} traversing the tracker.

Example Gaussian and double Gaussian vertex distributions are shown in Figure 8.4 from data sets 1a and 1b respectively. The true simulated beam-gas interaction distribu-

[1] Sum of two concentric Gaussian functions, with different widths.

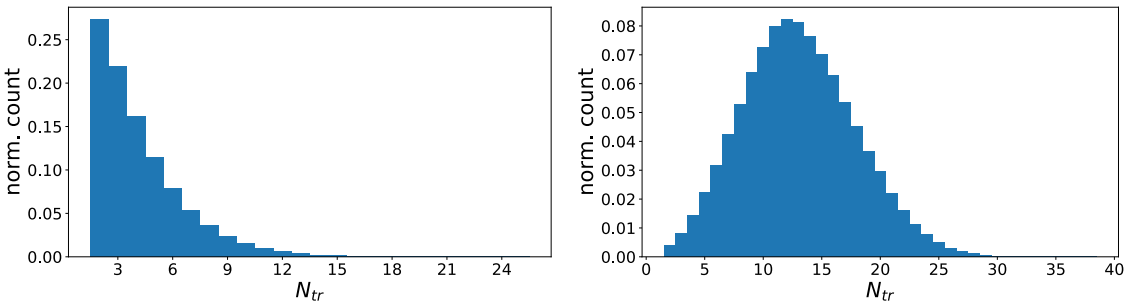

(a) Data set 1a.

(b) Data set 3, dedicated to SVM calibration.

Figure 8.3: Distributions of the number of reconstructed tracks per event (N_{tr}), for a dataset with unbiased track multiplicity (8.3a), and for a biased one (8.3b), dedicated to vertex resolution parametrisation with the SVM.

tions are shown in the left plots (purple distributions), and the raw reconstructed distributions, before response function unfolding, in the right plots (blue distributions). The reconstructed profiles are visibly broader than the true ones, due to the effect of the BGV response function.

It is noted that the beam is simulated here with a constant profile along the gas target volume. The effect discussed in Section 7.4 of the previous chapter is therefore not considered in this study.

8.2.1 Vertex resolution parametrisation with the number of tracks

The resolution parametrisation with the number of tracks N_{tr} is done by sorting the vertices per number of tracks used in the reconstruction step.

- For the TRM, the width $\sigma_{r^{\mathrm{TRM}}}$ of the residual distribution for a given N_{tr} is directly equal to the vertex resolution in the case of the TRM:

$$\sigma_{r^{\mathrm{TRM}}} = \sigma_{\mathrm{vtx}}(N_{\mathrm{tr}})\,. \tag{8.5}$$

  In Figure 8.1, the vertex resolution for $N_{\mathrm{tr}} = 7$ equals $147 \pm 8\,\mu\mathrm{m}$.

- For the SVM, with equal number of tracks $N_{\mathrm{tr,split}}$ used for both split vertices, the resolution of both vertices $\sigma_{\mathrm{vtx,split}}(N_{\mathrm{tr,split}})$ is the same and reads:

$$\sigma_{\mathrm{vtx}}(N_{\mathrm{tr,split}}) = \sigma_{r^{\mathrm{SVM}}}/\sqrt{2}\,, \tag{8.6}$$

  as detailed in Section 8.1.

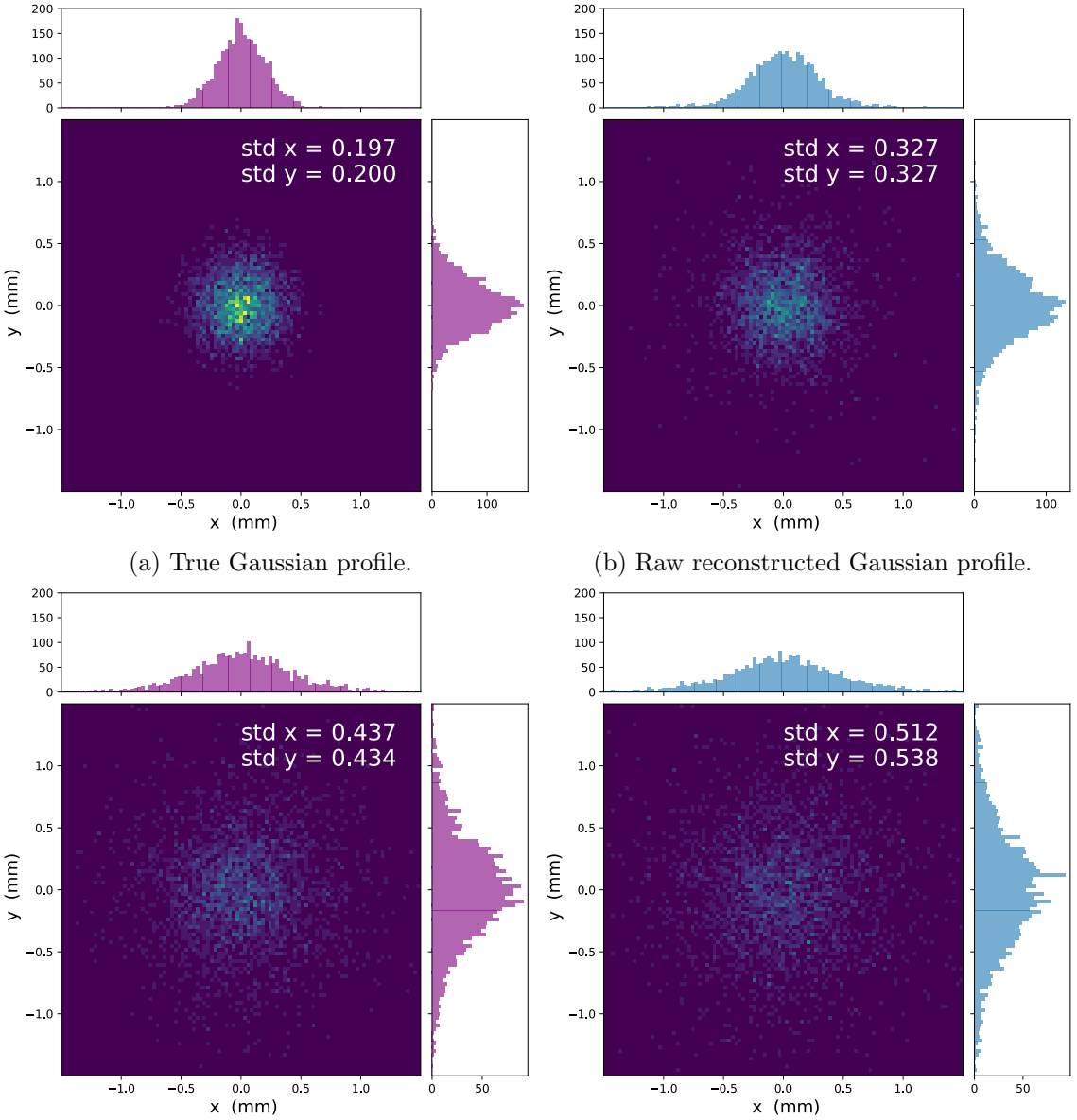

(a) True Gaussian profile.

(b) Raw reconstructed Gaussian profile.

(c) True double Gaussian profile.

(d) Raw reconstructed double Gaussian profile.

Figure 8.4: True (left) and raw reconstructed (right) Gaussian (top) and double-Gaussian (bottom) vertex distributions, before deconvolution of the response function. 2500 vertices are accumulated in each distribution, and the same scales are used for the two Gaussian profiles, generated from data set 1a, and for the two double Gaussian profiles from data set 1b. The standard deviation of each profile is given in white, and is visibly larger on the raw reconstructed profiles (right) compared to the true ones (left).

The SVM method therefore requires primary vertices with $N_{\text{tr}} = 2 \times N_{\text{tr,split}}$ (or $N_{\text{tr}} = 2 \times N_{\text{tr,split}} + 1$) to determine the resolution of vertices with $N_{\text{tr,split}}$. Since events with 4 or 5 primary tracks lead to split vertices with only 2 tracks, the parametrisation with the SVM requires vertices with at least 6 primary tracks. The biased data set 3 was generated for this purpose.

Figure 8.5 shows the N_{tr} parametrisation obtained with both the TRM and SVM, as stated in legend. For each plane $u = \{x, y\}$ of these two cases, data is fitted with a parametrisation curve, with the A, B and C parameters defined as:

$$\sigma_{\mathrm{vtx},u}(N_{\mathrm{tr}}) = \frac{A}{N_{\mathrm{tr}}^{B}} + C\,. \tag{8.7}$$

The obtained fit parameters are summarised in Table 8.1. For both methods, these parameters are very close between the x and y planes, which is expected due to the rotational symmetry of the instrument around the beam axis. Besides, although the SVM parameters are slightly larger than the TRM ones, values are comparable between the two methods, which validates the SVM as potential solution to measure the vertex resolution from experimental data.

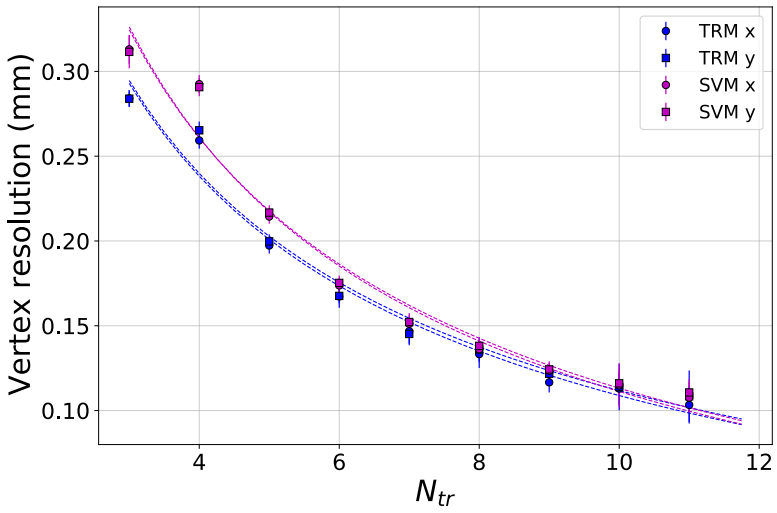

Figure 8.5: Parametrisation of the vertex resolution with the vertex track multiplicity N_{tr}, with events from the entire target z range.

Table 8.1: Vertex resolution parametrisation with N_{tr}, with vertices from the entire measurement region z range.

		A (mm)	B	C (mm)
TRM	x	0.70 ± 0.07	0.5 ± 0.3	-0.11 ± 0.18
	y	0.69 ± 0.07	0.5 ± 0.4	-0.09 ± 0.20
SVM	x	0.81 ± 0.07	0.6 ± 0.4	-0.10 ± 0.20
	y	0.80 ± 0.07	0.5 ± 0.4	-0.10 ± 0.20

The vertex resolution for a vertex reconstructed with N_{tr} tracks can therefore be

estimated using Equation 8.7 and the parameters from Table 8.1, either choosing the TRM or the SVM.

8.2.2 Comparison of the TRM and SVM methods on the entire z range

In the previous section, Figure 8.5 revealed that the vertex resolution is generally overestimated by the SVM, compared to the values obtained with the TRM. The two methods show a better agreement at high N_{tr}.

Figure 8.6a demonstrates how the average vertex resolution of the BGV is impacted by selecting events above a certain N_{tr} threshold. It can be seen that the vertex resolution of 164 µm, required to achieve a beam size measurement accuracy of 5%, is reached when considering all events with $N_{\mathrm{tr}} \geq 5$.

This resolution value was calculated in Section 4.3.2 of Chapter 4, assuming that σ_{vtx} could be known with a relative error smaller than 10%. The absolute relative discrepancy between the TRM and SVM is illustrated, in Figure 8.6b, for each event selection case. It can be seen that by selecting events with at least $N_{\mathrm{tr}} \geq 5$, the two methods agree with a relative error $< 10\%$. This confirms the hypothesis that the SVM method allows to estimate the response function with an uncertainty smaller than 10%.

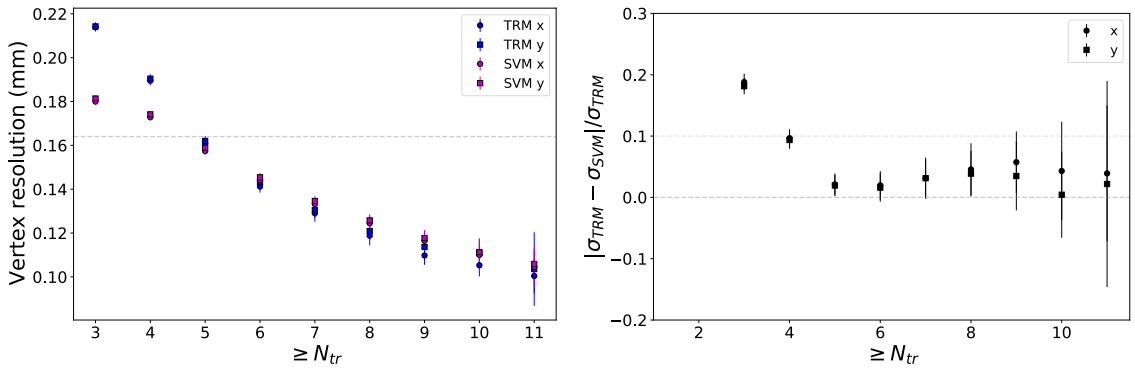

(a) (b)

Figure 8.6: Comparison of the average vertex resolution obtained with the TRM and SVM method, according to the minimum N_{tr} events selected. The resolutions obtained with both methods are shown in (8.6a), and there absolute, relative difference in (8.6b): $\frac{|\sigma_{\mathrm{vtx,TRM}} - \sigma_{\mathrm{vtx,SVM}}|}{\sigma_{\mathrm{vtx,TRM}}}$. Errors in (8.6b) are calculated by propagating vertex resolution errors.

8.2.3 Vertex resolution parametrisation with the longitudinal position

The vertex resolution is then parametrised as a function of the vertex longitudinal position within the 1 m long gas target volume.

For this purpose, the measurement region is longitudinally divided into equal sub-volumes, or *bins*. An example partition into 5 bins is shown in Figure 8.7, which represents the longitudinal vertex distribution for data set 1a. The average number of tracks per event traversing the tracker $N_{\mathrm{tr,av}}$ is indicated on the right scale, for each bin. Events generated in the most upstream bins are more numerous and provide on average more reconstructable tracks.

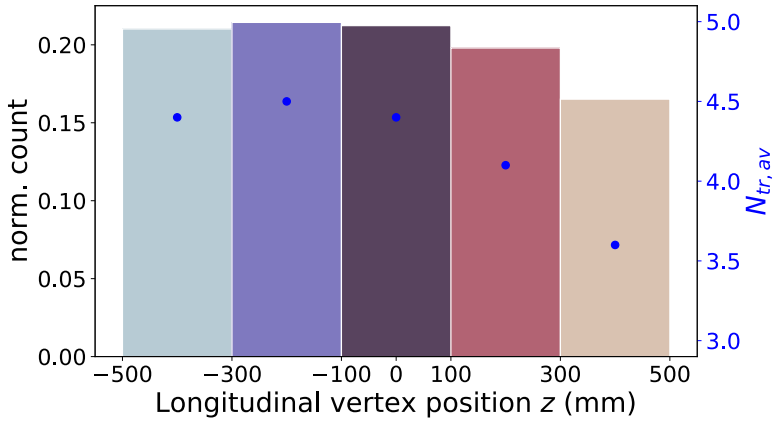

Figure 8.7: Longitudinal distribution of beam-gas interactions from data set 1a, with respect to the centre of the measurement region. The light blue bin is the furthest from the tracking detector and the beige bin is the closest. The average number of tracks per events traversing the detector is also indicated with the blue markers in each bin, referring to the right scale.

The vertex resolution is then parametrised as a function of N_{tr} in each sub-volume, as described in the previous section. Figure 8.8 shows the parametrisation curves obtained with the SVM. The vertex resolution is shown here as a function of both N_{tr} and z, with the two effects disentangled. A specific resolution can be assigned to each reconstructed vertex, depending on its track multiplicity and longitudinal position.

Comparing the curves obtained for the five bins, it is observed that better resolutions are achieved for the bins that are centred or slightly upstream of the centre of the gas target centre (dark purple and purple bins). It was seen in Chapter 5 that tracks from upstream events have higher momenta, whereas those generated closer to the tracking detector benefit from lower extrapolation errors, explaining why central bins show lower vertex resolution curves.

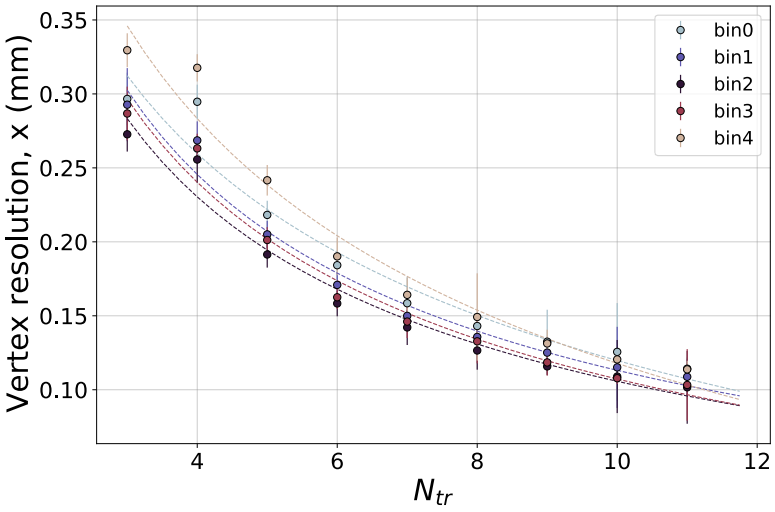

(a) Horizontal vertex resolution (x).

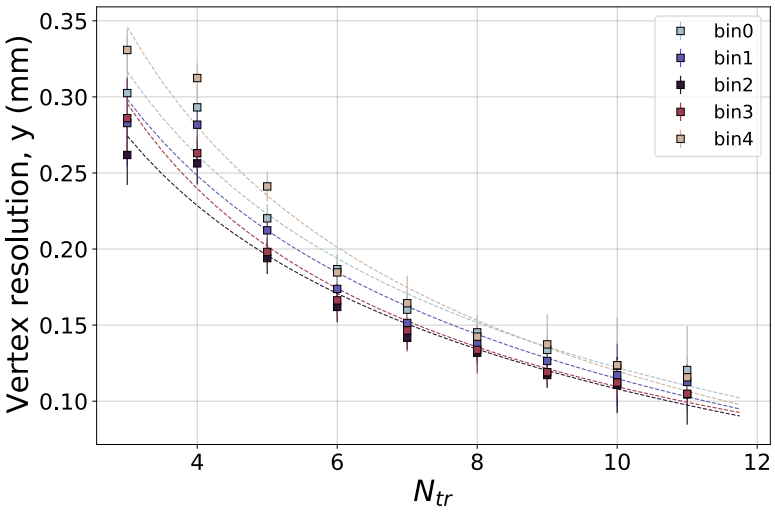

(b) Vertical vertex resolution (y).

Figure 8.8: Vertex resolution parametrisation with N_{tr}, along the measurement region divided into five, 20 cm long bins. The colour scale is identical to the one used in Figure 8.7: bin 0 is the most upstream one, with respect to the beam direction. The horizontal resolution is shown in the top (8.8a) graph, and the vertical one in the bottom (8.8b) one.

8.2.4 Experimental calibration of the vertex resolution

As previously mentioned, the vertex resolution will be experimentally calibrated in an dedicated data accumulation step.

Considering the track multiplicity distributions and event interaction rates presented in Chapter 5, 7 TeV proton beams generate 0.054% of inelastic beam-gas interactions with $N_{\mathrm{tr}} = 16$. The interaction rate is of such events is of 600 Hz and about 1 million are accumulated in 1 h of beam operation, which allows to determine the resolution of

vertices with $N_{\mathrm{tr,split}} = 8$. Considering that, based on Figure 8.7, reconstructed beam-gas interactions are almost homogeneously distributed along the longitudinal spread of the measurement region, one hour of data recording provides around 200 000 vertices with $N_{\mathrm{tr,split}} = 8$ in each bin, for a 5 bins partition. Around one hour of data accumulation with circulating beam at full intensity will therefore be sufficient to calibrate the vertex resolution, even at high track multiplicities.

For ion beams, about 100 000 interactions with $N_{\mathrm{tr}} = 16$ are generated in 1 h, corresponding to 25 000 events per longitudinal bin, if the volume is divided in 5. As expected from the interaction rates and difference in track multiplicities, a ten times longer integration time will be needed to calibrate the vertex resolution of ion beams with the same precision than for proton runs. This corresponds to an entire fill, but can be done parasitically.

8.2.5 Response function

The response function R is defined along each plane $u = \{x, y\}$, and is non-Gaussian, due to the mixture of vertices with different characteristics. However, R can be represented by a sum of K Gaussian functions g_k, each having a width $\sigma_{\mathrm{resp},k}$ and a relative weight c_k, as in Ref. [6, 7]:

$$R(u) = \sum_{k=1}^{K} c_k \, g_k(u; \sigma_{\mathrm{resp},k}) \, . \tag{8.8}$$

The K Gaussian functions are defined as:

$$g_k(u; \sigma) = \frac{1}{\sqrt{2\pi}\,\sigma} \, \exp\Big(- \frac{u^2}{2\,\sigma^2} \Big) \, . \tag{8.9}$$

The sum of the weights c_k is equal to 1. Each Gaussian function g_k corresponds to a group of c_k reconstructed vertices, of average vertex resolution $\sigma_{\mathrm{resp},k} = \langle \sigma_{\mathrm{vtx}} \rangle_k$.

For a given set of vertices, the vertex resolution of each vertex is determined as a function of its characteristics N_{tr} and z, and a response function, as defined in Eq. (8.8), is determined from the vertex resolution distribution. An example of such a distribution is shown in Figure 8.9a.

This distribution is divided into K vertex resolution groups, as indicated in Figure 8.9a, where the vertex resolutions of 2500 reconstructed vertices are split into $K = 4$ groups, separated by the green vertical lines. A Gaussian function g_k is attributed to each group, which contributes to R, as in Eq. (8.8). The relative population of each group k

corresponds to the weight c_k of the Gaussian function, and the Gaussian width $\sigma_{\text{resp},k}$ is given by the average vertex resolution in the group: $\sigma_{\text{resp},k} = \langle \sigma_{\text{vtx}} \rangle_k$. The four Gaussian functions obtained are shown in Figure 8.9b (grey curves), together with the response function (black curve).

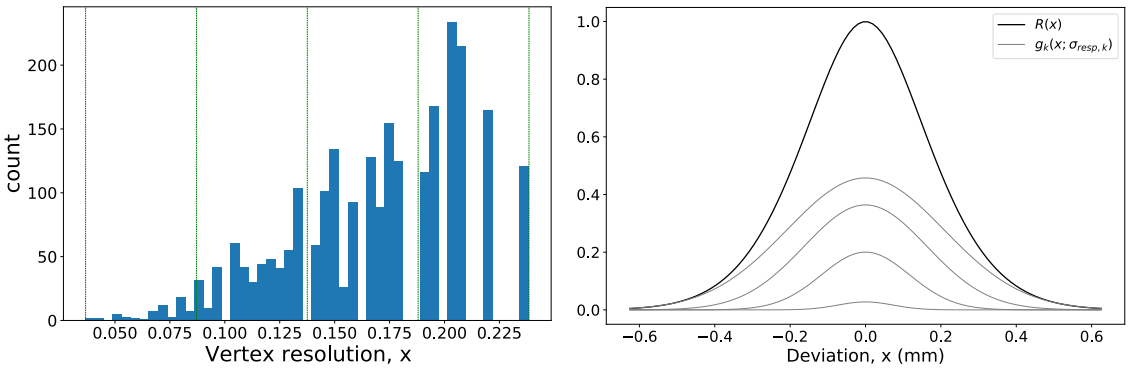

(a) Vertex resolution ($\sigma^{\text{SVM}}_{\text{vtx},x}$) distribution.

(b) Response function.

Figure 8.9: Example horizontal response function determination. The vertex resolution distribution, determined with the SVM, is shown in (8.9a) for a set of 2500 vertices from data set 1a, with $N_{\text{tr}} \geq 5$. This distribution is divided into four groups, separated by the vertical green lines. The corresponding response function is shown in (8.9b), which is the sum (black line) of the four Gaussian functions (grey lines), each associated to a vertex resolution group.

The obtained response functions were shown to be almost unchanged with the number of Gaussian functions used in their model. $K = 4$ is used in the following.

It is also seen from Figure 8.9a that a selection criteria on events with $N_{\text{tr}} \geq 5$ includes vertices with a resolution higher than the targeted value of 164 µm, which was already visible in Figure 8.8. This event selection criteria is kept here for demonstration.

8.3 Beam profile unfolding

Once the response function is known for a set of measured vertices, the beam profile can be unfolded from the raw measured profile.

8.3.1 Beam profile model

Two beam profile shapes were simulated along each transverse plane $u = \{x, y\}$:

- The Gaussian particle distribution, of width σ_{b} modelled in data sets 1a and 2 expresses:

$$\rho(u) = g(u; \mu, \sigma_{\text{b}}) \tag{8.10}$$

- And the double Gaussian distribution (data set 3), consists of the sum of a core and tail Gaussian functions, sharing the same mean μ:

$$\rho(u) = w_{u,c}\ g(u;\mu,\sigma_c) + (1-w_c)\ g(u;\mu,\sigma_t)\,, \tag{8.11}$$

  where w_c represents the weight of the core Gaussian function. The two function have different widths σ_c and σ_t, the narrowest one being the core function. Along each plane, the beam width is determined similarly to the residual distribution width in Section 8.1: $\sigma_\mathrm{b} = \sqrt{f_c\sigma_c^2 + f_t\sigma_t^2}$, with $f_c = \dfrac{w_c\sigma_c}{w_c\sigma_c + (1-w_c)\sigma_t}$ and $f_t = \dfrac{(1-w_c)\sigma_t}{p_c\sigma_c + (1-w_c)\sigma_t}$. With this representation, the tail population of the beam profile can be considered in each plane independently. The analysis is however constrained to symmetrical tail configurations.

8.3.2 Measured and unnfolded profiles

The measured profile is a convolution of the true beam profile $\rho(u)$ with the response function $R(u)$ specific to the sample of vertices:

$$M(u) = \int_{-\infty}^{\infty} R(u)\rho(u-\tau)\mathrm{d}\tau. \tag{8.12}$$

With R and ρ respectively being Gaussian and combination of K Gaussian functions, the measured distribution can be expressed analytically as a combination of Gaussian functions too:

- In the case of a Gaussian beam profile model:

$$M(u) = \sum_{k=1}^{K}\ c_k g(u;\mu,\sigma_k^*), \tag{8.13}$$

  with the width $\sigma_k^* = \sqrt{\sigma_\mathrm{b}^2 + \sigma_{\mathrm{resp},k}^2}$.

- In the case of a double Gaussian beam profile model:

$$M(u) = \sum_{k=1}^{K} c_k\ w_c g_{c,k}(u;\mu,\sigma_{c,k}^*) + c_k\ (1-w_c) g_{t,k}(u;\mu,\sigma_{t,k}^*), \tag{8.14}$$

  with the widths $\sigma_{c,k}^* = \sqrt{\sigma_c^2 + \sigma_{\mathrm{resp},k}^2}$ and $\sigma_{t,k}^* = \sqrt{\sigma_t^2 + \sigma_{\mathrm{resp},k}^2}$.

Once the response function is known, the measured vertex distribution along each plane is fitted with a least square method with the $M(u)$ function corresponding to a Gaussian or double Gaussian model, determining the beam parameters (σ_{b} for a Gaussian profile, σ_{c} and σ_{t} for a double Gaussian profile).

An example is shown in Figure 8.10, where a raw reconstructed vertex distribution (blue histogram), made up of 2500 events from data set 1a, is fitted with Eq. (8.13) (grey line). The grey dash line corresponds to the response function and the black curve, to the unfolded Gaussian profile. In Figure 8.11, this unfolded profile curve is shown on top of the true simulated distribution, where a good agreement is observed. In this figure, the curve and histogram are normalised so that their integral equals 1.

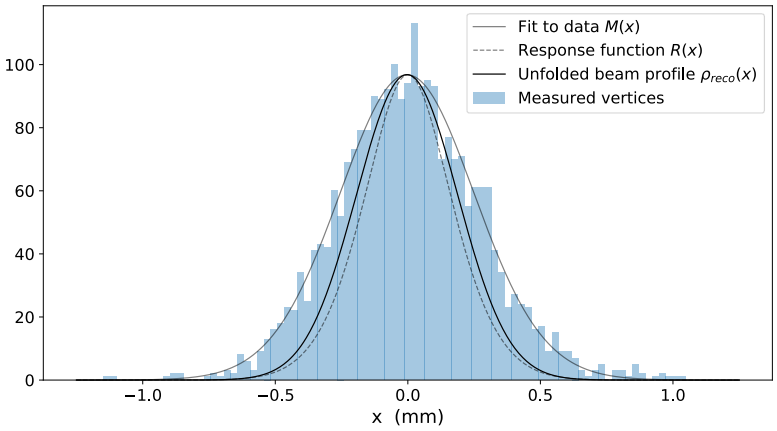

Figure 8.10: Raw reconstructed profile from data set 1a projected along x. The distribution of measured vertices is fitted with M (Eq. (8.13)). The grey dashed curve is response function R, and the black solid curve corresponds to the unfolded profile ρ_{reco}.

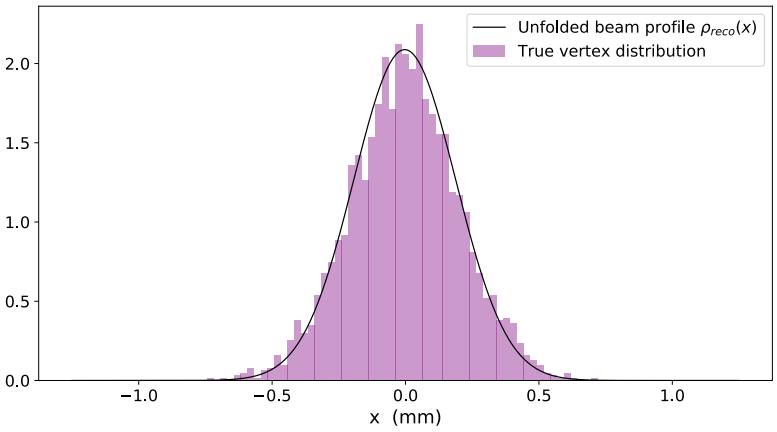

Figure 8.11: True simulated beam-gas vertex distribution (pink) and unfolded profile (black curve), from data set 1a projected along x.

8.4 Performance

The performance of the proposed HL-BGV design at reconstructing the beam size and profile is studied with a data set of 1000 profiles, built upon randomly selected vertices with $N_{\mathrm{tr}} \geq 5$, from data sets 2, 1a and 1b, with both SVM and TRM methods. TRM was solely used with data set 2, on account of the lack of a simulated data set with high track multiplicities at low beam energy. In this second case, all events with $N_{\mathrm{tr}} \geq 3$ are considered, as discussed in Section 4.3.2 of Chapter 4.

It was seen in Chapter 4 that the beam size accuracy, or systematic error, $\frac{\delta\sigma_{\mathrm{b}}}{\sigma_{\mathrm{b}}}$ is related to the vertex resolution σ_{vtx} and to its uncertainty $\delta\sigma_{\mathrm{vtx}}$ as follows:

$$\frac{\delta\sigma_{\mathrm{b}}}{\sigma_{\mathrm{b}}} = \frac{\sigma_{\mathrm{vtx}}^2}{\sigma_{\mathrm{b}}^2} \frac{\delta\sigma_{\mathrm{vtx}}}{\sigma_{\mathrm{vtx}}} \,. \tag{8.15}$$

The measurement precision, or statistical error, is noted here $\frac{\Delta\sigma_{\mathrm{b}}}{\sigma_{\mathrm{b}}}$ and depends on the amount of events accumulated in each beam size measurement.

For each reconstructed profile, the unfolded beam width $\sigma_{\mathrm{b,reco}}$ is compared to the true simulated one σ_{b} (obtained with fitting $\rho(u)$ from Equation (8.10) or (8.11), on the true simulated profile). The relative residual distribution for 1000 profiles generated with 2500 events each, from data set 1a, is shown in Figure 8.12, for both vertex resolution determination methods.

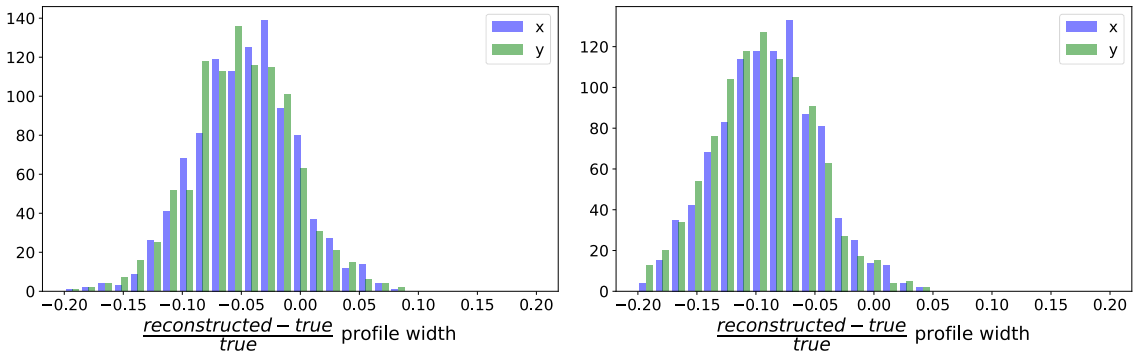

(a) TRM. (b) SVM.

Figure 8.12: Relative residual distributions between the unfolded and true simulated beam sizes, for Gaussian beam profiles generated with 7 TeV protons. The TRM is used in (8.12a) and the SVM one in (8.12b). Only events with $N_{\mathrm{tr}} \geq 5$ are considered.

The mean and standard deviation of the obtained residuals respectively provide an estimate of the beam size measurement accuracy and precision. For each tested data

Table 8.2: Beam size accuracy and precision, assessed for 1000 simulated Gaussian profiles with 2500 events each.

		450 GeV (Data set 2)		7 TeV (Data set 1a)	
		accuracy	precision	accuracy	precision
TRM	x	1.5 %	3.1 %	-4.4 %	4.1 %
	y	2.4 %	3.0 %	-4.8 %	4.0 %
SVM	x	-	-	-8.7 %	4.2 %
	y	-	-	-9.4 %	4.2 %

set, these results are summarised in Table 8.2 for Gaussian profiles. The uncertainties correspond to the errors on the fit parameters provided by the last fitting step.

8.4.1 Accuracy

This section discusses the level accuracy reached with simulated data, and mentions potential sources of systematic errors, together with mitigation solutions.

For 7 TeV Gaussian beam profiles, an accuracy better than 5% is reached with the TRM, which satisfies the specification set out in Chapter 4. With the SVM, the vertex resolution is generally overestimated compared to the TRM, leading to narrower unfolded profiles. Figure 8.12b shows that with the SVM, the beam size is almost systematically underestimated, with an average underestimate of 9%.

It is noted that, with a simulated profile width of 200 µm, the considered data leads to slightly larger $\frac{\delta\sigma_\mathrm{b}}{\sigma_\mathrm{b}}$ than would be reached with the beams expected to be encountered by the HL-BGVs ($\geq$ 232 µm), according to Equation (8.15). Nevertheless, 9% is far greater than the specification. A calibration of the SVM method with simulations shall be performed to quantify the discrepancy between these methods, and compensate the systematic beam width error.

At injection energy, the systematic error is the order of 2% with the TRM, as shown in Table 8.2 and Figure 8.13, where the above described method is applied to the 800 µm wide proton beam of data set 2.

When experimental data will be used, the accuracy may be degraded by detector misalignment. In order to exploit the full potential of TimePix4 detectors, the spatial resolution of which is in the order of 10 µm, their position, orientation and deformation should be known to a similar precision level. A mechanical alignment to a few hundreds of microns can be achieved at installation, which will be further improved by software

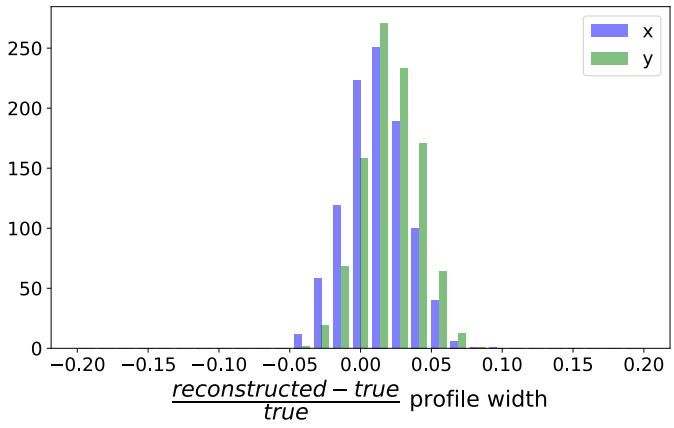

Figure 8.13: Relative residual distribution between the unfolded and true simulated beam sizes, for Gaussian beam profiles generated with 450 GeV protons. These results are obtained with the TRM method, due to the lack of 450 GeV events with high N_{tr} to perform the SVM calibration.

alignment methods, to be run regularly in operation. More details can be found in Ref. [2].

The vertex resolution determination (and therefore the response function and beam width accuracy) could be improved by considering the χ^2 of the track fit: e.g. by assigning weights to each vertex, according to the average χ^2 of its reconstructed tracks. The response function would be determined by considering a weighted vertex resolution distribution, and the beam profile unfolded as presented. An event or track selection based on the track quality could also be implemented, but at the cost of a degraded measurement precision.

A simple way to improve the measurement accuracy of a given measured data set is to restrict the event selection to those with higher track multiplicities: considering events with $N_{\mathrm{tr}} \geq 6$ instead of $N_{\mathrm{tr}} \geq 5$ leads to a beam width accuracy of 2% with the TRM and better than 5% with the SVM, for 7 TeV Gaussian beams. The precision would however be degraded, since 13% of beam-gas interactions generate $N_{\mathrm{tr}} \geq 5$, whereas 7% have $N_{\mathrm{tr}} \geq 6$ at collision energy. Alternatively, increasing the integration time per profile would prevent deteriorating their precision, although reducing the measurement rate.

8.4.2 Precision

A bunch width precision of about 4% is reached with both TRM and SVM methods at 7 TeV, for profiles including 2500 vertices, corresponding to a bunch-by-bunch integration time of about 1 min 45 sec. At injection energy, the statistical error on the bunch width is close to 3% with the TRM. The dependence of the precision on the number of events

within a measured profile is shown in Figure 8.14, reproducing the expected behaviour $\frac{\Delta\sigma_\mathrm{b}}{\sigma_\mathrm{b}} \propto 1/\sqrt{2N_\mathrm{tr}-2}$ discussed in Section 4.3.3 of Chapter 4.

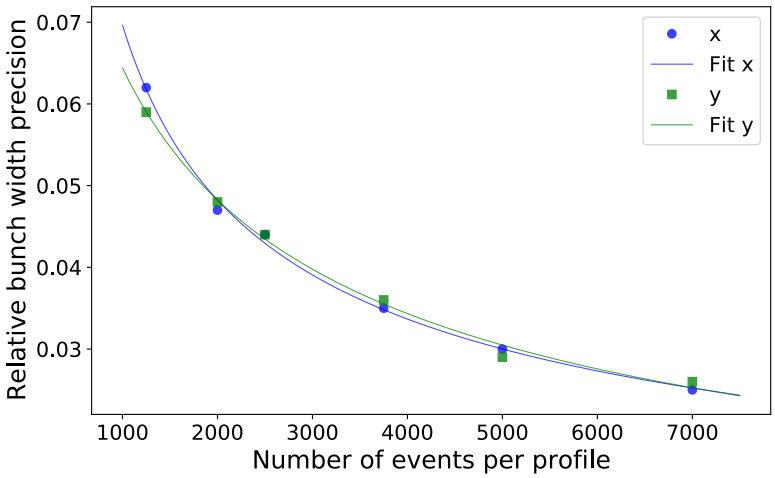

Figure 8.14: Relative beam width measurement precision (obtained with the SVM) as a function of the number of vertices per reconstructed profile, using data set 1a (7 TeV). The precision proportionality to $1/\sqrt{N_\mathrm{events}}$ is verified.

The expected bunch-by-bunch precision in 1 min accumulation time is higher than required by the specifications. To achieve the requested precision of 1%, a longer integration time, in the order of 2 min 30 sec will be needed, or a gas target pressure increase of 1×10^{-7} mbar.

The precision could also be improved by design changes, for instance by enlarging the tracker acceptance or using a different gas species to increase rate of useful event generation with increasing the average track multiplicity per detected event and/or the beam-gas interaction cross-section.

8.4.3 Beam profile reconstruction

The ability of the instrument to reconstruct beam profiles differing from a single Gaussian shape is tested with data set 1b. An example double Gaussian profile made of 2500 events is shown in Figure 8.15, where the initial distribution is shown to be well reproduced by the unfolded profile.

For 50 reconstructed profiles containing 2500 events each, the χ^2 value between the normalised unfolded profile and true simulated event distribution is calculated, and divided by the number of degrees of freedom (equal to the difference between the number of compared values and the number of fit parameters). Along both x and y planes, a mean

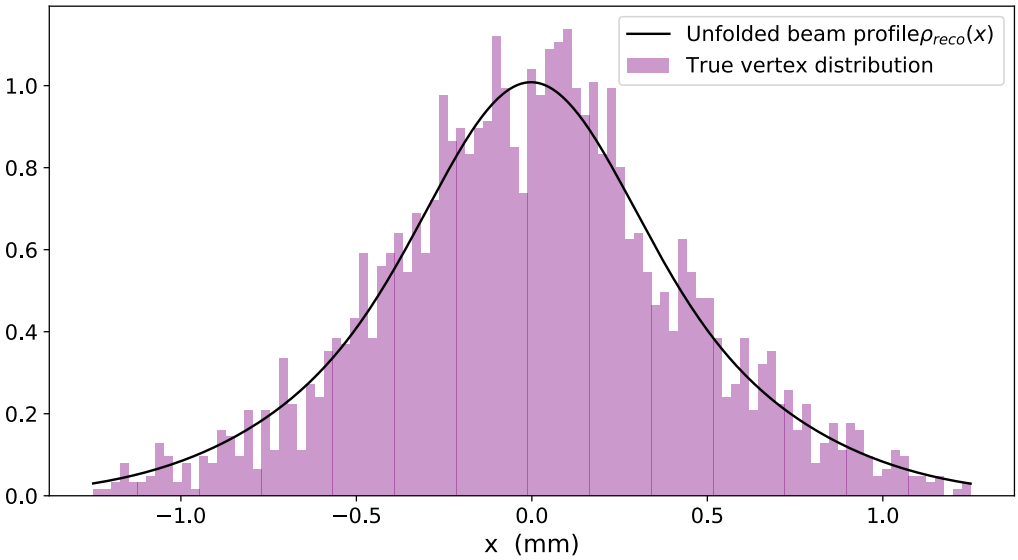

Figure 8.15: True simulated beam-gas vertex distribution (pink) and unfolded profile (black curve), from data set 1b projected along x.

reduced χ^2 of 1.5 is obtained for both TRM and SVM vertex resolution determination methods, with a standard deviation of 0.4. This result is very close to 1, showing a very good agreement between unfolded and true simulated beam particle distributions, for both SVM and TRM methods.

This concentric double Gaussian model allows to study beam profiles with symmetrical tails. Other models could be used, provided that their convolution with the response function has an analytical expression. Offline analyses of beam profile measurements performed by the BGV could then allow to compare various beam models and determine which one fits best to experimental non-Gaussian profile cases by comparing for instance the obtained χ^2 between $M(u)$ and the raw measured profile (as in Figure 8.10). With such a feature, tracking the beam profile evolution along the ramp could help to understand potential mechanisms of emittance blow-up.

It is noted that detectors misalignment and transverse gas target in-homogeneity would degrade the systematic error of both beam size and beam profile measurements.

8.5 Summary and outlook

The method presented in this chapter allows to unfold the absolute width of Gaussian and double Gaussian beam profiles from the distribution of measured vertices. The resolution

of each vertex is determined according to its characteristics (track multiplicity and longitudinal position), and the response function of the instrument is modelled with a sum of concentric Gaussian functions.

Regarding Gaussian profiles, by selecting events with $N_{\mathrm{tr}} \geq 5$, a beam size accuracy of 5% is reached for the most demanding beam types, when the vertex resolution is assessed using the true vertex position information. This number matches exactly the instrument specification, without leaving room for potential degradation of the beam accuracy with the implementation of the instrument (eg. due to detectors misalignment). The systematic error could be reduced to meet the specifications, with a more restrictive event selection, which would lower the measurement precision, or increase the integration time.

The $N_{\mathrm{tr}} \geq 5$ selection leads to a precision of 3% at injection and of 4% at collision energy, for an accumulation time of 1 min 45 sec.

The SVM data-driven method allows to determine the vertex resolution independent of the true simulated vertex position information. Nonetheless, this method introduces a systematic error which should be compensated with a correction factor determined from simulations.

The possibility to reconstruct double Gaussian beam profiles with symmetrical tails was demonstrated. This unfolded method could be used with more complex beam models, provided that their convolution with the instrument response function has an analytical expression.

Chapter 9

Outlook and conclusion

By the end of LHC Run 2 the demonstrator BGV was able to provide an absolute beam size measurement throughout the LHC energy cycle, which was independent of the beam intensity. A new design is proposed for the HL-BGV, additionally intended to measure the beam profile via beam-gas interaction vertices reconstruction. The future instrument is expected to be maintained in the long term by a small number of people and its design was made to ensure a reliable operation, with low risks of beam operation interruption due to instrument failure.

The overall HL-BGV design was guided by detailed Monte Carlo simulations and event reconstruction algorithms, which helped to shape the tracker, select gas target and detector technologies and determine the expected performance of the final configuration.

The HL-BGV tracker design is completely new, compact and based on silicon hybrid pixel detectors. The track reconstruction performance is improved by a high spatial resolution of the detectors, and by the pixel readout.

The distributed gas target technology is kept unchanged compared to the demonstrator, since its operation was successful. Its gas density map was carefully assessed, and the shape of the tank and pump positions were optimised to provide a homogeneous measurement volume, and a sharp pressure decrease outside of this region. The integrated pressure of the measurement region determines the beam size precision. The impact of the BGV target on beam operation was assessed, with negligible effects on the beam lifetime and emittance growth, when considering few hours of instrument operation per fill. The installation locations were carefully chosen, in order to prevent radiation spreading towards sensitive equipment. The HL-BGVs will still generate significant radiation levels,

and mitigation solutions shall be envisioned for the remaining devices downstream of the B1-BGV.

The tank dimensions were optimised to reduce its wakefield contributions, which were brought to negligible levels. This is a significant improvement with respect to the demonstrator device. With an optimised material budget, the exit window limits the amount of material crossed by secondary particles before reaching the tracking detector. The tracker acceptance is finally improved compared to the demonstrator instrument, thanks to a lower aperture section, placing the detector closer to the beam axis, where the track density is high.

A beam profile unfolding method is proposed, with a parametrisation of the vertex resolution as a function of the vertex longitudinal position and of the multiplicity of the tracks used to reconstruct the position of each vertex.

The expected performance of this instrument are the following:

- For Gaussian beams, a simulated beam size accuracy of about 2% is reached at injection energy, and better than 5% at collision energy, for the B2-BGV, which device will encounter narrower beams. A correction factor determined from simulations should be applied to the obtained measurements, to compensate for the systematic error introduced by the SVM data-driven method allowing for an independent beam size and profile measurement. The measurement accuracy of the final instrument can be improved with restricting the event selection to those with higher track multiplicities, to the cost of a degraded precision, or increased integration time.

- A bunch-by-bunch measurement precision of 3% at injection and 4% at collision energy is expected for an integration time of 1 min 45 sec for this same instrument. A precision of 1% could be reached with accumulating events during 2.5 min, or with increasing the gas pressure, to the cost of higher radiation levels.

- The capability of this device to reconstruct a double Gaussian beam profile was successfully demonstrated. Further investigations of the proposed method may allow to reconstruct more refined beam profile models.

In summary, the LHC machine would benefit from the HL-BGV with an absolute beam size and beam profile measurement all along the energy cycle. The required accuracy can be reached in an integration time of few minutes for bunch-by-bunch measurements. During the ramp in particular, bunch-by-bunch beam size measurements would allow

to study emittance growth mechanisms beyond existing models. Bunch-by-bunch beam profile measurement would also benefit to study effects that are highly sensitive to tails population, like electron clouds and beam-beam effects.

Measurements with ion beams would require longer integration times to reach the same precision relative to proton beams, and the vertex resolution calibration step would require an entire fill of data accumulation. In contrast, a good measurement accuracy is expected relative to proton beams, thanks to higher track multiplicities per ion-gas collision.

Appendix A

Error propagation on the emittance

Based on Equation (2.8), the error on the beam size σ_b expresses as a function of the emittance ε and local β-function β, following:

$$\Delta\sigma_\mathrm{b}^2 = \Big(\frac{\partial\sigma_\mathrm{b}}{\partial\beta}\Big)^2\Delta\beta^2 + \Big(\frac{\partial\sigma_\mathrm{b}}{\partial\varepsilon}\Big)^2\Delta\varepsilon^2\,, \tag{A.1}$$

with

$$\frac{\partial\sigma_\mathrm{b}}{\partial\beta} = \frac{1}{2}\,\varepsilon^{1/2}\,\beta^{-1/2}\,, \tag{A.2}$$

and

$$\frac{\partial\sigma_\mathrm{b}}{\partial\varepsilon} = \frac{1}{2}\,\varepsilon^{-1/2}\,\beta^{1/2}\,. \tag{A.3}$$

With replacing (A.2) and (A.3) in (A.4), one retrieves:

$$\Big(\frac{\Delta\sigma_\mathrm{b}}{\sigma_\mathrm{b}}\Big)^2 = \frac{1}{4\,\beta}\,\varepsilon\,\frac{\Delta\beta^2}{\beta\varepsilon} + \frac{1}{4\,\varepsilon}\,\beta\,\frac{\Delta\varepsilon^2}{\beta\varepsilon}\,, \tag{A.4}$$

and then:

$$\Big(\frac{\Delta\sigma_\mathrm{b}}{\sigma_\mathrm{b}}\Big)^2 = \frac{1}{4}\Big[\Big(\frac{\Delta\beta}{\beta}\Big)^2 + \frac{\Delta\varepsilon}{\varepsilon}\Big)^2\Big]\,. \tag{A.5}$$

Appendix B

Demonstrator BGV pressure data

B.1 Pressure gauge

Data recorded by the vacuum gauge installed along the tank of the demonstrator witnesses a quick rise and drop of the pressure inside the BGV tank when the gas injection system was successively turned ON and OFF, as shown in Figure B.1. This specific data set shows the pressure change in a fill during which the BGV acquired data for beam size measurement [8]. The pressure values on this record should be multiplied by a factor 4 in order to read the neon pressure. This factor comes from the fact that the gauge calibration was done with nitrogen. A comparison of the gauge sensitivity for different gas species is shown in Figure B.2.

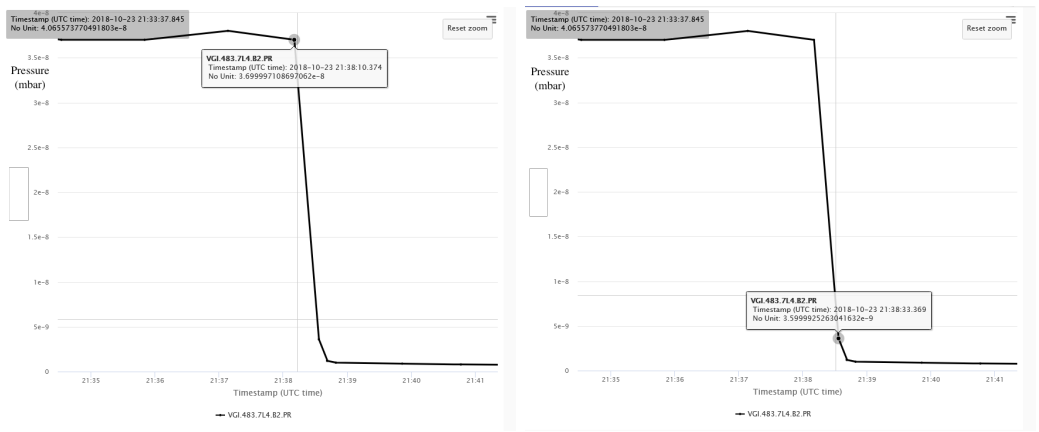

Figure B.1: Pressure data recorded by the demonstrator BGV pressure gauge in Fill 7334, on 23/10/2018, before and after the switch OFF of the gas injection system. Visualisation is done with the Timber application, accessing data from the CERN Accelerator Logging Service.

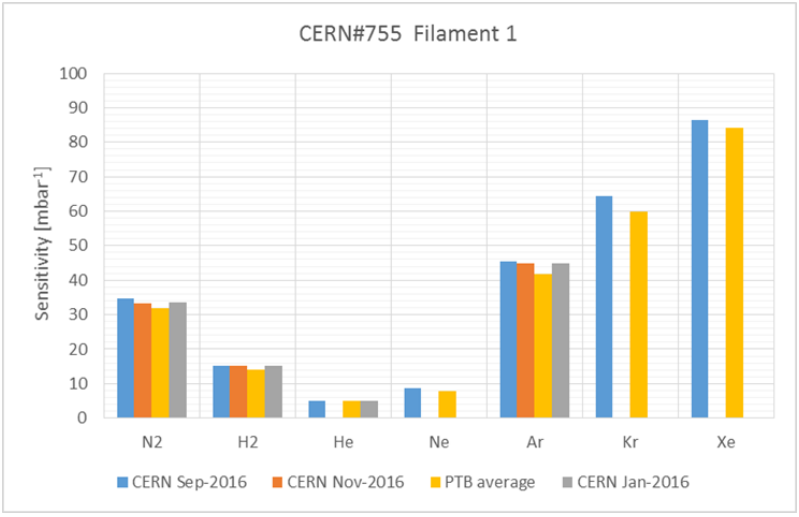

Figure B.2: Sensitivity calibration of a pressure gauge of the same model than the one used on the demonstrator BGV tank, for different gas species. *Courtesy R. Kersevan*

Appendix C

Upstream taper length impact on longitudinal impedance

In the following, the impact of the length of an upstream taper on the longitudinal impedance of a cavity is studied. The considered structure is a similar cavity than in Chapter 6, where the downstream end is already tapered over a length of 10 m. The evolution of the real longitudinal impedance with tapering the upstream tank extremity is shown in Figure C.1, and with adding an upstream taper in Figure C.2. The impact on the longitudinal effective impedance in these two cases is shown in Figure C.3.

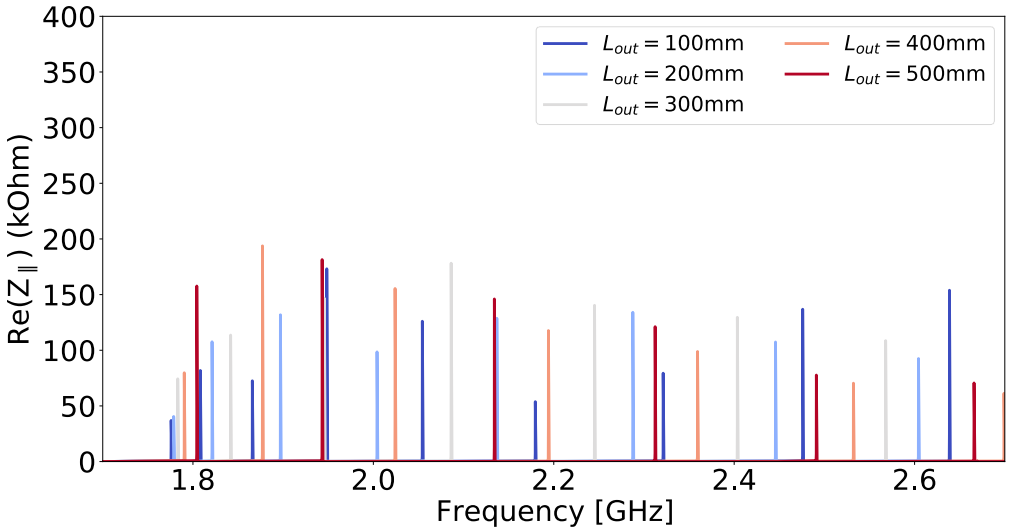

Figure C.1: Simulated real part of the longitudinal impedance of a PEC BGV gas tank with $L = 700\,\text{mm}$, $D = 130\,\text{mm}$ and $L_{\text{out}} = 10\,\text{mm}$, tapering the upstream tank extremity.

Compared to the case of the exit window (EW), the resonant modes a have much

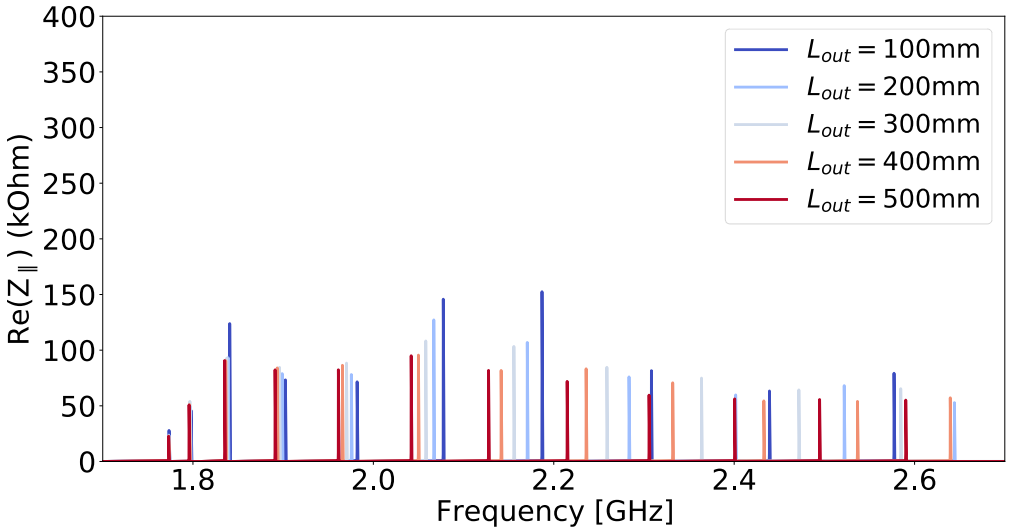

Figure C.2: Simulated real part of the longitudinal impedance of a PEC BGV gas tank with $L = 700\,\text{mm}$, $D = 130\,\text{mm}$ and $L_{\text{out}} = 10\,\text{mm}$, adding a taper volume at the upstream tank extremity.

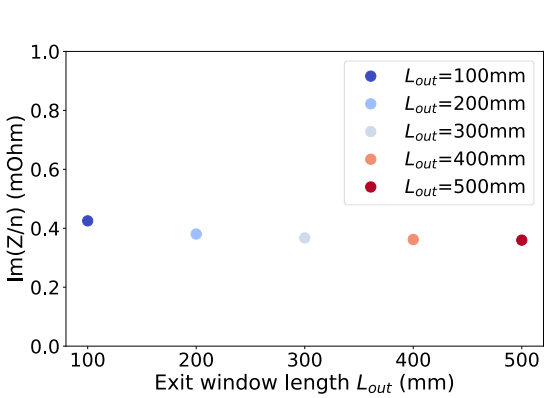

(a) Adding an upstream taper of length L_{in}.

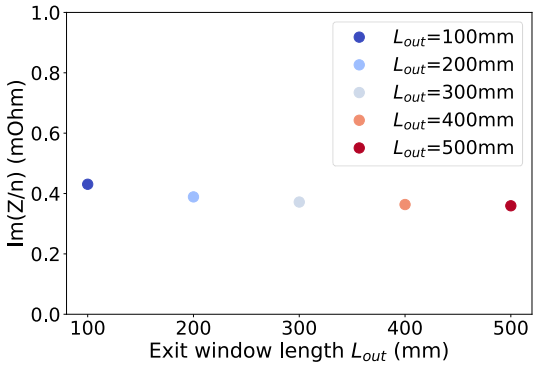

(b) Tapering the upstream end of the cavity by L_{in}.

Figure C.3: Longitudinal effective impedance evolution with L_{in}, with adding an upstream taper (C.3a) and with tapering the upstream end of the cavity (C.3b).

lower shunt impedance, thanks to the already tapered downstream extremity. The same conclusions than with tapering or adding a taper on the downstream end apply when considering the length of the upstream taper.

Appendix D

Main eigenmode parameters and resonant frequency of the final BGV gas tank

The simulated parameters and resonant frequency of the final HL-BGV vacuum tank main longitudinal eigenmodes are reported in Table D.1.

Table D.1: Simulated parameters and resonant frequency of the main longitudinal eigenmodes of the final HL-BGV setup.

Mode ID	Resonant frequency (GHz)	Shunt impedance (Ω)	Q factor
1	1.773	2900	5796
2	1.796	7000	5843
3	1.836	12 900	5869
4	1.892	12 800	5938
5	1.963	13 300	5977
6	2.044	15 500	6041
7	2.131	14 500	6039
8	2.219	13 700	5972

Appendix E

Interaction of higher mass gas (Ar, Xe) with ion (Pb) beams

Similarly to the study that was made for proton ions, the impact of using argon and xenon gas instead of neon on the BGV performance with ion beams was studied [2], and the main results are reported in Table E.1.

	Inelastic interaction rate per bunch	Average N_{tr} in tracker acceptance	Average track momentum
Neon ($A_{\mathrm{Ne}} = 20$)	1.5 Hz	21	6.3 GeV/c
Argon ($A_{\mathrm{Ar}} = 40$)	1.8 Hz	29	6.2 GeV/c
Xenon ($A_{\mathrm{Xe}} = 132$)	2.5 Hz	32	5.9 GeV/c

Table E.1: Comparison of beam-gas inelastic cross-sections and interaction rates for 7 Z TeV ion bunches on a 1 m-long target of neon, argon and xenon, at an average pressure of 1×10^{-7} mbar.

The same conclusions than with varying the gas species with proton beams are valid for lead ion beams: beam-gas interactions generate in average more tracks in the tracker acceptance, but the momentum of these tracks is lower in average.

Bibliography

[1] A. Alexopoulos, C. Barschel, E. Bravin, G. Bregliozzi, N. Chritin, B. Dehning, M. Ferro-Luzzi, M. Giovannozzi, R. Jacobsson, L. Jensen, R. Jones, V. Kain, R. Kieffer, R. Matev, M. Rihl, V. S. Guimaraes, R. Veness, S. Vlachos, B. Würkner, A. Bay, F. Blanc, S. Giani, O. Girard, G. Haefeli, P. Hopchev, A. Kuonen, T. Nakada, O. Schneider, M. Tobin, Z. Xu, R. Greim, T. Kirn, S. Schael, M. Wlochal, Non-invasive LHC transverse beam size measurement using inelastic beam-gas interactions, Physical Review Accelerators and Beams 22 (4) (2019) 042801. doi:10.1103/PhysRevAccelBeams.22.042801.
URL https://doi.org/10.1103/PhysRevAccelBeams.22.042801https://link.aps.org/doi/10.1103/PhysRevAccelBeams.22.042801

[2] H. Guerin and D. Hynds and B. Kolginger and T. D. Prelipcean and Ramos Garcia and J. Storey, Design Report of the HL-LHC Beam Gas Vertex (BGV) Monitor, Tech. rep., CERN, Geneva (2023).
URL https://edms.cern.ch/document/2823013/1

[3] O. S. Bruning, P. Collier, P. Lebrun, S. Myers, R. Ostojic, J. Poole, P. Proudlock, LHC Design Report, CERN Yellow Reports: Monographs, CERN, Geneva, 2004.
URL http://cds.cern.ch/record/782076

[4] O. Aberle, I. Béjar Alonso, O. Brüning, P. Fessia, L. Rossi, L. Tavian, M. Zerlauth, C. Adorisio, A. Adraktas, M. Ady, J. Albertone, L. Alberty, M. Alcaide Leon, A. Alekou, D. Alesini, B. A. Ferreira, P. A. Lopez, G. Ambrosio, P. Andreu Munoz, M. Anerella, D. Angal-Kalinin, F. Antoniou, G. Apollinari, A. Apollonio, R. Appleby, G. Arduini, B. A. Alonso, K. Artoos, S. Atieh, B. Auchmann, V. Badin,

T. Baer, D. Baffari, V. Baglin, M. Bajko, A. Ball, A. Ballarino, S. Bally, T. Bampton, D. Banfi, R. Barlow, M. Barnes, J. Barranco, L. Barthelemy, W. Bartmann, H. Bartosik, E. Barzi, M. Battistin, P. Baudrenghien, I. B. Alonso, S. Belomestnykh, A. Benoit, I. Ben-Zvi, A. Bertarelli, S. Bertolasi, C. Bertone, B. Bertran, P. Bestmann, N. Biancacci, A. Bignami, N. Bliss, C. Boccard, Y. Body, J. Borburgh, B. Bordini, F. Borralho, R. Bossert, L. Bottura, A. Boucherie, R. Bozzi, C. Bracco, E. Bravin, G. Bregliozzi, D. Brett, A. Broche, K. Brodzinski, F. Broggi, R. Bruce, M. Brugger, O. Brüning, X. Buffat, H. Burkhardt, J. Burnet, A. Burov, G. Burt, R. Cabezas, Y. Cai, R. Calaga, S. Calatroni, O. Capatina, T. Capelli, P. Cardon, E. Carlier, F. Carra, A. Carvalho, L. Carver, F. Caspers, G. Cattenoz, F. Cerutti, A. Chancé, M. C. Rodrigues, S. Chemli, D. Cheng, P. Chiggiato, G. Chlachidze, S. Claudet, J. Coello De Portugal, C. Collazos, J. Corso, S. Costa Machado, P. Costa Pinto, E. Coulinge, M. Crouch, P. Cruikshank, E. Cruz Alaniz, M. Czech, K. Dahlerup-Petersen, B. Dalena, G. Daniluk, S. Danzeca, H. Day, J. De Carvalho Saraiva, D. De Luca, R. De Maria, G. De Rijk, S. De Silva, B. Dehning, J. Delayen, Q. Deliege, B. Delille, F. Delsaux, R. Denz, A. Devred, A. Dexter, B. Di Girolamo, D. Dietderich, J. Dilly, A. Doherty, N. Dos Santos, A. Drago, D.Drskovic, D. D. Ramos, L. Ducimetière, I. Efthymiopoulos, K. Einsweiler, L. Esposito, J. Esteban Muller, S. Evrard, P. Fabbricatore, S. Farinon, S. Fartoukh, A. Faus-Golfe, G. Favre, H. Felice, B. Feral, G. Ferlin, P. Ferracin, A. Ferrari, L. Ferreira, P. Fessia, L. Ficcadenti, S. Fiotakis, L. Fiscarelli, M. Fitterer, J. Fleiter, G. Foffano, E. Fol, R. Folch, K. Foraz, A. Foussat, M. Frankl, O. Frasciello, M. Fraser, P. F. Menendez, J.-F. Fuchs, S. Furuseth, A. Gaddi, M. Gallilee, A. Gallo, R. G. Alia, H. G. Gavela, J. G. Matos, H. Garcia Morales, A. G.-T. Valdivieso, C. Garino, C. Garion, J. Gascon, C. Gasnier, L. Gentini, C. Gentsos, A. Ghosh, L. Giacomel, K. G. Hernandez, S. Gibson, C. Ginburg, F. Giordano, M. Giovannozzi, B. Goddard, P. Gomes, M. Gonzalez De La Aleja Cabana, P. Goudket, E. Gousiou, P. Gradassi, A. G. Costa, L. Grand-Clément, S. Grillot, J. Guillaume, M. Guinchard, P. Hagen, T. Hakulinen, B. Hall, J. Hansen, N. Heredia Garcia, W. Herr, A. Herty, C. Hill, M. Hofer, W. Höfle, B. Holzer, S. Hopkins, J. Hrivnak, G. Iadarola, A. Infantino, S. I. Bermudez, S. Jakobsen, M. Jebramcik, B. Jenninger, E. Jensen, M. Jones, R. Jones, T. Jones, J. Jowett, M. Juchno, C. Julie, T. Junginger, V. Kain, D. Kaltchev, N. Karastathis, P. Kardasopoulos, M. Karppinen, J. Keintzel, R. Ker-

sevan, F. Killing, G. Kirby, M. Korostelev, N. Kos, S. Kostoglou, I. Kozsar, A. Krasnov, S. Krave, L. Krzempek, N. Kuder, A. Kurtulus, R. Kwee-Hinzmann, F. Lackner, M. Lamont, A. Lamure, L. L. m, M. Lazzaroni, M. Le Garrec, A. Lechner, T. Lefevre, R. Leuxe, K. Li, Z. Li, R. Lindner, B. Lindstrom, C. Lingwood, C. Löffler, C. Lopez, L. Lopez-Hernandez, R. Losito, F. Maciariello, P. Macintosh, E. Maclean, A. Macpherson, P. Maesen, C. Magnier, H. M. Durand, L. Malina, M. Manfredi, F. Marcellini, M. Marchevsky, S. Maridor, G. Marinaro, K. Marinov, T. Markiewicz, A. Marsili, P. Martinez Urioz, M. Martino, A. Masi, T. Mastoridis, P. Mattelaer, A. May, J. Mazet, S. Mcilwraith, E. McIntosh, L. Medina Medrano, A. Mejica Rodriguez, M. Mendes, P. Menendez, M. Mensi, A. Mereghetti, D. Mergelkuhl, T. Mertens, L. Mether, E. Métral, M. Migliorati, A. Milanese, P. Minginette, D. Missiaen, T. Mitsuhashi, M. Modena, N. Mokhov, J. Molson, E. Monneret, E. Montesinos, R. Moron-Ballester, M. Morrone, A. Mostacci, N. Mounet, P. Moyret, P. Muffat, B. Muratori, Y. Muttoni, T. Nakamoto, M. Navarro-Tapia, H. Neupert, L. Nevay, T. Nicol, E. Nilsson, P. Ninin, A. Nobrega, C. Noels, E. Nolan, Y. Nosochkov, F. Nuiry, L. Oberli, T. Ogitsu, K. Ohmi, O. R., J. Oliveira, P. Orlandi, P. Ortega, J. Osborne, T. Otto, L. Palumbo, S. Papadopoulou, Y. Papaphilippou, K. Paraschou, C. Parente, S. Paret, H. Park, V. Parma, C. Pasquino, A. Patapenka, L. Patnaik, S. Pattalwar, J. Payet, G. Pechaud, D. Pellegrini, P. Pepinster, J. Perez, J. P. Espinos, A. P. Marcone, A. Perin, P. Perini, T. Persson, T. Peterson, T. Pieloni, G. Pigny, J. Pinheiro de Sousa, O. Pirotte, F. Plassard, M. Pojer, L. Pontercorvo, A. Poyet, D. Prelipcean, H. Prin, R. Principe, T. Pugnat, J. Qiang, E. Quaranta, H. Rafique, I. Rakhno, D. R. Duarte, A. Ratti, E. Ravaioli, M. Raymond, S. Redaelli, T. Renaglia, D. Ricci, G. Riddone, J. Rifflet, E. Rigutto, T. Rijoff, R. Rinaldesi, O. Riu Martinez, L. Rivkin, F. Rodriguez Mateos, S. Roesler, I. Romera Ramirez, A. Rossi, L. Rossi, V. Rude, G. Rumolo, J. Rutkovksi, M. Sabate Gilarte, G. Sabbi, T. Sahner, R. Salemme, B. Salvant, F. S. Galan, A. Santamaria Garcia, I. Santillana, C. Santini, O. Santos, P. S. Diaz, K. Sasaki, F. Savary, A. Sbrizzi, M. Schaumann, C. Scheuerlein, J. Schmalzle, H. Schmickler, R. Schmidt, D. Schoerling, M. Segreti, M. Serluca, J. Serrano, J. Sestak, E. Shaposhnikova, D. Shatilov, A. Siemko, M. Sisti, M. Sitko, J. Skarita, E. Skordis, K. Skoufaris, G. Skripka, D. Smekens, Z. Sobiech, M. Sosin, F. Soubelet, B. Spataro, G. Spiezia, G. Stancari, J. Steckert, G. Steele, G. Sterbini, M. Struik, M. Sugano, A. Szeberenyi, M. Taborelli, C. Tambasco,

R. T. Rego, L. Tavian, B. Teissandier, N. Templeton, M. Therasse, H. Thiesen, E. Thomas, A. Toader, E. Todesco, R. Tomás, F. Toral, R. Torres-Sanchez, G. Trad, N. Triantafyllou, I. Tropin, A. Tsinganis, J. Tuckamantel, J. Uythoven, A. Valishev, F. Van Der Veken, R. Van Weelderen, A. Vande Craen, B. Vazquez De Prada, F. Velotti, S. Verdu Andres, A. Verweij, N. V. Shetty, V. Vlachoudis, G. Volpini, U. Wagner, P. Wanderer, M. Wang, X. Wang, R. Wanzenberg, A. Wegscheider, S. Weisz, C. Welsch, M. Wendt, J. Wenninger, W. Weterings, S. White, K. Widuch, A. Will, G. Willering, D. Wollmann, A. Wolski, J. Wozniak, Q. Wu, B. Xiao, L. Xiao, Q. Xu, Y. Yakovlev, S. Yammine, Y. Yang, M. Yu, I. Zacharov, O. Zagorodnova, C. Zannini, C. Zanoni, M. Zerlauth, F. Zimmermann, A. Zlobin, M. Zobov, I. Zurbano Fernandez, High-Luminosity Large Hadron Collider (HL-LHC): Technical design report, CERN Yellow Reports: Monographs, CERN, Geneva, 2020. doi:10.23731/CYRM-2020-0010.

[5] T. L. collaboration, Precision luminosity measurements at LHCb, Journal of Instrumentation 9 (12) (2014) P12005–P12005. doi:10.1088/1748-0221/9/12/p12005.
URL https://doi.org/10.1088%2F1748-0221%2F9%2F12%2Fp12005

[6] P. Hopchev, Absolute luminosity measurements at LHCb, Ph.D. thesis, presented 25 Nov 2011 (2011).
URL https://cds.cern.ch/record/1433396

[7] C. Barschel, Precision luminosity measurement at LHCb with beam-gas imaging, Ph.D. thesis, presented 05 Mar 2014 (2014).
URL https://cds.cern.ch/record/1693671

[8] B. Wurkner, Measurement of the LHC Beam Profile Using the Beam Gas Vertex Detector, Ph.D. thesis, ph.D. thesis, Vienna, Tech. University, Germany (2019).
URL https://cds.cern.ch/record/2702690

[9] F. Landua, The CERN accelerator complex layout in 2022. Complexe des accélérateurs du CERN en janvier 2022General Photo.
URL http://cds.cern.ch/record/2813716

[10] H. Damerau, A. Funken, R. Garoby, S. Gilardoni, B. Goddard, K. Hanke, A. Lombardi, D. Manglunki, M. Meddahi, B. Mikulec, G. Rumolo, E. Shaposhnikova, M. Vretenar, J. Coupard, LHC Injectors Upgrade, Technical Design Report, 2014.

doi:10.17181/CERN.7NHR.6HGC.
URL http://cds.cern.ch/record/1976692

[11] The 300 GeV programme, CERN, Geneva, 1972, french version available : Le programme 300 GeV.
URL https://cds.cern.ch/record/104068

[12] W. Herr, B. Muratori, Concept of luminosity.
URL http://cds.cern.ch/record/941318

[13] Longer term lhc schedule.
URL https://lhc-commissioning.web.cern.ch/schedule/LHC-long-term.htm

[14] R. Bruce, T. Argyropoulos, H. Bartosik, R. De Maria, N. Fuster Martinez, M. A. Jebramcik, J. Jowett, N. Mounet, S. Redaelli, G. Rumolo, M. Schaumann, H. Timko, HL-LHC operational scenarios for Pb-Pb and p-Pb operation, Tech. rep., CERN, Geneva (Jul 2020).
URL http://cds.cern.ch/record/2722753

[15] E. J. N. Wilson, An introduction to particle accelerators, Oxford Univ. Press, Oxford, 2001.
URL https://cds.cern.ch/record/513326

[16] D. A. Edwards, M. J. Syphers, An introduction to the physics of high energy accelerators, Wiley, 1993. doi:10.1002/9783527617272.

[17] S. Redaelli, Beam cleaning and collimation systems, CERN Yellow Reports (2016) Vol 2 (2016): Proceedings of the 2014 Joint International Accelerator School: Beam Loss and Accelerator Protectiondoi:10.5170/CERN-2016-002.403.
URL https://e-publishing.cern.ch/index.php/CYR/article/view/243

[18] A. W. Chao, Physics of collective beam instabilities in high-energy accelerators, 1993.

[19] B. W. Zotter, S. Kheifets, Impedances and Wakes in High Energy Particle Accelerators, WORLD SCIENTIFIC, 1998. doi:10.1142/3068.

[20] E. Métral, T. Argyropoulos, H. Bartosik, N. Biancacci, X. Buffat, J. F. Esteban Muller, W. Herr, G. Iadarola, A. Lasheen, K. Li, A. Oeftiger, T. Pieloni,

D. Quartullo, G. Rumolo, B. Salvant, M. Schenk, E. Shaposhnikova, C. Tambasco, H. Timko, C. Zannini, A. Burov, D. Banfi, J. Barranco, N. Mounet, O. Boine-Frankenheim, U. Niedermayer, V. Kornilov, S. White, Beam Instabilities in Hadron Synchrotrons, IEEE Trans. Nucl. Sci. 63 (2) (2016) 1001–1050. doi:10.1109/TNS.2015.2513752.
URL http://cds.cern.ch/record/2262299

[21] Computer simulation technology (cst) studio, 3d electromagnetic simulation software, https://www.cst.com.

[22] J. L. Sirvent Blasco, Beam secondary shower acquisition design for the CERN high accuracy wire scannerPresented 12 Dec 2018.
URL https://cds.cern.ch/record/2640438

[23] G. Trad, J.-M. De Conto, F. Roncarolo, Development and Optimisation of the SPS and LHC beam diagnostics based on Synchrotron Radiation monitors, presented 22 Jan 2015 (Oct 2014).
URL https://cds.cern.ch/record/2266055

[24] D. Butti, E. Bravin, S. Gibson, G. Trad, Recent LHC SR Interferometer Simulations and Experimental Results, JACoW IBIC 2022 (2022) 88–91. doi:10.18429/JACoW-IBIC2022-MOP23.
URL https://cds.cern.ch/record/2852572

[25] M. Sapinski, W. Andreazza, B. Dehning, A. Guerrero, M. Patecki, R. Versteegen, The first experience with LHC beam gas ionization monitor, Tech. rep., CERN, Geneva (2012).
URL https://cds.cern.ch/record/1495085

[26] S. Levasseur, Development of a Hybrid Pixel Detector Based Transverse Profile Monitor for the CERN Proton Synchrotron, Ph.D. thesis, Royal Holloway, U. of London, presented 05 Dec 2019 (2019).
URL http://cds.cern.ch/record/2720090

[27] T. L. Collaboration, A. A. A. Jr, L. M. A. Filho, A. F. Barbosa, I. Bediaga, G. Cernicchiaro, G. Guerrer, H. P. L. Jr, A. A. Machado, J. Magnin, F. Marujo, J. M. de Miranda, A. Reis, A. Santos, A. Toledo, K. Akiba, S. Amato, B. de Paula,

L. de Paula, T. da Silva, M. Gandelman, J. H. Lopes, B. Maréchal, D. Moraes, E. Polycarpo, F. Rodrigues, J. Ballansat, Y. Bastian, D. Boget, I. D. Bonis, V. Coco, P. Y. David, D. Decamp, P. Delebecque, C. Drancourt, N. Dumont-Dayot, C. Girard, B. Lieunard, M. N. Minard, B. Pietrzyk, T. Rambure, G. Rospabe, S. T'Jampens, Z. Ajaltouni, G. Bohner, R. Bonnefoy, D. Borras, C. Carloganu, H. Chanal, E. Conte, R. Cornat, M. Crouau, E. Delage, O. Deschamps, P. Henrard, P. Jacquet, C. Lacan, J. Laubser, J. Lecoq, R. Lefèvre, M. Magne, M. Martemiyanov, M.-L. Mercier, S. Monteil, V. Niess, P. Perret, G. Reinmuth, A. Robert, S. Suchorski, K. Arnaud, E. Aslanides, J. Babel, C. Benchouk, J.-P. Cachemiche, J. Cogan, F. Derue, B. Dinkespiler, P.-Y. Duval, V. Garonne, S. Favard, R. L. Gac, F. Leon, O. Leroy, P.-L. Liotard, F. Marin, M. Menouni, P. Ollive, S. Poss, A. Roche, M. Sapunov, L. Tocco, B. Viaud, A. Tsaregorodtsev, Y. Amhis, G. Barrand, S. Barsuk, C. Beigbeder, R. Beneyton, D. Breton, O. Callot, D. Charlet, B. D'Almagne, O. Duarte, F. Fulda-Quenzer, A. Jacholkowska, B. Jean-Marie, J. Lefrancois, F. Machefert, P. Robbe, M.-H. Schune, V. Tocut, I. Videau, M. Benayoun, P. David, L. D. Buono, G. Gilles, M. Domke, H. Futterschneider, C. Ilgner, P. Kapusta, M. Kolander, R. Krause, M. Lieng, M. Nedos, K. Rudloff, S. Schleich, R. Schwierz, B. Spaan, K. Wacker, K. Warda, M. Agari, C. Bauer, D. Baumeister, N. Bulian, H. P. Fuchs, W. Fallot-Burghardt, T. Glebe, W. Hofmann, K. T. Knöpfle, S. Löchner, A. Ludwig, F. Maciuc, F. S. Nieto, M. Schmelling, B. Schwingenheuer, E. Sexauer, N. J. Smale, U. Trunk, H. Voss, J. Albrecht, S. Bachmann, J. Blouw, M. Deissenroth, H. Deppe, H. B. Dreis, F. Eisele, T. Haas, S. Hansmann-Menzemer, S. Hennenberger, J. Knopf, M. Moch, A. Perieanu, S. Rabenecker, A. Rausch, C. Rummel, R. Rusnyak, M. Schiller, U. Stange, U. Uwer, M. Walter, R. Ziegler, G. Avoni, G. Balbi, F. Bonifazi, D. Bortolotti, A. Carbone, I. D'Antone, D. Galli, D. Gregori, I. Lax, U. Marconi, G. Peco, V. Vagnoni, G. Valenti, S. Vecchi, W. Bonivento, A. Cardini, S. Cadeddu, V. DeLeo, C. Deplano, S. Furcas, A. Lai, R. Oldeman, D. Raspino, B. Saitta, N. Serra, W. Baldini, S. Brusa, S. Chiozzi, A. C. Ramusino, F. Evangelisti, A. Franconieri, S. Germani, A. Gianoli, L. Guoming, L. Landi, R. Malaguti, C. Padoan, C. Pennini, M. Savriè, S. Squerzanti, T. Zhao, M. Zhu, A. Bizzeti, G. Graziani, M. Lenti, M. Lenzi, F. Maletta, S. Pennazzi, G. Passaleva, M. Veltri, M. Alfonsi, M. Anelli, A. Balla, A. Battisti, G. Bencivenni, P. Campana, M. Carletti, P. Ciambrone, G. Corradi, E. Dané, A. DiVirgilio,

P. DeSimone, G. Felici, C. Forti, M. Gatta, G. Lanfranchi, F. Murtas, M. Pistilli, M. P. Lener, R. Rosellini, M. Santoni, A. Saputi, A. Sarti, A. Sciubba, A. Zossi, M. Ameri, S. Cuneo, F. Fontanelli, V. Gracco, G. Miní, M. Parodi, A. Petrolini, M. Sannino, A. Vinci, M. Alemi, C. Arnaboldi, T. Bellunato, M. Calvi, F. Chignoli, A. D. Lucia, G. Galotta, R. Mazza, C. Matteuzzi, M. Musy, P. Negri, D. Perego, G. Pessina, G. Auriemma, V. Bocci, A. Buccheri, G. Chiodi, S. D. Marco, F. Iacoangeli, G. Martellotti, R. Nobrega, A. Pelosi, G. Penso, D. Pinci, W. Rinaldi, A. Rossi, R. Santacesaria, C. Satriano, G. Carboni, M. Iannilli, A. M. Rodrigues, R. Messi, G. Paoluzzi, G. Sabatino, E. Santovetti, A. Satta, J. Amoraal, G. van Apeldoorn, R. Arink, N. van Bakel, H. Band, T. Bauer, A. Berkien, M. van Beuzekom, E. Bos, C. Bron, L. Ceelie, M. Doets, R. van der Eijk, J.-P. Fransen, P. de Groen, V. Gromov, R. Hierck, J. Homma, B. Hommels, W. Hoogland, E. Jans, F. Jansen, L. Jansen, M. Jaspers, B. Kaan, B. Koene, J. Koopstra, F. Kroes, M. Kraan, J. Langedijk, M. Merk, S. Mos, B. Munneke, J. Palacios, A. Papadelis, A. Pellegrino, O. van Petten, T. du Pree, E. Roeland, W. Ruckstuhl, A. Schimmel, H. Schuijlenburg, T. Sluijk, J. Spelt, J. Stolte, H. Terrier, N. Tuning, A. V. Lysebetten, P. Vankov, J. Verkooijen, B. Verlaat, W. Vink, H. de Vries, L. Wiggers, G. Y. Smit, N. Zaitsev, M. Zupan, A. Zwart, J. van den Brand, H. J. Bulten, M. de Jong, T. Ketel, S. Klous, J. Kos, B. M'charek, F. Mul, G. Raven, E. Simioni, J. Cheng, G. Dai, Z. Deng, Y. Gao, G. Gong, H. Gong, J. He, L. Hou, J. Li, W. Qian, B. Shao, T. Xue, Z. Yang, M. Zeng, B. Muryn, K. Ciba, A. Oblakowska-Mucha, J. Blocki, K. Galuszka, L. Hajduk, J. Michalowski, Z. Natkaniec, G. Polok, M. Stodulski, M. Witek, K. Brzozowski, A. Chlopik, P. Gawor, Z. Guzik, A. Nawrot, A. Srednicki, K. Syryczynski, M. Szczekowski, D. V. Anghel, A. Cimpean, C. Coca, F. Constantin, P. Cristian, D. D. Dumitru, D. T. Dumitru, G. Giolu, C. Kusko, C. Magureanu, G. Mihon, M. Orlandea, C. Pavel, R. Petrescu, S. Popescu, T. Preda, A. Rosca, V. L. Rusu, R. Stoica, S. Stoica, P. D. Tarta, S. Filippov, Y. Gavrilov, L. Golyshkin, E. Gushchin, O. Karavichev, V. Klubakov, L. Kravchuk, V. Kutuzov, S. Laptev, S. Popov, A. Aref'ev, B. Bobchenko, V. Dolgoshein, V. Egorychev, A. Golutvin, O. Gushchin, A. Konoplyannikov, I. Korolko, T. Kvaratskheliya, I. Machikhiliyan, S. Malyshev, E. Mayatskaya, M. Prokudin, D. Rusinov, V. Rusinov, P. Shatalov, L. Shchutska, E. Tarkovskiy, A. Tayduganov, K. Voronchev, O. Zhiryakova, A. Bobrov, A. Bondar, S. Eidelman, A. Kozlinsky, L. Shekhtman, K. S. Beloous, R. I.

Dzhelyadin, Y. V. Gelitsky, Y. P. Gouz, K. G. Kachnov, A. S. Kobelev, V. D. Matveev, V. P. Novikov, V. F. Obraztsov, A. P. Ostankov, V. I. Romanovsky, V. I. Rykalin, A. P. Soldatov, M. M. Soldatov, E. N. Tchernov, O. P. Yushchenko, B. Bochin, N. Bondar, O. Fedorov, V. Golovtsov, S. Guets, A. Kashchuk, V. Lazarev, O. Maev, P. Neustroev, N. Sagidova, E. Spiridenkov, S. Volkov, A. Vorobyev, A. Vorobyov, E. Aguilo, S. Bota, M. Calvo, A. Comerma, X. Cano, A. Dieguez, A. Herms, E. Lopez, S. Luengo, J. Garra, L. Garrido, D. Gascon, A. G. de Valenzuela, C. Gonzalez, R. Graciani, E. Grauges, A. P. Calero, E. Picatoste, J. Riera, M. Rosello, H. Ruiz, X. Vilasis, X. Xirgu, B. Adeva, X. C. Vidal, D. M. Santos, D. E. Pereira, J. L. F. Pazos, A. G. Torreira, C. L. Gómez, A. P. Alvarez, E. P. Trigo, M. P. Casasús, C. R. Cobo, P. R. Pérez, J. J. Saborido, M. Seco, P. V. Regueiro, P. Bartalini, A. Bay, M.-O. Bettler, F. Blanc, J. Borel, B. Carron, C. Currat, G. Conti, O. Dormond, Y. Ermoline, P. Fauland, L. Fernandez, R. Frei, G. Gagliardi, N. Gueissaz, G. Haefeli, A. Hicheur, C. Jacoby, P. Jalocha, S. Jimenez-Otero, J.-P. Hertig, M. Knecht, F. Legger, L. Locatelli, J.-R. Moser, M. Needham, L. Nicolas, A. Perrin-Giacomin, J.-P. Perroud, C. Potterat, F. Ronga, O. Schneider, T. Schietinger, D. Steele, L. Studer, M. Tareb, M. T. Tran, J. van Hunen, K. Vervink, S. Villa, N. Zwahlen, R. Bernet, A. Büchler, J. Gassner, F. Lehner, T. Sakhelashvili, C. Salzmann, P. Sievers, S. Steiner, O. Steinkamp, U. Straumann, J. van Tilburg, A. Vollhardt, D. Volyanskyy, M. Ziegler, A. Dovbnya, Y. Ranyuk, I. Shapoval, M. Borisova, V. Iakovenko, V. Kyva, O. Kovalchuk, O. Okhrimenko, V. Pugatch, Y. Pylypchenko, M. Adinolfi, N. H. Brook, R. D. Head, J. P. Imong, K. A. Lessnoff, F. C. D. Metlica, A. J. Muir, J. H. Rademacker, A. Solomin, P. M. Szczypka, C. Barham, C. Buszello, J. Dickens, V. Gibson, S. Haines, K. Harrison, C. R. Jones, S. Katvars, U. Kerzel, C. Lazzeroni, Y. Y. Li, G. Rogers, J. Storey, H. Skottowe, S. A. Wotton, T. J. Adye, C. J. Densham, S. Easo, B. Franek, P. Loveridge, D. Morrow, J. V. Morris, R. Nandakumar, J. Nardulli, A. Papanestis, G. N. Patrick, S. Ricciardi, M. L. Woodward, Z. Zhang, R. J. U. Chamonal, P. J. Clark, P. Clarke, S. Eisenhardt, N. Gilardi, A. Khan, Y. M. Kim, R. Lambert, J. Lawrence, A. Main, J. McCarron, C. Mclean, F. Muheim, A. F. Osorio-Oliveros, S. Playfer, N. Styles, Y. Xie, A. Bates, L. Carson, F. da Cunha Marinho, F. Doherty, L. Eklund, M. Gersabeck, L. Haddad, A. A. Macgregor, J. Melone, F. McEwan, D. M. Petrie, S. K. Paterson, C. Parkes, A. Pickford, B. Rakotomiaramanana, E. Rodrigues, A. F. Saavedra,

F. J. P. Soler, T. Szumlak, S. Viret, L. Allebone, O. Awunor, J. Back, G. Barber, C. Barnes, B. Cameron, D. Clark, I. Clark, P. Dornan, A. Duane, C. Eames, U. Egede, M. Girone, S. Greenwood, R. Hallam, R. Hare, A. Howard, S. Jolly, V. Kasey, M. Khaleeq, P. Koppenburg, D. Miller, R. Plackett, D. Price, W. Reece, P. Savage, T. Savidge, B. Simmons, G. Vidal-Sitjes, D. Websdale, A. Affolder, J. S. Anderson, S. F. Biagi, T. J. V. Bowcock, J. L. Carroll, G. Casse, P. Cooke, S. Donleavy, L. Dwyer, K. Hennessy, T. Huse, D. Hutchcroft, D. Jones, M. Lockwood, M. McCubbin, R. McNulty, D. Muskett, A. Noor, G. D. Patel, K. Rinnert, T. Shears, N. A. Smith, G. Southern, I. Stavitski, P. Sutcliffe, M. Tobin, S. M. Traynor, P. Turner, M. Whitley, M. Wormald, V. Wright, J. H. Bibby, S. Brisbane, M. Brock, M. Charles, C. Cioffi, V. V. Gligorov, T. Handford, N. Harnew, F. Harris, M. J. J. John, M. Jones, J. Libby, L. Martin, I. A. McArthur, R. Muresan, C. Newby, B. Ottewell, A. Powell, N. Rotolo, R. S. Senanayake, L. Somerville, A. Soroko, P. Spradlin, P. Sullivan, I. Stokes-Rees, S. Topp-Jorgensen, F. Xing, G. Wilkinson, M. Artuso, I. Belyaev, S. Blusk, G. Lefeuvre, N. Menaa, R. Menaa-Sia, R. Mountain, T. Skwarnicki, S. Stone, J. C. Wang, L. Abadie, G. Aglieri-Rinella, E. Albrecht, J. André, G. Anelli, N. Arnaud, A. Augustinus, F. Bal, M. C. B. Pazos, A. Barczyk, M. Bargiotti, J. B. Lopes, O. Behrendt, S. Berni, P. Binko, V. Bobillier, A. Braem, L. Brarda, J. Buytaert, L. Camilleri, M. Cambpell, G. Castellani, F. Cataneo, M. Cattaneo, B. Chadaj, P. Charpentier, S. Cherukuwada, E. Chesi, J. Christiansen, R. Chytracek, M. Clemencic, J. Closier, P. Collins, P. Colrain, O. Cooke, B. Corajod, G. Corti, C. D'Ambrosio, B. Damodaran, C. David, S. de Capua, G. Decreuse, H. Degaudenzi, H. Dijkstra, J.-P. Droulez, D. D. Ramos, J. P. Dufey, R. Dumps, D. Eckstein, M. Ferro-Luzzi, F. Fiedler, F. Filthaut, W. Flegel, R. Forty, C. Fournier, M. Frank, C. Frei, B. Gaidioz, C. Gaspar, J.-C. Gayde, P. Gavillet, A. Go, G. G. Abril, J.-S. Graulich, P.-A. Giudici, A. G. Elias, P. Guglielmini, T. Gys, F. Hahn, S. Haider, J. Harvey, B. Hay, J.-A. H. Morata, J. H. Alvarez, E. van Herwijnen, H. J. Hilke, G. von Holtey, W. Hulsbergen, R. Jacobsson, O. Jamet, C. Joram, B. Jost, N. Kanaya, J. K. Refolio, S. Koestner, M. Koratzinos, R. Kristic, D. Lacarrère, C. Lasseur, T. Lastovicka, M. Laub, D. Liko, C. Lippmann, R. Lindner, M. Losasso, A. Maier, K. Mair, P. Maley, P. M. Vila, G. Moine, J. Morant, M. Moritz, J. Moscicki, M. Muecke, H. Mueller, T. Nakada, N. Neufeld, J. Ocariz, C. P. Aranda, U. Parzefall, M. Patel, M. Pepe-Altarelli, D. Piedigrossi, M. Pivk, W. Pokorski,

S. Ponce, F. Ranjard, W. Riegler, J. Renaud, S. Roiser, A. Rossi, L. Roy, T. Ruf, D. Ruffinoni, S. Saladino, A. S. Varela, R. Santinelli, S. Schmelling, B. Schmidt, T. Schneider, A. Schöning, A. Schopper, J. Seguinot, W. Snoeys, A. Smith, A. C. Smith, P. Somogyi, R. Stoica, W. Tejessy, F. Teubert, E. Thomas, J. T. Alarcon, O. Ullaland, A. Valassi, P. Vannerem, R. Veness, P. Wicht, D. Wiedner, W. Witzeling, A. Wright, K. Wyllie, T. Ypsilantis, The lhcb detector at the lhc, Journal of Instrumentation 3 (08) (2008) S08005. doi:10.1088/1748-0221/3/08/S08005.
URL https://dx.doi.org/10.1088/1748-0221/3/08/S08005

[28] L. Collaboration, LHCb Tracker Upgrade Technical Design Report, Tech. rep. (2014).
URL https://cds.cern.ch/record/1647400

[29] A. Alexopoulos, C. Barchel, A. Bay, F. Blanc, E. Bravin, G. Bregliozzi, N. Chritin, B. Dehning, M. Ferro-Luzzi, S. Gianì, M. Giovannozzi, O. Girard, R. Greim, G. Haefeli, P. Hopchev, R. Jacobsson, L. Jensen, O. Rhodri Jones, V. Kain, W. Karpinski, T. Kirn, A. Kuonen, R. Matev, T. Nakada, M. Rihl, V. Salustino Guimaraes, S. Schael, O. Schneider, A. Schultz von Dratzig, G. Schwering, M. Tobin, R. Veness, Q. Veyrat, S. Vlachos, M. Wlochal, B. Wiirkner, Z. Xu, First LHC transverse beam size measurements with the beam gas vertex detector, J. Phys. : Conf. Ser. 874 (CERN-ACC-2017-315. 1) (2017) 012086. 6 p.
URL https://cds.cern.ch/record/2276055

[30] A. Lechner, B. Auchmann, T. Baer, C. Bahamonde Castro, R. Bruce, F. Cerutti, L. S. Esposito, A. Ferrari, J. M. Jowett, A. Mereghetti, F. Pietropaolo, S. Redaelli, B. Salvachua, M. Sapinski, M. Schaumann, N. V. Shetty, V. Vlachoudis, E. Skordis, Validation of energy deposition simulations for proton and heavy ion losses in the cern large hadron collider, Phys. Rev. Accel. Beams 22. doi:10.1103/PhysRevAccelBeams.22.071003.
URL https://link.aps.org/doi/10.1103/PhysRevAccelBeams.22.071003

[31] B. D. Leverington, The LHCb Upgrade Scintillating Fibre Tracker, PoS TIPP2014 (2014) 113. doi:10.22323/1.213.0113.
URL https://cds.cern.ch/record/2014696

[32] S. Papadopoulou, F. Antoniou, I. Efthymiopoulos, M. Hostettler, G. Iadarola, N. Karastathis, S. Kostoglou, Y. Papaphilippou, G. Trad, Monitoring and modelling of the LHC emittance and luminosity evolution in 2018 (2019) WEPTS046doi:10.18429/JACoW-IPAC2019-WEPTS046.
URL http://cds.cern.ch/record/2693256

[33] G. Trad, A. Alexopoulos, E. Bravin, D. Butti, R. Kieffer, F. Roncarolo, S. Vlachos, B. Wurkner, LHC Emittance Measurements in Run 2 (2019) 117–123.
URL https://cds.cern.ch/record/2750285

[34] G. Arduini, A. Dabrowski, M. Lamont, J. Wenninger, K. Wittenburg, Lhc beam size measurement review: Findings, comments and recommendations (2019).
URL https://indico.cern.ch/event/837340/attachments/1924743/3185135/LHC_Beam_Size_Measurement_Review_-_Findings_Comments_Recommendations.pdf

[35] Y. Papaphilippou, H. Bartosik, G. Rumolo, D. Manglunki, Operational Beams for the LHCdoi:10.5170/CERN-2015-002.80.
URL https://cds.cern.ch/record/2031187

[36] L. Lyons, A Practical Guide to Data Analysis for Physical Science Students, Cambridge University Press, 1991. doi:10.1017/CBO9781139170321.

[37] R. Alemany-Fernández, et al., Cross-Calibration of the LHC Transverse Beam-Profile Monitors, in: Proc. of International Particle Accelerator Conference (IPAC'17), Copenhagen, Denmark, May 2017, no. 8 in International Particle Accelerator Conference, JACoW, Geneva, Switzerland, 2017, pp. 437–440, https://doi.org/10.18429/JACoW-IPAC2017-MOPAB130. doi:https://doi.org/10.18429/JACoW-IPAC2017-MOPAB130.
URL http://jacow.org/ipac2017/papers/mopab130.pdf

[38] H. Ku, Notes on the use of propagation of error formulas, Journal of Research of the National Bureau of Standards. Section C: Engineering and Instrumentationdoi:https://dx.doi.org/10.6028/jres.070C.025.

[39] P. Hopchev, V. Baglin, C. Barschel, E. Bravin, G. Bregliozzi, N. Chritin, B. Dehning, M. Ferro-Luzzi, C. Gaspar, M. Giovannozzi, E. Van Herwijnen, R. Jacobsson,

L. Jensen, O. Rhodri Jones, N. Jurado, V. Kain, M. Kuhn, B. Luthi, P. Magagnin, R. Matev, N. Neufeld, J. Panman, M. Rihl, V. Salustino Guimaraes, B. Salvant, R. Veness, A. Bay, F. Blanc, S. Gianì, G. Haefeli, T. Nakada, B. Rakotomiaramanana, O. Schneider, M. Tobin, Q. Veyrat, Z. Xu, R. Greim, W. Karpinski, T. Kirn, S. Schael, A. Schultz Von Dratzig, G. Schwering, M. Wlochal, A beam gas vertex detector for beam size measurement in the LHC, IPAC 2014: Proceedings of the 5th International Particle Accelerator Conference (2014) 3680–3683doi:10.18429/JACoW-IPAC2014-THPME175.

[40] T. e. a. Pierog, Crmc (cosmic ray monte carlo package).
URL https://web.ikp.kit.edu/rulrich/crmc.html

[41] S. Boogert, et al., Pyg4ometry : A Tool to Create Geometries for Geant4, BDSIM, G4Beamline and FLUKA for Particle Loss and Energy Deposit Studies, in: Proc. 10th International Particle Accelerator Conference (IPAC'19), Melbourne, Australia, 19-24 May 2019, no. 10 in International Particle Accelerator Conference, JACoW Publishing, Geneva, Switzerland, 2019, pp. 3244–3247. doi:doi:10.18429/JACoW-IPAC2019-WEPTS054.

[42] S. Agostinelli, J. Allison, K. Amako, J. Apostolakis, H. Araujo, P. Arce, M. Asai, D. Axen, S. Banerjee, G. Barrand, F. Behner, L. Bellagamba, J. Boudreau, L. Broglia, A. Brunengo, H. Burkhardt, S. Chauvie, J. Chuma, R. Chytracek, G. Cooperman, G. Cosmo, P. Degtyarenko, A. Dell'Acqua, G. Depaola, D. Dietrich, R. Enami, A. Feliciello, C. Ferguson, H. Fesefeldt, G. Folger, F. Foppiano, A. Forti, S. Garelli, S. Giani, R. Giannitrapani, D. Gibin, J. Gómez Cadenas, I. González, G. Gracia Abril, G. Greeniaus, W. Greiner, V. Grichine, A. Grossheim, S. Guatelli, P. Gumplinger, R. Hamatsu, K. Hashimoto, H. Hasui, A. Heikkinen, A. Howard, V. Ivanchenko, A. Johnson, F. Jones, J. Kallenbach, N. Kanaya, M. Kawabata, Y. Kawabata, M. Kawaguti, S. Kelner, P. Kent, A. Kimura, T. Kodama, R. Kokoulin, M. Kossov, H. Kurashige, E. Lamanna, T. Lampén, V. Lara, V. Lefebure, F. Lei, M. Liendl, W. Lockman, F. Longo, S. Magni, M. Maire, E. Medernach, K. Minamimoto, P. Mora de Freitas, Y. Morita, K. Murakami, M. Nagamatu, R. Nartallo, P. Nieminen, T. Nishimura, K. Ohtsubo, M. Okamura, S. O'Neale, Y. Oohata, K. Paech, J. Perl, A. Pfeiffer, M. Pia, F. Ranjard, A. Rybin, S. Sadilov, E. Di Salvo, G. Santin, T. Sasaki, N. Savvas, Y. Sawada,

S. Scherer, S. Sei, V. Sirotenko, D. Smith, N. Starkov, H. Stoecker, J. Sulkimo, M. Takahata, S. Tanaka, E. Tcherniaev, E. Safai Tehrani, M. Tropeano, P. Truscott, H. Uno, L. Urban, P. Urban, M. Verderi, A. Walkden, W. Wander, H. Weber, J. Wellisch, T. Wenaus, D. Williams, D. Wright, T. Yamada, H. Yoshida, D. Zschiesche, Geant4 — a simulation toolkit, NIM A 506 (3) (2003) 250–303. doi:https://doi.org/10.1016/S0168-9002(03)01368-8.
URL https://www.sciencedirect.com/science/article/pii/S0168900203013688

[43] P. Zyla, et al., Review of Particle Physics, PTEP 2020 (8) (2020) 083C01. doi:10.1093/ptep/ptaa104.

[44] J. Carvalho, Compilation of cross sections for proton–nucleus interactions at the hera energy, Nuclear Physics A 725 (2003) 269–275. doi:https://doi.org/10.1016/S0375-9474(03)01597-5.
URL https://www.sciencedirect.com/science/article/pii/S0375947403015975

[45] M. Ferro-Luzzi, Beam-gas interactions (2020). arXiv:2006.06490.

[46] F. W. Bopp, J. Ranft, R. Engel, S. Roesler, Antiparticle to particle production ratios in hadron-hadron and d-au collisions in the dpmjet-iii monte carlo model, Phys. Rev. C 77 (2008) 014904. doi:10.1103/PhysRevC.77.014904.
URL https://link.aps.org/doi/10.1103/PhysRevC.77.014904

[47] H. Guerin, S. Gibson, O. Jones, R. Kieffer, B. Kolbinger, T. Lefèvre, B. Salvant, J. Storey, R. Veness, C. Zamantzas, The HL-LHC Beam Gas Vertex Monitor - Simulations for Design Optimisation and Performance Study, in: Proc. IPAC'21, no. 12 in International Particle Accelerator Conference, JACoW Publishing, Geneva, Switzerland, 2021, pp. 2120–2123, https://doi.org/10.18429/JACoW-IPAC2021-TUPAB278. doi:10.18429/JACoW-IPAC2021-TUPAB278.
URL https://jacow.org/ipac2021/papers/tupab278.pdf

[48] B. Kolbinger, S. Gibson, H. Guerin, O. Jones, R. Kieffer, T. Lefèvre, A. Salzburger, J. Storey, R. Veness, C. Zamantzas, The HL-LHC Beam Gas Vertex Monitor - Performance and Design Optimisation Using Simulations, in: Proc. IBIC'21, no. 10 in International Beam Instrumentation Conference, JACoW Publishing, Geneva,

Switzerland, 2021, pp. 249–253. doi:10.18429/JACoW-IBIC2021-TUPP21.
URL https://jacow.org/ibic2021/papers/tupp21.pdf

[49] F. Sauli, Gem: A new concept for electron amplification in gas detectors, Nuclear Instruments and Methods in Physics Research Section A: Accelerators, Spectrometers, Detectors and Associated Equipment 386 (2) (1997) 531–534. doi:https://doi.org/10.1016/S0168-9002(96)01172-2.
URL https://www.sciencedirect.com/science/article/pii/S0168900296011722

[50] F. Fallavollita, D. Fiorina, J. A. Merlin, Advanced aging study on triple-gem detectors, Journal of Physics: Conference Series 1498 (1) (2020) 012038. doi:10.1088/1742-6596/1498/1/012038.
URL https://dx.doi.org/10.1088/1742-6596/1498/1/012038

[51] M. Čarná, K. Dučevová, M. Hejtmánek, O. Konček, M. Marčišovský, Evaluation of the timepix chip radiation hardness using a 60co source, Nuclear Instruments and Methods in Physics Research Section A: Accelerators, Spectrometers, Detectors and Associated Equipment 732 (2013) 501–505, vienna Conference on Instrumentation 2013. doi:https://doi.org/10.1016/j.nima.2013.06.088.
URL https://www.sciencedirect.com/science/article/pii/S0168900213009340

[52] W. Snoeys, Advances in monolithic pixel detectors, Nuclear Instruments and Methods in Physics Research Section A: Accelerators, Spectrometers, Detectors and Associated Equipment (2024) 169481doi:https://doi.org/10.1016/j.nima.2024.169481.
URL https://www.sciencedirect.com/science/article/pii/S0168900224004078

[53] R. Kieffer, A. Alexopoulos, M. G. Berges, T. Marriott-Dodington, L. Fosse, O. Jones, S. Gibson, H. Guerin, J. Storey, R. Veyness, S. Vlachos, B. Wurkner, C. Zamantzas, The beam gas vertex profile monitoring station for HL-LHC, in: presented at the 12th Int. Particle Accelerator Conf. (IPAC'21), JACoW Publishing, 2019. doi:doi:10.18429/JACoW-IPAC2019-WEPGW082.

[54] V. Kudryavtsev, T. Maltsev, L. Shekhtman, Spatial resolution of triple-gem detectors, Nuclear Instruments and Methods in Physics Research Section A: Accelerators, Spectrometers, Detectors and Associated Equipment 936 (2019) 482–484, frontier Detectors for Frontier Physics: 14th Pisa Meeting on Advanced Detectors. doi:https://doi.org/10.1016/j.nima.2018.10.140.
URL https://www.sciencedirect.com/science/article/pii/S0168900218314542

[55] B. Ketzer, M. Altunbas, K. Dehmelt, J. Ehlers, J. Friedrich, B. Grube, S. Kappler, I. Konorov, S. Paul, A. Placci, L. Ropelewski, F. Sauli, L. Schmitt, F. Simon, Triple gem tracking detectors for compass, IEEE Transactions on Nuclear Science 49 (5) (2002) 2403–2410. doi:10.1109/TNS.2002.803891.

[56] N. Wermes, Pixel detectors for particle physics and imaging applications, Nuclear Instruments and Methods in Physics Research Section A: Accelerators, Spectrometers, Detectors and Associated Equipment 512 (1) (2003) 277–288, proceedings of the 9th European Symposium on Semiconductor Detectors: New Developments on Radiation Detectors. doi:https://doi.org/10.1016/S0168-9002(03)01905-3.
URL https://www.sciencedirect.com/science/article/pii/S0168900203019053

[57] X. Llopart, R. Ballabriga, M. Campbell, L. Tlustos, W. Wong, Timepix, a 65k programmable pixel readout chip for arrival time, energy and/or photon counting measurements, Nuclear Instruments and Methods in Physics Research Section A: Accelerators, Spectrometers, Detectors and Associated Equipment 581 (1) (2007) 485 – 494, vCI 2007. doi:https://doi.org/10.1016/j.nima.2007.08.079.
URL http://www.sciencedirect.com/science/article/pii/S0168900207017020

[58] T. Poikela, J. Plosila, T. Westerlund, M. Campbell, M. D. Gaspari, X. Llopart, V. Gromov, R. Kluit, M. van Beuzekom, F. Zappon, V. Zivkovic, C. Brezina, K. Desch, Y. Fu, A. Kruth, Timepix3: a 65k channel hybrid pixel readout chip with simultaneous ToA/ToT and sparse readout, Journal of Instrumentation 9 (05) (2014) C05013–C05013. doi:10.1088/1748-0221/9/05/c05013.
URL https://doi.org/10.1088%2F1748-0221%2F9%2F05%2Fc05013

[59] X. Llopart, J. Alozy, R. Ballabriga, M. Campbell, R. Casanova, V. Gromov, E. H. M. Heijne, T. Poikela, E. Santin, V. Sriskaran, L. Tlustos, A. Vitkovskiy, Timepix4, a large area pixel detector readout chip which can be tiled on 4 sides providing sub-200 ps timestamp binning, JINST 17 (01) (2022) C01044. doi:10.1088/1748-0221/17/01/C01044.
URL https://cds.cern.ch/record/2825271

[60] H. Sandberg, Development of a Novel Transverse Beam Profile and Emittance Monitor for the CERN Proton Synchrotron, Ph.D. thesis, Manchester U., presented 2020 (2020).
URL https://cds.cern.ch/record/2747870

[61] W. Snoeys, Monolithic pixel detectors for high energy physics, Nuclear Instruments and Methods in Physics Research Section A: Accelerators, Spectrometers, Detectors and Associated Equipment 731 (2013) 125–130, pIXEL 2012. doi:https://doi.org/10.1016/j.nima.2013.05.073.
URL https://www.sciencedirect.com/science/article/pii/S0168900213006840

[62] T. Fritzsch, K. Zoschke, M. Woehrmann, M. Rothermund, F. Huegging, O. Ehrmann, H. Oppermann, K. D. Lang, Flip chip assembly of thinned chips for hybrid pixel detector applications, Journal of Instrumentation 9 (05) (2014) C05039. doi:10.1088/1748-0221/9/05/C05039.
URL https://dx.doi.org/10.1088/1748-0221/9/05/C05039

[63] R. Bruce, C. Bracco, R. De Maria, M. Giovannozzi, S. Redaelli, R. Tomas Garcia, F. M. Velotti, J. Wenninger, Updated parameters for HL-LHC aperture calculations for proton beams, Tech. rep., CERN, Geneva (2017).
URL http://cds.cern.ch/record/2274330

[64] L. G. N. M. G. R. B. S. R. T. H. Bartosik, R. De Maria, 209th HiLumi WP2 Meeting (10 2022). [link].
URL https://indico.cern.ch/event/1211846/

[65] A. Vanmaele, M., External finite element approximations of eigenvalue problems, ESAIM: Mathematical Modelling and Numerical Analysis - Modélisation

Mathématique et Analyse Numérique 27 (5) (1993) 565–589.
URL http://eudml.org/doc/193715

[66] R. Bailey (Ed.), CAS - CERN Accelerator School: RF for Accelerators: Ebeltoft, Denmark 8 - 17 Jun 2010. Proceedings of the CAS - CERN Accelerator School: Specialised Course on RF for Accelerators, Ebeltoft, Denmark, 8 - 17 Jun 2010. CAS - CERN Accelerator School: RF for Accelerators, CERN, CERN, Geneva, 2012, comments: 20 lectures, 460 pages. doi:10.5170/CERN-2011-007.
URL http://cds.cern.ch/record/1231364

[67] B. Salvant, private communication.

[68] H. Padamsee, J. Knobloch, T. Hays, RF Superconductivity for Accelerators, Wiley Series in Beam Physics and Accelerator Technology, Wiley, 1998.
URL https://books.google.fr/books?id=2leaQgAACAAJ

[69] P. Baudrenghien, M. Angoletta, T. Argyropoulos, L. Arnaudon, T. Bohl, O. Brunner, A. Butterworth, E. Ciapala, F. Dubouchet, J. Esteban-Muller, J. Ferreira-Bento, D. Glenat, G. Hagmann, W. Hofle, D. Jacquet, M. Jaussi, S. Kouzue, D. Landre, J. Lollierou, P. Maesen, P. M. Yanez, T. Mastoridis, J. Molendijk, C. Nicou, J. Noirjean, G. Papotti, A. Pashnin, G. Pechaud, J. Pradier, J. Sanchez-Quesada, E. Shaposhnikova, M. Schokker, D. Stellfeld, J. Tuckmantel, D. Valuch, U. Wehrle, F. Weierud, The LHC RF System - Experience with Beam Operation, in: Proc. of IPAC 2011, San Sebastian, Spain, 2011.
URL https://accelconf.web.cern.ch/IPAC2011/papers/mopc054.pdf

[70] M. T. Ramos Garcia, S. G., private communication.

[71] CATIA.
URL https://www.3ds.com/fr/produits-et-services/catia/

[72] C. Benvenuti, J. Cazeneuve, P. Chiggiato, F. Cicoira, A. Escudeiro Santana, V. Johanek, V. Ruzinov, J. Fraxedas, A novel route to extreme vacua: the non-evaporable getter thin film coatings, Vacuum 53 (1) (1999) 219–225. doi:https://doi.org/10.1016/S0042-207X(98)00377-7.
URL https://www.sciencedirect.com/science/article/pii/S0042207X98003777

[73] C. Benvenuti, P. Chiggiato, P. Costa Pinto, A. Escudeiro Santana, T. Hedley, A. Mongelluzzo, V. Ruzinov, I. Wevers, Vacuum properties of tizrv non-evaporable getter films, Vacuum 60 (1) (2001) 57–65, the Sixth European Vacuum Conference. doi:https://doi.org/10.1016/S0042-207X(00)00246-3.
URL https://www.sciencedirect.com/science/article/pii/S0042207X00002463

[74] F. Mazzolini, The use of NEG pumps and coatings in large vacuum systems: experience and limitationsdoi:10.5170/CERN-2007-003.341.
URL https://cds.cern.ch/record/1047075

[75] H. Henke, W. Bruns, Calculation of Wake Potentials in General 3D Structures, in: Proc. of EPAC 2006, Edinburgh, Scotland, 2006.
URL https://cds.cern.ch/record/1078921

[76] I. Karpov, private communication.

[77] S. Calatroni, private communication.

[78] J. T. Dorothy Hoffman, Bawa Singh, Handbook of Vacuum Science and Technology.

[79] J. Ullrich, R. Moshammer, A. Dorn, R. Dörner, L. P. H. Schmidt, H. Schmidt-Böcking, Recoil-ion and electron momentum spectroscopy: reaction-microscopes, Reports on Progress in Physics 66 (9) (2003) 1463. doi:10.1088/0034-4885/66/9/203.
URL https://dx.doi.org/10.1088/0034-4885/66/9/203

[80] V. Tzoganis, C. P. Welsch, A non-invasive beam profile monitor for charged particle beams, Applied Physics Letters 104 (20) (2014) 204104. arXiv:https://pubs.aip.org/aip/apl/article-pdf/doi/10.1063/1.4879285/14301816/204104_1_online.pdf, doi:10.1063/1.4879285.
URL https://doi.org/10.1063/1.4879285

[81] H. Zhang, A. Alexandrova, A. Jeff, V. Tzoganis, C. Welsch, Characterizing Supersonic Gas Jet-based Beam Profile Monitors (2016) MOPMR046doi:10.18429/JACoW-IPAC2016-MOPMR046.
URL https://cds.cern.ch/record/2207319

[82] A. Salehilashkajani, H. D. Zhang, M. Ady, N. Chritin, P. Forck, J. Glutting, O. R. Jones, R. Kersevan, N. Kumar, T. Lefevre, T. Marriott-Dodington, S. Mazzoni, I. Papazoglou, A. Rossi, G. Schneider, O. Sedlacek, S. Udrea, R. Veness, C. P. Welsch, A gas curtain beam profile monitor using beam induced fluorescence for high intensity charged particle beams, Applied Physics Letters 120 (17) (2022) 174101. arXiv:https://pubs.aip.org/aip/apl/article-pdf/doi/10.1063/5.0085491/16480328/174101_1_online.pdf, doi:10.1063/5.0085491.
URL https://doi.org/10.1063/5.0085491

[83] O. Sedlacek, O. Stringer, C. Welsch, A. Webber-Date, H. Zhang, M. Ady, A. R. Churchman, S. Mazzoni, A. Rossi, M. Sameed, G. Schneider, C. C. Sequeiro, K. Sidorowski, R. Veness, P. Forck, S. Udrea, Gas Jet Based Fluorescence Profile Monitor for Low Energy Electrons and High Energy Protons at LHC, in: Proc. IBIC'23, International Beam Instrumentation Conference, 2023. doi:https://doi.org/10.18429/JACoW-IBIC2023-WE3I01.

[84] R. Veness, M. Ady, C. C. Sequeiro, P. Forck, N. Kumar, T. Lefèvre, S. Mazzoni, I. Papazoglou, A. Rossi, A. Salehilashkajani, G. Schneider, O. Sedláček, K. Sidorowski, O. Stringer, S. Udrea, C. Welsch, H. Zhang, Design of a Prototype Gas Jet Profile Monitor for Installation Into the Large Hadron Collider at CERN, in: Proc. 13th International Particle Accelerator Conference (IPAC'22), no. 13 in International Particle Accelerator Conference, JACoW Publishing, Geneva, Switzerland, 2022, pp. 363–366. doi:10.18429/JACoW-IPAC2022-MOPOPT048.
URL https://jacow.org/ipac2022/papers/mopopt048.pdf

[85] A. M. Hansen, D. Haberberger, J. Katz, D. Mastrosimone, R. K. Follett, D. H. Froula, Supersonic gas-jet characterization with interferometry and Thomson scattering on the OMEGA Laser System, Review of Scientific Instruments 89 (10) (2018) 10C103. arXiv:https://pubs.aip.org/aip/rsi/article-pdf/doi/10.1063/1.5036645/16721554/10c103_1_online.pdf, doi:10.1063/1.5036645.
URL https://doi.org/10.1063/1.5036645

[86] G. Bregliozzi, Neon Venting of Activated NEG Beam Pipes in the CERN LHC Long Straight Sections without Losing Vacuum Performance, in: Particle Accelerator Conference (PAC 09), 2010, p. MO6RFP006.

[87] A. Rossi, Estimates of Residual Gas Density in the LHCdoi:10.5170/CERN-2009-003.26.
URL https://cds.cern.ch/record/1184445

[88] A. F. Ismail, Gas separation membranes : polymeric and inorganic, Springer, 2015. doi:10.1007/978-3-319-01095-3.

[89] D. W. Breck, Zeolite molecular sieves: structure, chemistry, and use [by] Donald W. Breck, Wiley, 1973.

[90] R. Kersevan, M. Ady, Recent Developments of Monte-Carlo Codes Molflow+ and Synrad+, in: Proc. 10th International Particle Accelerator Conference (IPAC'19), Melbourne, Australia, 19-24 May 2019, no. 10 in International Particle Accelerator Conference, Geneva, Switzerland, 2019, pp. 1327–1330, melbourne, Australia. doi:doi:10.18429/JACoW-IPAC2019-TUPMP037.

[91] R. Kersevan, private communication.

[92] D. S, Scientific Foundations of Vacuum Technique , New York: Wiley, 1962.

[93] A. Galloro, private communication (2022).

[94] D. Prelipcean, BGV beam-gas collisions at IR4 and related radiation levels and heat loads (2 2022).
URL https://indico.cern.ch/event/1129683/

[95] D. Prelipcean, Radiation levels produced by the operation of the beam gas vertex monitor in the lhc tunnel at ir4, in: Proc. 14th International Particle Accelerator Conference, no. 14 in IPAC'23 - 14th International Particle Accelerator Conference, JACoW Publishing, Geneva, Switzerland, 2023, pp. 4578–4581. doi:doi:10.18429/jacow-ipac2023-thpl082.
URL https://indico.jacow.org/event/41/contributions/2501

[96] Radiation to electronics (R2E) at CERN.
URL https://r2e.web.cern.ch/

[97] M. Brugger, R2E and availability, in: In. Proc. of Workshop on LHC Performance, Chamonix, France, 2014.

[98] R. Alia, M. Brugger, F. Cerutti, S. Danzeca, A. Ferrari, S. Gilardoni, Y. Kadi, M. Kastriotou, A. Lechner, C. Martinella, O. Stein, Y. Thurel, A. Tsinganis, S. Uznanski, LHC and HL-LHC: Present and future radiation environment in the high-luminosity collision points and rha implications, IEEE Transactions on Nuclear Science PP (2017) 1–1. doi:10.1109/TNS.2017.2776107.

[99] E. B. Holzer, B. Dehning, E. Effinger, J. Emery, G. Ferioli, J. Gonzalez, E. Gschwendtner, G. Guaglio, M. Hodgson, D. Kramer, R. Leitner, L. Ponce, V. Prieto, M. Stockner, C. Zamantzas, Beam loss monitoring system for the lhc, IEEE Nuclear Science Symposium 2 (2005) 1052 – 1056. doi:10.1109/NSSMIC.2005.1596433.

[100] G. Spiezia, P. Peronnard, A. Masi, M. Brugger, M. Brucoli, S. Danzeca, R. G. Alia, R. Losito, J. Mekki, P. Oser, R. Gaillard, L. Dusseau, A new radmon version for the lhc and its injection lines, IEEE Transactions on Nuclear Science 61 (6) (2014) 3424–3431. doi:10.1109/TNS.2014.2365046.

[101] N. Mokhov, I. Rakhno, I. Tropin, F. Cerutti, L. Esposito, A. Lechner, Energy deposition studies for the High-Luminosity Large Hadron Collider inner triplet magnets. Energy Deposition Studies for the High-Luminosity Large Hadron Collider Inner Triplet Magnets, Phys. Rev. Spec. Top. Accel. Beams 18 (2015) 051001, 24 pp. arXiv:1504.00594, doi:10.1103/PhysRevSTAB.18.051001.
URL https://cds.cern.ch/record/2006710

[102] D. Prelipcean, Comparison between measured radiation levels and FLUKA simulations at CHARM and in the LHC tunnel of P1-5 within the R2E project in Run 2, presented 29 Jul 2021 (2021).
URL https://cds.cern.ch/record/2777059

[103] K. Biłko, C. Bahamonde Castro, M. Brugger, R. García Alía, Y. Kadi, A. Lechner, G. Lerner, O. Stein, Radiation Environment in the LHC Arc Sections During Run 2 and Future HL-LHC Operations, IEEE Trans. Nucl. Sci. 67 (7) (2020) 1682–1690. doi:10.1109/TNS.2020.2970168.

[104] D. Möhl, Sources of emittance growthdoi:doi:10.5170/CERN-2006-012.45.
URL https://cds.cern.ch/record/1005037

[105] M. Kuhn, Transverse Emittance Measurement and Preservation at the LHC, Ph.D. thesis, Hamburg U. (2016).

[106] S. Papadopoulou, F. Antoniou, I. Efthymiopoulos, M. Hostettler, G. Iadarola, N. Karastathis, S. Kostoglou, Y. Papaphilippou, G. Trad, What do we understand on the Emittance Growth? (2019) 199–205.
URL https://cds.cern.ch/record/2750416

[107] F. Zimmermann, Electron cloud effects in the LHCdoi:10.5170/CERN-2002-001.47.
URL https://cds.cern.ch/record/585562

[108] G. Bregliozzi, private communication (2022).

[109] T. C. Collaboration, Description and performance of track and primary-vertex reconstruction with the cms tracker, Journal of Instrumentation 9 (10) (2014) P10009. doi:10.1088/1748-0221/9/10/P10009.
URL https://dx.doi.org/10.1088/1748-0221/9/10/P10009